



HAL
open science

Multi-component gauge-dependent quantum gases

Nicolas Victorin

► **To cite this version:**

Nicolas Victorin. Multi-component gauge-dependent quantum gases. Quantum Gases [cond-mat.quant-gas]. Université Grenoble Alpes, 2019. English. NNT : 2019GREAY049 . tel-02513450

HAL Id: tel-02513450

<https://theses.hal.science/tel-02513450>

Submitted on 20 Mar 2020

HAL is a multi-disciplinary open access archive for the deposit and dissemination of scientific research documents, whether they are published or not. The documents may come from teaching and research institutions in France or abroad, or from public or private research centers.

L'archive ouverte pluridisciplinaire **HAL**, est destinée au dépôt et à la diffusion de documents scientifiques de niveau recherche, publiés ou non, émanant des établissements d'enseignement et de recherche français ou étrangers, des laboratoires publics ou privés.

THÈSE

Pour obtenir le grade de

DOCTEUR DE LA COMMUNAUTE UNIVERSITE GRENOBLE ALPES

Spécialité : **Physique théorique**

Arrêté ministériel : 25 mai 2016

Présentée par

Nicolas VICTORIN

Thèse dirigée par **Anna Minguzzi**, Directeur de Recherche CNRS

préparée au sein du **Laboratoire de Physique et de
Modélisation des Milieux Condensés** dans l'**École Doctorale
de Physique**

Gaz quantiques à plusieurs composantes sous champ de jauge

Multi-component gauge-dependent quantum gases

Thèse soutenue publiquement le **18 octobre 2019**,
devant le jury composé de :

Monsieur Simone Fratini

Directeur de Recherche, Institut Néel, Président

Monsieur Laurent Longchambon

Maitre de conférence, Laboratoire de Physique des Lasers, Examineur

Monsieur Michele Modugno

Professeur, Dpto. De Fisica Teorica e Historia de la Ciencia Facultad de
Ciencia y Tecnologia, Rapporteur

Madame Anna Minguzzi

Directeur de Recherche CNRS, Communauté Université Grenoble Alpes,
Directeur de Thèse

Monsieur Nicolas Pavloff

Professeur, Laboratoire de Physique Théorique et Modèles Statistiques,
Rapporteur



Multi-component Gauge-Dependent Quantum Gases

Contents

| | | |
|----------|---|-----------|
| I | Two component ring under gauge fluxes | 11 |
| 1 | Artificial gauge fields with ultra-cold atoms in optical lattices | 13 |
| 1.1 | Optical lattices | 13 |
| 1.1.1 | Bose-Hubbard model | 14 |
| 1.1.2 | Ring shaped lattice | 16 |
| 1.2 | Gauge field | 16 |
| 1.2.1 | Analogy between rotation and magnetic field, persistent currents . . . | 17 |
| 1.2.2 | Magnetism and quantum physics | 18 |
| 1.2.3 | Lattice systems | 20 |
| 1.3 | Peculiarities of one dimensional systems | 22 |
| 1.3.1 | Condensation and coherence properties in 1D | 24 |
| 2 | Mean-field of the double ring | 27 |
| 2.1 | Gross-Pitaevskii equation | 27 |
| 2.2 | The model | 28 |
| 2.3 | Non interacting regime | 30 |
| 2.3.1 | Persistent and chiral currents | 32 |
| 2.3.2 | Infinite system - Variational Ansatz | 33 |
| 2.4 | Mesoscopic effects and commensurability of the flux | 34 |
| 2.4.1 | Vortex configurations on a finite double ring lattice | 34 |
| 2.4.2 | Fate of the single vortex in the Meissner phase | 34 |
| 2.4.3 | Spiral interferograms | 37 |
| 2.5 | Mean-field ground state phase diagram | 40 |
| 2.5.1 | Coupled discrete nonlinear Schrödinger equations (DNLSE) | 40 |
| 2.5.2 | Persistent currents for interacting bosons on the double ring lattice . . | 41 |
| 3 | Bogoliubov excitations | 45 |
| 3.1 | Diagonalization of general quadratic Hamiltonian | 46 |
| 3.2 | Bogoliubov formalism | 47 |
| 3.2.1 | Zero frequency modes | 49 |
| 3.2.2 | Josephson effect | 49 |
| 3.3 | Model and method | 52 |
| 3.3.1 | Bogoliubov De-Gennes equations of the double ring | 52 |

| | | |
|-----------|---|------------|
| 3.3.2 | Dynamical structure factor | 54 |
| 3.3.3 | Static structure factor | 56 |
| 3.4 | Excitation spectrum as a probe of the phases of the two-leg bosonic ring ladder | 56 |
| 3.4.1 | Meissner phase | 57 |
| 3.4.2 | Biased-ladder phase | 60 |
| 3.4.3 | Vortex Phase | 60 |
| 3.4.4 | Experimental probe of dynamical structure factor | 61 |
| 3.5 | Coherence properties and supersolidity | 63 |
| 3.5.1 | One-body density matrix | 63 |
| 3.5.2 | Static structure factor - probe of solidity | 64 |
| 3.6 | Small ring limit and nature of the excitations | 65 |
| 3.7 | Bogoliubov excitation spectrum for the lowest single-particle branch | 66 |
| 3.8 | Details on the approximation | 68 |
| 4 | Hard-core bosons | 71 |
| 4.1 | Tonks-Girardeau Bose-Fermi mapping | 72 |
| 4.2 | Fragmentation | 75 |
| 4.3 | Fragmented Fermi seas | 76 |
| 4.3.1 | Bose-Fermi mapping | 78 |
| 4.4 | Numerical results | 79 |
| 4.4.1 | Fidelity with respect to fragmented states | 79 |
| 4.4.2 | Currents | 81 |
| 4.4.3 | Current-current correlations | 82 |
| 4.4.4 | Density-density correlations | 82 |
| 4.4.5 | One-body density matrix and momentum distribution | 83 |
| 5 | Quantum fluctuation effects, Luttinger liquid description | 91 |
| 5.1 | Bosonization and Luttinger liquid | 91 |
| 5.1.1 | Correlation functions | 92 |
| 5.1.2 | Sine-Gordon model | 93 |
| 5.2 | Luttinger liquid description of the double ring | 95 |
| 5.2.1 | Derivation of the Luttinger Liquid Hamiltonian of the double ring | 95 |
| 5.2.2 | Meissner-Vortex transition | 96 |
| 5.2.3 | Mode expansion | 99 |
| 5.2.4 | Weak link | 101 |
| 5.2.5 | Current and correlations functions in the vortex phase | 102 |
| II | Polaritons in honeycomb lattice | 109 |
| 6 | Exciton-Polaritons and the honeycomb lattice | 111 |
| 6.1 | Exciton-polaritons | 112 |
| 6.1.1 | Polariton-polariton interaction | 114 |

Contents

| | | |
|----------|--|------------|
| 6.1.2 | The driven-dissipative mean-field Gross-Pitaevskii equation | 116 |
| 6.1.3 | Steady state and bistability | 116 |
| 6.2 | Honeycomb lattice | 119 |
| 6.2.1 | Berry phase | 121 |
| 6.2.2 | Brillouin zone selection | 123 |
| 6.2.3 | Coupling to photonic bath vacuum | 124 |
| 7 | Bogoliubov excitation spectrum of polaritons in honeycomb lattice | 127 |
| 7.1 | Bogoliubov excitation spectrum | 127 |
| 7.1.1 | Stability analysis | 131 |
| 7.2 | Experimental excitation spectrum | 132 |
| 7.2.1 | Experimental realization | 133 |
| 7.2.2 | Retarded Green's function | 134 |
| 8 | Conclusion and perspectives | 137 |
| A | Diagonalization of the non interacting Hamiltonian | 141 |
| B | Numerical method for the solution of the DNLSE | 143 |
| C | Interference patterns of expanding rings | 145 |
| D | Rigol's method for hard-core bosons | 147 |
| E | Conformal field approach | 149 |
| F | Retarded Green's function | 151 |

Introduction



THE first observation of Bose-Einstein condensation (BEC) in dilute atomic vapors [1] has been a breakthrough both fundamentally, verifying theoretical concept predicted by Bose [2] and Einstein [3] several decades ago, and experimentally, because in order to reach the BEC regime with ultra-cold atoms a temperature of the order of $10^{-9}K$ had to be reached revealing the statistical property of quantum particles. Since then, a new field has emerged and experimentalists are able to study this artificial matter in a very clean and controllable way both for bosons and fermions. Interactions between atoms can be long-ranged [4] or short-ranged [1]. In the latter case, the strength of the interaction can be tuned using Feshbach resonances. Light-matter interaction is the key tool to confine atoms and the shape of the confining potential can now be controlled with very high precision. Such cold-atom systems allow us to explore a whole range of fundamental phenomena that are extremely difficult or impossible to study in real materials, such as Bloch oscillation, Mott-superfluid transition, topology of band structure, orbital magnetism just to name a few. Specially designed optical lattice experiments are paving the way to study condensed-matter problems where particles are confined into a periodical potential. Recent experimental advances using ultra-cold quantum gases have allowed to engineer the coupling between different internal states of the atoms, in order to realize synthetic gauge fields [5, 6, 7]. The dynamics of the center-of-mass of a neutral atom which moves in a properly designed laser field, is analogue to the dynamics of a charged particle in a magnetic field, on the influence of a Lorentz-like force. The corresponding Aharonov-Bohm phase is related to the Berry's phase that emerges when the atom adiabatically follows one of the dressed states of the atom-laser interaction [5]. These progresses allow the quantum simulation of a large class of Hamiltonians. Indeed, condensed matter phenomena under strong magnetic fields are still intriguing and are at the center of modern research. For instance, topological states of matter are realized in quantum Hall systems, which are insulating in the bulk, but bear conducting edge states [8].

A ladder is the simplest geometry where one can get some insight on two-dimensional quantum systems subjected to a synthetic gauge field [9, 10]. The bosonic linear ladder has been the subject of intense theoretical work. The phase diagram has been established by means of field-theoretical methods [11, 12], and intensive DMRG simulations [13]. Those studies, in addition to common features of Bose-Hubbard models such as superfluid and Mott insulating phases, revealed new exciting phases of matter induced by the magnetic field: chiral superfluid phases, chiral Mott insulating phases displaying Meissner currents [12, 14] and vortex-Mott insulating phases [15]. In the weakly interacting regime, an additional phase has been predicted [16] a biased ladder phase characterized by an imbalanced population of the bosons between the two legs, explicitly breaking \mathbb{Z}_2 symmetry. This phase was shown to be stable in the interacting case, except for a special value of the applied flux, where umklapp processes destabilize it [17]. The dependence of the

critical flux separating Meissner and vortex phase on inter particle interactions has been also studied [18]. In parallel to these theoretical advances, the experimental realization of the bosonic flux ladder has been reported in optical lattices [19] as well as for lattices in synthetic dimensions, both for fermions and bosons [20, 21].

As in the case of cold atoms, exciton-polaritons in semiconductor microcavities are an ideal model system to simulate and engineer condensed matter systems. They allow for the control of the density, the temperature of the sample, and, in the case of lattice systems, the topology of the band structure. It is possible to directly image exciton polaritons thanks to their photonic component: all the statistical properties of the intracavity polariton field are contained in the far-field of the polariton luminescence [22]. The possibility of realizing coupled micropillars thanks to deep etching of a planar structure [23, 24] has opened the way towards the engineering of lattices for polaritons with controlled tunneling and deep on-site potentials with arbitrary geometry. The honeycomb lattice is one of such intriguing condensed matter system where topological effects arise. One of the most interesting aspects of the honeycomb lattice problem is that its low-energy excitations are mass-less, chiral, Dirac particles. This particular dispersion, that is only valid at low energies, mimics the physics of quantum electrodynamics (QED) for mass-less particles except for the fact that in honeycomb lattice the Dirac particles move with a speed of sound v_S , which is 300 times smaller than the speed of light c . Hence, many of the unusual properties of QED such as the Klein paradox [25] can show up in graphene but at much smaller speeds or, identically, energy scales.

In the first part of this thesis, i.e chapters 2, 3, 4 and 5, we consider a system made of two one-dimensional coupled lattice rings subjected to different fluxes in each leg. This specific bosonic ladder corresponds to different boundary conditions with respect to the case of a linear ladder. In particular, this double ring lattice geometry allows to study persistent currents in dimension larger than one [26], which shows promising applications for atomtronics developments [27, 28]. We focus on a planar geometry with concentric rings, as could be realized eg with dressed potentials [29], or using co-propagating Laguerre-Gauss beams [30].

The first part of the thesis is organized as follows:

In chapter 1 we introduce some key concepts about cold-atoms experiments focusing on the trapping of atoms by light potential in optical lattices. We also provide some information about gauge-dependent phenomena by connecting to the notion of Aharonov-Bohm effect. Finally we discuss the peculiarities of bosons in one dimensional systems. Then throughout the next chapters 2, 3, 4 and 5 the theoretical methods employed to describe the model studied in different physical regimes are introduced, and original results are presented.

In chapter 2 the non-interacting regime of the two one-dimensional coupled lattice



rings subjected to different fluxes in each leg is derived. After identifying the vortex and Meissner phases, we discuss specific features of the double ring lattice geometry, as the appearance of a vortex in the Meissner phase and parity effect in the vortex phase arising from the commensurability of the total flux. Through a numerical study we then explore the dilute, weak-interacting regime and address the nature of the ground state at mean-field level. In particular we identify known phases [16] such as the Meissner, vortex and biased-ladder phases as well as the effect of commensurability of the total flux. The persistent current is shown to be a good observable to identify the different phase of the system. Finally, we propose the spiral interferogram images obtained by interference among the two rings during time of flight expansion as a probe of vortex-carrying phases, specifically adapted to the ring geometry. The results outlined in this chapter can be found in the following published article:

Nicolas Victorin, Frank Hekking, and Anna Minguzzi. Bosonic double ring lattice under artificial gauge fields. Phys. Rev. A, 98:053626, Nov 2018

In chapter 3, using both numerical and analytic approaches, we explore the excitation spectrum of two one-dimensional coupled lattice rings subjected to different fluxes in each leg. The excitation spectrum in Meissner, biased-ladder and vortex phase is explicitly shown via the dynamical structure factor. We show that the vortex phase has supersolid properties stemming from the combination of coherence and spatial order. Then the nature of the Bogoliubov modes is studied revealing Josephson oscillation between the two rings. The results outlined in this chapter can be found in the following arxiv article: Nicolas Victorin, Paolo Pedri and Anna Minguzzi. Excitation spectrum and supersolidity of a two-leg bosonic ring ladder. arXiv:1910.06410, Oct 2019

In chapter 4 we explore the regime of infinitely strong interactions on the double ring. We make use of the exact mapping into fermions via the Jordan-Wigner transformation, that is made possible in a peculiar physical regime at strong magnetic flux and weak coupling between the rings. Using both analytic and exact diagonalization, fragmentation of the ground-state is explicitly shown ranging from a fragmentation in momentum space at weak interaction to a fragmented Fermi sea at infinite interaction. The regime of fragmented Fermi sea is then characterized via different physical observables. The results outlined in this chapter can be found in the following published article:

Nicolas Victorin, Tobias Haug, Leong-Chuan Kwek, Luigi Amico, and Anna Minguzzi. Non-classical states in strongly correlated bosonic ring ladders. Phys. Rev.A, 99:033616, Mar 2019.

In chapter 5 we explore the intermediate regime of interactions. Thanks to a mode expansion and re-fermionization approach of the bosonized Hamiltonian of the double ring under gauge flux, we show the peculiarities of finite size periodic boundary condition on the current in the double ring. A rotating barrier is then introduced and we show a gap opening in the spin sector of the energy spectrum. The dynamical structure factor is derived revealing the decomposition in spin and charge mode of the excitation spectrum at

low energy. The results outlined in this chapter is the outcome of an on going work.

In the second part of this thesis, i.e Chapters 6 and 7, we consider a system of exciton polaritons in honeycomb lattice. Driven by experiment realization of the model in Institut Néel in the group of Maxime Richard, we explore the Bogoliubov excitation spectrum of the model as well as its observation in relation with relevant experimental procedures.

The second part of the thesis is organized as follows:

In chapter 6 we review some key concepts about exciton-polariton in microcavities. Then we study the honeycomb lattice and its low energy properties. We outline the concept of Brillouin zone selection mechanism and we provide a new interpretation in terms of dark-state.

In chapter 7 we explore the Bogoliubov excitation spectrum of exciton-polaritons in honeycomb lattice structure. We show that this Bogoliubov spectrum exhibit a instability of the C point of the bistability curve that is usually stable for polariton in microcavities. Superfluid properties below and above the C point arises at momentum away from the momentum of the laser pump that populate one of the Dirac point of the system. Finally we see that the theory derived in this chapter models experimental observation of the excitation spectrum of interacting polaritons in honeycomb lattice.

The second part of this thesis is part of an on going work.

List of published and soon to be published work

The original results presented in this thesis have been published in the following articles:

(i) Nicolas Victorin, Frank Hekking, and Anna Minguzzi. Bosonic double ring lattice under artificial gauge fields. Phys. Rev. A, 98:053626, Nov 2018

Subject of part I, chapter 2

(ii) Nicolas Victorin, Tobias Haug, Leong-Chuan Kwek, Luigi Amico, and Anna Minguzzi. Non-classical states in strongly correlated bosonic ring ladders. Phys. Rev.A, 99:033616, Mar 2019.

Subject of part I, chapter 4

(iii) Nicolas Victorin, Paolo Pedri and Anna Minguzzi. Excitation spectrum and supersolidity of a two-leg bosonic ring ladder. arXiv:1910.06410, Oct 2019

Subject of part I, chapter 3

(iv) Nicolas Victorin, Roberta Citro and Anna Minguzzi. Luttinger Liquid description of a two-leg bosonic ring ladder subjected to gauge fluxes. In preparation.

Subject of part I, chapter 5

(v) Petr Stepanov, Nicolas Victorin, Anna Minguzzi and Maxime Richard. Experimental observation of the excitation spectrum of an interacting gas of polariton in

a honeycomb lattice. In preparation.
Subject of part II

Part I

Two component ring under gauge fluxes

Chapter 1

Artificial gauge fields with ultra-cold atoms in optical lattices



THIS chapter will focus on the necessary tools to understand the content of Part I of this manuscript. The relevant concepts of optical lattices, gauge fields and the emerging phenomena of ultra-cold gases placed under those constraints will be introduced. Also, the peculiarities of bosonic one dimensional many-body systems will be reviewed. All other necessary concepts will be introduced at the beginning of each forthcoming chapter.

1.1 Optical lattices

Using the sensitivity of the electrons of an atom to an oscillating electric field $\mathbf{E}(\mathbf{r}, t)$ it is possible to engineer a trapping potential for neutral atoms. Indeed, the interaction between electrons and an electric field made by laser field induce a dipole moment that oscillates with the imposed laser field, far from resonance reads

$$d_i^\pm(t) = \sum_{j=x,y,z} \alpha_{ij}(\omega_L) E_j^\pm(\mathbf{r}, t) \quad (1.1)$$

where d_i^\pm is the i^{th} component of the dipole moment, ω_L the laser frequency and $\alpha_{ij}(\omega_L)$ the matrix elements of the complex polarizability tensor characteristic the response of the atoms to the applied electric field. The energy shift is then $\Delta E = \mathbf{d} \cdot \mathbf{E}$ and for a fully isotropic response of the medium to applied electric field it is diagonal, i.e $\alpha_{ij} = \alpha \delta_{ij}$,

$$\Delta E(\mathbf{r}, t) = -2\text{Re}[\alpha] I(\mathbf{r}, t) \propto \frac{I(\mathbf{r}, t)}{\Delta} \quad (1.2)$$

where $I(\mathbf{r}, t)$ is the laser beam intensity and $\Delta = \omega_L - \omega_1$ is the detuning of the laser frequency to the frequency of the first excited state of the atom. The last equation means

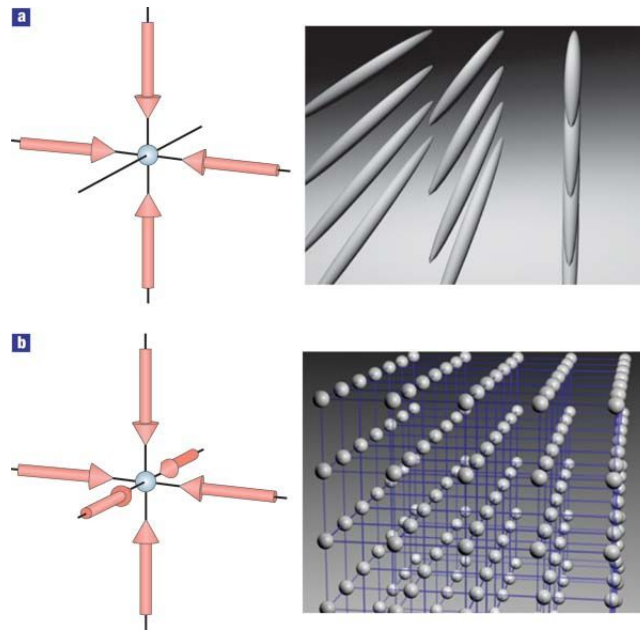


Figure 1.1: Schematic pictures of optical lattice potentials created by counter-propagating lasers: (a) 2D array of quasi-1D tubes and (b) 3D simple cubic lattice. From [32].

that the atoms feel an optical potential created by the spatial pattern of the laser field intensity. This technique is widely used for trapping atoms [31]. Upon changing the sign of the detuning Δ it is possible to change the sign of the potential and therefore its attractive or repulsive character.

Optical lattices are formed using light confinement forming periodic intensity pattern thanks to interference of two or more laser beams. The simplest optical lattice can be made with two laser beams with the same wavelength, with paths which are in opposite direction. Their interference creates a 1D periodic intensity pattern of period half their wavelength, of the form

$$V(x) = V_0 \sin^2(kx) \quad (1.3)$$

with $k = 2\pi/\lambda$, λ being the wavelength of the lasers that form the standing wave and V_0 the depth of the optical lattice proportional to the intensity of the laser beam. It is possible then to create complex lattice structures by creating complex interference patterns playing with wavelength, angle, polarization, shape and number of the laser beams.

1.1.1 Bose-Hubbard model

A relevant Hamiltonian for lattice models is the Bose-Hubbard Hamiltonian that is useful to treat a lattice system in tight binding approximation and has proven to be the relevant one to describe bosonic atoms with repulsive interaction in a periodic lattice potential [33]. We will review here its derivation as it will be helpful for the next chapters 2, 3, 4,

1.1. Optical lattices

5 and in Part II of this thesis. The Bose-Hubbard Hamiltonian can be derived from the general second quantized form of many-body Hamiltonian

$$H = \int d\mathbf{r} \psi^\dagger(\mathbf{r}) h_{\mathbf{r}} \psi(\mathbf{r}) + \int d\mathbf{r}' \int d\mathbf{r} \psi^\dagger(\mathbf{r}) \psi^\dagger(\mathbf{r}') V_{\mathbf{r},\mathbf{r}'} \psi(\mathbf{r}') \psi(\mathbf{r}), \quad (1.4)$$

where $h_{\mathbf{r}}$ is a general differential operator acting on the bosonic field operators $\psi(\mathbf{r})$ representing the kinetic energy and the external potential, and the second term $V_{\mathbf{r},\mathbf{r}'}$ is the inter-particle interactions. In the specific case of atoms in an optical lattice, $h_{\mathbf{r}} = -\frac{\hbar^2}{2m} \nabla_{\mathbf{r}}^2 + V_{\text{latt}}(\mathbf{r}) + V_{\text{ext}}(\mathbf{r})$ where $V_{\text{latt}}(\mathbf{r})$ represents the lattice confining potential and $V_{\text{ext}}(\mathbf{r})$ an external potential. In typical cold-atom experiments the quantum gas is very dilute, with densities typically ranging from 10^{13} to 10^{15} cm^{-3} . Interactions between atoms are nevertheless very important and are well characterized by two-body contact interactions at low energy. The interactions are then described by a single parameter, the s-wave scattering length a_s , which enters into the contact two-body interaction potential $V_{\mathbf{r},\mathbf{r}'} = g\delta(\mathbf{r} - \mathbf{r}')$ where $g = \frac{4\pi\hbar^2 a_s}{m}$. The s-wave scattering length is tunable using Feshbach resonances [34]. This provides to the cold-atoms experiments a unique playground to study effect of interactions between particles for a large range of interaction strengths. Considering deep lattice potentials, we use a tight-binding approximation that consists in expanding bosonic field operator on the basis of Wannier functions of the lowest band,

$$\psi(\mathbf{r}) = \sum_i b_i w(\mathbf{r} - \mathbf{r}_i), \quad (1.5)$$

where b_i and b_i^\dagger are respectively the annihilation and creation operators of a particle localized in the i^{th} lattice site, satisfying bosonic commutation rules $[b_i, b_j^\dagger] = \delta_{ij}$. This approximation works also for interacting bosonic gases as long as the typical interaction between particles is not enough to excite the population of higher bands. One then obtains the Bose-Hubbard Hamiltonian by taking into account only nearest neighbor hopping and contact interactions,

$$H = - \sum_{\langle i,j \rangle} \left(J_{ij} b_i^\dagger b_j + \text{h.c.} \right) + \frac{U}{2} \sum_i n_i (n_i - 1), \quad (1.6)$$

where $\langle i, j \rangle$ is restricting the sum to nearest neighbors and $n_i = b_i^\dagger b_i$ is the number operator of bosons on each site. The coefficients J_{ij} is interpreted as the rate of tunneling between site i to j through the lattice potential barrier and it is given by

$$J_{ij} = - \int d\mathbf{r} w^*(\mathbf{r} - \mathbf{r}_i) \left[-\frac{\hbar^2 \nabla_{\mathbf{r}}^2}{2m} + V_{\text{ext}}(\mathbf{r}) + V_{\text{latt}}(\mathbf{r}) \right] w(\mathbf{r} - \mathbf{r}_j). \quad (1.7)$$

As the Wannier functions are strongly localized in the tight binding approximation, the on-site interaction U is given by

$$U = g \int d\mathbf{r} |w(\mathbf{r})|^4. \quad (1.8)$$

1.1.2 Ring shaped lattice

The geometry of the lattice that one can consider depends on the intensity pattern formed by the interference of the laser beams. Therefore, a large class of lattices can be considered e.g cylindrical optical lattices[30]. Those lattices can be formed using Laguerre-Gauss beams carrying angular momentum [35, 36], see Fig. 1.2. Another way of forming ring

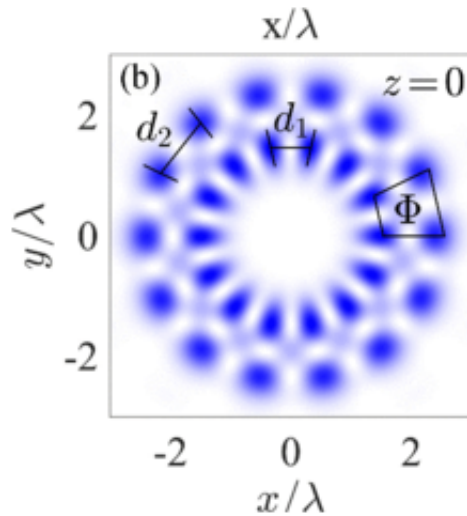


Figure 1.2: Two rings geometry, formed by two Laguerre-Gauss beams with flux per placket Φ . From [30].

shaped lattice is to use the idea of synthetic dimensions that uses the internal degrees of freedom of the atoms to generate extra transverse dimensions [37].

1.2 Gauge field

In the context of the standard model, gauge theories describe three of the four fundamental forces of nature, electromagnetism $U(1)$, weak $SU(2) \times U(1)$ and strong $SU(3)$ forces. These symmetries imply invariance of the Lagrangian and define conserved charges that are linked to the bosons that mediates those forces. In the context of condensed matter, those gauge symmetries are widely used and many-body quantum system subjected to external magnetic fields exhibit rich and intriguing behaviour. Integer and fractional quantum Hall effects are examples of such physical effects, where the transverse transport of a 2D system induced by external magnetic field exhibits plateaus corresponding to

1.2. Gauge field

an integer or fractional multiple of e^2/h [38], e and h being the electron charge and the Planck's constant, respectively. This effect arises for charged particles with applied magnetic field but can also be induced by an artificial magnetic field on neutral bosonic atoms. Several ways of inducing magnetic like dependence on neutral atoms are possible, to cite a few :

- *rotating trapped ultra-cold gases*: using to analogy between Lorentz and Coriolis force[39, 40]: with this technique it is possible to create Abelian gauge fields.
- *laser induced gauge fields in optical lattices*: exploiting properties of laser-assisted tunneling [41] (see Fig. 1.3) it is possible to access the regime of large magnetic field.

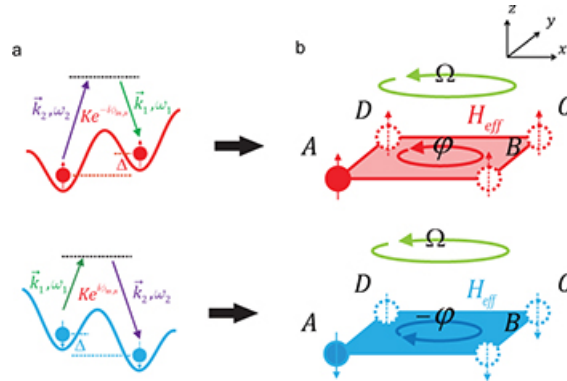


Figure 1.3: Laser assisted tunneling is a way of implementing gauge field in optical lattice. Using internal degrees of freedom of the neutral atoms: with this technique it is possible to implement a complex hopping. From [42]

1.2.1 Analogy between rotation and magnetic field, persistent currents

Let's consider a fluid of neutral particles confined in a trap that is rotating at frequency Ω around the z axis. We show here below that the dynamics of a fluid is equivalent to charged particles subjected to magnetic field. One can link magnetic and rotation frequency in the following way

$$q\mathbf{B} = 2m\Omega \quad \text{with} \quad \Omega = \Omega\mathbf{e}_z \quad (1.9)$$

where q is the charge of the particle and m the mass. The rotation induce a Coriolis force on the fluid that is $\mathbf{F}_C = 2M\mathbf{v} \times \Omega$ that is very similar to the Lorentz force acting on charge particle $\mathbf{F}_L = q\mathbf{v} \times \mathbf{B}$. Let's draw the analogy a little bit deeper by considering the full quantum Hamiltonian problem of the rotating fluid, this time in first quantization. Let's consider a quantum particle of mass m evolving in a one dimensional ring of circumference L , radius R and rotating defect turning at velocity $\mathbf{v}_\theta = v\mathbf{e}_\theta$

$$\hat{H}(t) = \frac{\hat{p}_\theta^2}{2m} + \delta(R\theta - vt) = -\frac{\hbar^2}{2mR^2} \partial_\theta^2 + \delta(R\theta - vt) \quad (1.10)$$

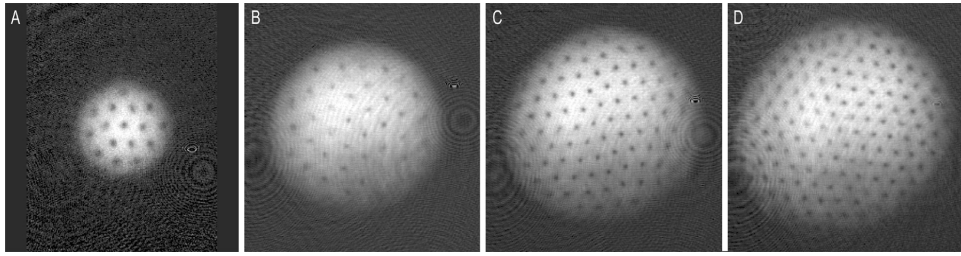


Figure 1.4: Experimentally observed vortex lattice arising from the rotation of a bosonic atomic BEC. The pictures show different configuration of the number of vortices in the sample. Taken from [44].

One can eliminate the time dependence in the Hamiltonian by a unitary transformation $\hat{U}(t) = \exp(i\Omega\hat{L}_z t/\hbar)$ where \hat{L}_z is the angular momentum operator $\hat{L}_z = -i\hbar\partial_\theta$. The Hamiltonian transforms into

$$\hat{H}' = \hat{U}(t)^\dagger \hat{H}(t) \hat{U}(t) = \frac{\hbar^2}{2mR^2} (-i\hbar\partial_\theta - qA_\theta)^2 + \delta(\theta) + V_{\text{centr}} \quad (1.11)$$

where V_{centr} represents the centrifugal effect $V_{\text{centr}} = -\frac{1}{2}mR^2\Omega^2$ and $q\mathbf{A} = m\boldsymbol{\Omega} \times \hat{\mathbf{r}}$. The action of the unitary transformation $\hat{U}(t)$ is to change the frame of reference of the system to the moving frame of angular frequency Ω so that the momentum of the particle in the moving frame is shifted by the analogue of a magnetic vector potential. The only difference is the centrifugal potential effect, however for a 1D ring this contribution can be considered as a constant shift of the full spectrum so that it will not be relevant. For 2D systems this contribution tends to push the particles away from the center and one cannot have a toy model of orbital magnetism on a neutral gas. To overcome this problem the confining trap is turning at frequency equal to the confinement frequency so that the centrifugal contribution cancel out with the trapping contribution and one can observe 2D gauge dependent physics [5, 43]. This analogy allowed to experimentally access gauge dependent physics and create vortex lattices in BEC experiments [44]. Figure 1.4 shows an example of a vortex lattice.

1.2.2 Magnetism and quantum physics

Continuum case : The Maxwell equation for the magnetic field \mathbf{B} in the absence of magnetic monopoles $\nabla_{\mathbf{r}} \cdot \mathbf{B}(\mathbf{r}) = 0$ implies $\mathbf{B}(\mathbf{r}) = \nabla_{\mathbf{r}} \times \mathbf{A}(\mathbf{r})$. It shows that the equation is invariant under transformation of the vector potential up to a gradient term a scalar field $\phi(\mathbf{r})$, meaning that two vector potentials $\mathbf{A}(\mathbf{r})$ and $\mathbf{A}(\mathbf{r})'$ where $\mathbf{A}(\mathbf{r})' = \mathbf{A}(\mathbf{r}) + \nabla_{\mathbf{r}}\phi(\mathbf{r})$ lead to the same magnetic field. This gauge invariance can be absorbed at the level of the quantum Hamiltonian

$$H = \frac{1}{2m} \int d\mathbf{r} \psi^\dagger(\mathbf{r}) [-i\hbar\nabla_{\mathbf{r}} - q\mathbf{A}(\mathbf{r})]^2 \psi(\mathbf{r}) \quad (1.12)$$

1.2. Gauge field

where q is the charge of the particle, by a redefinition of the momentum operator

$$\hat{\mathbf{p}} \rightarrow \hat{\mathbf{p}}' = -i\hbar \nabla_{\mathbf{r}} + q \nabla_{\mathbf{r}} \phi(\mathbf{r}) \quad (1.13)$$

or by a change of gauge of the field operators

$$\psi(\mathbf{r}) \rightarrow \psi(\mathbf{r})' = \hat{U}\psi(\mathbf{r}) = e^{\frac{iq}{\hbar}\phi(\mathbf{r})}\psi(\mathbf{r}) \quad (1.14)$$

This defines a U(1) gauge invariance. One important fact is that the invariance of the magnetic field upon a shift of the vector potential by a gradient term lies on the fact that the space is connected, meaning that a closed loop can be deformed continuously into a dot. This will not be the case for a particle evolving in a space where a singularity is present. The Aharonov–Bohm effect [45] is such an example.

The Aharonov-Bohm effect is the sensitivity of the phase of the wave function to the vector potential of the magnetic field. Let's consider (see Fig.1.5) a charged particle evolving in a plane with a solenoid creating a non-zero magnetic field only inside itself. The Hamiltonian describing such a setup is the following

$$H = \frac{(\hat{\mathbf{p}} - q\mathbf{A}(\mathbf{r}))^2}{2m}. \quad (1.15)$$

Outside of the solenoid we have no magnetic field so that $\nabla \times \mathbf{A}(\mathbf{r}) = \mathbf{B}(\mathbf{r}) = 0$. As we said earlier, the vector potential of the magnetic field can be expressed as the gradient of a scalar field only if the space is simply connected (i.e. there is no singularity of the magnetic field). We can only define a vector potential for different paths but not enclosing the discontinuity. For the two beams of Fig.1.5 we can define such a vector potential that we'll call $\mathbf{A}_{III}(\mathbf{r}) = \nabla \chi_{III}(\mathbf{r})$ associated to wave function $\Psi_{III} = e^{\frac{i}{\hbar}q\chi_{III}(\mathbf{r})}\Psi_0(\mathbf{r})$ where the phase has been absorbed into the wave function and $\Psi_0(\mathbf{r})$ is wave-function without magnetic field. The dephasing between the two wave functions at a point \mathbf{r} is then

$$\phi = \frac{q}{\hbar}(\chi_I(\mathbf{r}) - \chi_{II}(\mathbf{r})) = \frac{q}{\hbar} \oint_{\mathcal{C}} \mathbf{A}(\mathbf{r}) d\mathbf{r} = 2\pi \frac{\Phi}{\Phi_0} \quad (1.16)$$

where Φ is flux in the solenoid and Φ_0 the quantum of flux. Such an effect is remarkable as the presence of a magnetic field yields a dephasing of the particles circulating around it without encountering it: the particles are affected by the flux of this magnetic field as a direct consequence of the gauge invariance of the quantum theory. This phase is said to be topological as it is not depending on the path chosen.

The persistent current phenomenon arises from the Aharonov-Bohm effect which affects the quantum dynamics of charged particles in a multiply-connected geometry [45] (i.e. with holes). In condensed-matter physics the study of persistent currents has emerged in the context of metallic rings under magnetic fields at very low temperature. If quantum phase coherence is large compared to the size of the system and thermal fluctuations are

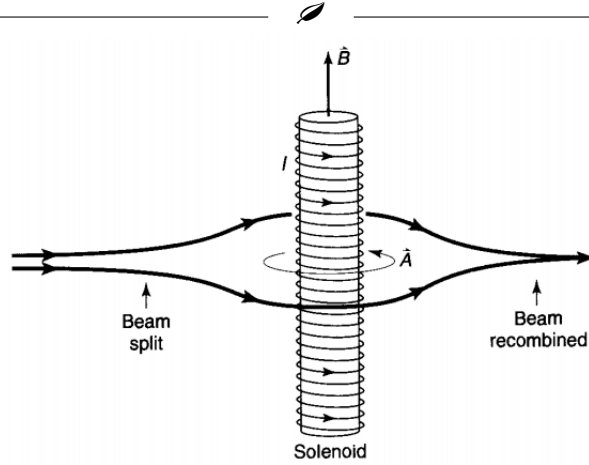


Figure 1.5: Representation of the Aharonov set-up: incoming electrons take two alternative paths around a solenoid. The beam is then recombined and interference is observed. Figure from [46].

weak enough, persistent currents manifest themselves as dissipationless currents even in the absence of any applied voltage [47]. Persistent currents were first observed in solid state superconductors electronic systems subjected to a magnetic field [48].

Mathematically, the persistent current is defined [49] through the Hellman-Feynman theorem as $I = -\frac{1}{\Phi_0} \langle \partial_\Phi H \rangle = -\frac{1}{\Phi_0} \partial_\Phi \langle H \rangle$. For a homogeneous system without impurities, the spectrum is $E_n = \left(n - \frac{2\pi}{L} \Phi / \Phi_0 \right)^2$, where $n \in \mathbb{Z}$ labels the different angular momentum state. The persistent current is then an oscillating function of period fixed by the quantum of flux Φ_0 . Impurities will break the rotational invariance and couple the different angular momentum states of the system. This will introduce a gap between the different energy levels E_n corresponding to momentum n for any value of repulsive interactions (Leggett's theorem [50]).

We see from Eq.(1.11) that even a moderate concentration of impurities will affect the current amplitude. Nevertheless, the persistent current is stronger than one can think. Indeed, when performing a gauge transformation, $\psi(\theta) \rightarrow e^{iqA_\theta} \psi(\theta)$ one removes the A_θ dependence in the Hamiltonian on the price of twisting the boundary condition ($\psi(0) = e^{2\pi A_\theta} \psi(2\pi)$). The persistent current is then seen as a measure of the sensitivity of the spectrum to the twist, so that even in presence of disorder the persistent current does not vanish. This fact has been observed in metallic rings in a disordered environment [51].

Of course, rotating Bose-Einstein condensates made of ultra-cold atoms, being in a superfluid state, will exhibit coherence properties analogue to electronic superconducting system and dissipationless flow is likely to occur [52].

1.2.3 Lattice systems

In a lattice two length scales are competing, the inter-site distance a and the magnetic length $l = \sqrt{\hbar/qB}$. Their ratio can be expressed as the ratio of the magnetic flux Φ and

1.2. Gauge field

the quantum of flux Φ_0 . When Φ is much smaller than Φ_0 nothing more is expected than for the case of a single particle whereas for $\Phi \approx \Phi_0$ the physics will change drastically and can create fractal structure in the energy spectrum (Hofstadter butterfly [53]). Artificial materials, such as the ones which can be implemented in cold atoms experiments [6, 7] are able to access those regimes since the inter-site distance can be tuned so that it becomes comparable with the magnetic length. In the tight binding approximation, (see Eq.1.6), we consider the Bose-Hubbard Hamiltonian. For simplicity we will consider a 1D chain

$$H = -J \sum_l \left(a_{l+1}^\dagger a_l + \text{h.c.} \right). \quad (1.17)$$

In the presence of a magnetic field perpendicular to the sample, we have to take into account the Aharonov-Bohm phase that is accumulated by a particle from a site l to l' of the lattice

$$\phi(l \rightarrow l') = \frac{q}{\hbar} \int_{\mathbf{r}_l}^{\mathbf{r}_{l'}} \mathbf{A}(\mathbf{r}_m) \cdot d\mathbf{r}_m \quad (1.18)$$

At the level of the Bose-Hubbard Hamiltonian this phase can be included via the Peierls substitution [54] in the tunneling coefficient $J \rightarrow J e^{i\phi}$ for a constant magnetic field. Thus the Hamiltonian reads

$$H = -J \sum_l \left(a_{l+1}^\dagger a_l e^{i\phi} + \text{h.c.} \right). \quad (1.19)$$

2D lattice The situation for a square lattice is analogous. The 2D lattice Bose-Hubbard Hamiltonian is

$$H = -J \sum_{m,n} \left(a_{m+1,n}^\dagger a_{m,n} + a_{m,n+1}^\dagger a_{m,n} + \text{h.c.} \right). \quad (1.20)$$

Due to the presence of the magnetic field, the hopping is complex due to the Peierls substitution, of phase $\phi_{m,n}^i = q A_{m,n}^i / \hbar$ at site $\{m, n\}$ in direction $i = \{x, y\}$. So that the Hamiltonian transform into

$$H = -J \sum_{m,n} \left(e^{i\phi_{m,n}^x} a_{m+1,n}^\dagger a_{m,n} + e^{i\phi_{m,n}^y} a_{m,n+1}^\dagger a_{m,n} + \text{h.c.} \right) \quad (1.21)$$

For a homogeneous magnetic field the flux is fixed and equal for each plaquette (as denoted by Φ in 1.6), $\Phi = \phi_{m,n}^x + \phi_{m+1,n}^y - \phi_{m,n+1}^x - \phi_{m,n}^y$ and represents the gauge invariant quantity of the square lattice. All along this thesis we will consider the Landau gauge, under which the vector potential is aligned to a certain direction of space x or y . When it is aligned in the x direction, the vector potential is $\mathbf{A} = (-By, 0, 0)$ and we are in the situation considered by Atala *et al* in the experiment on bosonic ladders[19] (see Fig. 2.2). In the case of the lattice system it corresponds to the configuration where all the phases of the vertical transition are zero and all horizontal ones increase linearly with the lattice position l . The gauge that we will consider later in our theoretical work is the one where the

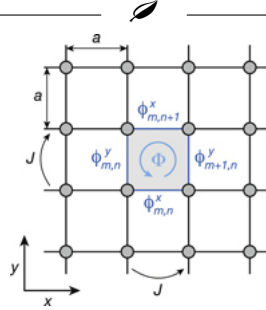


Figure 1.6: Schematic representation of a 2D lattice with gauge dependent hopping of Peierls phases $\phi_{m,n}^i$, with $i = \{x, y\}$. From [55].

vector potential is aligned in the y direction so that $\mathbf{A} = (0, xB, 0)$ and the corresponding lattice flux are non zero only along x , taking the advantage of having a flux dependent tunneling that doesn't depend on the lattice position makes the calculations easier.

In the case of the ring geometry, the description follows closely the one presented here, except that the space coordinates are now cylindrical (see Sec. 2.2).

1.3 Peculiarities of one dimensional systems

The physics of many-body one-dimensional (1D) Bose systems is very different from that of ordinary three-dimensional (3D) bosonic gases. For example, by decreasing the particle density n , a usual 3D quantum many-body system becomes more ideal, whereas in a 1D Bose gas the role of interactions becomes more important. The reason is that at temperatures T close to zero, the kinetic energy of a particle at the mean inter-particle separation $1/n$ scales as $K \propto n^2$ and it decreases with decreasing density n faster than the interaction energy per particle, $I \propto n$. The ratio of the interaction to kinetic energy, $\gamma = I/K$, characterizes the different physical regimes of the 1D quantum gas (see Fig 1.9). This ratio has first been introduced in the context of the Lieb-Liniger model [56, 57] which is the model describing many-body bosons in 1D interacting with delta potential. The Lieb-Liniger many-body Hamiltonian in second quantization reads

$$H = -\frac{\hbar^2}{2m} \int dx \Psi^\dagger(x) \Delta_x \Psi(x) + \frac{g_{1D}}{2} \int dx \Psi(x)^\dagger \Psi(x)^\dagger \Psi(x) \Psi(x) \quad (1.22)$$

with $\Psi(x)$ the bosonic field operator and g_{1D} the interacting strength. The Lieb-Liniger parameter is defined as $\gamma = \frac{mg_{1D}}{n_0 \hbar^2}$. This model is integrable, and Bethe ansatz allows to derive exact expressions for the ground state energy, its excitations (see Fig 1.7) and the static correlations of the system at arbitrary interaction strength [58]. However, analytic expressions are difficult to compute. Expansions around the strongly and weakly interacting regime are known, while for intermediate γ numerical calculations give very accurate results. For a small value of γ the gas is in a weakly interacting regime where particle tends to be delocalized on the length of the system, in this regime mean-field theory is applicable (see chapter 2 and 3). For a large value of γ , the gas enters the Tonks–Girardeau

1.3. Peculiarities of one dimensional systems

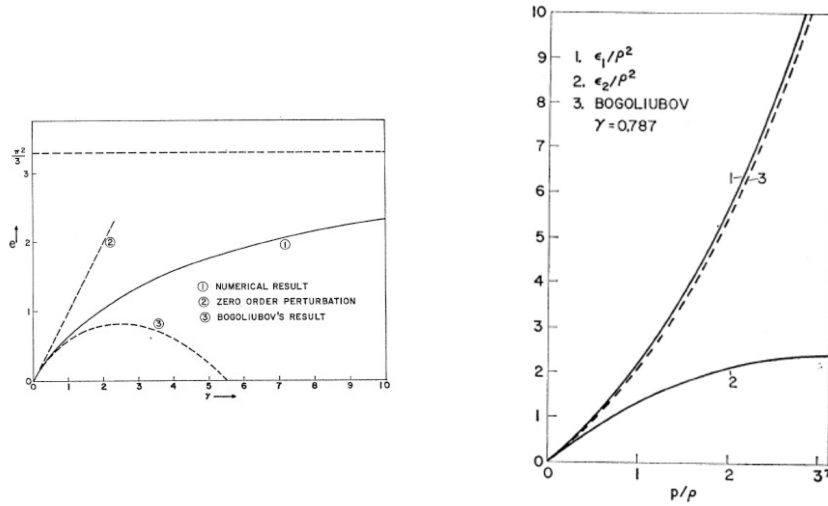


Figure 1.7: **a)** Ground-state energy of the Lieb-Liniger model versus interaction strength, from [56]. **b)** Excitation spectrum of the Lieb-Liniger model, showing two branches. One is called Lieb-I and corresponds to sound like excitations corresponding to the Bogoliubov modes at weak interactions (as we can see that line 1 and 3 are close to each other), the second branch corresponds to umklapp processes and are interpreted as holes in the corresponding Fermi sea. Their low-energy behaviour can be captured within Luttinger-Liquid theory (see Chap. 5). From [57].

(TG) regime, where the repulsion between particles strongly decreases the wave function at short inter-particle distances (see chapter 4.1 for more details and method of solution). At intermediate values of γ , the Luttinger-liquid framework well describes the low-energy properties of the 1D gas (see chapter 5).

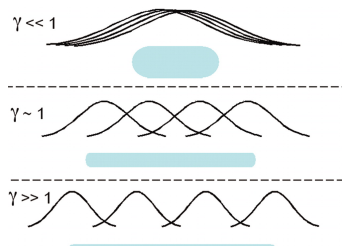


Figure 1.8: Sketch of the 1D bosonic cloud illustrating the size and separation of single-particle wave functions for different value of γ . Taken from [59]

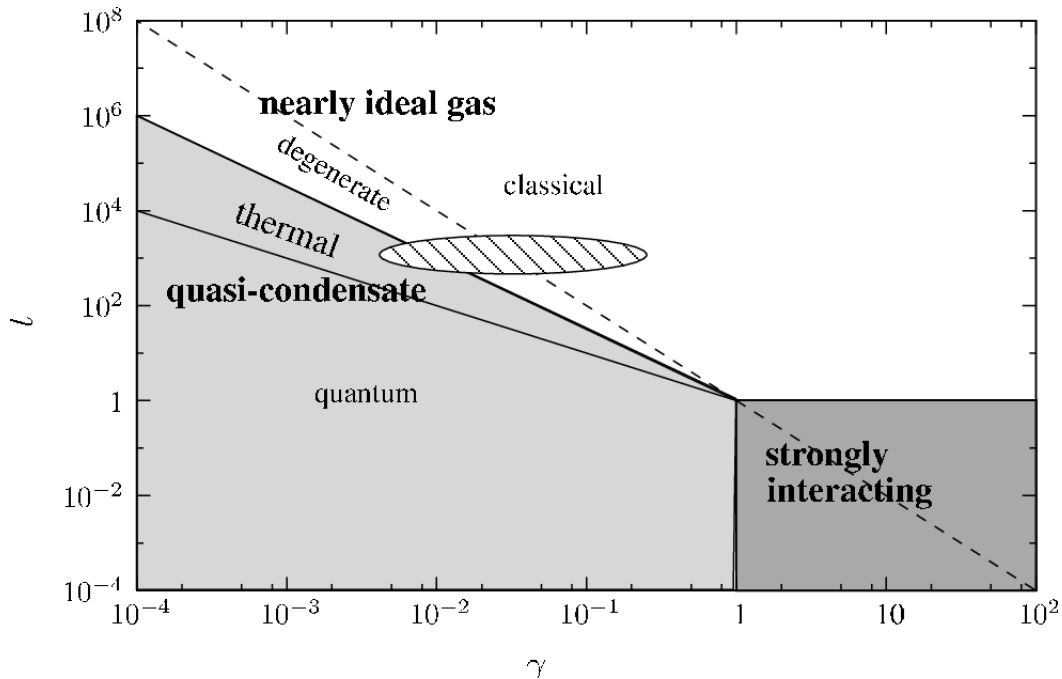


Figure 1.9: Physical regimes of a 1D Bose gas with repulsive contact interactions in the parameter space (γ, t) , where γ is the Lieb-Liniger parameter and t the re-scaled temperature. Taken from [60].

1.3.1 Condensation and coherence properties in 1D

Mathematically, as we will later see in chapter 4, the concept of Bose-Einstein condensation (BEC) is well defined for a system of interacting particles as the macroscopic occupation of the largest eigenvalue of the one-body density matrix $g^{(1)}(x, x') = \langle \Psi^\dagger(x) \Psi(x') \rangle$, where we recall that $\Psi(x)$ is the bosonic field operator. This description is due to Penrose and Onsager [61] and is the most rigorous criterion for the identification of BEC but it's not the only one. Coherence properties in a BEC are large and off-diagonal-long range order emerges in the one-body density matrix [62]. Those two criteria define what is a true condensate in the sense that it has macroscopic coherence properties characterized by the off-diagonal long range order and a macroscopic occupation of the ground-state.

Taking those definitions as a cornerstone for the nature of a true condensate we see that a system of interacting bosonic particles confined in one dimension does not respect this criterion in the thermodynamic limit. As the dimensionality is strongly reduced, fluctuations in one dimension are enhanced and prevent the appearance of a true condensate. It has been shown [63] that the momentum distribution $n(q)$ diverges at small q as $q^{\frac{1}{2K}-1}$, so that in 1D the condition $\int dq n(q) = N$ shows the absence of BEC. Indeed, long-range order is not present in both 1D and 2D [64] at finite temperature and we talk about quasi-long range as the one-body density matrix displays a power law decay $g^{(1)}(x, x') \propto |x - x'|^{-\frac{1}{2K}}$. In the above expressions K is the Luttinger parameter and is associated to the compress-

1.3. Peculiarities of one dimensional systems

ibility of the system, see Chapter 5. For a finite system size, finite number of particles, and at very low temperatures, instead, the system can show macroscopic occupation of the ground state and the phase coherence can cover the whole system, thus reaching a true-condensate regime [65] (see Fig. 1.10).

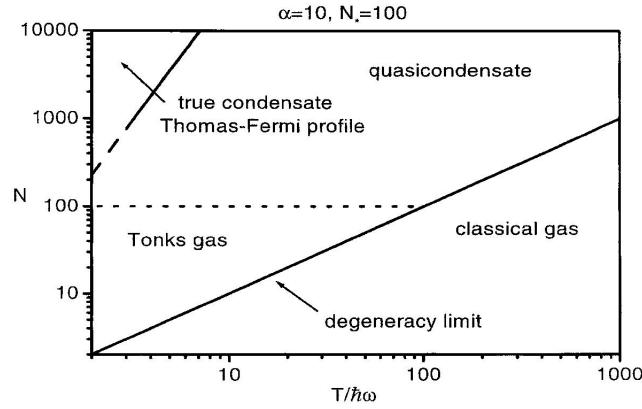


Figure 1.10: Regime of quantum degeneracy in a harmonically trapped quantum gas in the parameter space $(T/\hbar\omega, N)$ where T is the temperature and N the number of particles. The regime of quasi-condensation is shown and true condensation appears at low temperature for a large number of particle. The parameter N_* represents a critical number of particle for $N \gg N_*$ the gas is weakly interacting and when $N \ll N_*$ we enter the so called Tonks regime where bosons are strongly interacting. Taken from [65].

1.3. Peculiarities of one dimensional systems



Chapter 2

Mean-field of the double ring



THIS chapter is organized as follows. In Sec 2.1 we provide a quick review of the Gross-Pitaevskii equation. Then in Sec 2.2 we introduce the model a Bose gas confined in a double ring lattice under gauge fields. In Sec 2.3 we will study the properties of the non interacting gas identifying the vortex and Meissner phases. Mesoscopic effects in the system will be shown in Sec 2.4 as the appearance of a vortex in the Meissner phase and parity effect in the vortex phase, and the behavior of persistent currents. We also propose the spiral interferogram images obtained by interference among the two rings during time of flight expansion as a probe of vortex-carrying phases, specifically adapted to the ring geometry. Finally in Sec 2.5, we will explore, through a numerical study the dilute, weak-interacting regime and address the nature of the ground state at mean field level. In particular we identify known phases such as the Meissner, vortex and biased-ladder phases [16] as well as the effect of commensurability of the total flux.

2.1 Gross-Pitaevskii equation

As we have discussed in the introduction, a Bose-Einstein condensate is obtained from a collection of bosons sharing a macroscopic occupation of the ground state at very low temperatures. We will consider here the regime where the action of the non-condensed part on the condensate is negligible. We will focus on the energy of the ground state and use this to obtain information about the system. A general representation of an Hamiltonian in second quantized form reads

$$H = \int d\mathbf{r} \psi^\dagger(\mathbf{r}) h_{\mathbf{r}} \psi(\mathbf{r}) + \int d\mathbf{r}' \int d\mathbf{r} \psi^\dagger(\mathbf{r}) \psi^\dagger(\mathbf{r}') V_{\mathbf{r},\mathbf{r}'} \psi(\mathbf{r}') \psi(\mathbf{r}), \quad (2.1)$$

where $h_{\mathbf{r}}$ is a general one-body differential operator acting on the bosonic field operators $\psi(\mathbf{r})$, containing the kinetic energy and the external potential and the second term $V_{\mathbf{r},\mathbf{r}'}$ represents the inter-particle interaction. The Heisenberg equation of motion for the

bosonic field operator is

$$i\hbar \frac{d}{dt} \psi(\mathbf{r}, t) = [\psi(\mathbf{r}, t), H] = \frac{\delta H}{\delta \psi^\dagger(\mathbf{r}, t)} \quad (2.2)$$

$$= h_{\mathbf{r}} \psi(\mathbf{r}, t) + \int d\mathbf{r}' \psi^\dagger(\mathbf{r}', t) V_{\mathbf{r}, \mathbf{r}'} \psi(\mathbf{r}', t) \psi(\mathbf{r}, t) \quad (2.3)$$

The Gross-Pitaevskii equation is the equation of motion of the bosonic field in classical approximation, meaning that the quantum fluctuations and hence correlation between particles are neglected, so that the bosonic field is approximated as an averaged field. The Gross-Pitaevskii equation is then obtained by replacing the bosonic field operator by a classical field $\psi \rightarrow \sqrt{N_0} \phi$, where N_0 is the number of condensed particles, thus obtaining

$$i\hbar \partial_t \phi(\mathbf{r}, t) = \left[h_{\mathbf{r}} + N_0 \int d\mathbf{r}' V_{\mathbf{r}, \mathbf{r}'} |\phi(\mathbf{r}', t)|^2 \right] \phi(\mathbf{r}, t) \quad (2.4)$$

Generally, the Gross-Pitaevskii equation [63] was first derived and mostly studied is the special case of contact interparticle interaction, i.e $V_{\mathbf{r}, \mathbf{r}'} = g \delta(\mathbf{r} - \mathbf{r}')$ where $g = \frac{4\pi\hbar^2 a_s}{m}$ coming from the two-body scattering problem where a_s is the s-wave scattering length,

$$i\hbar \partial_t \phi(\mathbf{r}, t) = [h_{\mathbf{r}} + g N_0 |\phi(\mathbf{r}, t)|^2] \phi(\mathbf{r}, t). \quad (2.5)$$

This equation is also called *non-linear Schrodinger equation*.

2.2 The model

Bosons trapped in a ladder pierced by a magnetic field provide a minimal and quasi-one dimensional setup to study the interplay between orbital magnetism and interactions. In particular, the system as described in Fig 2.1 and by Hamiltonian (2.6) (in another gauge and linear configuration) displays chiral Meissner currents. It has been already experimentally realized in a linear configuration [19]. Its phases are illustrated in the diagram of Fig 2.2. Below a critical inter-leg coupling strength, the chiral current decreases in good agreement with the theoretical prediction of a vortex lattice phase [12].

In our work, published in [66], we consider a Bose gas confined in a double ring lattice see Fig 2.2. In the tight-binding approximation we model the system using the Bose-Hubbard model:

$$\begin{aligned} \hat{H} &= \hat{H}_0 + \hat{H}_{int} = \\ &- \sum_{l=1, p=1, 2}^{N_s} J_p \left(a_{l,p}^\dagger a_{l+1,p} e^{i\Phi_p} + a_{l+1,p}^\dagger a_{l,p} e^{-i\Phi_p} \right) \\ &- K \sum_{l=1}^{N_s} \left(a_{l,1}^\dagger a_{l,2} + a_{l,2}^\dagger a_{l,1} \right) + \frac{U}{2} \sum_{l=1, p=1, 2}^{N_s} a_{l,p}^\dagger a_{l,p}^\dagger a_{l,p} a_{l,p} \end{aligned} \quad (2.6)$$

2.2. The model

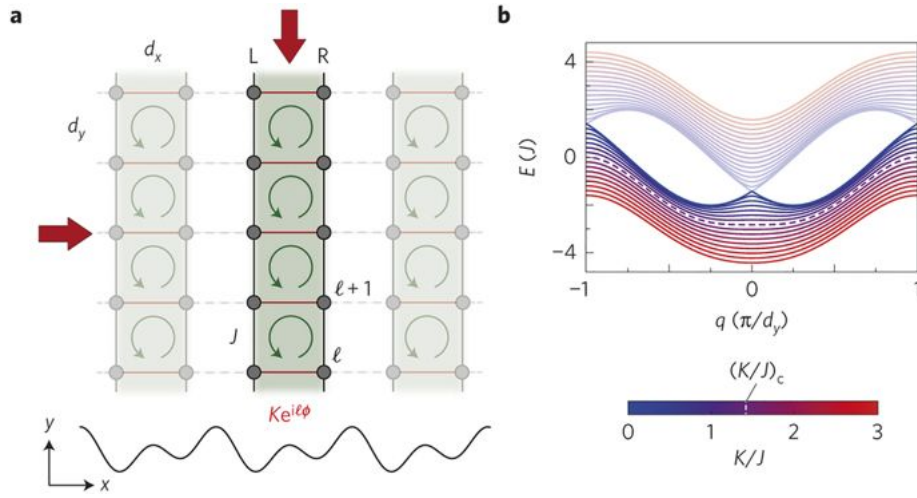


Figure 2.1: **a)** Schematic representation of the experimental setup of Ref [19] and **b)** energy levels. An effective homogeneous magnetic field in each ladder is realized through laser-induced tunneling (red arrows) between the left (L) and right (R) legs of the ladder. Taken from [19]. The gauge here is changed with respect to Eq (2.6) by $a_{l,1} \rightarrow e^{i(\phi/2)l} a_{l,1}$ and $a_{l,2} \rightarrow e^{-i(\phi/2)l} a_{l,2}$.

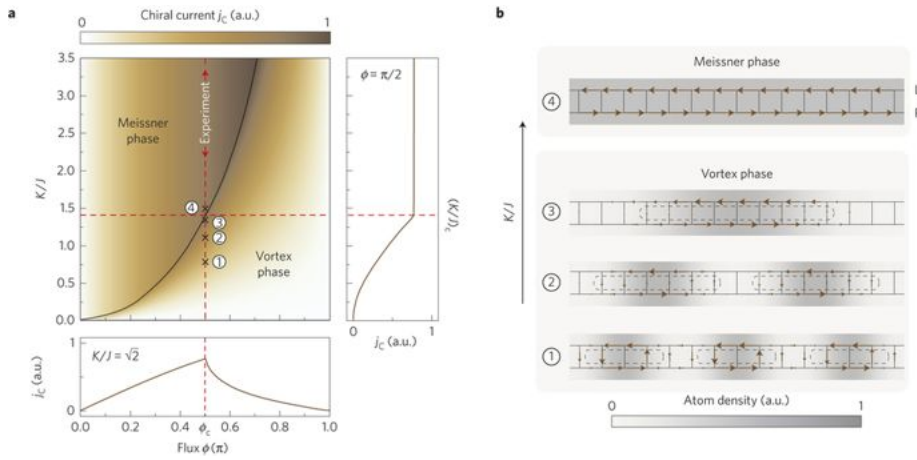


Figure 2.2: **a)** Phase diagram of ladder chiral current as order parameter for the distinctive Meissner and Vortex phases. **b)** Theoretically calculated individual currents and particle densities for the different values of K/J . Taken from [19]

where the angular position on the double ring lattice is given by $\theta_l = \frac{2\pi}{N_s} l$ where l is an integer $l \in [1, N_s]$ with N_s the number of sites in each ring. In Eq (2.6) J_1 and J_2 are respectively the tunneling amplitude from one site to an other along each ring, the parameter K is the tunneling amplitude between the two rings, connecting only sites with the same position index l and $\Phi_{1,2}$ are the fluxes threading the inner and outer ring respectively. In the case where the gauge fields are induced by applying a rotation to each ring one has $\Phi_i = \frac{2\pi}{N_s} \frac{\tilde{\Phi}_i}{\Phi_0}$,

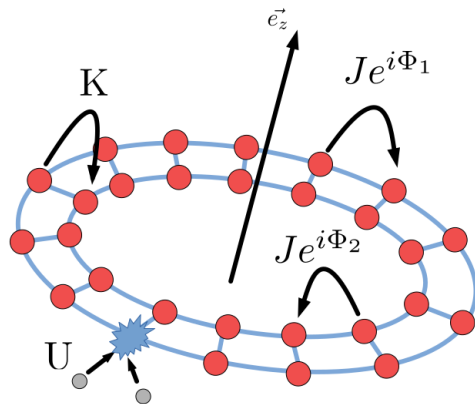


Figure 2.3: Representation of the geometry studied in this work: co-planar ring lattices of radii R_1 and R_2 with the same number of sites, with inter-ring tunnel energy K and intra-ring tunnel energies $J e^{i\Phi_p}$, with $p = 1, 2$.

with $\tilde{\Phi}_i = \Omega R_i^2$, Ω being the angular rotation frequency, R_i radius of ring i , $\Phi_0 = 2\pi\hbar/m$ the Coriolis flux quantum. As $J_i \approx \frac{\hbar^2}{2mR_i^2}$, to lowest order we can consider $J_1 \approx J_2$ corresponding to two rings close to each other, or realized using adjusted lattice potential. In the following, it will be useful to introduce the relative flux $\phi = \Phi_1 - \Phi_2$ and average flux $\Phi = (\Phi_1 + \Phi_2)/2$.

2.3 Non interacting regime

We first proceed by analyzing the non-interacting problem. The diagonalization of H_0 (see Appendix A for details) yields the following two-band Hamiltonian:

$$\hat{H}_0 = \sum_k \alpha_k^\dagger \alpha_k E_+(k) + \beta_k^\dagger \beta_k E_-(k), \quad (2.7)$$

where

$$\begin{pmatrix} a_{k,1} \\ a_{k,2} \end{pmatrix} = \begin{pmatrix} v_k & u_k \\ -u_k & v_k \end{pmatrix} \begin{pmatrix} \alpha_k \\ \beta_k \end{pmatrix}, \quad (2.8)$$

and the functions u_k and v_k depend on the parameters ϕ and K/J (see Appendix A for details), the momentum in units of inverse lattice spacing takes discrete values given by $k = \frac{2\pi n}{N_s}$, with $n = 0, 1, 2, \dots, N_s - 1$ and the dispersion relation $E_\pm(k)$ reads

$$E_\pm(k) = -2J \cos(\phi/2) \cos(k - \Phi) \pm \sqrt{K^2 + (2J)^2 \sin^2(\phi/2) \sin^2(k - \Phi)}. \quad (2.9)$$

2.3. Non interacting regime

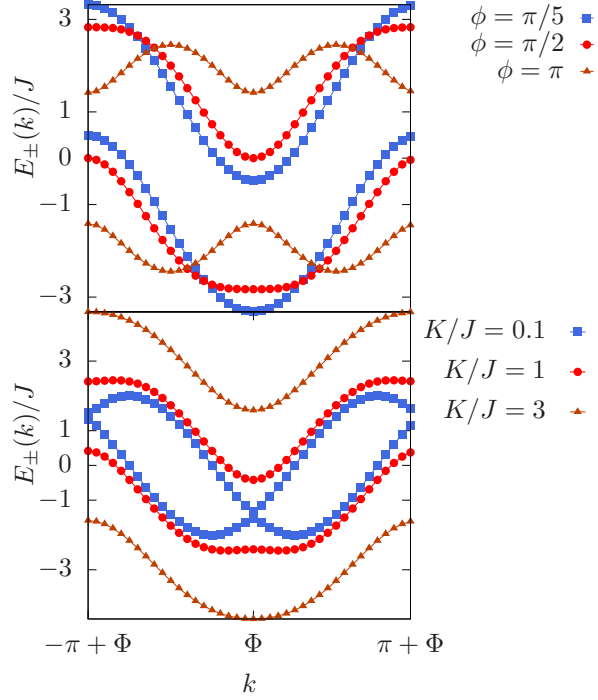


Figure 2.4: Energy spectrum (in units of J with $N_s = 40$ sites on each ring) as a function of wavevector k (in units of inverse lattice spacing) of non-interacting bosons on a double ring lattice, for several values of the tunneling ratio K/J at fixed relative flux $\phi = \pi/2$ (bottom) and several values of ϕ at fixed $K/J = \sqrt{2}$ (top).

We see that the only influence of the average flux Φ is to shift in momentum space the energy spectrum.

The relevant ground-state properties are obtained from the low-energy branch of the spectrum since, for a finite size-ring, at $T = 0$ and $U = 0$ the bosons form a condensate in the lowest-energy state available. At varying tunneling ratio K/J and relative flux ϕ , two possible situations arise from the lowest-energy branch $E_-(k)$ (see Fig. 2.4). When $E_-(k)$ has a single minimum, the bosons condense in the state $k = \Phi$, corresponding to the Meissner phase, while one has a vortex phase when $E_-(k)$ has two minima and bosons condense with the same occupancy in each of the two minima k_1 and k_2 given by

$$k_{1,2} = \Phi \mp \arccos \left[\cot \left(\frac{\phi}{2} \right) \sqrt{\left(\frac{K}{2J} \right)^2 + \sin^2 \left(\frac{\phi}{2} \right)} \right]. \quad (2.10)$$

Other possible occupancies of the two minima are discussed in Appendix A. The vortex to Meissner phase transition has been experimentally observed in bosonic linear flux ladders [19]. At fixed K/J value, the critical flux where the transition appears is obtained by

determining the change of curvature in $E_-(k = \Phi)$, thus yielding [11]:

$$\phi_c = 2 \arccos \left[\sqrt{\left(\frac{K}{4J}\right)^2 + 1} - \left(\frac{K}{4J}\right) \right]. \quad (2.11)$$

The Meissner phase is characterized by vanishing transverse currents

$$j_{l,\perp} = iK \langle a_{l,1}^\dagger a_{l,2} - a_{l,2}^\dagger a_{l,1} \rangle, \quad (2.12)$$

the longitudinal currents on each ring, defined as

$$j_{l,p} = iJ \langle a_{l,p}^\dagger a_{l+1,p} e^{i\Phi_p} - a_{l+1,p}^\dagger a_{l,p} e^{-i\Phi_p} \rangle, \quad (2.13)$$

are opposite and the chiral current, i.e $J_c = \sum_l \langle j_{l,1} - j_{l,2} \rangle$ is saturated. The vortex phase is characterized by a modulated density, jumps of the phase of the wave function, and non-zero, oscillating transverse currents which create a vortex pattern. This is illustrated in Fig.2.6, which shows the longitudinal and transverse current configurations both in the Meissner and in the vortex phase.

2.3.1 Persistent and chiral currents

We proceed next to study the persistent currents on the ring. They are defined as $I_p = \frac{\partial \langle H \rangle}{\partial \Phi_p}$. Since for the Hamiltonian (2.6) one has $\frac{\partial \langle H \rangle}{\partial \Phi} = 0$, we obtain that $I_1 = -I_2 = I$ and we have a correspondence between chiral current J_c and persistent current:

$$J_c = 2I = \frac{\partial \langle H \rangle}{\partial \phi}. \quad (2.14)$$

In particular, Fig 2.5 represents the dependence of the excitation spectrum branches on the relative flux. In order to obtain the persistent currents for each value of ϕ we identify the lowest-energy branch as defined piece-wise by following the lowest-energy part of $E_-(k)$ (see Fig. 2.5 upper panel). The persistent current is then readily obtained by deriving this curve with respect to the flux ϕ . The resulting persistent current as a function of relative flux ϕ is illustrated in Fig. 2.5 (bottom panel). By increasing the relative flux at fixed K/J , the system undergoes a transition from Meissner to vortex phase. For low ϕ values, the particle stays in the branch $E_-(k = \Phi)$ as long as it is in the Meissner phase. At the critical value ϕ_c for entering the vortex phase, the persistent current displays a jump, and takes an angular momentum value equal to $\Phi + 2\pi/N_s$. As the flux ϕ increases, the persistent currents display several other jumps, each corresponding to the appearance of a vortex pair in the ring. We notice that the total number of jumps in the current curve corresponds to $N_s/2$, ie the maximal number of vortex pairs on the ring.

2.3. Non interacting regime

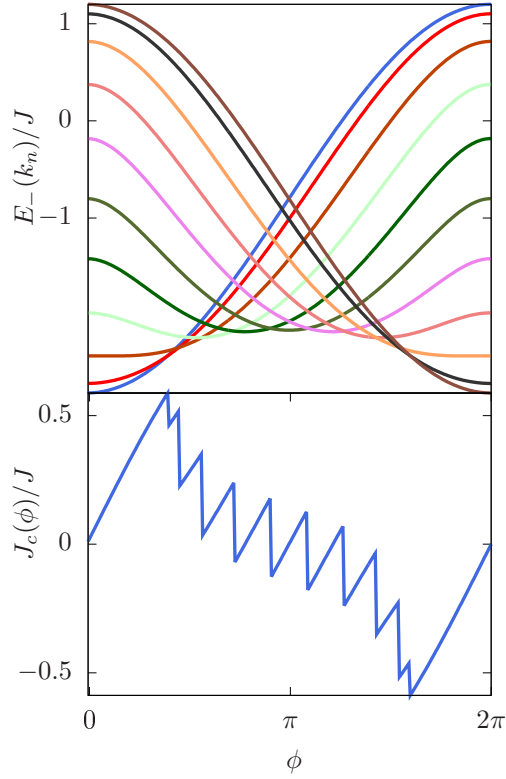


Figure 2.5: Upper panel: Excitation branches $E_-(k_n, \phi)$ as a function of the relative flux ϕ (dimensionless) for various values of $k_n = \frac{2\pi}{N_s} n$, $n \in [0, N_s/2]$. At $\phi = 0$, one has $E_-(k_0, \phi) < E_-(k_1, \phi) < \dots < E_-(k_n, \phi)$ (blue to brown curves, from bottom to top). The energy of the lowest excitation branch is the lower envelope of these curves and is used to calculate the chiral current. Lower panel: chiral current, obtained from Eq. (2.14), as a function of ϕ . In both panels we have taken $N_s = 20$, $\Phi = 0$ and $K/J = 0.8$.

2.3.2 Infinite system - Variational Ansatz

In the case of non interacting bosons, when the single-particle spectrum has two degenerate minima, the many-body ground state energy is highly degenerate as it corresponds to all possible partitions of the particles among the two minima. In the presence of interactions this degeneracy is broken. Introducing the variational ansatz

$$|\Phi_N\rangle = \frac{1}{\sqrt{N!}} \left(\cos(\theta/2) \beta_{k_1}^\dagger + \sin(\theta/2) \beta_{k_2}^\dagger \right)^N |0\rangle, \quad (2.15)$$

which is valid in weakly interacting regime, Wei and Mueller [16] have identified two phases, corresponding to two different partitions of the bosons on the minima k_1 and k_2 : a vortex phase, when each minimum is occupied by $N/2$ bosons, occurring if $1 - 6u_{k_1} v_{k_1} > 0$; and a

biased ladder phase, characterized by symmetry breaking and full occupancy of only one of the two minima, occurring when $1 - 6u_{k_1}v_{k_1} < 0$. The biased ladder phase is characterized by the absence of density modulations and different density values on the two rings.

2.4 Mesoscopic effects and commensurability of the flux

2.4.1 Vortex configurations on a finite double ring lattice

Figure 2.8 shows the distribution of the phase and density of the condensate wave function of the non-interacting gas in the vortex phase, which reads

$$\psi_{l,p} = \sqrt{\frac{N}{2N_s}} \left(\delta_{p,1}(u_{k_1} e^{ik_1 l} + u_{k_2} e^{ik_2 l}) + \delta_{p,2}(v_{k_1} e^{ik_1 l} + v_{k_2} e^{ik_2 l}) \right), \quad (2.16)$$

for various values of the system parameters. The number N_v of vortices is obtained by counting the number of jumps in the phase. Since it is also associated to the number of oscillations in the density, which are characterized by the wavevector $k = k_2 - k_1$, it is readily obtained as $N_v = N_s(k_2 - k_1)/2\pi$. Recalling that the value of the total flux Φ fixes the position of the minima of the dispersion relation (2.9), in the case where the total flux is multiple of $\frac{\pi}{N_s}$ we obtain specific features associated to the commensurability of Φ with the allowed values of the discrete wavevector k . Figure 2.7 depicts the various possibilities. When $\Phi = 2j \frac{\pi}{N_s}$, with j integer number, the dispersion relation is centered on an allowed value of the quantized momentum k . In this case vortices start to form when the dispersion relation displays a double-minima structure, and the number of vortices is even.

On the other hand, when $\Phi = (2j + 1) \frac{\pi}{N_s}$ the value of Φ falls among two adjacent values of quantized momentum k (see again Fig.2.7). In this case, in the vortex phase, the distance among the two minima corresponds to an odd multiple of $\frac{\pi}{N_s}$, giving rise to an odd number of vortices. Quite interestingly, in the Meissner phase, ie for a choice of parameters ϕ and K/J leading to a single minimum in the single-particle excitation dispersion $E_-(k)$, for $\Phi = (2j + 1) \frac{\pi}{N_s}$ we find a nontrivial pattern in the current profiles, corresponding to a single vortex configuration (see Fig.2.6, third panel). This is a mesoscopic effect associated to the finite size and the geometry of the ring. As we shall see below, however, this vortex is more fragile than those appearing in the vortex phase, and is destroyed in the presence of interactions.

2.4.2 Fate of the single vortex in the Meissner phase

As discussed in Sec.2.4.1, in the case when the total flux $\Phi = (2j + 1) \frac{\pi}{N_s}$ and the system is in the Meissner phase, the non-interacting solution predicts the formation of a single vortex. We explore here the fate of such a vortex in the presence of weak interactions.

A first answer is provided by the variational ansatz introduced in Ref.[16] specialized to the case where the bosons occupy two neighbouring momentum states of the single-

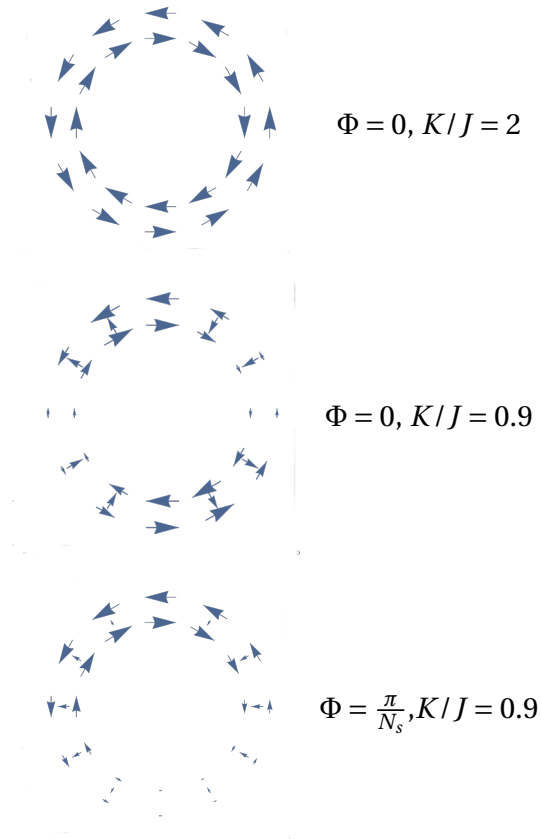


Figure 2.6: Representation of the current patterns for non-interacting bosons on a double ring lattice in various parameter regimes as indicated on the figure. The length of arrows is proportional to the amplitude of the current field. The currents fields are minimal at the core of the vortex, where also the density drops. Upper panel: Meissner phase. Middle panel: vortex phase, case of two vortices. Lower panel: single vortex in the Meissner phase. In all panels, $\phi = \pi/2$ and $N_s = 12$.

2.4. Mesoscopic effects and commensurability of the flux

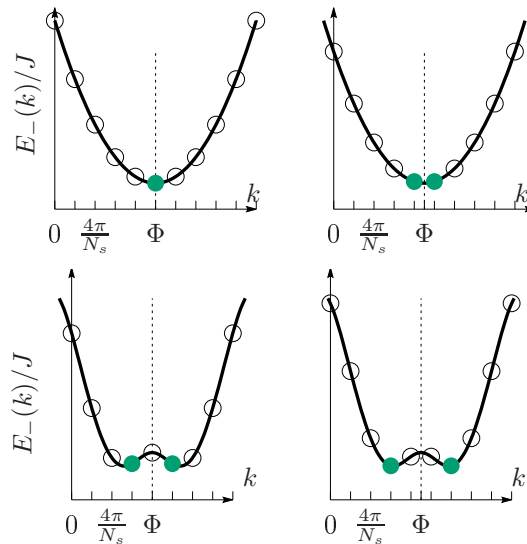


Figure 2.7: Scheme of the occupancy of the single-particle levels by non-interacting bosons at zero temperature (filled green circles), on the single-particle dispersion relation in the energy-momentum plane (empty circles joined by line), for various choices of total flux Φ (dashed vertical line). In the Meissner phase, when $\Phi = 2j \frac{\pi}{N_s}$ (left top panel, with $\Phi = 10\pi/N_s$) bosons condense in the $k = \Phi$ mode. When $\Phi = (2j + 1) \frac{\pi}{N_s}$ (right top panel, with $\Phi = 9\pi/N_s$), Φ lies between two momentum modes, the lowest-energy states are doubly degenerate and the system supports a vortex in the Meissner phase. In the vortex phase, when $\Phi = 2j \frac{\pi}{N_s}$ (bottom left panel, with $\Phi = 8\pi/N_s$) we find an even number of vortices, whereas when $\Phi = (2j + 1) \frac{\pi}{N_s}$ (bottom right panel, with $\Phi = 9\pi/N_s$) the number of vortices is odd. Notice that the scheme is completely general for values of Φ equal to any odd or even multiple of π/N_s .

particle excitation spectrum centered around $k = \Phi$, in the case where it has a single minimum (as shown in Fig. 5, upper left panel):

$$|\Psi_N\rangle = \frac{1}{\sqrt{N!}} \left(\cos(\theta/2) \beta_{\Phi+\pi/N_s}^\dagger + \sin(\theta/2) \beta_{\Phi-\pi/N_s}^\dagger \right)^N |0\rangle. \quad (2.17)$$

One readily obtains, if $1 - 6u_{\Phi+\pi/N_s}^2 v_{\Phi+\pi/N_s}^2 < 0$, that the total energy is minimized by the choice $\theta = \pi$, while one has $\theta = \pi/2$ if $1 - 6u_{\Phi+\pi/N_s}^2 v_{\Phi+\pi/N_s}^2 > 0$. However, by using the results of Appendix A for the amplitudes u_k and v_k , one readily finds that in the Meissner phase $1 - 6u_{\Phi+\pi/N_s}^2 v_{\Phi+\pi/N_s}^2$ is always negative, and we conclude that lowest-energy solution is of biased-ladder type.

We have verified this prediction by the numerical solution of the DNLSE, and we confirm that no vortex is found at finite interactions and the density profile is of biased-ladder type, as illustrated in Fig. 2.9 and in the phase diagram (Fig. 2.11, lower panel). By performing calculations at varying system size, we find that the imbalance among the two

2.4. Mesoscopic effects and commensurability of the flux

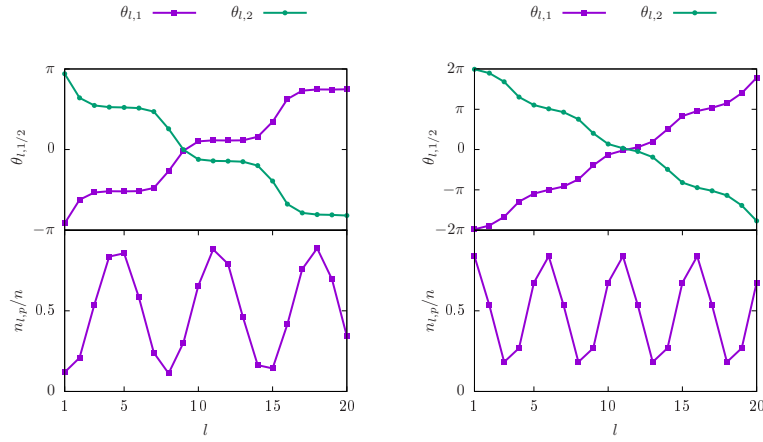


Figure 2.8: Phase and density profiles of the condensate wavefunction for non-interacting bosons along the double ring lattice as a function of the lattice index. Top panel: odd number of vortices for average flux $\Phi = \pi/N_s$. Bottom panel: even number of vortices for $\Phi = 0$. The other parameters are $K/J = 0.8$, $\phi = \pi/2$, $N_s = 20$ and $n = N/N_s$.

rings decreases with increasing N_s .

It is interesting to notice that this is different from the case of the biased ladder phase BL-V obtained for values of flux corresponding to even multiples of π/N_s . In this case, the particle imbalance does not depend on N_s and the phase is also found in the thermodynamic limit.

2.4.3 Spiral interferograms

It has been shown [67, 68, 69] that it is possible to reconstruct the phase pattern of ring trapped Bose-Einstein condensate by studying its interference pattern with a reference disk-shaped condensate placed at the center of the ring. Using a similar principle, we show here that the interference pattern of two concentric rings allows to characterize the vortices in the bosonic double ring lattice.

Assuming that the distance between neighbouring sites on each ring is larger than the difference of the radii of the two rings, the main contribution to the interference process is due to radially overlapping condensates belonging to the same site index in each ring (ie with the same angular coordinate). In this case, the wave function after a time t_{TOF} from releasing the double ring trap is given by (see Appendix D for details):

$$\Psi_p(r, \theta_l) \approx \tilde{\Psi}_0(k_{s,p}) e^{i\hbar \frac{k_{s,p}^2}{2m} t_{TOF}} e^{i\phi_{l,p}} \sqrt{n_{l,p}} \quad (2.18)$$

where $\phi_{l,p}$ and $n_{l,p}$ are respectively the phase and the number of particles of a condensate on the ring p at site l , and $k_{s,p} = \frac{(R_p - r)(-1)^p m}{\hbar t_{TOF}}$ is related to the velocity at which each

2.4. Mesoscopic effects and commensurability of the flux

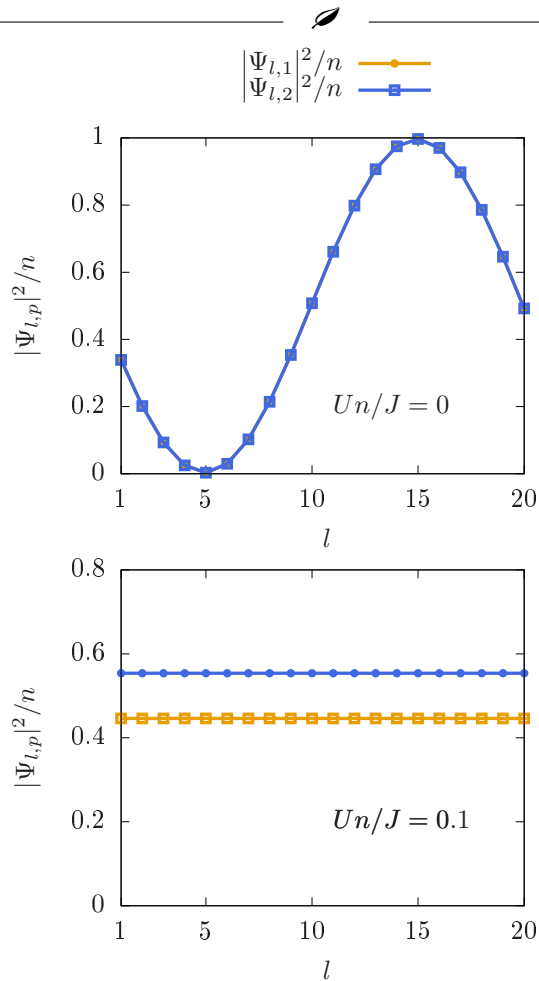


Figure 2.9: Density profile for a double ring lattice of interacting bosons with total flux $\Phi = \pi/N_s$, in the absence of interactions, single vortex in the Meissner phase (upper panel) and for weak repulsive interactions biased-ladder (BL-M) phase (lower panel). The other parameters are $N_s = 20, K/J = 2, \phi = \pi/2$.

wave function evolve after releasing the trap. The interference pattern intensity is given by $I(r, \theta) = 2 \text{Re}[\Psi_1^*(r, \theta)\Psi_2(r, \theta)]$. By recalling that in density-phase representation

$$\sqrt{n_{l,1}n_{l,2}}e^{i(\phi_{l,1}-\phi_{l,2})} = \langle a_{l,2}^\dagger a_{l,1} \rangle, \quad (2.19)$$

we obtain the following intensity distribution in the polar plane (r, θ_l) :

$$I(r, \theta_l) = \langle a_{l,1}^\dagger a_{l,1} \rangle + \langle a_{l,2}^\dagger a_{l,2} \rangle + 2\text{Re} \left[e^{i\Delta_R} e^{iQr} \langle a_{l,1}^\dagger a_{l,2} \rangle \right] \quad (2.20)$$

with $Q = \frac{m(R_1 - R_2)}{\hbar t_{TOF}}$ and $\Delta_R = \frac{(R_2^2 - R_1^2)m}{\hbar t_{TOF}}$.

In order to analyze typical interference profiles in the various phases, we start from the non-interacting regime. In this case, using the results of Appendix A, in the Meissner

2.4. Mesoscopic effects and commensurability of the flux

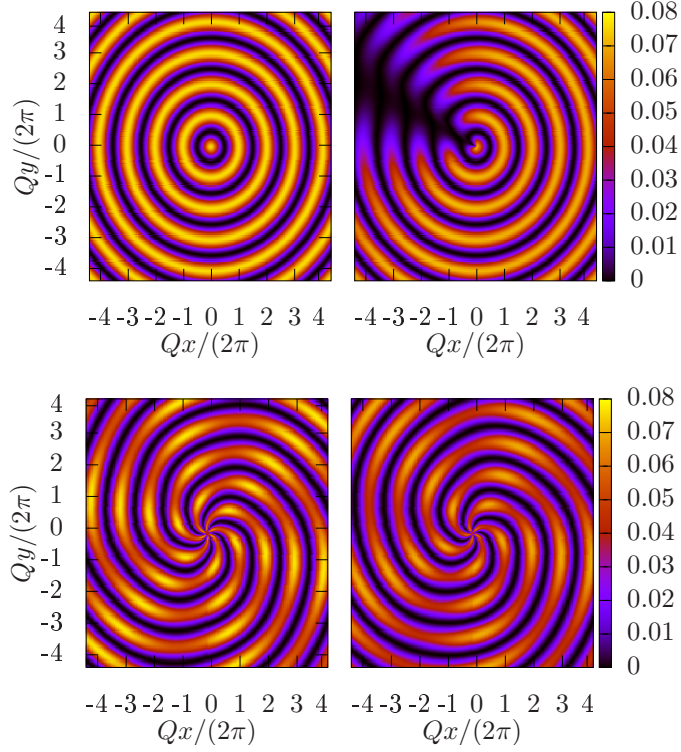


Figure 2.10: Spiral interferogram in the Meissner phase (upper panels) with $K/J = 1.5$, $\phi = \pi/2$ and $Un/J = 0.3$, $\Phi = 0$ (upper left panel), $Un/J = 0$, $\Phi = \frac{\pi}{N_s}$ (upper right panel), and in the vortex phase (lower panels) taking $K/J = 0.1, Un/J = 0.3$, $\phi = \pi/3$, with $\Phi = 0$ (lower left panel), and $\Phi = \frac{\pi}{N_s}$ (lower right panel). In all panels $N_s = 35$.

phase one readily obtains

$$I(r, \theta_l) \propto \frac{1}{N_s} \cos(Qr + \Delta_R) + n_{\theta_l} \quad (2.21)$$

where $n_{\theta_l} = \langle a_{l,1}^\dagger a_{l,1} + a_{l,2}^\dagger a_{l,2} \rangle$. This corresponds to an interference pattern made of concentric rings, as illustrated in the first panel of Fig.2.10.

In the case of a single vortex in the Meissner phase, (second panel of Fig.2.10) the interference pattern displays a line of dislocations, which are due to the phase slip and vanishing of the density in correspondence of the vortex core.

In the vortex phase, Eq.(2.20) yields

$$\begin{aligned} I(r, \theta_l) &\propto \frac{1}{N_s} [2u_{k_1} v_{k_1} \cos(Qr + \Delta_R) \\ &+ v_{k_1}^2 \cos(\theta_l(k_2 - k_1) - \Delta_R - Qr) \\ &+ u_{k_1}^2 \cos(\theta_l(k_2 - k_1) + \Delta_R + Qr)] \\ &+ n_{\theta_l}. \end{aligned} \quad (2.22)$$

In this case, the interference pattern is composed of a term which is constant along θ , that gives rise to concentric rings and two spirals patterns with uniform intensity each of them corresponding to one of the two ring, one going clockwise and the other counter-clockwise. The superposition of the three contributions yields a modulated spiral pattern, shown in Fig.2.10. This method, which is specific for the ring geometry, is a very powerful characterization of the vortex phase, as the number of branches in the pattern yields the number of vortices in the system. This allows in particular to evidence the possibility of having even or odd number of vortices, depending on the value of the total flux. As a final remark we notice that the interference pattern is dependent on the choice of gauge, other choices will lead to different spiral interferogram pictures.

2.5 Mean-field ground state phase diagram

2.5.1 Coupled discrete nonlinear Schrödinger equations (DNLSE)

In order to explore in a broader way the weakly-interacting regime, we study the ground state of the system in the mean-field approximation, obtained by neglecting the quantum fluctuations and correlations.

We start from the equations of motion for the bosonic field operators in the Heisenberg picture:

$$i\hbar \frac{da_{l,p}(t)}{dt} = [a_{l,p}(t), H]. \quad (2.23)$$

Taking the mean-field approximation, ie setting $\Psi_{l,p}(t) = \langle a_{l,p}(t) \rangle$ we obtain two coupled discrete non-linear Schrödinger equations (DNLSE):

$$\begin{aligned} i\partial_t \Psi_{l,1}(t) &= -J\Psi_{l+1,1}(t)e^{i(\Phi+\phi/2)} - J\Psi_{l-1,1}(t)e^{-i(\Phi+\phi/2)} \\ &\quad - K\Psi_{l,2}(t) + U|\Psi_{l,1}(t)|^2\Psi_{l,1}(t) \end{aligned} \quad (2.24)$$

$$\begin{aligned} i\partial_t \Psi_{l,2}(t) &= -J\Psi_{l+1,2}(t)e^{i(\Phi-\phi/2)} - J\Psi_{l-1,2}(t)e^{-i(\Phi-\phi/2)} \\ &\quad - K\Psi_{l,1}(t) + U|\Psi_{l,2}(t)|^2\Psi_{l,2}(t) \end{aligned} \quad (2.25)$$

This is the lattice version of the Gross-Pitaevskii equation 2.4 generalized to the two ring case. The above equations are expected to hold for weak interactions and large number of particle on each site.

The corresponding energy functional is given by

$$\begin{aligned} E[\Psi_1, \Psi_2] &= -J \sum_{l,p} \left(\Psi_{l,p}^* \Psi_{l+1,p} e^{i\Phi_p} + c.c \right) \\ &\quad - K \sum_l \left(\Psi_{l,1}^* \Psi_{l,2} + c.c \right) + \frac{U}{2} \sum_{l,p} |\Psi_{l,p}|^4, \end{aligned} \quad (2.26)$$

where $\Psi_p = \{\Psi_{l,p}\}$.

2.5. Mean-field ground state phase diagram

We use a split-step Fourier transform method [70] to solve the discrete time dependent NLSE and perform imaginary-time evolution to obtain the ground state of the system with the normalization condition,

$$\sum_{l=1}^{N_s} \sum_{p=1,2} |\Psi_{l,p}|^2 = N \quad (2.27)$$

where N is the number of particles in the system. We use the numerical solution of the DNLS (3.20) to explore the nature of the ground state at varying interactions and inter-ring tunnel coupling, as identified by the ratios Un/J and K/J , with $n = N/N_s$. For simplicity of the analysis, we choose a fixed value $\phi = \pi/2$ for the relative flux. Our results are illustrated in Fig. 2.11, showing the particle imbalance among the two rings $\Delta = |\sum_l \langle n_{l,1} - n_{l,2} \rangle| / N$. For a choice of total flux Φ corresponding to an even multiple of π/N_s (upper panel of Fig. 2.11) at varying interaction and tunnel parameters we identify three phases: the vortex (V) and Meissner (M) phases found in the non-interacting regime, as well as the biased-ladder phase (BL-V) predicted by the variational ansatz. We have denoted this latter phase BL-V since it is competing with the vortex phase, and are both obtained from the ansatz when the single-particle spectrum has a double minimum structure. The white triangles in Fig. 2.9 represent the frontiers between biased-ladder phase and the two other phase, namely vortex phase and Meissner phase as calculated with the variational ansatz including finite size effects ¹. The agreement between the variational approach and numerical calculation shows that the ansatz is well suited to capture the relevant features of the double ring lattice. Figure 2.12 shows the corresponding density profiles of the various phases: biased-ladder, Meissner and vortex phases are illustrated in panels (BL-V), (M) and (V) respectively. For values of total flux corresponding to an odd multiple of π/N_s (lower panel of Fig. 2.11) in place of the Meissner phase admitting a single vortex, as predicted in absence of interactions, we find a biased-ladder phase (denoted as BL-M in the figure). As it will be discussed in section V.B, this is a mesoscopic effect due to the finite size of the ring – the imbalance decreases with increasing number of sites on the ring.

2.5.2 Persistent currents for interacting bosons on the double ring lattice

The numerical solution of the DNLS allows also to obtain the persistent currents in the presence of weakly repulsive interactions. Figure 2.13 shows the dependence on persistent currents amplitude on relative flux ϕ for the interacting double ring lattice. As compared to the non-interacting case, notable differences occur at increasing ϕ when the phase boundary is crossed: due to the presence of the intermediate biased-ladder phase, the jumps in the persistent current are suppressed as they are associated to the creation of vortices. For the parameter choice used in Fig. 2.13 one can then identify both the tran-

¹We take the wave functions of the ansatz (Eq. (3.51)) corresponding to the various phases (BL-V,V,M) and we compare their energies calculated from Eq. (2.26) to obtain the phase boundaries.

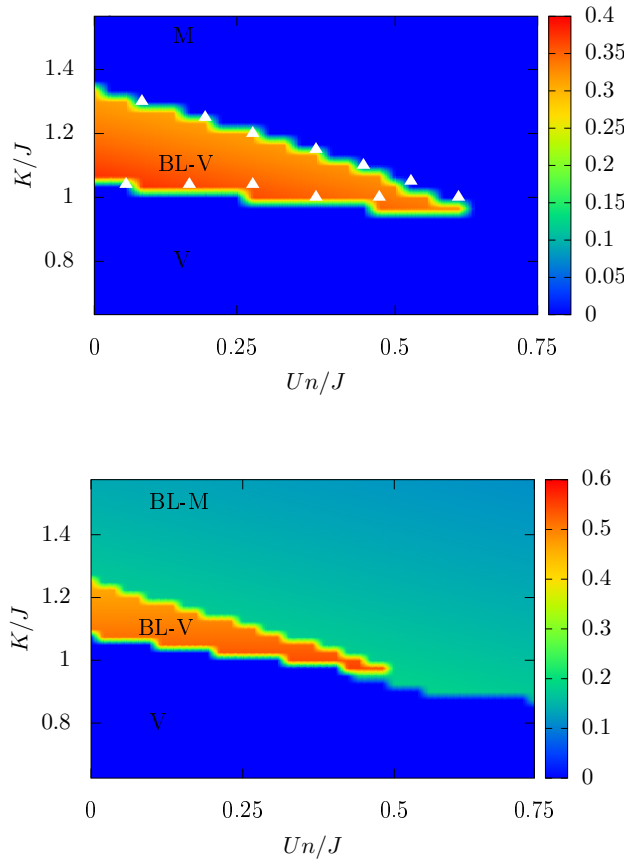


Figure 2.11: Color map of the imbalance among particle numbers in each ring, in the $(K/J, Un/J)$ plane, for (upper panel) $\phi = \pi/2$, $\Phi = 6\pi/N_s$ and $N_s = 20$, (lower panel) $\phi = \pi/2$, $\Phi = \pi/N_s$ and $N_s = 20$. The letters indicate the parameter regimes where we find a biased-ladder phase (BL-V) where the single-particle spectrum has a double minimum, a Meissner phase (M), a vortex phase (V) and a biased-ladder phase (BL-M) where the single-particle spectrum has a single minimum. The corresponding density profiles are illustrated in Fig. 2.12 and 2.9. White triangles represent the frontiers between biased-ladder phase the two other phase, namely vortex phase and Meissner phase as calculated with the variational ansatz including finite size effect.

sition from Meissner to biased ladder and from the latter to the vortex phase. Persistent currents thus provide a powerful tool to explore the phases of the double ring lattice.

2.5. Mean-field ground state phase diagram

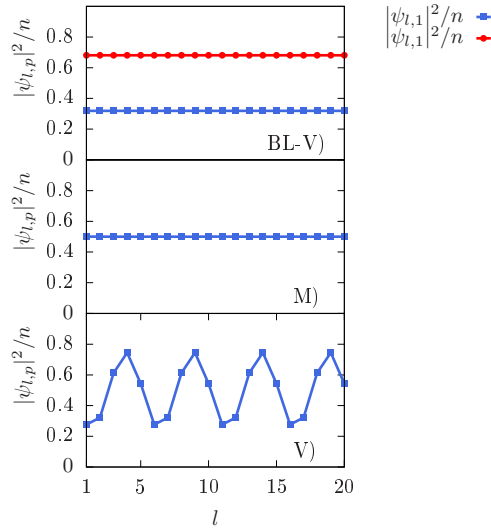


Figure 2.12: Density profiles along each ring as a function of the lattice index along the ring, with $N_s = 20$, $\phi = \pi/2$, $\Phi = 6\pi/N_s$, in the various phases identified in the diagram of Fig. 2.11: with parameter $\phi = \pi/2$, $N_s = 20$, $Un/J = 0.05$ and biased-ladder phase (BL-V), for $K/J = 1.1$; Meissner phase (M), for $K/J = 2$; vortex phase (V), for $K/J = 0.5$ and $Un/J = 0.3$.

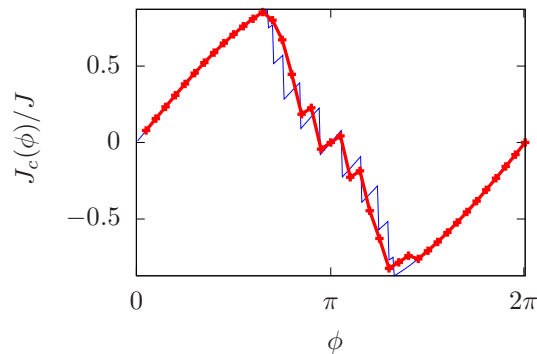


Figure 2.13: Chiral currents in units of J as a function of the relative flux ϕ (dimensionless) for non-interacting bosons (blue, thin solid line) and weakly interacting ones $Un/J = 0.1$ (red, thick solid line) for $N_s = 20$ and $K/J = 3$.

Conclusions of the chapter

In this chapter, we have studied the ground-state properties of weakly interacting bosons on a double ring lattice, subjected to two gauge fields. Depending on the ratio between inter-ring and intra-ring tunnel energies, as well on the relative flux, the bosons are found

2.5. Mean-field ground state phase diagram

to be in the Meissner or vortex phases, previously identified for the linear ladder geometry. As specific of the ring geometry, for the non interacting gas, we have found a parity effect on the number of vortices in the system, which originates from the commensurability of total flux with respect to allowed momentum states on the rings. Also, for special values of total flux Φ , due to finite size effects, we have found that the ground state may host a single vortex even in the Meissner phase. The analysis of persistent currents shows that at varying relative flux it is possible to identify both the Meissner and vortex phase. In the latter, due to finite-size of the double ring lattice, it is possible to monitor the appearance of pairs of vortices at increasing ϕ . We have then considered the effect of weakly repulsive interactions, as described within a mean-field approach. We have identified the biased ladder phase and shown that the Meissner phase becomes imbalanced at odd value of the total flux Φ due to mesoscopic effects. Even in the presence of interactions, the study of persistent currents is a useful tool to characterize the various phases.

Finally, we have proposed the interference patterns among the two rings as probe of the various phases, specifically adapted to the our ring geometry, yielding in particular spiral images in the presence of vortices.

An analysis beyond mean-field suggests that the very small ring lattice at weak filling displays fragmentation [71] in a similar way as what is found for spin-orbit coupled Bose gases [72]. In outlook, it would be interesting to explore the crossover from mean-field to fragmented state at decreasing the lattice filling and size.

Chapter 3

Bogoliubov excitations

UPEROLIDITY is a combined effect of solid order and superfluid flow. In order for a system to form a supersolid it has to break two symmetries, continuous translational symmetry (discrete rotational symmetry in our case) to create a crystal order and $U(1)$ symmetry in order to create a condensate. The concept of supersolidity was first introduced in the context of Helium more than 50 years ago [73, 74]. This peculiar state of matter seems contradictory as it combines a dissipationless flow that emerges from the Bose-Einstein condensation, hence from the delocalization of atoms under the sample that makes the atomic gas ordered in momentum space and an order in real space emerging from the localization of atoms in a periodic crystalline structure. Experiments in the beginning of the century revealed the possibility of supersolid behavior in ^4He [75, 76]. It has later been made clear that the superflow in solid Helium was due to imperfections that change the bulk modulus of the crystal [77] so that the dislocations in the crystal are superfluid [78] but not the system itself.

With ultra-cold atoms, a supersolid has been realized based on self organization of a Bose-Einstein condensate in a cavity [79]. Key ingredients for emergence of supersolidity is long range interactions [80] an idea first introduced by Gross [81], or peculiar single-particle dispersion. An example of this second case is provided by spin-orbit coupled Bose gases where supersolidity has also been studied [82, 83]. Experimentally, crystal order has been evidenced by the observation of stripes. However, visibility of the fringes of the density is a major issue to overcome and is due to interspecies interaction.

In this chapter, we consider a two-leg bosonic ring lattice subjected to two gauge fields. Here, thanks to the peculiar geometry of the system the inter-species interactions can be completely suppressed hence providing a new arena for studying supersolidity in a condition of high fringe visibility. As for the case of spin-orbit coupled Bose gas, there is no explicit long range interaction in two-leg bosonic ring ladder but it emerges as an effective low energy property due to the effect of gauge field and tunneling coupling between the rings.

The chapter is organized as follows. In Secs. 3.1 and 3.2 we review some key aspect of the Bogoliubov theory and the Josephson effect. Before studying the properties of the

3.1. Diagonalization of general quadratic Hamiltonian

excitation spectrum in the phases of the ring ladder in Sec. 3.3 and 3.4, we will remind the reader with the system we are considering and the method used. The study of the excitation spectrum in Sec 3.4 reveals in the Meissner phase a single Goldstone mode, associated to the condensation in the only minimum of the single-particle dispersion relation and a slowing down of the group velocity. In the biased ladder phase, in addition to the phonon branch a roton minimum is found. This is a precursor of the vortex phase, in agreement with previous studies [16]. In the vortex phase, two Goldstone modes are clearly observed, indicating that the ground state breaks two symmetries: the $U(1)$ and rotational symmetry. The spontaneous breaking of the $U(1)$ symmetry, associated to condensation, which implies superfluidity. A further proof of the coherence properties of the system is provided by the calculation of the first-order spatial correlation function in Sec 3.5. We then provide various indications of crystal order. First of all, in the excitation spectrum of the vortex phases we find a folding of the Brillouin zone. This is a consequence of the formation of a vortex lattice in the mean-field condensate density. Furthermore, the analysis of the static structure factor shows the emergence of a peak at finite wavevector, corresponding to the density modulation along the rings. Putting together the various evidences of coherence properties and crystalline order, we obtain a clear indication of supersolidity. Coupled rings under gauge flux hence provide a novel platform for the experimental study of supersolid order with ultracold atoms.

Finally, in the last part of the chapter, in Sec 3.6, we address some features peculiar to the finite ring case, and in particular the emergence of Josephson modes for weakly coupled rings in the Meissner phase. These modes correspond to dynamical coherent oscillation of particles between the rings, hence providing a further indication of the coherence among the two rings [84].

3.1 Diagonalization of general quadratic Hamiltonian

In second quantization a quadratic non-Hermitian Hamiltonian can be cast in a general way as follows

$$H = \sum_{\alpha,\beta} A_{\alpha,\beta} a_{\alpha}^{\dagger} a_{\beta} + \frac{1}{2} \sum_{\alpha,\beta} \left[B_{\alpha,\beta} a_{\alpha}^{\dagger} a_{\beta}^{\dagger} + B_{\alpha,\beta}^{*} a_{\beta} a_{\alpha} \right] \quad (3.1)$$

where B is a symmetric matrix $B_{\alpha,\beta} = B_{\beta,\alpha}$ and A is taken as hermitian $A_{\alpha,\beta} = A_{\beta,\alpha}^{*}$. This type of matrices is often encountered in physics, eg, to name a few in the Hartree-Fock, BCS theory and of course Bogoliubov Hamiltonian.

The Heisenberg equation of motion reads

$$i\hbar\partial_t \begin{pmatrix} \mathbf{u}_k \\ \mathbf{v}_k \end{pmatrix} = \mathcal{L} \begin{pmatrix} \mathbf{u}_k \\ \mathbf{v}_k \end{pmatrix} \quad \text{with} \quad \mathcal{L} = \begin{pmatrix} A & B \\ -B^{*} & -A^{*} \end{pmatrix} \quad (3.2)$$

We see here that the non-hermiticity of the \mathcal{L} matrix comes directly from the commutation properties of the bosons, while \mathcal{L} is Hermitian for fermions.

3.2. Bogoliubov formalism

Eigenvalues from symmetry of the dynamical matrix \mathcal{L} The dynamical matrix \mathcal{L} satisfies several relations that put constraints on its spectrum. One has

$$\mathcal{L}^\dagger = \eta^{-1} \mathcal{L} \eta \quad \eta = \eta^{-1} = \begin{pmatrix} 1 & 0 \\ 0 & -1 \end{pmatrix} \quad (3.3)$$

$$\mathcal{L}^* = -\sigma \mathcal{L} \sigma \quad \sigma = \sigma^{-1} = \begin{pmatrix} 0 & 1 \\ 1 & 0 \end{pmatrix} \quad (3.4)$$

Equation (3.3) implies that \mathcal{L} is said to be pseudo-hermitian, because it is hermitian under a modified scalar product $\langle \mathbf{X}_1, \mathbf{X}_2 \rangle = \mathbf{X}_1^* \cdot \eta \mathbf{X}_2$ and $\langle \mathcal{L} \mathbf{X}_1, \mathbf{X}_2 \rangle = \langle \mathbf{X}_1, \mathcal{L} \mathbf{X}_2 \rangle$ for any vector \mathbf{X}_1 and \mathbf{X}_2 . This modified scalar product is not a real scalar product as it is not strictly positive so that the eigenvalues of \mathcal{L} are not necessarily real and \mathcal{L} might also not be diagonalizable. But let's suppose that it is diagonalizable. In this case we have the following eigenvalue problem

$$\mathcal{L} \begin{pmatrix} \mathbf{u}_k \\ \mathbf{v}_k \end{pmatrix} = \epsilon_k \begin{pmatrix} \mathbf{u}_k \\ \mathbf{v}_k \end{pmatrix} \quad (3.5)$$

From Eq.(3.3) we see that if ϵ_k is an eigenvalue of \mathcal{L} , then ϵ_k^* is also an eigenvalue. The second symmetry property of the dynamical matrix \mathcal{L} implies that the spectrum is divided in two families \mathcal{F}_+ and \mathcal{F}_- , with respectively eigenvectors $(\mathbf{u}_k, \mathbf{v}_k)^T$, $(\mathbf{v}_k^*, \mathbf{u}_k^*)^T$ and eigenvalues $\epsilon_k > 0$ and $-\epsilon_k > 0$. Then all together this implies that if ϵ_k is an eigenvalue of \mathcal{L} then ϵ_k^* , $-\epsilon_k^*$ and $-\epsilon_k$ also are eigenvalues.

It should be noticed that the pseudo hermiticity (3.3) implies that the normalization condition is changed, and reads

$$\langle \mathbf{u}_k | \mathbf{u}_{k'} \rangle - \langle \mathbf{v}_k | \mathbf{v}_{k'} \rangle = \delta_{k,k'} \quad \text{for family } \mathcal{F}_+ \quad (3.6)$$

$$\langle \mathbf{u}_k | \mathbf{u}_{k'} \rangle - \langle \mathbf{v}_k | \mathbf{v}_{k'} \rangle = -\delta_{k,k'} \quad \text{for family } \mathcal{F}_-. \quad (3.7)$$

3.2 Bogoliubov formalism

The Bogoliubov formalism considers quantum fluctuations around the mean-field ground state by separating the fluctuations $\delta \hat{\Psi}(\mathbf{r})$ from the mean-field wave function $\Phi(\mathbf{r})$. This is well suited in the presence of a condensate of mean-field mode $\Phi(\mathbf{r})$ which is macroscopically occupied, so that the bosonic field is expressed as follows

$$\hat{\Psi}(\mathbf{r}) = \Phi(\mathbf{r}) a_\Phi + \delta \hat{\Psi}(\mathbf{r}) \quad (3.8)$$

where a_Φ is a bosonic field operator annihilating the mode $\Phi(\mathbf{r})$ of the condensate. The Bogoliubov approximation holds as long as $\delta \hat{\Psi}(\mathbf{r})$ is small compared to $\Phi(\mathbf{r}) a_\Phi$ in the following sense

$$\int d\mathbf{r} \langle \delta \hat{\Psi}^\dagger(\mathbf{r}) \delta \hat{\Psi}(\mathbf{r}) \rangle \ll \int d\mathbf{r} \Phi^* \Phi \langle a_\Phi^\dagger a_\Phi \rangle = \langle a_\Phi^\dagger a_\Phi \rangle = N_0 \quad (3.9)$$

where N_0 is the number of condensed particle. The non-condensed particles are thought of as being in the grand canonical ensemble where the condensate mode act as a reservoir for the non-condensed ones. It then crucial to introduce a chemical potential to treat the fluctuations of non-condensed particles. The Hamiltonian (1.4) of bosons in continuum with contact interactions at second order in the fluctuations field, reads

$$H = \frac{1}{2} \int d\mathbf{r} (\delta\hat{\Psi}^\dagger(\mathbf{r}), \delta\hat{\Psi}(\mathbf{r})) \begin{pmatrix} -\frac{\hbar^2}{2m} \nabla^2 + V(\mathbf{r}) - \mu + 2g|\Phi(\mathbf{r})|^2 & g\Phi(\mathbf{r})^2 \\ g(\Phi(\mathbf{r})^2)^* & -\frac{\hbar^2}{2m} \nabla^2 + V(\mathbf{r}) - \mu + 2g|\Phi(\mathbf{r})|^2 \end{pmatrix} \begin{pmatrix} \delta\hat{\Psi}(\mathbf{r}) \\ \delta\hat{\Psi}^\dagger(\mathbf{r}) \end{pmatrix} \quad (3.10)$$

One needs to find the transformation to quasi-particles $\hat{\gamma}_\nu$ such that the Bogoliubov Hamiltonian takes diagonal form $H = \sum_\nu \hbar\omega_\nu \hat{\gamma}_\nu^\dagger \hat{\gamma}_\nu$. A general transformation reads

$$\delta\hat{\Psi}(\mathbf{r}) = \sum_{\nu u} \left[u_\nu(\mathbf{r}) \hat{\gamma}_{\nu u} - v_\nu^*(\mathbf{r}) \hat{\gamma}_\nu^\dagger \right] \quad (3.11)$$

with a priori unknown functions $u_\nu(\mathbf{r})$ and $v_\nu(\mathbf{r})$. Imposing the fact that Bogoliubov Hamiltonian takes diagonal form implies that the functions u_ν and v_ν should satisfy the following equation of motion, called Bogoliubov de Gennes equations.

$$\eta \mathcal{L} \begin{pmatrix} u_\nu(\mathbf{r}) \\ v_\nu(\mathbf{r}) \end{pmatrix} = \hbar\omega_\nu \begin{pmatrix} u_\nu(\mathbf{r}) \\ v_\nu(\mathbf{r}) \end{pmatrix}, \quad (3.12)$$

where matrix \mathcal{L} is called the dynamical matrix and η accounts for the non-hermiticity of the problem, and it reads as follows,

$$\mathcal{L} = \begin{pmatrix} -\frac{\hbar^2}{2m} \nabla^2 + V(\mathbf{r}) - \mu + 2g|\Phi(\mathbf{r})|^2 & -g\Phi(\mathbf{r})^2 \\ g(\Phi(\mathbf{r})^2)^* & -\frac{\hbar^2}{2m} \nabla^2 + V(\mathbf{r}) - \mu + 2g|\Phi(\mathbf{r})|^2 \end{pmatrix}, \quad \eta = \begin{pmatrix} 1 & 0 \\ 0 & -1 \end{pmatrix} \quad (3.13)$$

This eigenvalue problem define a non self-adjoint eigenvalue problem that will be the topic of the next paragraph. Let's consider a spatially homogeneous condensate with repulsive contact interaction at zero temperature. In this case the mode of the condensate is $\phi(\mathbf{r}) = 1/L^{d/2}$, where d is the dimension of the system and L its length, the chemical potential is given by $\mu = \rho g$ and the eigenfunctions of \mathcal{L} are plane waves due to the translational invariance of the system:

$$u_{\mathbf{k}}(\mathbf{r}) = \frac{U_{\mathbf{k}}}{L^{d/2}} e^{i\mathbf{k}\cdot\mathbf{r}} \quad \text{with} \quad |u_{\mathbf{k}}|^2 - |v_{\mathbf{k}}|^2 = 1 \quad (3.14)$$

$$v_{\mathbf{k}}(\mathbf{r}) = \frac{V_{\mathbf{k}}}{L^{d/2}} e^{i\mathbf{k}\cdot\mathbf{r}} \quad (3.15)$$

$$(3.16)$$

Diagonalization of the corresponding \mathcal{L} matrix yields the Bogoliubov spectrum

$$\epsilon_k = \left[\frac{\hbar k^2}{2m} \left(\frac{\hbar^2 k^2}{2m} + 2\mu \right) \right]^{1/2}. \quad (3.17)$$

3.2. Bogoliubov formalism

An interesting fact is that for attractive interactions an instability of the condensate arises and a condensate is stable only for a low number of particles $\frac{\hbar^2}{2m} \left(\frac{2\pi}{L}\right)^2 < 2\rho|g|$. For repulsive interaction no dynamical instability is present and so the condensate is stable. In the small momentum limit (see Fig. 3.1) the excitation spectrum is linear $\epsilon(k) = ck$ with sound velocity $c = \sqrt{\frac{g\rho}{m}}$ and the corresponding collective excitations are phonons associated to the Goldstone mode of the $U(1)$ symmetry breaking. At large momentum the excitations behave like free particles $\epsilon(k) = \frac{\hbar^2 k^2}{2m} + g\rho$. This excitation spectrum can be seen in Fig. 3.1 where both theoretical and experimental are represented. In order to link to the further part II of the thesis Fig. 3.2 displays the experimentally measured excitation spectrum of an excitation-polariton condensate where the same features appear and Bogoliubov theory is applicable (as we shall see later, we will use it to treat exciton-polariton condensates).

3.2.1 Zero frequency modes

A special solution of eigenvalue problem (3.12) is given by functions $u(\mathbf{r})$ and $v(\mathbf{r})$ proportional to the ground state, that will be called zero frequency solutions $u_0(\mathbf{r}) = v_0(\mathbf{r}) = \alpha\Phi(\mathbf{r})$ solution of $(\mathcal{L}_{11} + \mathcal{L}_{12})\Phi = 0$ where $\alpha \in \mathbb{C}$. The contribution of this solution to the wave function is a phase shift $2i\text{Im}[\alpha]\Phi(\mathbf{r})$ and should not be considered as excitations, therefore they correspond to the Goldstone mode of the $U(1)$ symmetry breaking [88].

3.2.2 Josephson effect

Originally the Josephson effect has been predicted [89] and observed between two superconductors separated by a weak link. It is a macroscopic quantum phenomena of coherent oscillation of Cooper pairs between the two superconductors without any applied voltage (dc Josephson). Application of a voltage (V) induces an alternative current due to the dependence of the phase ϕ of the Cooper pair to the voltage $\dot{\phi} = \frac{2e}{\hbar}V$, where $2e$ is the charge of the Cooper pair. In the context of trapped cold-atom gases the Josephson effect has been predicted and observed in a system of two condensates spatially separated in a double well structure [90] (see Fig. 3.3). Such a system is represented by standard Josephson Hamiltonian in its two-mode version of the Bose-Hubbard model

$$H = -\frac{E_J}{N} (a^\dagger b + b^\dagger a) + \frac{E_c}{4} \left[(a^\dagger a)^2 + (b^\dagger b)^2 \right] \quad (3.18)$$

where E_J is the Josephson coupling energy, E_c the charging energy, annihilation operators a and b correspond to the condensate wavefunctions of the left and right well. The physics of these experiments is based on the macroscopic coherent tunneling of atoms between the wells, and is very similar to that of the Josephson effect between two superconductors connected by an insulating junction. Three physical situations arise:

- In the so called Rabi regime where $E_c \ll E_J/N^2$ the atoms are all in the bonding state and behave independently so that the effect of interaction can be neglected.

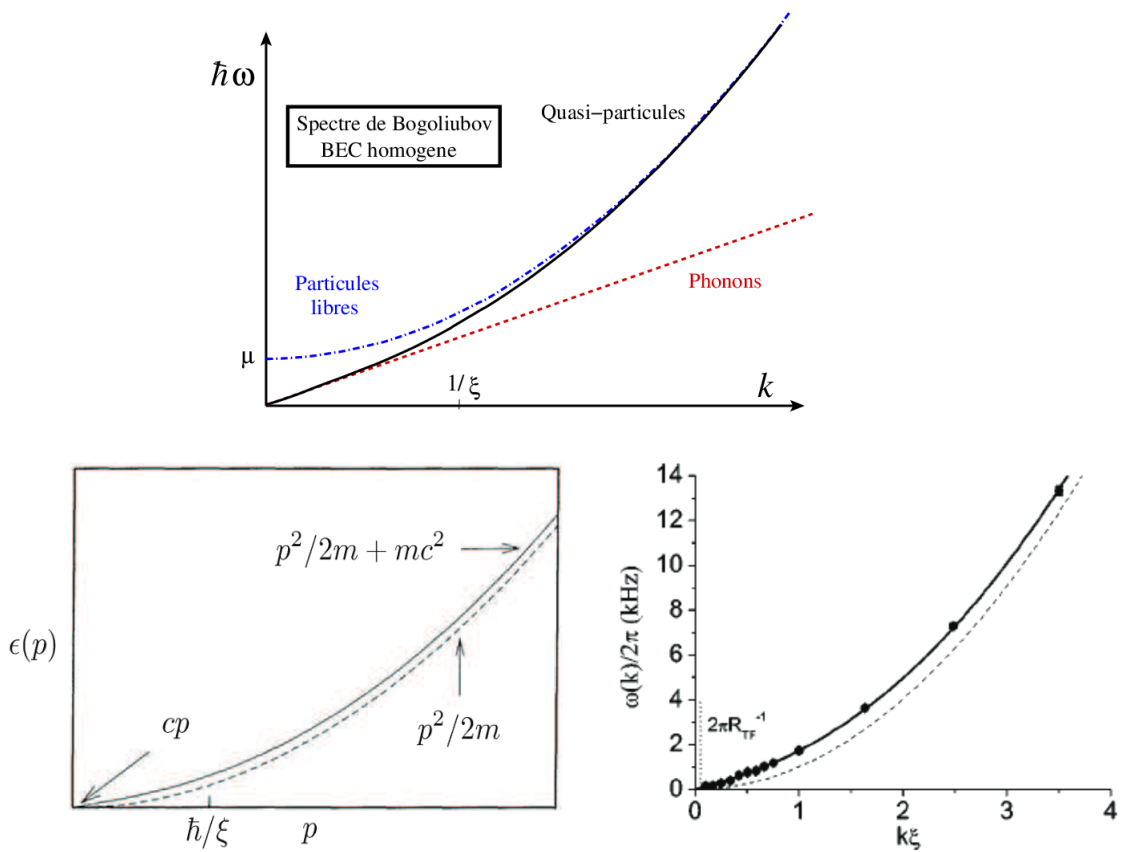


Figure 3.1: The upper panel represents the excitation spectrum of an homogeneous BEC from [85]. Lower panels: Left panel, theoretical spectrum where the transition from phononic behaviour at low frequency $\epsilon(p) = cp$ to the free particle behaviour $\epsilon(p) = p^2/2m + mc^2$ is outlined. Right panel, measured excitation spectrum in an atomic BEC using light scattering, from [86].

The phase is well-defined and excitations correspond to the anti-bonding state. The tunnel dynamic corresponds to a sinusoidal Rabi oscillation between the two wells at frequency fixed by the energy of the modes.

- In the Josephson regime, $E_c/N^2 \ll E_c \ll E_J$, the ground state has still a well-defined phase, but the excitation forms a collective motion called Josephson plasmon. The effect of the interaction becomes more important in the dynamics as it will change the oscillation of the collective motion. The oscillation frequency of the Josephson modes is directly linked to the Bogoliubov spectrum.
- In the Fock regime $E_J \ll E_c$, the Josephson link is dominated by the interaction energy and n is a good quantum number. Therefore the ground state has a well-defined

3.2. Bogoliubov formalism

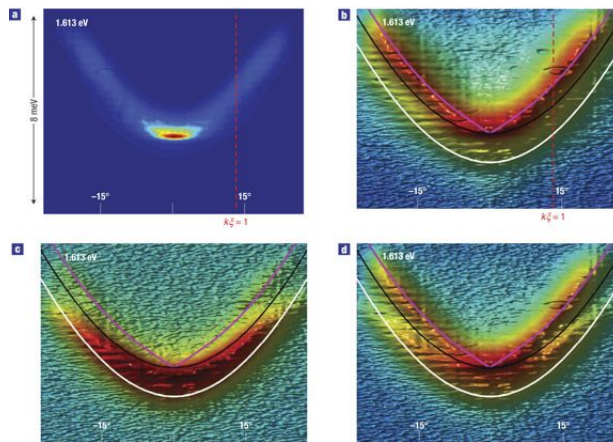


Figure 3.2: Observed light intensity from an exciton-polariton condensate (see Chapter 6.3) in a linear plot of intensity (up left panel) and in a logarithmic plot of intensity (right panel). Taken from [87].

atom number on each side, the phase is completely undefined.

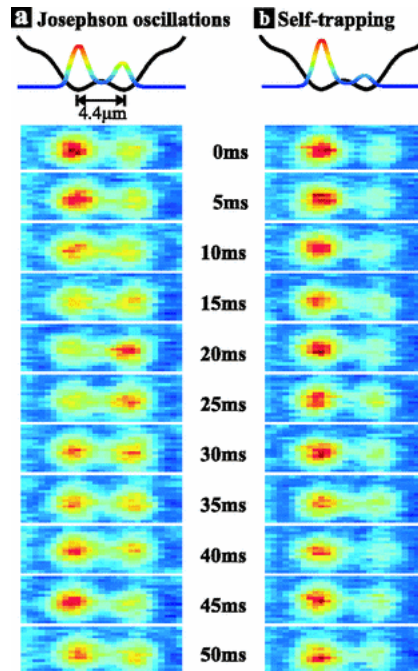


Figure 3.3: From [90]. Observation of the tunneling dynamics of two weakly linked Bose-Einstein condensates in a symmetric double-well potential. Left: time-resolved Josephson oscillations. Right: macroscopic quantum self-trapping

The Gross-Pitaevskii approach yields the same excitation spectrum as the one obtained by solving directly the time-independent Bogoliubov-deGennes equations. This approach of

the time-independent Bogoliubov-deGennes equations will be used later in this chapter to characterize the Josephson oscillation in the double ring.

3.3 Model and method

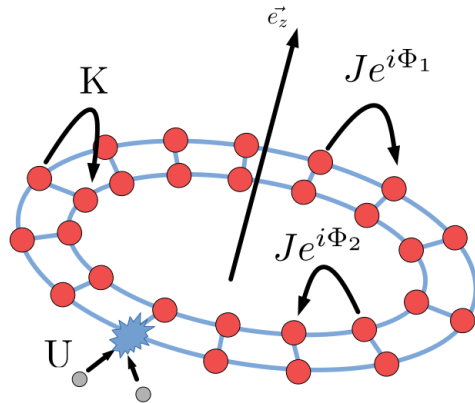


Figure 3.4: Reminder of the sketch of the system studied in this work: coplanar ring lattices of radii R_1 and R_2 with the same number of sites, with inter-ring tunnel energy K , intra-ring tunnel energies $J e^{i\Phi_p}$ with $p = 1, 2$ and contact interaction strength U .

We consider a Bose gas confined in a double ring lattice (See Fig. 3.4). In the tight-binding approximation we model the system using the Bose-Hubbard Hamiltonian (2.6) which we report here for sake of clarity,

$$\begin{aligned} \hat{H} &= \hat{H}_0 + \hat{H}_{int} = \\ &- \sum_{l=1, p=1,2}^{N_s} J_p \left(a_{l,p}^\dagger a_{l+1,p} e^{i\Phi_p} + a_{l+1,p}^\dagger a_{l,p} e^{-i\Phi_p} \right) \\ &- K \sum_{l=1}^{N_s} \left(a_{l,1}^\dagger a_{l,2} + a_{l,2}^\dagger a_{l,1} \right) + \frac{U}{2} \sum_{l=1, p=1,2}^{N_s} a_{l,p}^\dagger a_{l,p}^\dagger a_{l,p} a_{l,p} \end{aligned} \quad (3.19)$$

where we recall that the angular position on the double ring is given by $\theta_l = \frac{2\pi}{N_s} l$ where l is an integer $l \in [1, N_s]$ with N_s the number of sites in each ring, J_1 and J_2 are the tunneling amplitudes from one site to another along each ring, K is the tunneling amplitude between the two rings and $\Phi_{1,2}$ are the fluxes threading the inner and outer ring respectively.

3.3.1 Bogoliubov De-Gennes equations of the double ring

In order to obtain the excitation spectrum of the double ring in the Bogoliubov approximation, following [91] we start from the Heisenberg equations of motion for the bosonic field operators $\hat{a}_{l,\alpha}$ and we replace $\hat{a}_{l,\alpha}$ in the quantum Hamiltonian (2.6) by $\hat{a}_{l,\alpha} = \Psi_{l,\alpha}^{(0)} + \delta \hat{a}_{l,\alpha}$.

3.3. Model and method

The field $\Psi_{l,\alpha}^{(0)}$ is the ground-state condensate wave function, solution of the coupled discrete non linear Schrödinger equation (3.20) below,

$$\begin{aligned}\mu\Psi_{l,1} &= -J\Psi_{l+1,1}e^{i(\Phi+\phi/2)} - J\Psi_{l-1,1}e^{-i(\Phi+\phi/2)} \\ &\quad - K\Psi_{l,2} + U|\Psi_{l,1}|^2\Psi_{l,1} \\ \mu\Psi_{l,2}(t) &= -J\Psi_{l+1,2}e^{i(\Phi-\phi/2)} - J\Psi_{l-1,2}e^{-i(\Phi-\phi/2)} \\ &\quad - K\Psi_{l,1} + U|\Psi_{l,2}|^2\Psi_{l,2}\end{aligned}\quad (3.20)$$

where $\Phi = \frac{\Phi_1 + \Phi_2}{2}$ and $\phi = \Phi_1 - \Phi_2$ and μ is the chemical potential. In the following, we will consider for simplicity $\Phi = 0$. Expansion and truncation of the Hamiltonian to quadratic order in $\delta\hat{a}_{l,p}$, $\delta\hat{a}_{l,p}^\dagger$ yields the Bogoliubov Hamiltonian

$$\hat{H}_{Bog} = \left(\delta\hat{\mathbf{a}}_1^\dagger, \delta\hat{\mathbf{a}}_1, \delta\hat{\mathbf{a}}_2^\dagger, \delta\hat{\mathbf{a}}_2 \right) H^{(2)} \begin{pmatrix} \delta\hat{\mathbf{a}}_1 \\ \delta\hat{\mathbf{a}}_1^\dagger \\ \delta\hat{\mathbf{a}}_2 \\ \delta\hat{\mathbf{a}}_2^\dagger \end{pmatrix}, \quad (3.21)$$

with

$$H^{(2)} = \begin{pmatrix} \mathbf{A}_1 & \mathbf{B}_1 & -\mathbf{K} & 0 \\ \mathbf{B}_1^* & \mathbf{A}_1^* & 0 & -\mathbf{K} \\ -\mathbf{K} & 0 & \mathbf{A}_2 & \mathbf{B}_2 \\ 0 & -\mathbf{K} & \mathbf{B}_2^* & \mathbf{A}_2^* \end{pmatrix}, \quad (3.22)$$

where the matrix A_p with $p = 1, 2$ is given by

$$\mathbf{A}_p = \begin{pmatrix} 2U|\Psi_{1,p}^{(0)}|^2 & -Je^{i\Phi_p} & \cdots & -Je^{-i\Phi_p} \\ -Je^{-i\Phi_p} & 2U|\Psi_{2,p}^{(0)}|^2 & \cdots & \\ \vdots & \vdots & \ddots & \vdots \\ -Je^{i\Phi_p} & \cdots & 2U|\Psi_{N_s-1,p}^{(0)}|^2 & -Je^{i\Phi_p} \\ & & -Je^{-i\Phi_p} & 2U|\Psi_{N_s,p}^{(0)}|^2 \end{pmatrix}, \quad (3.23)$$

and B_p and K_p are diagonal matrices of dimension $N_s \times N_s$, i.e.

$$\mathbf{B}_p = \text{diag}(U(\Psi_{1,p}^{(0)})^2, \dots, U(\Psi_{N_s,p}^{(0)})^2) \quad (3.24)$$

$$\mathbf{K} = K\mathbf{I}, \quad (3.25)$$

with \mathbf{I} the identity matrix. We search then a transformation to quasi-particle operators $\hat{\gamma}_\nu$ for an excitation in mode $\nu = \mu, n$, where μ the quantum number related to the quasi-momentum of the Bogoliubov particles and n is the band index $n = 1, 2$. The Bogoliubov Hamiltonian takes diagonal form:

$$H_{Bog} = \sum_\nu \hbar\omega_\nu \gamma_\nu^\dagger \gamma_\nu \quad (3.26)$$

We use the following general transformation, where the operators γ_v follow usual bosonic commutation rules, $[\gamma_v, \gamma_{v'}] = 0$, $[\gamma_v, \gamma_{v'}^\dagger] = \delta_{v,v'}$.

$$\delta \hat{a}_{l,1} = \sum_v h_{v,l}^{(1)} \gamma_v - Q_{v,l}^{*(1)} \gamma_v^\dagger, \quad (3.27)$$

$$\delta \hat{a}_{l,2} = \sum_v h_{v,l}^{(2)} \gamma_v - Q_{v,l}^{*(2)} \gamma_v^\dagger, \quad (3.28)$$

As next step, we substitute Eq. (3.28) into the equation of motion, and use the following properties

$$[\gamma_v, H] = \hbar \omega_v \gamma_v \quad (3.29)$$

$$[\gamma_v^\dagger, H] = -\hbar \omega_v \gamma_v^\dagger. \quad (3.30)$$

Finally, by equating the coefficients of the different modes $\{h_v^{(p)}, Q_v^{(p)}\}$ we obtain that the modes have to verify the following eigenvalue problem, corresponding to the Bogoliubov-De Gennes equations for the ring ladder:

$$\epsilon_v \begin{pmatrix} \mathbf{h}_v^{(1)} \\ \mathbf{Q}_v^{(1)} \\ \mathbf{h}_v^{(2)} \\ \mathbf{Q}_v^{(2)} \end{pmatrix} = \begin{pmatrix} \mathbf{A}_1 - \mu \mathbf{I} & \mathbf{B}_1 & -\mathbf{K} & 0 \\ -\mathbf{B}_1^* & -\mathbf{A}_1^* + \mu \mathbf{I} & 0 & \mathbf{K} \\ -\mathbf{K} & 0 & \mathbf{A}_2 - \mu \mathbf{I} & \mathbf{B}_2 \\ 0 & \mathbf{K} & -\mathbf{B}_2^* & -\mathbf{A}_2^* + \mu \mathbf{I} \end{pmatrix} \begin{pmatrix} \mathbf{h}_v^{(1)} \\ \mathbf{Q}_v^{(1)} \\ \mathbf{h}_v^{(2)} \\ \mathbf{Q}_v^{(2)} \end{pmatrix}, \quad (3.31)$$

where $\mathbf{h}_v^{(p)} = (h_{v,1}^{(p)} \dots h_{v,l}^{(p)} \dots h_{v,N_s}^{(p)})^T$ and $\mathbf{Q}_v^{(p)} = (Q_{v,1}^{(p)} \dots Q_{v,l}^{(p)} \dots Q_{v,N_s}^{(p)})^T$ and the chemical potential is $\mu = \langle \Psi_{(0)} | H_0 | \Psi_{(0)} \rangle + 2 \langle \Psi_{(0)} | H_{int} | \Psi_{(0)} \rangle$. The eigenmodes satisfy the following orthogonality relations which follow from commutation relations among γ_v :

$$\sum_{v,p} h_{v,l}^p (h_{v,l'}^{(p)})^* - Q_{v,l}^p (Q_{v,l'}^{(p)})^* = \delta_{l,l'} \quad (3.32)$$

$$\sum_{l,p} h_{v,l}^p (h_{v',l}^{(p)})^* - Q_{v,l}^p (Q_{v',l}^{(p)})^* = \delta_{v,v'}. \quad (3.33)$$

3.3.2 Dynamical structure factor

The dynamical structure factor is a powerful tool to study correlations in many-body systems both theoretically and experimentally. It corresponds to the space- and time- Fourier transform of the density-density correlation function. The poles of the dynamical structure correspond to the collective excitation spectrum of the system. For a single-component one-dimensional system, the dynamical structure factor is defined as follows [92]

$$S(q, \omega) = \sum_{v \neq 0} |\langle v | \hat{\rho}_q | 0 \rangle|^2 \delta(\omega - \omega_v) \quad (3.34)$$

3.3. Model and method

where the sum runs on all the modes, q and ω are the momentum and energy transferred by the probe to the sample, $|v\rangle$ are many-body eigenstates of the system and $|0\rangle$ is the ground state, corresponding to the vacuum of Bogoliubov quasi-particles, $\hat{\rho}_q$ is the density fluctuation operator in momentum space and $\omega_s = E_v - E_0$ is the energy difference between excited and ground state.

For the case of coupled rings, since the excitations belong to both rings, we need to define several dynamical structure factors: $S_{p,p'}(q, \omega)$ with $p, p' = 1, 2$ being the ring index, and

$$S_{p,p'}(q, \omega) = \sum_{v \neq 0} |\langle v | \hat{\rho}_q^{(p,p')} | 0 \rangle|^2 \delta(\omega - \omega_v) \quad (3.35)$$

with

$$\hat{\rho}_q^{(p,p')} = \sum_k \hat{a}_{k+q,p}^\dagger \hat{a}_{k,p'}, \quad (3.36)$$

and q and k are wavevectors corresponding to the longitudinal momentum along each ring, i.e we have set $\hat{a}_{k,p} = (1/\sqrt{N_s}) \sum_j \exp(ikaj) \hat{a}_{j,p}$ Using the expansion onto Bogoliubov modes, Eq.(3.28), one can show that

$$S_{p,p'}(q, \omega) = \sum_{v \neq 0} \left| \sum_l \left(\Psi_{l,p'}^{(0)} h_{v,l}^{*(p)} - \Psi_{l,p}^{*(0)} Q_{v,l}^{*(p')} \right) e^{iq l} \right|^2 \delta(\omega - \omega_v) \quad (3.37)$$

In order to understand the low energy properties of the system, it is useful to refer to operators $\hat{\alpha}_k, \hat{\beta}_k$ that diagonalize the single-particle non-interacting Hamiltonian H_0 (see Appendix A). In particular, the low-energy properties of the system under study are governed by the lowest excitation branch associated to the operator β_k (see Eq.A.3). The dynamical structure factor $S_{\beta,\beta}$ relative to the β_k particles gives us access to the properties of the low-energy excitation spectrum

$$S_{\beta,\beta}(q, \omega) = \sum_{v \neq 0} |\langle v | \hat{\rho}_q^{(\beta)} | 0 \rangle|^2 \delta(\omega - \omega_v) \quad (3.38)$$

where $\hat{\rho}_q^{(\beta)} = \sum_k \beta_{k+q}^\dagger \beta_k$. Using Eq.(3.28) and Eq.(3.37), the dynamical structure factor in the Bogoliubov approximation reads

$$\begin{aligned} S_{\beta,\beta}(q, \omega) &= \sum_{s \neq 0} \left| \sum_k u_{k+q} u_k \left((\tilde{h}_{s,k+q}^{(1)})^* \tilde{\Psi}_{k,1}^{(0)} - (\tilde{\Psi}_{k+q,1}^{(0)} \tilde{Q}_{s,-k}^{(1)})^* \right) \right. \\ &\quad + v_{k+q} v_k \left((\tilde{h}_{s,k+q}^{(2)})^* \tilde{\Psi}_{k,2}^{(0)} - (\tilde{\Psi}_{k+q,2}^{(0)} \tilde{Q}_{s,-k}^{(2)})^* \right) \\ &\quad + u_{k+q} v_k \left((\tilde{h}_{s,k+q}^{(1)})^* \tilde{\Psi}_{k,2}^{(0)} - (\tilde{\Psi}_{k+q,1}^{(0)} \tilde{Q}_{s,-k}^{(2)})^* \right) \\ &\quad \left. + v_{k+q} u_k \left((\tilde{h}_{s,k+q}^{(2)})^* \tilde{\Psi}_{k,1}^{(0)} - (\tilde{\Psi}_{k+q,2}^{(0)} \tilde{Q}_{s,-k}^{(1)})^* \right) \right|^2 \delta(\omega - \omega_s) \end{aligned} \quad (3.39)$$

where $\tilde{h}_{v,k}$, $\tilde{Q}_{v,k}$ and $\tilde{\Psi}_{k,p}^{(0)}$ are the Fourier transforms of $h_{v,l}^{(\alpha)}, Q_{v,\alpha}^{(\alpha)}$ of the excitation and of condensate wavefunction $\Psi_{l,\alpha}^{(0)}$ respectively.

3.4. Excitation spectrum as a probe of the phases of the two-leg bosonic ring ladder

Non-interacting limit: by taking the ground state as being $|0\rangle = \frac{1}{\sqrt{2}}(|k_1\rangle + |k_2\rangle)$ the structure factor is easily computed as being

$$S_{\beta,\beta}(q, \omega) = \frac{1}{2}(\delta(\omega - \omega_{q+k_1}) + \delta(\omega - \omega_{q+k_2})) \quad (3.40)$$

with $\omega_k = E_-(k) - E_-(k_1)$. We see that it consist in two bands that coincide only for $k_1 = k_2 = 0$ (Meissner phase) or $k_1 = -k_2 = -\pi$.

3.3.3 Static structure factor

The static structure factor yields information on spatial long-range order, eg crystal or density wave order, hence it is particularly suited to address the spatial modulations emerging in the vortex phase (see Sec. 3.4.3 below). The static structure factor is defined as

$$S_{(p,p')}(q) = \sum_{\nu} Z_{\nu}^{(p,p')}(q) \quad (3.41)$$

where $Z_{\nu}(q) = \left| \langle \nu | \rho_q^{p,p'} | 0 \rangle \right|^2$. In order to access the properties of supersolidity we need to compute the total static structure factor $S_{tot}(q) = S_e(q) + S(q)$, which takes into account both elastic and inelastic scattering. Inelastic scattering is captured by $S(q)$ and elastic scattering corresponds to the so-called disconnected dynamic structure factor $S_e(q) = Z_{\nu=0}(q)$ [92].

3.4 Excitation spectrum as a probe of the phases of the two-leg bosonic ring ladder

For the lattice ring three phases are known: the Meissner (M), vortex (V) and biased-ladder (BL) phase. A schematic phase diagram for the infinite-ladder limit is illustrated in Fig.3.5. It is obtained by minimizing the mean-field energy with respect to the Ansatz $|\Psi\rangle = \frac{1}{\sqrt{N!}} \left(\cos(\theta) \beta_{k_1}^{\dagger} + \sin(\theta) \beta_{k_2}^{\dagger} \right)^N |0\rangle$ [16], where β_k are the field operator creating a particle in the lowest band related to the non-interacting problem and $k_{1/2}$ are the lowest mode of the non-interacting spectrum (see Appendix A). The Meissner phase is characterized by vanishing expectation value of the transverse currents $j_{l,\perp} = iK \langle a_{l,1}^{\dagger} a_{l,2} - a_{l,2}^{\dagger} a_{l,1} \rangle$; the longitudinal currents on each ring, defined as $j_{l,p} = iJ \langle a_{l,p}^{\dagger} a_{l+1,p} e^{i\Phi_p} - a_{l+1,p}^{\dagger} a_{l,p} e^{-i\Phi_p} \rangle$, are opposite and the chiral current, i.e $J_c = \sum_l \langle j_{l,1} - j_{l,2} \rangle$ is saturated. The vortex phase is characterized by a modulated density, jumps of the phase of the wave function, and non-zero, oscillating transverse currents which create a vortex pattern. The biased-ladder phase has only longitudinal currents as in the Meissner phase, but displays and imbalanced population between the two rings.

3.4. Excitation spectrum as a probe of the phases of the two-leg bosonic ring ladder

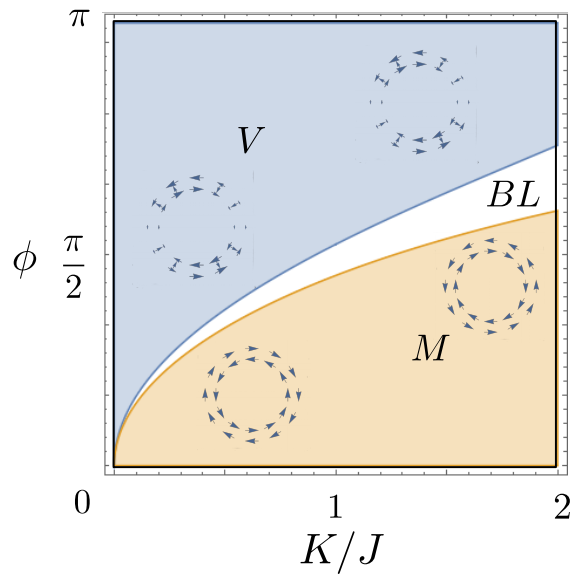


Figure 3.5: Phase diagram of the infinite double ring lattice as a function of the flux ϕ per plaquette and tunnel ratio K/J for interaction strength $Un/J = 0.01$. The Meissner (M), vortex (V) and biased ladder (BL) phases are indicated on the figure, and the typical current pattern is sketched.

3.4.1 Meissner phase

In the Meissner phase, the ground-state solution for the condensate wave function is uniform in space and corresponds to a condensate occupying the $k = 0$ state that is the minimum of the single particle dispersion (see Appendix A).

The lowest branch of the spectrum shows a single phononic Goldstone mode at small wave vector k . A simplified expression can be obtained by performing the Bogoliubov approximation on the lower branch of the single-particle spectrum [16]. It reads

$$\epsilon_k^M = \frac{1}{2} \sqrt{(Un + 2\tilde{\epsilon}_k)^2 - (2Unu_k v_k)^2} \quad (3.42)$$

with $\tilde{\epsilon}_k = E_-(k) - E_-(0)$ and u_k, v_k defined in Appendix A. Fig. 3.6 shows the dynamical structure factor as obtained by the numerical diagonalization of the Bogoliubov DeGennes equations. The poles of the dynamical structure factor in the frequency-wavevector plane are in excellent agreement with Eq.(3.42), also shown in the figure.

The Meissner excitation spectrum takes imaginary eigenvalues as the uniform mean-field solution becomes unstable owing to the fact that the true mean-field solution is a vortex wave function. With this criterion it is possible to control the boundaries between the Meissner and vortex phase [18] and also to the biased ladder phase. We see that interaction favors the Meissner phase compared to the vortex phase and biased-ladder phase. One noteworthy fact occurs when the coupling between the rings is sufficiently low and interaction strong so that interplay between interaction and kinetic energy affects the low momentum properties of the excitation spectrum. As the non-interacting spectrum in

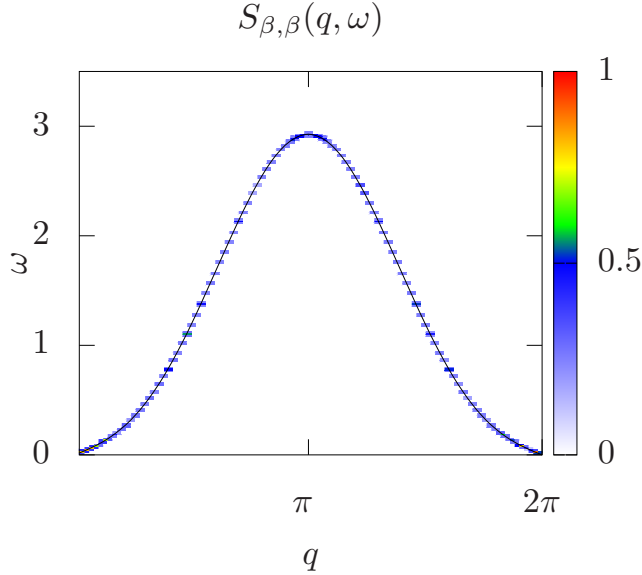


Figure 3.6: Excitation spectrum (black line) and dynamical structure factor in the lowest branch (β) basis in the Meissner phase, in the frequency-wavevector plane (color map) for $Un/J = 0.2$, $\phi = \pi/2$, $K/J = 3$.

this regime is of vortex type with two minima there is a reminiscence of the vortex pattern that tends to slow the group velocity near the momentum minima k_1 and k_2 . The excitation spectrum can be computed analytically also in this case. As the mean-field solution is uniform in space so that $\Psi_{l,p} = \sqrt{N/2N_s} = \sqrt{n}$. The equation of motion for the Bogoliubov modes can be expanded in plane wave solutions $h_{v,l}^{(p)} = h_q^{(p)} e^{iq_l}$, $Q_{v,l}^{(p)} = Q_q^{(p)} e^{iq_l}$, where v is identified as the plane-wave momentum q longitudinal to the rings. It reads

$$\epsilon(q) \begin{pmatrix} h_q^{(1)} \\ Q_q^{(1)} \\ h_q^{(2)} \\ Q_q^{(2)} \end{pmatrix} = \begin{pmatrix} \epsilon_+(q) + Un & -Un & -K & 0 \\ Un & -\epsilon_-(q) - Un & 0 & K \\ -K & 0 & \epsilon_-(q) + Un & -Un \\ 0 & K & Un & -\epsilon_+(q) + Un \end{pmatrix} \begin{pmatrix} h_q^{(1)} \\ Q_q^{(1)} \\ h_q^{(2)} \\ Q_q^{(2)} \end{pmatrix} \quad (3.43)$$

where $\epsilon_{\pm}(q) = -2J[\cos(q \pm \phi/2) - \cos(\phi/2)] + K$.

This matrix is diagonalizable and the positive eigenvalues read

3.4. Excitation spectrum as a probe of the phases of the two-leg bosonic ring ladder

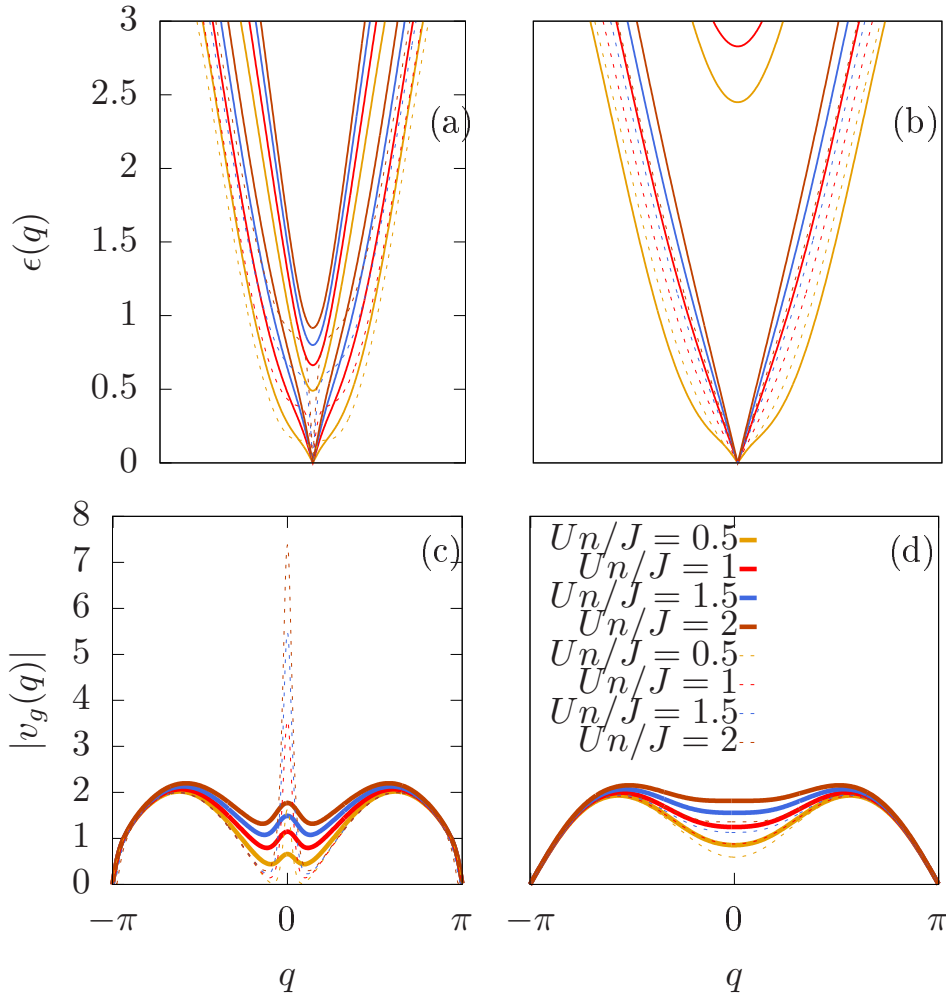


Figure 3.7: (upper panels) Excitation spectrum in the Meissner phase for (a) $\phi = \pi/4$, $K/J = 0.1$ and (b) $\phi = \pi/4$, $K/J = 1$ for several values of the interaction strength as mentioned in panel (d). (bottom panel) Corresponding group velocity as a function of momentum q for (c) $\phi = \pi/4$, $K/J = 0.1$ and (d) $\phi = \pi/4$, $K/J = 1$ for several values of the interaction strength as mentioned in panel (d). Solid lines correspond to the Meissner excitation spectrum taking into account both lower and upper branch of the non-interacting problem (see Eq. 3.44). Dashed lines correspond to the lowest band approximation (see Eq. 3.42).

$$\epsilon(q) = \frac{1}{\sqrt{2}} \left\{ \epsilon_+^2 + \epsilon_-^2 + 2(\epsilon_+ + \epsilon_-)Un + 2K^2 \right. \\ \left. \pm \sqrt{(\epsilon_+^2 - \epsilon_-^2)^2 + 4Un(\epsilon_+^3 + \epsilon_-^3 - \epsilon_-^2\epsilon_+ + \epsilon_+^2\epsilon_-) + 4K^2[(\epsilon_+ + \epsilon_-)^2 + 4Un(\epsilon_+ + \epsilon_- + Un)]} \right\}^{1/2} \quad (3.44)$$

For a similar derivation see Ref.[18].

3.4. Excitation spectrum as a probe of the phases of the two-leg bosonic ring ladder

The main effect of the coupling among the lower and upper branch is to change the sound velocity at low momenta and to reduce the region where the spectrum is linear (see Fig 3.4.1). Comparing lowest branch approximation of the Meissner excitation spectrum (Eq.3.42) and the analytic solution of the full problem (Eq.3.44) we see (see Fig.3.4.1) that band repulsion plays an important role in the lowering of the group velocity near $k \rightarrow 0$ and increase it near the minima (See Fig.3.4.1 panel (c)).

3.4.2 Biased-ladder phase

In the biased-ladder phase, as well as in the vortex phase, the single-particle dispersion relation has two minima at $k = k_1, k_2$. In the biased ladder phases only one of the two minima is macroscopically populated. The excitation spectrum shows a phononic Goldstone mode and a rotonic structure [16]. A similar behaviour is found in spin-orbit coupled Bose gases [93]. At fixed flux ϕ , when decreasing the coupling K between the ring, the vortex phase is accessed through a softening of the roton minimum. The system enters the vortex phase when the roton minimum decreases down to a critical (non zero) value thus indicating a first-order transition, similarly to what predicted for dipolar gases [94].

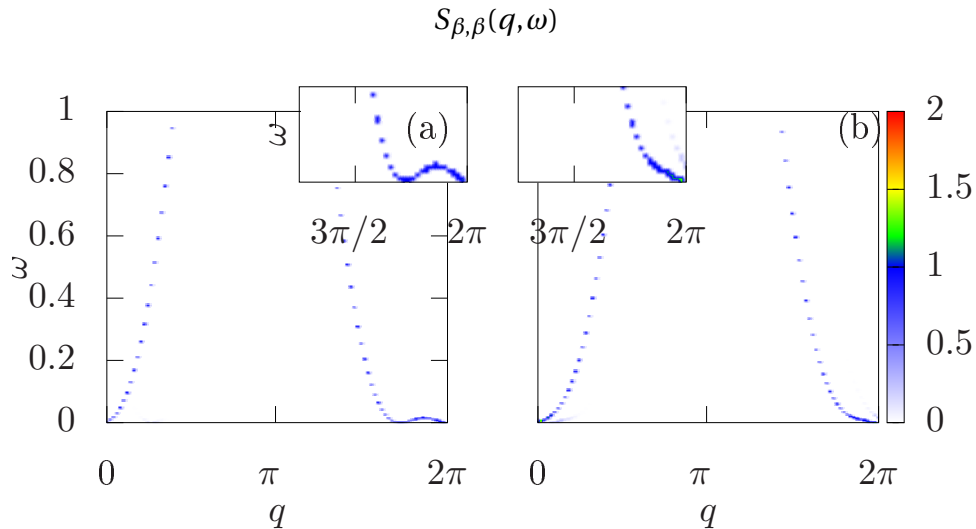


Figure 3.8: (a) Dynamical structure factor for the biased-ladder phase, with $N_s = 100, Un/J = 0.01, \phi = \pi/2$ and $K/J = 1.15$, (b) dynamical structure factor for the biased-ladder phase, with $N_s = 100, Un/J = 0.05, \phi = \pi/2$ and $K/J = 1.4$

3.4.3 Vortex Phase

At the mean field level, the vortex phase is characterized by a fragmented condensate, occupying the two momentum modes $k = k_1, k_2$ corresponding to the minima of the single-particle dispersion relation [16].

3.4. Excitation spectrum as a probe of the phases of the two-leg bosonic ring ladder

The numerical result for the dynamical structure factor $S_{\beta,\beta}(q, \omega)$ in the vortex phase is shown in Fig.3.9. We find various minima of the dispersion relation for $q = 0$ and $q = k_2 - k_1$ as well as at the points $q = 2\pi$ and $q = 2\pi - (k_2 - k_1)$. Two linear dispersion branches are found around each of these minima, characterized by two different sound velocities.

An analysis of the dynamical structure factor in log scale (see Fig. 3.9.b) shows a folding of the Brillouin zone for the excitations, corresponding to the underlying ground-state vortex superlattice felt by the Bogoliubov excitations. Specifically, for the parameters chosen in the calculation of Fig.3.9 we have that the ground state density profile has a modulation with wavevector $k_1 - k_2$, leading to a $\frac{2\pi}{k_1 - k_2}$ -times folding of the excitation spectrum, i.e 5-times in the case of Fig 3.9.

The overall features of the excitation spectrum can be understood by comparing it with the one in the $K = 0$ case. In this regime the rings are independent and the excitation spectrum is given by two branches, obtained by solving the Bogoliubov equations for each ring separately:

$$\begin{aligned} \epsilon_k^{V(1)} &= -\frac{1}{2} \left(\epsilon_{k+k_1} - \epsilon_{k-k_1} \pm \sqrt{(\epsilon_{k+k_1} + \epsilon_{k-k_1})^2 + 4U|\psi_0|^2(\epsilon_{k+k_1} + \epsilon_{k-k_1})} \right) \\ \epsilon_k^{V(2)} &= -\frac{1}{2} \left(\epsilon_{k+k_2} - \epsilon_{k-k_2} \pm \sqrt{(\epsilon_{k+k_2} + \epsilon_{k-k_2})^2 + 4U|\psi_0|^2(\epsilon_{k+k_2} + \epsilon_{k-k_2})} \right) \end{aligned} \quad (3.45)$$

where $\epsilon_k = 2J(1 - \cos(k))$. Exploiting a low-energy model (see Sec.3.7) we can then understand qualitatively the behaviour of the excitation spectrum at small but finite K . In this regime, the excitations can tunnel from one ring to the other with k -dependent interaction parameters \tilde{U} and \tilde{U} (see Appendix 3.7). These scattering events break the degeneracy of the sound velocities around each minimum.

In Fig. 3.10 we show the different dynamical structure in the ring basis. The off-diagonal dynamical structure factors show the symmetry relation $S_{12}(q, \omega) = S_{21}(q, -\omega)$.

3.4.4 Experimental probe of dynamical structure factor

In ultra-cold atomic gases in an elongated geometry the dynamical structure factor can be measured using two-photon optical Bragg spectroscopy [95, 86], according to the following scheme: two laser beams are impinged upon the condensate, and the difference in the wave vectors of the beams defines the momentum transfer $\hbar q$, and the frequency difference defines the energy transfer $\hbar\omega$ to the fluid. Both the values of q and ω can be tuned by changing the angle between the two beams and varying the frequency difference of the two laser beams. A way of probing the excitation spectrum of the double ring studied in this work is to use angular momentum spectroscopy [96]: in this case, one needs two laser beams denoted by 1,2 in high-order Laguerre-Gauss modes with optical angular momenta $l_{1,2}$ and frequencies $\omega_{1,2}$. Their corresponding electric fields read $E_{1,2}(r) = f_{l_{1,2}}(r) e^{-il_{1,2}\theta - i\omega_{1,2}t}$ where the radial mode functions $f_l(r) \propto (r/r_0)^{|l|} e^{r^2/2r_0^2}$ need to be chosen in order to match the shape of the double ring to probe.

3.4. Excitation spectrum as a probe of the phases of the two-leg bosonic ring ladder

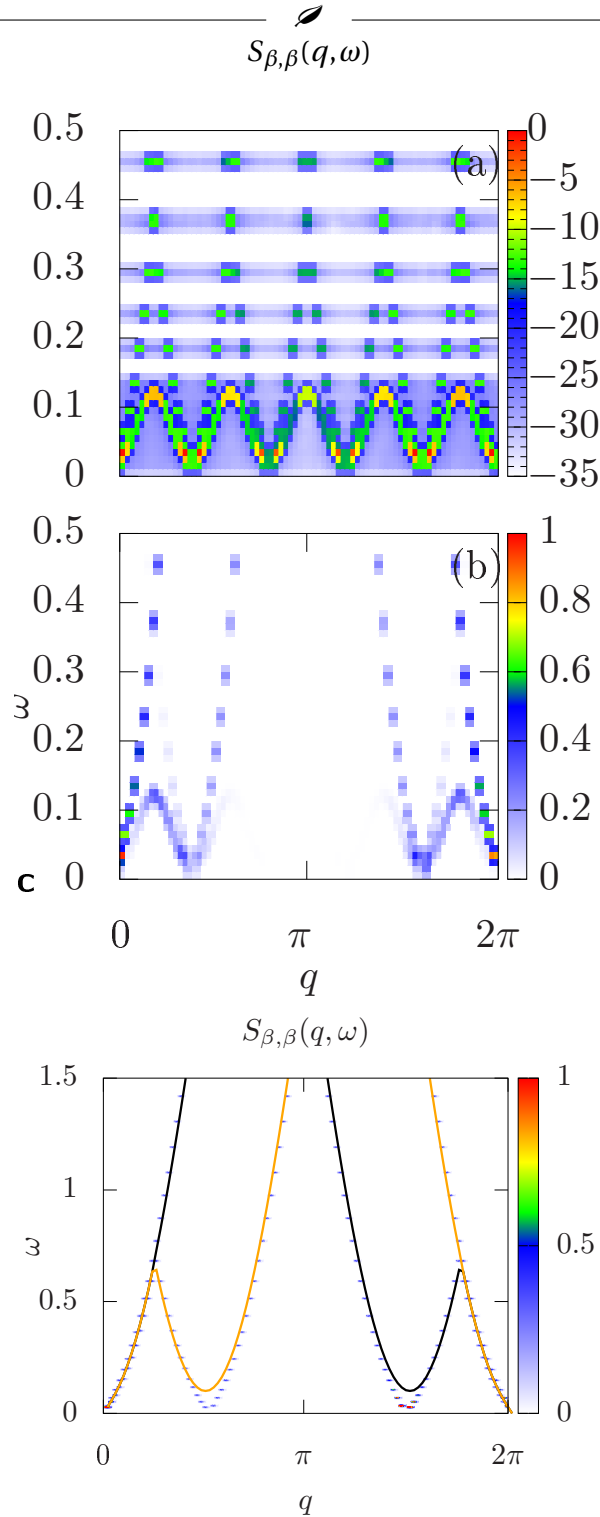


Figure 3.9: (a) Dynamical structure factor in the vortex phase for $K/J = 0.8$; (b) same as (a) but in log scale scale; (c) dynamical structure factor for $K/J = 0$. The other parameters used in all the panels are $\phi = \pi/2$, $Un/J = 0.2$, $N_s = 80$.

3.5. Coherence properties and supersolidity

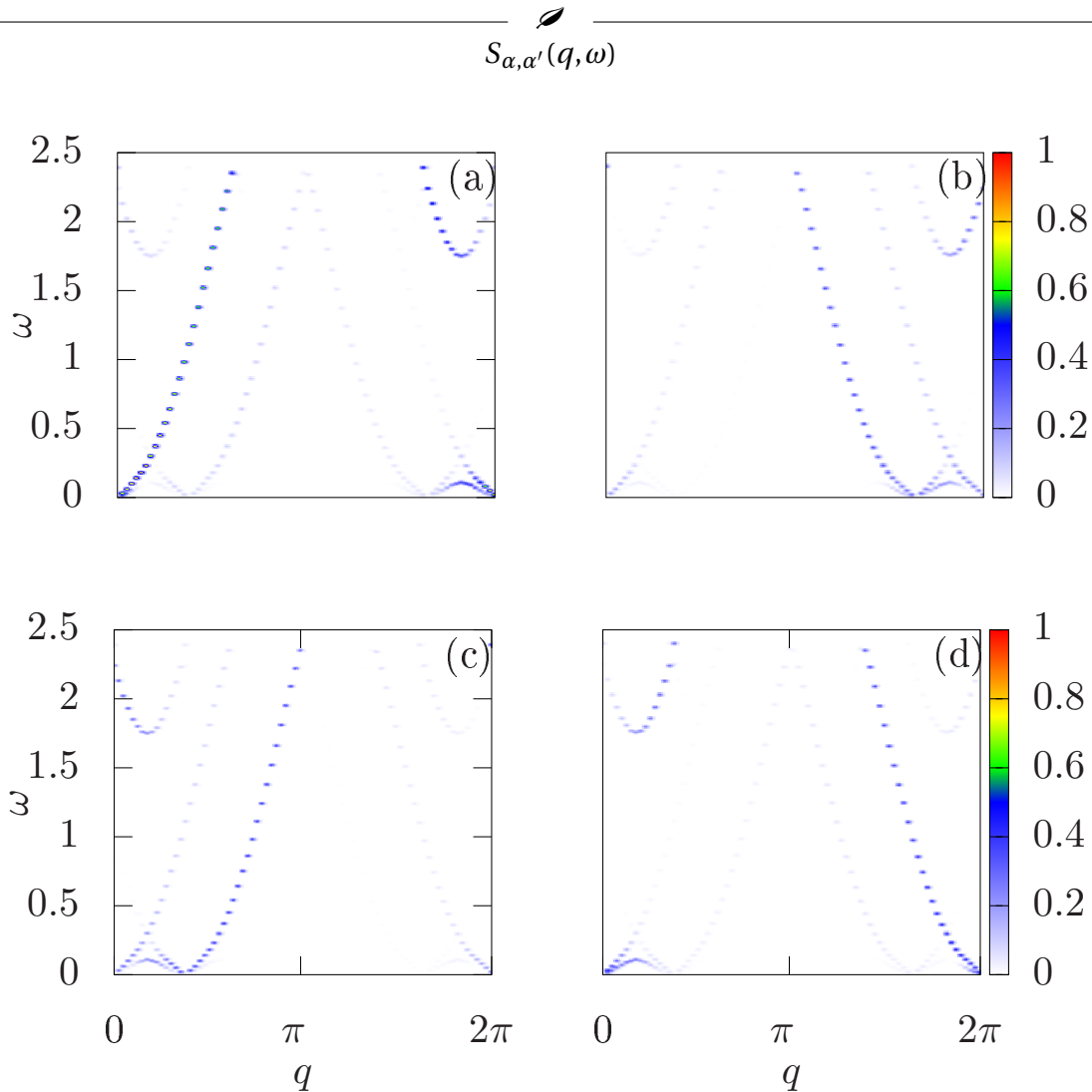


Figure 3.10: Dynamical structure factor $S_{\alpha,\alpha'}(q,\omega)$ in the ring basis in the vortex phase for $\phi = \pi/2$, $N_s = 80$, $K/J = 0.8$ and $Un/J = 0.2$. With a) $S_{1,1}(q,\omega)$, b) $S_{1,2}(q,\omega)$, c) $S_{2,1}(q,\omega)$ and d) $S_{2,2}(q,\omega)$

3.5 Coherence properties and supersolidity

3.5.1 One-body density matrix

In order to study the coherence properties of the system we consider the one-body density matrix $\rho_{\alpha,\alpha'}^{(1)}(j,l) = \langle \hat{a}_{j,\alpha}^\dagger \hat{a}_{l,\alpha'} \rangle$, which in the Bogoliubov approximation reads [97, 98]

$$\rho_{\alpha,\alpha'}^{(1)}(j,l) = \sqrt{\rho_{j,\alpha}^{(0)} \rho_{l,\alpha'}^{(0)}} \exp \left(-\frac{1}{2} \sum_s \left| \frac{Q_{s,j}^{(\alpha)}}{|\Psi_{j,\alpha}^{(0)}|} - \frac{Q_{s,l}^{(\alpha')}}{|\Psi_{l,\alpha'}^{(0)}|} \right|^2 \right), \quad (3.46)$$

where the function in the exponential relates to the fluctuation of the phase of the condensate and $\rho_{l,\alpha}^{(0)}$ stands for the mean-field ground-state density profile of each ring. Since the system is inhomogeneous the one-body density matrix does not depend only on the coordinate difference $j - l$. Therefore, to estimate the coherence we study the averaged first-order correlation function defined as

$$g_{(\alpha,\alpha')}^{(1)}(l) = \sum_j \rho_{(\alpha,\alpha')}^{(1)}(j, j+l) / \sqrt{\rho_{j,\alpha} \rho_{j+l,\alpha'}}. \quad (3.47)$$

Figure 3.11 shows the $g^{(1)}$ correlations in the vortex phase. As the coupling K/J between

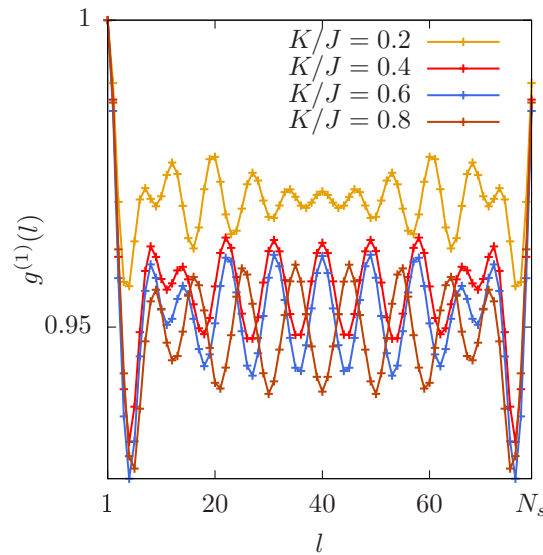


Figure 3.11: Degree of coherence in the vortex phase for $\phi = \pi/2$, $N_s = 80$ and $Un/J = 0.2$. Where $\alpha = \alpha' = 1$.

the rings increases, we notice that the correlations in the ring decrease. However, even for large values of K/J the coherence in the vortex phase stays high even at large distances. This corresponds to a large condensate fraction, thereby implying Bose-Einstein condensation (BEC) and superfluidity.

3.5.2 Static structure factor - probe of solidity

In order to probe the spatial crystalline order expected in the vortex phase we compute the total static structure factor $S_{\text{tot}}(k)$, which is illustrated in Fig. 3.12. We clearly see a peak at wavevectors $k = k_2 - k_1$ and $k = 2\pi - (k_2 - k_1)$, revealing the crystalline order associated to the spatial modulations of the condensate density profile.

3.6. Small ring limit and nature of the excitations

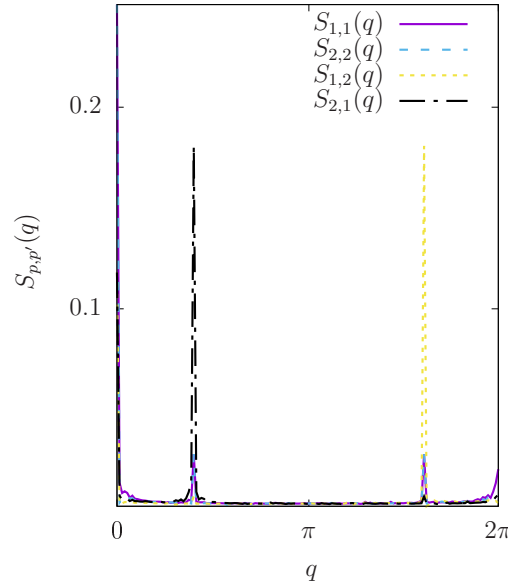


Figure 3.12: Total static structure factor for $\phi = \pi/2$, $N_s = 150$, $K/J = 0.8$ and $Un/J = 0.2$.

3.6 Small ring limit and nature of the excitations

We report in this section a study on the nature of the excitations in the different phases of the system. For this purpose, we calculate the density fluctuations $\delta n_{l,p}^v$ defined as $\langle s | \rho_{l,p} | 0 \rangle$ which can be obtained from the Bogoliubov eigenmodes $h_{v,l}^{(p)}$ and $Q_{v,l}^{(p)}$ according to

$$\delta n_{l,p}^v = 2 \text{Re} \left[\Psi_{l,p}^{(0)} (h_{v,l}^{(p)})^* - (\Psi_{l,p}^{(0)})^* Q_{v,l}^{(p)} \right]. \quad (3.48)$$

Our results for the density fluctuations of chosen low-energy modes are shown in Fig. 3.13. Among the various types of excitation modes, in addition to the phononic Goldstone modes propagating along each ring, we identify the Josephson mode, typical of a finite ring system, which is characterized by spatially homogeneous density fluctuations and out-phase oscillations of the relative populations among the two rings, as in the small-amplitude dynamics of the Josephson effect [99, 100]. We see in Fig. 3.13 that a uniform Josephson mode occurs at low energy in the Meissner phase for low enough coupling among the rings, whereas higher excited modes are of phonons of charge (ie in-phase) type. Close to the phase boundary, in the vortex phase we find that the lowest excitation is a spin (ie out-of-phase) oscillation. In the nearby Meissner phase the lowest excitation become phonon of charge type, as well as in the biased-ladder phase. The Josephson modes are found in the Meissner phase for weak tunnel coupling K/J and weak flux ϕ . In order to estimate the parameter regime where phonon or Josephson modes are present in the ring, we provide here below some estimates based on energy scales. In the Meissner phase, close to $k \rightarrow 0$ the spectrum has a linear behaviour,

3.7. Bogoliubov excitation spectrum for the lowest single-particle branch

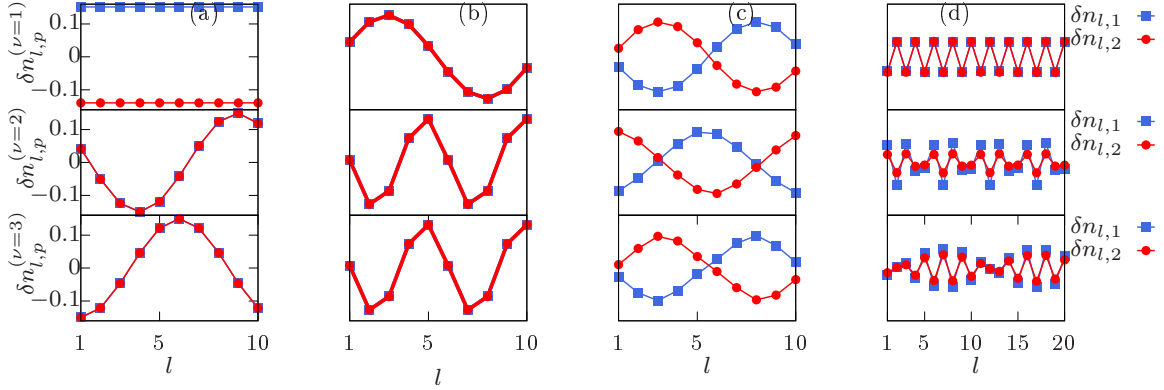


Figure 3.13: Excitation eigenmodes $\delta n_{l,p}$, as a function of the position l along each ring (blue lines with squares $p = 1$, red lines with squares $p = 2$) for the first three excited Bogoliubov modes. a) Josephson out-of-phase mode and two in-phase phonon modes in the Meissner phase for $N_s = 10$, $K/J = 0.1$, $\phi = 0.1$, $Un/J = 0.1$; b) in-phase phonon modes in the Meissner phase for $N_s = 10$, $K/J = 0.8$, $\phi = 0.1$, $Un/J = 0.2$; c) out-of-phase mode in the vortex phase for $N_s = 10$, $K/J = 0.01$, $\phi = \pi/4$, $Un/J = 0.2$; d) in-phase modes in the biased-ladder phase with $N_s = 20$, $K/J = 1$ and $\phi = \pi/2$.

$$\epsilon_k^M \approx E_{ph}k + \tau(k^2) \quad (3.49)$$

where

$$E_{ph}/J = \frac{J2\pi}{KN_s} \sqrt{\frac{U}{J} \left(\frac{K^2}{J^2} \cos(\phi/2) + \left(\frac{U}{J} - 2\frac{K}{J} \right) \sin(\phi/2)^2 \right)}. \quad (3.50)$$

When comparing it to the energy of the Josephson mode which scales as the band gap between the upper and lower branch of the excitation spectrum $E_{gap} \approx K$ we predict that the region where Josephson modes are allowed appears at very low K and ϕ (see Fig 3.14). This is in agreement with the numerical simulations. Moreover, we obtain that Josephson region shrinks at increasing the number of sites in the ring, thereby showing that the Josephson modes are a finite-size effect.

3.7 Bogoliubov excitation spectrum for the lowest single-particle branch

In this part, using the following ansatz (3.51)

$$|\Psi\rangle = \frac{1}{\sqrt{N!}} \left(\beta_{k_1}^\dagger e^{-i\psi_1} + \beta_{k_2}^\dagger e^{-i\psi_2} \right)^N |0\rangle \quad (3.51)$$

3.7. Bogoliubov excitation spectrum for the lowest single-particle branch

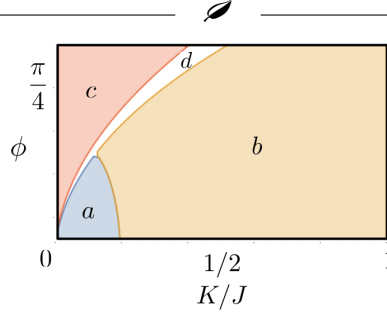


Figure 3.14: Sketch of phase diagram at fixed interaction strength $Un/J = 0.2$ and $N_s = 10$ as deduced from the analysis of the excitation eigenmodes, summarizing the cases illustrated in Fig. 3.13. The coloured regions marked by letters indicate: a) Meissner phase with lowest mode of Josephson type, b) Meissner phase with lowest mode of charge type, c) Vortex phase with lowest mode of spin type, d) Biased-ladder phase with lowest mode of charge type.

for the ground state, we study the excitation spectrum of the vortex phase by analyzing the Bogoliubov excitations on top of the lowest single-particle excitation branch β . The contributions from the upper branch, which corresponds to particles created by the operators \hat{a}_k , are negligible when the interaction strength is much smaller than the gap among the lower and upper branch of the single-particle spectrum.

In order to perform the Bogoliubov analysis we start from the original Hamiltonian (2.6) and compute the interacting part of the Hamiltonian in the free particle diagonal basis $\{\beta_k^\dagger, \beta_k\}$ (see [11]). we obtain

$$H_{int} = \frac{U}{2N_s} \sum_{q,k,r} K(k-q, r+q, k, r) \beta_{k-q}^\dagger \beta_{r+q}^\dagger \beta_k \beta_r \quad (3.52)$$

where the kernel K is given by $K(q_1, q_2, q_3, q_4) = u_{q_1} u_{q_2} u_{q_3} u_{q_4} + v_{q_1} v_{q_2} v_{q_3} v_{q_4}$.

Here we see that the restriction to the lowest branch yields a one-dimensional Bose gas with effective non-zero range interaction potential. We then proceed by performing the Bogoliubov approximation: we assume that the states k_1 and k_2 are macroscopically occupied and so approximate the operators in those states by \mathbb{C} -numbers:

$$\beta_{k_1} = \sqrt{N_0/2} e^{i\psi_1} \quad (3.53)$$

$$\beta_{k_2} = \sqrt{N_0/2} e^{i\psi_2} \quad (3.54)$$

where N_0 is the number of condensed particles in the whole system. We then rewrite the Hamiltonian keeping up all terms up to quadratic order in operators $\beta_{k \neq k_1, k_2}$, $\beta_{k \neq k_1, k_2}^\dagger$. In order to conserve particle number within the Bogoliubov approximation we write the number of condensed particles as a function of the total particle number using relation $N_0 = N - \sum_{k \neq (k_1, k_2)} \beta_k^\dagger \beta_k$. This procedure yields the following quadratic Hamiltonian:

$$H = H^{(0)} + H_{Bog}, \quad (3.55)$$

where $H^{(0)}$ is the mean field energy in the vortex phase given by:

$$\begin{aligned}
 H^{(0)} &= NE_-(k_1) + \frac{UNn}{4} \left[1 + 2u_{k_1}^2 v_{k_1}^2 \right] \\
 H_{Bog} &= \sum_{k \neq (k_1, k_2)} \tilde{\epsilon}_k \beta_k^\dagger \beta_k + \sum_k \beta_{2k_1+k}^\dagger \beta_{-k}^\dagger U_{1,k} + h.c \\
 &+ \sum_k \beta_{2k_2+k}^\dagger \beta_{-k}^\dagger U_{2,k} + h.c + \sum_k \beta_{k_1+k_2+k}^\dagger \beta_{-k}^\dagger U_{12,k} + h.c \\
 &+ \sum_k \beta_{k_1-k_2+k}^\dagger \beta_k (\tilde{U}_{12,k} + c.c) + \sum_k \beta_{k_2-k_1+k}^\dagger \beta_k (\tilde{U}_{12,k} + c.c)
 \end{aligned} \tag{3.56}$$

where the coefficients $\tilde{\epsilon}_k$ and U_k are detailed in Appendix C (corresponding to the Feynman diagrams of Fig. 3.15) and $n = \frac{N}{N_s}$. Writing down the Heisenberg equations of motion for the operators of the excitations leads to $4N_s + 1$ coupled algebraic equations. Due to the large dimensionality of the matrix to diagonalize, we make a low energy approximation: i.e we impose a cut-off k_c around each of the two minima in momentum space. This allows us to truncate the hierarchy of equations and reduce the eigenvalue problem to four coupled equations (see Appendix C for more details):

$$i\hbar \partial_t \begin{pmatrix} \beta_{1,k}^\dagger \\ \beta_{1,-k} \\ \beta_{2,k}^\dagger \\ \beta_{2,-k} \end{pmatrix} = L \begin{pmatrix} \beta_{1,k}^\dagger \\ \beta_{1,-k} \\ \beta_{2,k}^\dagger \\ \beta_{2,-k} \end{pmatrix} \tag{3.57}$$

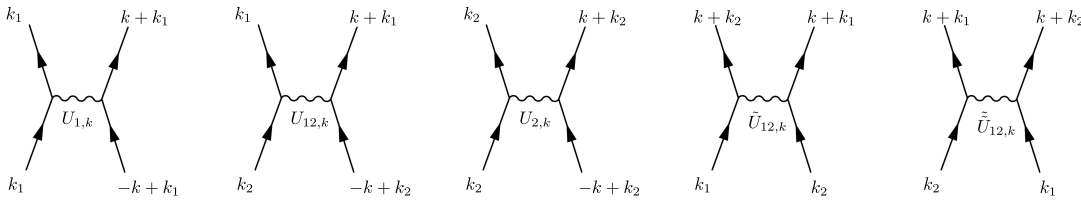


Figure 3.15: Diagrams corresponding to the major scattering processes between modes of the condensates and excitations.

3.8 Details on the approximation

As the mean-field solution is a periodically oscillating function, the excitations are like particles in a periodic potential. If K/J is strong enough we are in a regime where the amplitude of the mean field solution is relatively strong so we can try to model our excitation in a tight binding regime as done in [101]. In the next section we will use numerical

3.8. Details on the approximation

simulations (one can see in those simulation that low-energy modes are indeed localized in the lattice created by the mean field solution). From this approximated Hamiltonian we can compute the equation of motion for each operators. We notice when computing the equation of motion for the operator β_{k_1-k} that it is linked to higher excitation modes $\beta_{-2k_2+k_1-k}$ and $\beta_{2k_2-k_1+k}^\dagger$ (see Eq 3.58).

$$\begin{aligned} i\partial_t \beta_{k_1-k} &= \tilde{\epsilon}_{k_1-k} \beta_{k_1-k} + 2U_{1,-k_1+k} \beta_{k_1+k}^\dagger \\ &+ 2U_{2,-k_1+k} \beta_{2k_2-k_1+k}^\dagger + 2ReU_{12,-k_1+k} \beta_{k_2+k} \\ &+ 2Re\tilde{U}_{12,2k_2+k} \beta_{k_2-k} + 2Re\tilde{\tilde{U}}_{12,-2k_2+k_1-k} \beta_{-2k_2+k_1-k} \end{aligned} \quad (3.58)$$

The goal of our approximation is to claim that this higher mode will be negligible at low energy since they correspond to high energy excitation. But this hold if the two minima are away from the peculiar value of $\pm\pi/2$ since cause to periodicity of the system $\beta_{-2k_2-k_1}$ will be close to β_{k_2} and so be relevant mode. In our study we are at $\phi = \pi/2$ so that $k_{2,1} \approx \Phi \pm \pi/4$ and indeed prevent the relevance of those higher modes. Cutting all those modes gives us the following evolution matrix:

$$L = \begin{pmatrix} -\tilde{\epsilon}_{k_1+\lambda} & -2e^{-2i\psi_1} U_{1,-k_1+\lambda}^* & -2\cos(\psi_1 - \psi_2) \tilde{\tilde{U}}_{12,k_1+\lambda} & -2e^{-i(\psi_1+\psi_2)} U_{12,-k_1-\lambda}^* \\ 2e^{2i\psi_1} U_{1,-k_1+\lambda} & \tilde{\epsilon}_{k_1-\lambda} & 2e^{i(\psi_1+\psi_2)} U_{12,-k_1+\lambda} & 2\cos(\psi_1 - \psi_2) \tilde{\tilde{U}}_{12,k_1-\lambda} \\ -2\cos(\psi_1 - \psi_2) \tilde{\tilde{U}}_{12,k_1+\lambda} & -2e^{-i(\psi_1+\psi_2)} U_{12,-k_2-\lambda}^* & -\tilde{\epsilon}_{k_1-\lambda} & -2e^{-2i\psi_2} U_{2,-k_2-\lambda}^* \\ 2e^{i(\psi_1+\psi_2)} U_{12,-k_2+\lambda} & 2\cos(\psi_1 - \psi_2) \tilde{\tilde{U}}_{12,k_2-\lambda} & 2e^{2i\psi_2} U_{2,-k_2+\lambda} & \tilde{\epsilon}_{k_1+\lambda} \end{pmatrix} \quad (3.59)$$

Where all the functions stand for:

$$\begin{aligned} \tilde{\epsilon}_k &= E_-(k) - E_-(k_1) - \frac{UN}{2N_s} \left(1 + 2u_{k_1}^2 v_{k_1}^2 \right) \\ &+ \frac{UN}{N_s} \left(u_{k_1}^2 u_k^2 + v_{k_1}^2 v_k^2 \right) + \frac{UN}{N_s} \left(u_{k_2}^2 u_k^2 + v_{k_2}^2 v_k^2 \right) \end{aligned} \quad (3.60)$$

$$U_{1,k} = \frac{UN}{4N_s} K(k_1, k_1, 2k_1 + k, -k) \quad (3.61)$$

$$U_{2,k} = \frac{UN}{4N_s} K(k_2, k_2, 2k_2 + k, -k) \quad (3.62)$$

$$U_{12,k} = \frac{UN}{4N_s} 2K(k_1 + k_2 + k, -k, k_1, k_2) \quad (3.63)$$

$$\tilde{U}_{12,k} = \frac{2UN}{N_s} K(k_1, k_2, k_1 - k_2 + k, k) \quad (3.64)$$

$$\tilde{\tilde{U}}_{12,k} = \frac{2UN}{N_s} K(k_1, k_2, k_2 - k_1 + k, k) \quad (3.65)$$

This approximation is justified for $K/J \ll 1$ and values of ϕ preventing higher order coupling between the minima in k-space ($k+3k_d$ lying in another minimum) By analyzing the eigenvalues of the evolution matrix L we find that they can take imaginary values and are complex conjugate pairs [102] indicating the failure of the low-energy approximation.

Conclusions of the chapter

In conclusion, in this work we have performed a detailed study of the excitation spectrum of a weakly interacting Bose gas in a two-leg bosonic ring ladder subjected to an artificial gauge flux. For all the three phases expected at weak interactions, i.e the Meissner, vortex and biased ladder phase, we have solved the Bogoliubov-de Gennes equations for the ring ladder and calculated the dynamical structure factor. For a cigar-shaped gas and for a one-dimensional gas in a linear atomic wave-guide, the dynamical structure factor has been already experimentally measured. Here we propose that it is accessed in the ring geometry by angular momentum spectroscopy.

Our main predictions are a single phonon-like dispersion at long wavelength in the Meissner phase, a roton minimum emerging in the biased-ladder phase and two phonic branches in the vortex phase. Furthermore, we find evidence of the underlying spatially modulated structure of the vortex phase in the spectrum by a folding of the Brillouin zone of the excitations.

Using the Bogoliubov excitations eigenmodes, we have also calculated the first-order correlation function, monitoring the coherence of the gas, and found that it remains high all over the ring. This feature, together with the diagonal long-range order in the vortex phase is hallmarking the supersolid nature of the fluid. The emergence of supersolidity in this system is quite remarkable, as, at difference from the spin-orbit coupled Bose gas, the visibility of the fringes can be arbitrarily tuned thanks to the absence of interspecies contact interactions in the current model.

Finally, we have shown the emergence of Josephson excitations in a finite ring, corresponding to population imbalance oscillations among the two rings. We have found that the Josephson modes appear both in the Meissner and vortex phase, in the latter case we have found both homogeneous oscillations as well as spin-like excitations carrying a longitudinal momentum.

In outlook, it would be interesting to study the excitation spectrum at larger interaction strengths, where the nature of the ground state changes onto a fragmented condensate [71] or a fragmented Fermi sphere [103] at intermediate and large interactions respectively, as we should see in the next Chapter.

Chapter 4

Hard-core bosons



IN this chapter we study the ground state of a bosonic ring ladder under a gauge flux in the vortex phase, corresponding to the case where the single-particle dispersion relation has two degenerate minima. By combining exact diagonalization and an approximate fermionization approach we show that the ground state of the system evolves from a fragmented state of two single-particle states at weak inter-particle interactions to a fragmented state of two Fermi seas at large interactions. Fragmentation is inferred from the study of the eigenvalues of the reduced single-particle density matrix as well as from the calculation of the fidelity of the states. We characterize these non-classical states by the momentum distribution, the chiral currents and the current-current correlations.

A bosonic system is in a single Bose-Einstein condensate if its single-particle density matrix has one macroscopic eigenvalue (i.e order of the number of particles) [61]. If the single-particle density matrix has more than one macroscopically occupied eigenvalue, then the state is named fragmented [104, 105]. Nozières and Saint James [104] demonstrated that no fragmentation can take place in a homogeneous Bose gas with repulsive interactions. For dispersion relations with degenerate minima, instead, fragmented states may emerge [106, 107, 72].

Such a type of dispersion relation occurs in the vortex phase of double ring lattices, displaying in particular a two-minima structure. Here, we investigate the nature of the system's ground state at arbitrary interactions. The mean-field approach assumes a coherent state, made of a superposition of single-particle occupancies of each minimum. However, it has been shown that the ground state at small lattice fillings and weak interactions is indeed a fragmented state constructed with single-particle momentum states [71]. This result can be related to the studies of spin-orbit coupled systems, which share the same type of Hamiltonian as bosonic flux ladders, and where the fragmentation was also observed with an *ab-initio* numerical study [72]. In this work, we explore the fate of the fragmented state at increasing interactions. In particular, we show that strong repulsive interactions destroy the fragmented single-particle state, and give rise to a novel type of non-classical state, which can be described as a fragmentation of two Fermi spheres.

The ground state crossover is analyzed by studying the correlation functions as implied in the the one-body density matrix and the specific changes in the configuration of the currents flowing in the ladder.

The chapter is organized as follows. In Sec.4.1 we introduce the necessary tools on the Bose-Fermi mapping. In Sec.4.2 we review the physics of fragmentation largely inspired by [105] which provide a more complete description of fragmentation in many-body system. In Sec.4.3, we introduce the model Hamiltonian and discuss the different properties of the ground states in the different physical regimes of the ladder; in addition we sketch the analytical methods (an approximate fermionization scheme) that we employ to study the different system's observables we refer to. In the Sec.4.4, we present the results obtained with the analytical methods and compare them with the exact diagonalization; our findings are corroborated by the study of the configuration of currents flowing in the ring ladder. Finally Sect. 4.4.5, is devoted to a summary and concluding remarks.

4.1 Tonks-Girardeau Bose-Fermi mapping

We consider a system of one-dimensional bosons interacting via contact interaction $v(x - x') = g\delta(x - x')$ at infinitely strong interactions $g \rightarrow \infty$ an exact solution provided by the Bose-Fermi mapping [108]. This method is extremely powerful as it can deal with arbitrary external potential of the Lieb-Liniger Hamiltonian (1.22). It allows to evaluate the exact many-body wave function with trapping potential. The idea of the mapping lies on the fact that the physics is dominated by the interaction between the particle and bosons cannot occupy the same position in space. This constraint mimics the Pauli exclusion's principle for fermions, and causes the bosons to show fermionic properties. Therefore, the many-body wave function of bosons can be written in terms of the non-interacting fermionic wave function, times a mapping function $\mathcal{A}(x_1, \dots, x_N) = \prod_{j < l} \text{sign}(x_j - x_l)$

$$\Psi_{\text{TG}}(x_1, \dots, x_N) = \mathcal{A}(x_1, \dots, x_N) \frac{1}{\sqrt{N!}} \det[\psi_l(x_m)] \quad (4.1)$$

where $\psi_l(x_m)$ are the eigenfunctions of the non-interacting problem and the determinant of such set of function is the Slater determinant that provide the solution of a non-interacting many-body fermionic system. The mapping factor \mathcal{A} restores the symmetry properties of the bosonic gas under exchange of particles. The Tonks-Girardeau gas [108], proposed more than 50 years ago, was experimentally realized on a lattice [109](see Fig 4.1) and in a one-dimensional atomic wave-guide [59].

Observables that only depend on the absolute value of the wave function of hard-core bosons within the Tonks-Girardeau mapping are the same as those of free fermions as the overall phase factor emerging from the mapping factor \mathcal{A} cancels. For example, the density profile and the density correlation functions will be the same. On the other hand, quantities connecting wave functions in different point in space like the one-body density matrix or the momentum distribution will have a different behavior than the one of an

4.1. Tonks-Girardeau Bose-Fermi mapping

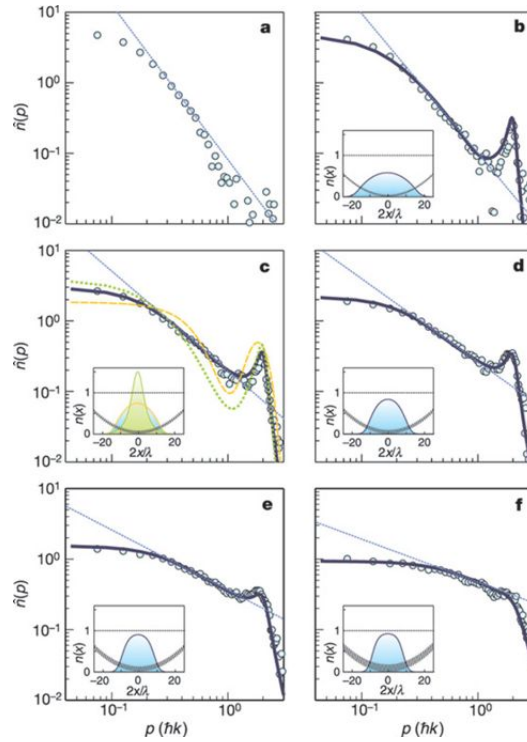


Figure 4.1: Momentum distribution of the 1D atomic gas in an optical lattice. The dots represent measured data whereas the lines correspond to the computed momentum distributions. The green dotted line represents ideal bosons, the yellow dashed line represents the ideal Fermi gas and the gray solid line represents the TG gas. Due to the non-uniformity of the TG gas on the lattice, the slope of the linear part in the double logarithmic plot deviates from the expected $1/2$ behaviour of the uniform TG gas indicated in short dashes (Figure from [109])

ideal Fermi gas (see Fig 4.2). The momentum distribution of a Tonks-Girardeau gas will display $k^{-1/2}$ divergences when $k \rightarrow 0$ whereas for ideal fermions the momentum distribution is a flat Fermi surface (see Fig 4.2).

On a one-dimensional lattice the Bose-Fermi mapping, from bosonic b_l operator to fermionic c_l at site l , is ensured via the Jordan-Wigner transformation [111]

$$c_l = \prod_{j=1}^{l-1} e^{i\pi b_j^\dagger b_j} b_l. \quad (4.2)$$

This transformation ensures that the fermionic operators c_l have anti-commutation relation i.e., $\{c_l, c_m^\dagger\} = \delta_{l,m}$. Moreover, due to the space Pauli exclusion principle, the bosonic operators have mixed commutation relation, i.e. $[b_l, b_m^\dagger] = [b_l^\dagger, b_m^\dagger] = [b_l, b_m] = 0$ when $m \neq l$ and $\{b_l, b_m^\dagger\} = 1$ when $m = l$ so that we indeed get a mixed algebra of on-site fermion

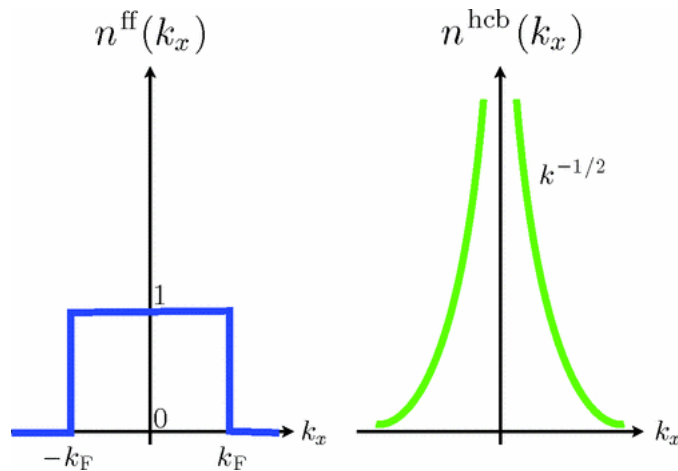


Figure 4.2: Schematic representation of the momentum distribution of an ideal Fermi gas ($n^{ff}(k_x)$) and Tonks-Girardeau gas ($n^{hcb}(k_x)$). Taken from [110]

and off-site bosons, this really underlying the fact that local quantities for fermions and hard-core bosons are the same and off-diagonal correlations will differ. Hard-core bosons on a finite lattice periodic system display ensure a similar behavior with some additional mesoscopic effects (see Fig 4.3) namely that the divergence in the momentum distribution at $k = 0$ is removed [112]. The peak in the momentum distribution at $k = 0$, $n_{k=0}$ scales as $n_{k=0} = C(\rho)\sqrt{N}$ where N is the number of particles and C a density dependent function finite size correction appears so that $n_{k=0}$ will scale as $n_{k=0} = C(\rho)\sqrt{N} - D(\rho)$.

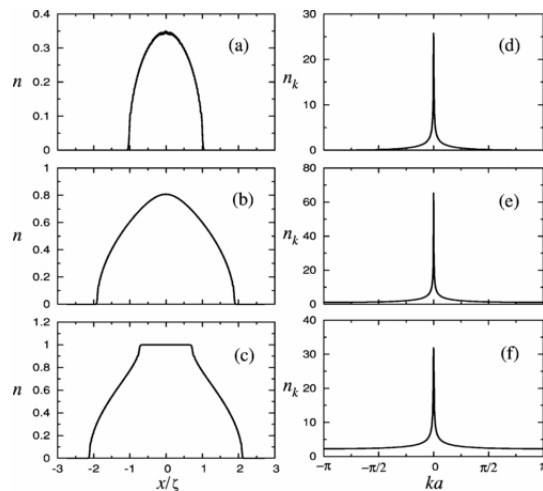


Figure 4.3: Density profile (left panels) and momentum distribution (right panels) of a gas of hard-core bosons on a one-dimensional lattice. Taken from [112]

4.2 Fragmentation

As mentioned in chapter 1.3.1 the concept of BEC is defined as the macroscopic occupation of the first eigenvalue of the one-body density matrix $\rho^{(1)}(\mathbf{r}, \mathbf{r}') = \langle \psi^\dagger(\mathbf{r})\psi(\mathbf{r}') \rangle$, where ψ stands for the bosonic field operators. In the basis of an orthogonal set of eigenfunctions $f_i(\mathbf{r})$ (natural orbitals) with corresponding eigenvalue N_i , i.e $\int \rho^{(1)}(\mathbf{r}, \mathbf{r}') f_i(\mathbf{r}') d\mathbf{r}' = N_i f_i(\mathbf{r})$, the one-body density matrix takes a diagonal form

$$\rho^{(1)}(\mathbf{r}, \mathbf{r}') = \sum_i N_i f_i(\mathbf{r}')^* f_i(\mathbf{r}) \quad (4.3)$$

and $\sum_i N_i = N$, where N is the number of particle in the system. Fragmentation is defined as the macroscopic occupancy of a $q > 1$ eigenvalue, i.e that $N_{i < q} \sim O(N)$ and $N_{i > q} \sim O(N^0)$. Many different kinds of fragmentation can occur in physical bosonic system [105]. The condensate can be fragmented in space or momentum space. One historical example is the Nozières one [104] which is a model of N bosons belonging to two internal states labeled 1 and 2. This model can for example describe a double well in the quantum regime and the Hamiltonian reads as follows

$$H = \epsilon_1 a_1^\dagger a_1 + \epsilon_2 a_2^\dagger a_2 + \frac{g}{2} (a_1^\dagger a_2^\dagger a_2 a_1 + n_1 n_1 + n_2 n_2), \quad (4.4)$$

where g is the interaction strength between the bosons and can be either repulsive ($g > 0$) or attractive ($g < 0$). The ground state is made of N_1 bosons in well 1 and N_2 bosons in well 2. For repulsive interactions $g > 0$ and the ground state is two-fold degenerate with state $|N, 0\rangle$ and $|0, N\rangle$. For $g < 0$ the ground state however is fragmented with Fock-state $|\text{Frag}\rangle = \frac{a_1^{N_1} a_2^{N_2}}{\sqrt{N_1! N_2!}} |0\rangle$. One has then to compare the energies of two different states, a fragmented state and a single condensate state

$$|\text{Frag}\rangle = \frac{a_1^{N_1} a_2^{N_2}}{\sqrt{N_1! N_2!}} |0\rangle \quad |\text{Bec}\rangle = \frac{a_1^N}{\sqrt{N!}} |0\rangle \quad (4.5)$$

where the one-body density matrix reads for each one

$$\rho^{\text{Frag}} = \langle a_i^\dagger a_j \rangle = \begin{pmatrix} N_1 & 0 \\ 0 & N_2 \end{pmatrix} \quad \rho^{\text{Bec}} = \langle a_i^\dagger a_j \rangle = \begin{pmatrix} N_1 & 0 \\ 0 & 0 \end{pmatrix} \quad (4.6)$$

If one looks only at the interaction energy (i.e $\epsilon_1 = \epsilon_2 = 0$) when comparing the energy of the gas in fragmented state and BEC state we see that

$$\Delta E = \langle H \rangle_{\text{Frag}} - \langle H \rangle_{\text{Bec}} = g N_0 N_1 \quad (4.7)$$

so that interactions play a key role on the ground state property of the gas: when $g > 0$ (repulsive interactions) it prevents from having a fragmented state whereas when $g < 0$ the condensate will be fragmented. The situation changes when considering states spatially

separated as in the case of the double well. The Hamiltonian is slightly changed, compared to the situation explained earlier, in order to add tunneling between the wells and to remove interaction between species.

$$H = -t \left(a_1^\dagger a_2 + a_2^\dagger a_1 \right) + \frac{g}{2} (n_1(n_1 - 1) + n_2(n_2 - 1)) \quad (4.8)$$

This system is exactly solvable [105], we will not give the derivation here but provide the important physical results. For $g = 0$, the single particle eigenstates are the symmetric state $(a_1 + a_2)/\sqrt{2}|0\rangle$ with energy $E_s = -t$ and anti-symmetric state $(a_1 - a_2)/\sqrt{2}|0\rangle$ with energy $E_a = t$ so that the symmetric state describes the ground state of the system that is a coherent state of this symmetric eigenstates $|Coh\rangle = \frac{1}{2^N N!} \left(a_1^\dagger + a_2^\dagger \right)^N |0\rangle$ which is clearly not fragmented. In the case of non-zero interactions the physical situation will be quite different as the ground state will depend again on the sign of the interactions. For attractive interactions the ground state is fragmented as the fluctuation in the number of particles are suppressed and the transition from coherent state to fragmented state is induced by the increase of the phase fluctuation. When interactions are repulsive the ground state will be a Schrödinger cat-like state $|Cat\rangle = 1/\sqrt{2}(|N, 0\rangle + |0, N\rangle)$ as the interaction term $g/4(n_1 - n_2)^2$ will favor a different number of particle in the two wells.

An important conclusion is that the fragmented state in this example is favored in mesoscopic system as the transition from coherent to fragmented state takes place for $t/g > 1/N$ [105]. In what follows we will study the fragmentation effects in the double ring lattice under gauge fields. Even though we saw that in double well structure the fragmentation is deeply linked to the sign of the interaction, in the double ring the fragmentation arise more from the degeneracy of the single particle dispersion relation than from the interaction process as said in the introduction. Indeed, if the single-particle dispersion relation exhibits degeneracy of the lowest energy state, then the condensation can take place in any of those minima or simultaneously in all of them.

4.3 Fragmented Fermi seas

The concepts of fragmentation and fermionization introduced so far will be useful to understand the strongly interacting regime for the double ring system that we will study now in the quantum regime. In the tight-binding approximation we model the system using the Bose-Hubbard Hamiltonian (2.6)

$$\begin{aligned} \hat{H} &= \hat{H}_0 + \hat{H}_{int} = \\ &- \sum_{l=1, p=1, 2}^{N_s} J_p \left(a_{l,p}^\dagger a_{l+1,p} e^{i\Phi_p} + a_{l+1,p}^\dagger a_{l,p} e^{-i\Phi_p} \right) \\ &- K \sum_{l=1}^{N_s} \left(a_{l,1}^\dagger a_{l,2} + a_{l,2}^\dagger a_{l,1} \right) + \frac{U}{2} \sum_{l=1, p=1, 2}^{N_s} a_{l,p}^\dagger a_{l,p}^\dagger a_{l,p} a_{l,p} \end{aligned} \quad (4.9)$$

4.3. Fragmented Fermi seas

where we recall that the angular position on the double ring is given by $\theta_l = \frac{2\pi}{N_s}l$ where l is an integer $l \in [1, N_s]$ with N_s the number of sites in each ring, J_1 and J_2 are the tunneling amplitudes from one site to another along each ring, K is the tunneling amplitude between the two rings, $\Phi_{1,2}$ are the fluxes threading the inner and outer ring respectively and U the on-site interaction. As in chapter 2, we introduce the relative flux $\phi = \Phi_1 - \Phi_2$ and average flux $\Phi = (\Phi_1 + \Phi_2)/2$. We will restrict our self to the case of $\Phi = 0$.

In order to characterize the ground state of the system we use various observables: the momentum distribution in ring p is defined as $n_{k,p} = \langle \hat{a}_{k,p}^\dagger \hat{a}_{k,p} \rangle$, with

$$\hat{a}_{k,p} = \frac{1}{\sqrt{L}} \sum_{m=1}^L \hat{a}_{m,p} e^{imk}, \quad (4.10)$$

where k is the wavevector in units of inverse lattice spacing. The current operator at position m along the same ring is defined as $\hat{j}_{m,p}^\parallel = -iJ(\hat{a}_{m,p}^\dagger \hat{a}_{m+1,p} - \text{h.c.})$, where p labels the rings. We define the chiral current in the ladder as $\hat{j}_c = \frac{1}{L} \sum_m (\hat{j}_{m,1}^\parallel - \hat{j}_{m,2}^\parallel)$. The inter-ring current operator at site m is $\hat{j}_m^\perp = -iK(\hat{a}_{m,1}^\dagger \hat{a}_{m,2} - \text{h.c.})$. Correspondingly, we define the current-current correlation of the current between the rings $\langle \hat{j}_0^\perp \hat{j}_m^\perp \rangle$ and the current inside the ring $\langle \hat{j}_0^\parallel \hat{j}_m^\parallel \rangle$. We also investigate the density-density correlations in the leg $\Delta n_m = \langle \hat{n}_0 \hat{n}_m \rangle - \langle \hat{n}_0 \rangle \langle \hat{n}_m \rangle$ and between legs $\Delta n_m^\perp = \langle \hat{n}_0^1 \hat{n}_m^2 \rangle - \langle \hat{n}_0^1 \rangle \langle \hat{n}_m^2 \rangle$.

By Fourier transforming, the Hamiltonian (Eq. 4.9) is readily expressed in momentum space (see Appendix A). It is useful to transform the above Hamiltonian to a new basis, which is diagonal in absence of interactions. We call this the ‘‘diagonal’’ basis. By using the transformation

$$\begin{pmatrix} \hat{a}_{k,1} \\ \hat{a}_{k,2} \end{pmatrix} = \begin{pmatrix} v_k & u_k \\ -u_k & v_k \end{pmatrix} \begin{pmatrix} \hat{\alpha}_k \\ \hat{\beta}_k \end{pmatrix}, \quad (4.11)$$

where u_k and v_k are given by

$$v_k = \sqrt{\frac{1}{2} \left(1 + \frac{\sin(2\pi\phi) \sin(k)}{\sqrt{(K/2J)^2 + \sin^2(2\pi\phi) \sin^2(k)}} \right)} \quad (4.12)$$

$$u_k = \sqrt{\frac{1}{2} \left(1 - \frac{\sin(2\pi\phi) \sin(k)}{\sqrt{(K/2J)^2 + \sin^2(2\pi\phi) \sin^2(k)}} \right)} \quad (4.13)$$

the non-interacting part of the Hamiltonian becomes

$$\hat{H}_0 = \sum_k E_+(k) \hat{\alpha}_k^\dagger \hat{\alpha}_k + E_-(k) \hat{\beta}_k^\dagger \hat{\beta}_k, \quad (4.14)$$

with $E_\pm = -2J \cos(k) \cos(2\pi\phi) \pm \sqrt{K^2 + 4J^2 \sin^2(k) \sin^2(2\pi\phi)}$. In the vortex phase the lowest branch $E_-(k)$ of the dispersion relation has two degenerate minima at

$$k_{1,2} = \pm \arcsin \sqrt{\sin^2(2\pi\phi) - \frac{K^2}{(2J \tan(2\pi\phi))^2}} \quad (4.15)$$

It will be useful to study the momentum distributions in the diagonal basis, ie the one of the lower branch $n_\beta(k) = \langle \hat{\beta}_k^\dagger \hat{\beta}_k \rangle$ and the one of the upper branch $n_\alpha(k) = \langle \hat{\alpha}_k^\dagger \hat{\alpha}_k \rangle$

In the vortex phase, for very small ring-ring coupling K and small, non-zero interaction strength U , the ground state is fragmented, *i.e.* displays macroscopic occupation of the two single-particle momentum states $k_{1,2}$ as described by the the ansatz [71]

$$|\Psi_0^{(sp)}\rangle = \hat{\beta}_{k=k_1}^\dagger{}^{N/2} \hat{\beta}_{k=k_2}^\dagger{}^{N/2} |0\rangle. \quad (4.16)$$

Notice that the ground state is built only with the field operators β associated to the lowest branch of the dispersion relation, and the problem has been mapped to an effectively one-dimensional one. In the presence of interactions, the effective one-dimensional Hamiltonian restricted to the lowest branch reads

$$\begin{aligned} \hat{H} = & \sum_k E_-(k) \hat{\beta}_k^\dagger \hat{\beta}_k \\ & + \frac{U}{2N_s} \sum_{q,k,r} \kappa(k-q, r+q, k, r) \hat{\beta}_{k-q}^\dagger \hat{\beta}_{r+q}^\dagger \hat{\beta}_k \hat{\beta}_r \end{aligned} \quad (4.17)$$

where the kernel $\kappa(k-q, r+q, k, r) = u_{k-q} u_{r+q} u_k u_r + v_{k-q} v_{r+q} v_k v_r$ is an effective interaction potential in momentum space, which has some involved momentum structure. However, if the ratio K/J is small, the parameters u_k and v_k can be approximated as constants for wavevector k close to k_1 and k_2 . In this case, for the sake of finding the ground state, the Hamiltonian is equivalent to the one of a one-dimensional Bose gas with contact interactions with a single-particle dispersion $E_-(k)$.

At increasing interaction strength, clearly the fragmented single-particle state ansatz (4.16) is not expected to describe the ground state state of the system well, since repulsive interactions give rise to a spread in momentum occupancy. In the regime $U \rightarrow \infty$ of very strong repulsion, we predict an effective fermionization of the ground state, ie two particles cannot occupy the same single-particle state and we propose the following fragmented Fermi-sea ansatz:

$$|\Psi_0^{(Fs)}\rangle = \prod_{-k_F+k_1 < k < k_F+k_1} \hat{c}_k^\dagger \prod_{-k_F+k_2 < k < k_F+k_2} \hat{c}_k^\dagger |0\rangle. \quad (4.18)$$

where k_F is the Fermi wavevector corresponding to $N/2$ particles and \hat{c}_k^\dagger the fermionic creation operator for the lower band of the non-interacting Hamiltonian (e.g. $\{\hat{c}_k^\dagger, \hat{c}_{k'}^\dagger\} = \delta_{k,k'}$, where $\{\cdot\}$ is the anti-commutator). This ansatz is only valid as long as the Fermi energy is smaller than the energy of the upper band, i.e $E_{\text{Fermi}} < E_+(k)$.

4.3.1 Bose-Fermi mapping

Using the fragmented Fermi sea ground state, in the $U = \infty$ limit we calculate the one-body density matrix and the momentum distribution of the gas using a mapping onto

4.4. Numerical results

non interacting fermions. In detail, we Fourier transform the ansatz into real space, then apply the Jordan-Wigner transformation introduced in Sec 4.1

$$\hat{b}_i^\dagger = c_i^\dagger \prod_{j=1}^{i-1} e^{-i\pi c_j^\dagger c_j} \quad \hat{b}_i = \prod_{j=1}^{i-1} e^{i\pi c_j^\dagger c_j} c_i \quad (4.19)$$

Hard-core bosons and non-interacting fermions have the same spectrum in one dimension. Differences between the two appears in off-diagonal correlation functions, eg in the one-body density matrix. Using the relation between the one-body density matrix ρ_{ij} and the one-particle Green's function $G_{ij} = \langle b_i b_j^\dagger \rangle$

$$\rho_{ij} = \langle b_i^\dagger b_j \rangle = G_{ij} + \delta_{ij}(1 - G_{ii}), \quad (4.20)$$

we calculate the one-body density matrix using a method developed by Rigol and Muramatsu [112]. In particular the one-particle Green's function can be expressed in term of our ansatz and fermionic operators according to

$$\begin{aligned} G_{ij} &= \langle \Psi_0^{(HCB)} | b_i b_j^\dagger | \Psi_0^{(HCB)} \rangle \\ &= \langle \Psi_0^{(Fs)} | \prod_{p=1}^{i-1} e^{i\pi c_p^\dagger c_p} c_i c_j^\dagger \prod_{s=1}^{j-1} e^{-i\pi c_s^\dagger c_s} | \Psi_0^{(Fs)} \rangle \end{aligned} \quad (4.21)$$

where $|\Psi_0^{(HCB)}\rangle$ is the ground state for hard-core bosons.

4.4 Numerical results

4.4.1 Fidelity with respect to fragmented states

In order to infer the nature of the ground state of the system we calculate the fidelity of the ground state obtained by exact diagonalization of the many-body Hamiltonian with the Lanczos algorithm and we project it onto the two ansatz states discussed in Sec.4.3, i.e. we take $F = |\langle \Psi_0 | \psi_{GS} \rangle|^2$, where $|\Psi_0\rangle$ is either the single-particle fragmented state Eq.(4.16) or the Fermi-sea fragmented state Eq.(4.18). Notice that since we use a real-space basis for the numerical diagonalization we perform first a Fourier transform of the ansatz state onto real-space.

Our results are shown in Fig.4.4. In the left panel we show that the fidelity with respect to the single-particle fragmented state decreases at increasing interactions. In the right panel, we show that the fidelity with respect to the fragmented Fermi sea increases with interaction. For weak inter-ring coupling, we reach nearly unity fidelity for $U/J > 10$ for any flux, thus confirming the validity of our ansatz.

For strong inter-ring coupling, where the description of hard-core bosons breaks down, we find that the fidelity stays below one for any interaction and its value depends strongly on the choice of flux values. In this case there is no simple analytical description since bosons belonging to the lower band interact with a long-range interacting potential.

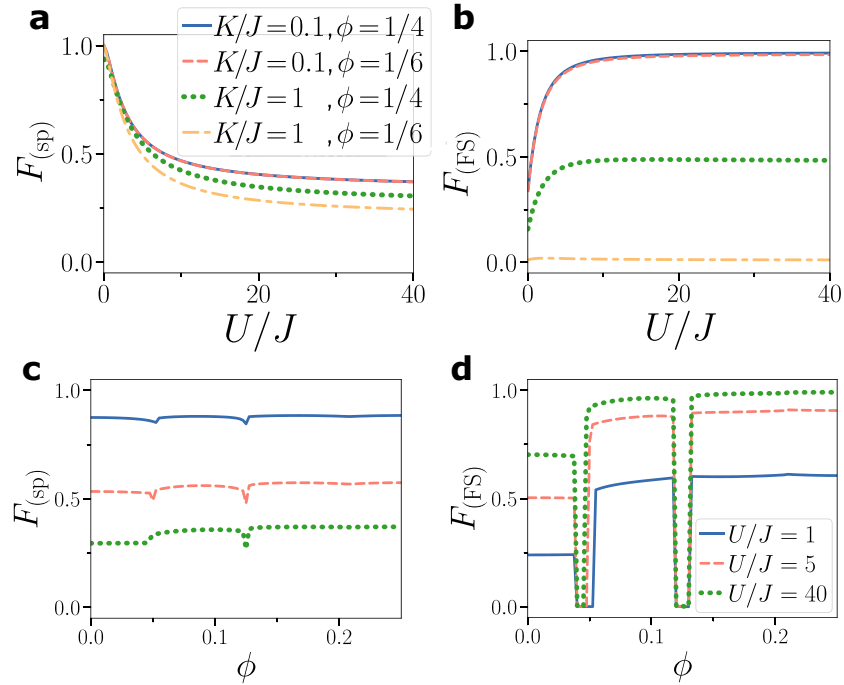


Figure 4.4: Fidelity (dimensionless) of the ground state obtained from numerical diagonalization as a function of respectively interaction strength in units of tunnel energy J and flux ϕ (dimensionless): **a)** and **c)** with respect to the single-particle fragmented state $|\Psi_0^{(sp)}\rangle$ and **b)** and **d)** with respect to the fragmented Fermi sea $|\Psi_0^{(FS)}\rangle$. The parameters used are $L = 12$, $N = 6$. The values of K/J and ϕ are indicated in the figure legend for **a)** and **b)**. For panels **c)** and **d)** interaction strength are specified in the figure legend and $K/J = 0.1$. A third dip occurs in panels **c)** and **d)**, in correspondence of the third jump in the chiral current but is not resolved in this figure.

4.4. Numerical results

Fidelity at varying flux (see Fig.4.4 panels **c**) and **d**) exhibit discontinuities associated to change of quantized momenta and jumps in the chiral current (see Fig.4.5**a**). At those transitions the eigenvalues of the single-particle density matrix are 4-fold degenerate implying that the description in terms of the single-particle fragmented state (4.16) and fragmented Fermi sea (4.18) ansatz breaks down.

In the following, we provide an analysis of the observables characterizing the ground state of the system and identify the ones needed to infer the fragmented nature of the state in the vortex phase.

4.4.2 Currents

First, we show that the study of chiral currents can be used to identify unequivocally the vortex phase in parameter space, both in the interacting and non-interacting regime.

The Hamiltonian (4.9) in absence of interactions features the Meissner to vortex transition. At weak interactions, an additional biased ladder phase is found. At stronger interactions, chiral Mott insulating phase with Meissner like current and vortex Mott insulating phase are predicted [15, 13].

In Fig.4.5a) we show the chiral current as a function of the gauge field ϕ in the non-interacting case. The Meissner phase has an increasing chiral current, whereas the current decreases in the vortex phase. For finite-sized rings, the current acquires a step structure, each jump being associated to a integer change of the phase winding. This signals the formation of a vortex pair in the rings [66]. In Fig.4.5b) we show the chiral current at increasing inter-ring tunneling K/J . We see that a change of behaviour occurs in the chiral currents in correspondence to the transition from the vortex phase at low values of K/J to the Meissner phase at large K/J : a jump in the chiral current is found in the finite size-system while the chiral current is continuous with discontinuous derivative in the infinite-size limit. We expect the transition to be of first order in analogy to the case of spin-orbit-coupled bosons [113].

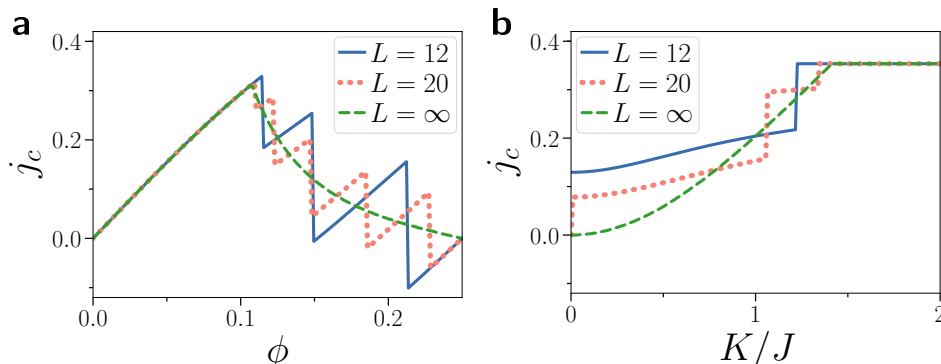


Figure 4.5: Chiral current j_c (in units of J) **a**) as a function of flux ϕ (dimensionless) for $K/J = 1$ for different ring lengths L . **b**) as a function of inter-ring coupling K (in units of J) for $\phi = 1/8$. In both panels we have taken $U = 0$ and half filling of the lattice.

The chiral current for interacting systems is shown in Fig.4.6. We see that even though interactions smooth out the steps of the current and reduces the positions of the steps to lower values of K/J , overall it is still possible to infer the vortex phase as the regime where chiral current has a decreasing and oscillating behaviour as a function of the flux ϕ . Similarly to the non-interacting case, the transition from vortex to Meissner phase is visible by studying the dependence of chiral current on inter-ring coupling K/J .

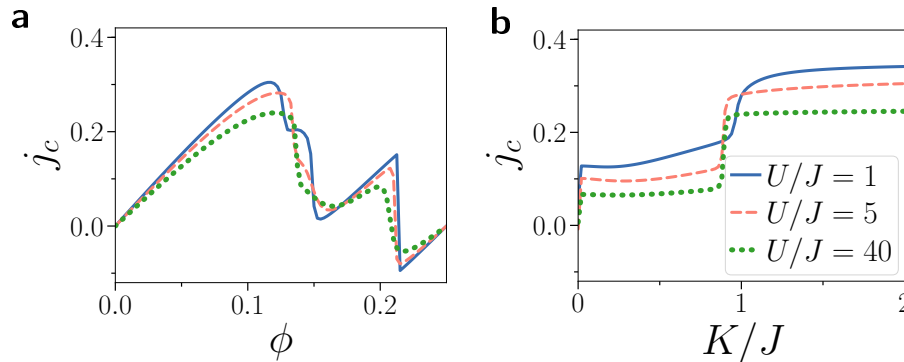


Figure 4.6: **a)** Chiral current (in units of J) as a function of flux ϕ (dimensionless) for $K/J = 1$ and on-site interaction U/J as indicated in the legend **b)** Chiral current as function of inter-ring coupling K/J for $\phi = 1/8$ and interaction strength as indicated in the legend. The other parameters are $L = 12$ and $N = 6$ particles.

4.4.3 Current-current correlations

Another way to identify the vortex phase is the study of current-current correlations [114].

For linear ladders the ground state in the vortex phase is characterized by a vortex structure along the ladder, a modulation of the density along the legs, and a modulation of the current between rungs. In the case of coupled lattice rings, corresponding to periodic boundary conditions, these features are not visible since the ground state displays rotational invariance. In this case as the vortex phase sets in, the mentioned features are encoded in the correlation functions. In particular, the current-current correlation $\langle j_0^\perp j_x^\perp \rangle$, where j_x^\perp is the current operator for the current between the rings, show a clear vortex structure in Fig.4.7.

4.4.4 Density-density correlations

Next, we show that density-density correlations of the ground state may be used to infer the onset of strong correlations and the fermionized regime.

A hallmark of fermionization is the presence of Friedel-like oscillations, characterized by wavevector $2k_F$, with k_F the Fermi wavevector. These are found e.g. in the density-density correlation function Δn_m , shown in Fig.4.8 along one chosen ring (same results are found for the other ring). For small inter-ring coupling, we observe the build-up of

4.4. Numerical results

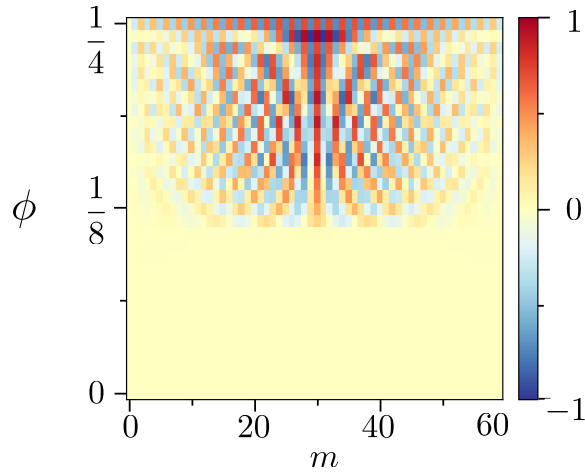


Figure 4.7: Inter-ring current-current correlation function $\langle j_0^\perp j_x^\perp \rangle$ in units of J^2 at varying flux ϕ (dimensionless) and lattice position m for $L = 60$, $N_p = 2$, $U/J = 1$ and $K/J = 1$.

Friedel-like oscillations at increasing interaction, with wavelength corresponding to four times the lattice spacing, corresponding to the chosen average lattice filling in each ring. For large values of K/J , the system is not any more quasi-one-dimensional. In this case we find that the wavelength of Friedel oscillations changes with the applied flux.

4.4.5 One-body density matrix and momentum distribution

Finally, in this section we show that the study of the first-order correlations and momentum distribution allows us to obtain information about fragmentation.

The momentum distribution in each ring A and B is plotted in Fig.4.9. We see that at weak inter-ring coupling the momentum distribution is centered in each of the two minima $k = k_1$ or k_2 , corresponding to the applied gauge flux on each ring.

The momentum distribution in the diagonal basis, corresponding to occupation of lower and upper excitation branch in momentum space, is plotted in Fig.4.10 and 4.11 for two choices of the inter-ring coupling. It displays a two-peak structure, corresponding to the two minima of the single-particle dispersion relation $k = k_1, k_2$. We notice first that most of the population occupies the lower branch, while the upper branch population is two orders of magnitude smaller. This validates the reduction to an effective one-dimensional system corresponding to the lower branch discussed in Sec.4.3. Focusing on the lower-branch momentum distribution, we notice that at strong interactions the momentum distribution broadens due to interaction effects as well as develops large-momentum tails characteristic of strongly-interacting regime. The peaks remain well defined even in the fermionized limit, as typical of bosonic statistics, though their width coincides with the kinetic energy of the corresponding Fermi gas. The width of the momentum distribution for bosons and fermions is shown in the Appendix.

The width of the momentum distribution $\kappa = \sum_k k^2 n_k$ is shown in Fig.4.12. At increas-

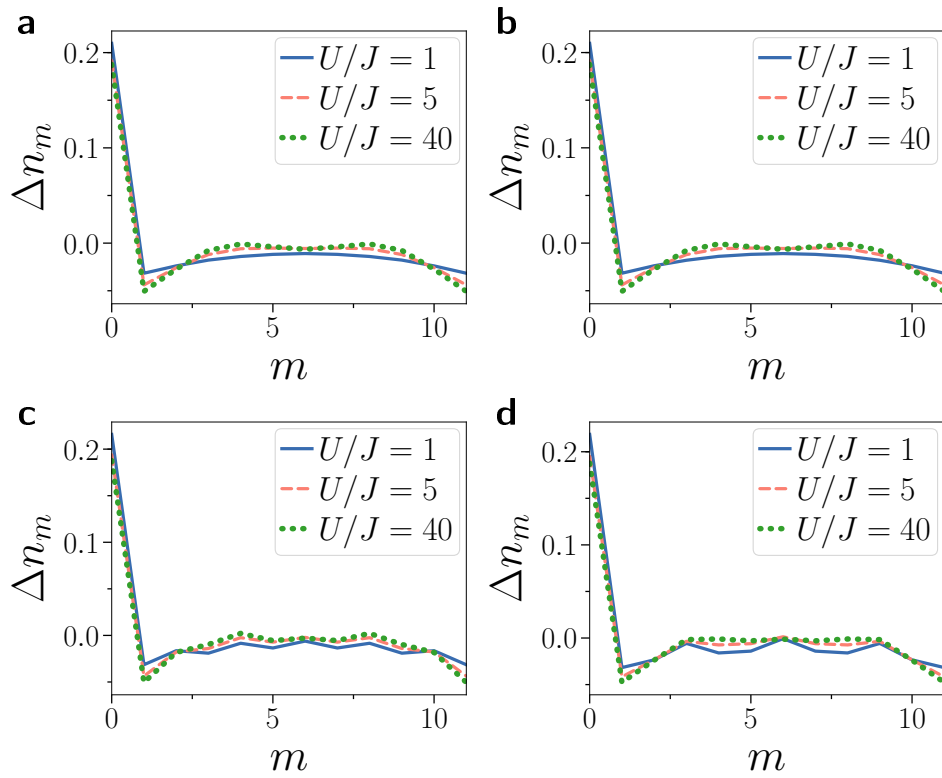


Figure 4.8: Density-density correlation function Δn_m (dimensionless) as a function of the position m along the lattice. **a)** $K/J = 0.1$, $\phi = 1/4$ **b)** $K/J = 0.1$, $\phi = 1/6$ **c)** $K/J = 1$, $\phi = 1/4$ **d)** $K/J = 1$, $\phi = 1/6$. The other parameters are $N = 6$, $L = 12$ and the flux ϕ is dimensionless.

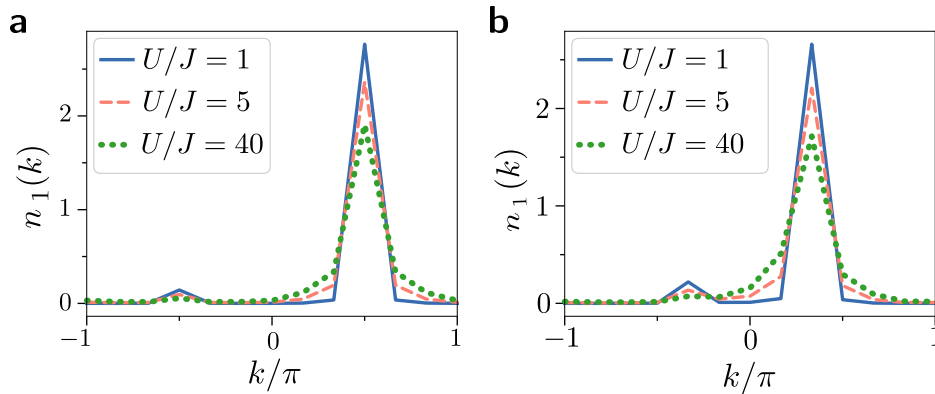


Figure 4.9: Momentum distribution (dimensionless) as a function of the wavevector k (in units of inverse of lattice spacing) in the leg basis for leg 1 with **a)** $K/J = 1$, $\phi = 1/4$ **b)** $\phi = 1/6$. The momentum distribution in ring 2 is the same graph reflected at zero momentum. The calculations are performed with $N = 6$ particles in total in the two rings and $L = 12$ sites per ring.

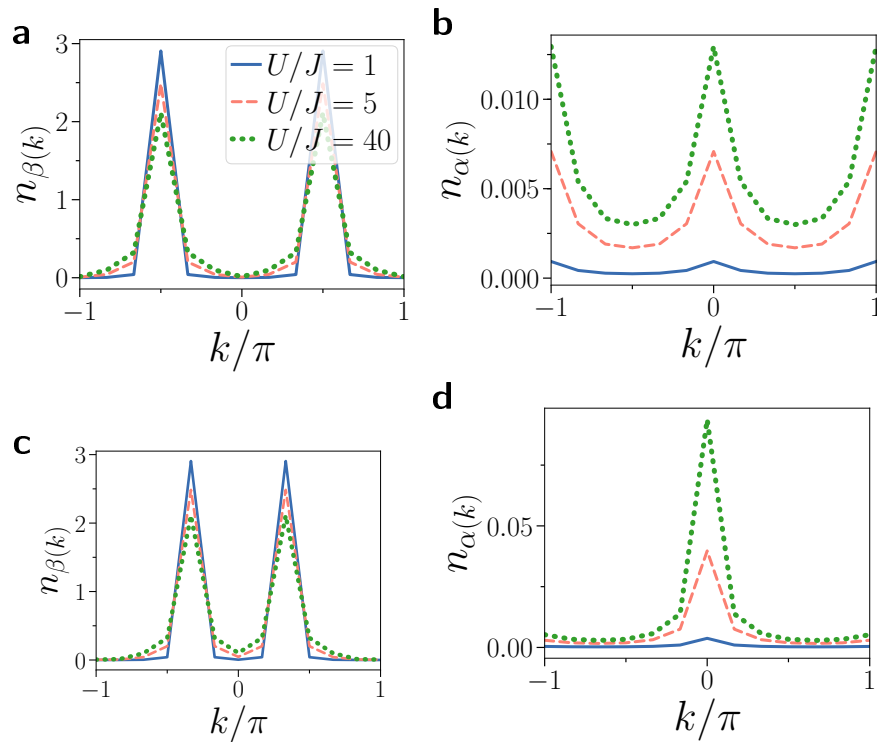


Figure 4.10: Momentum distribution (dimensionless) as a function of the wavevector k (in units of inverse of lattice spacing) in the diagonal basis for weak inter-ring coupling $K/J = 0.1$ with **a,b**) $\phi = 1/4$ **c,d**) $\phi = 1/6$. **a,c**) shows the lowest branch, **b,d**) shows the upper branch. We take $N = 6$ particles in total in the two rings and $L = 12$ sites per ring.

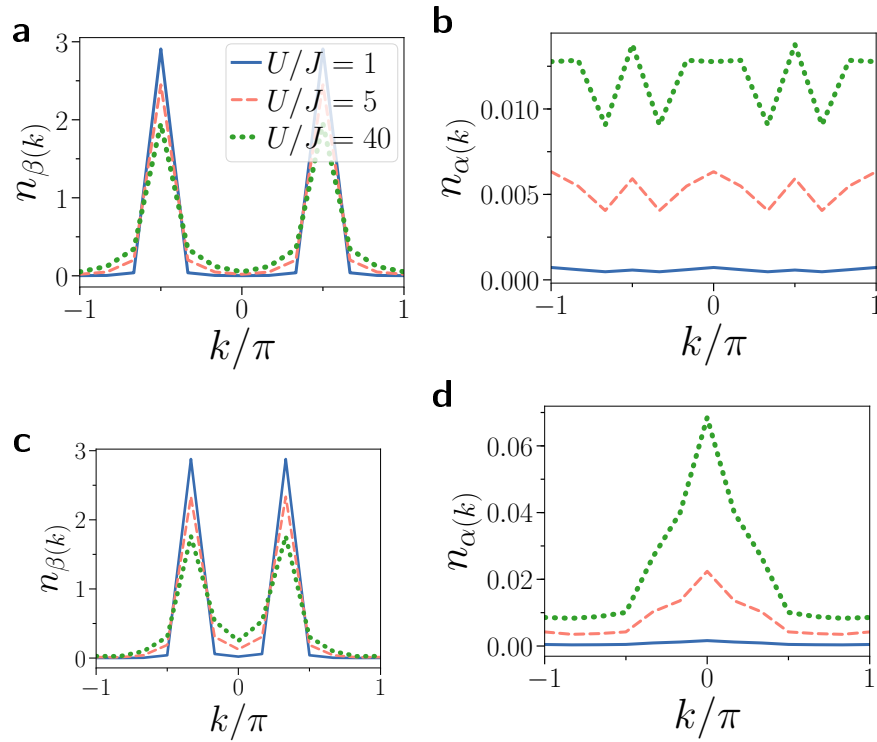


Figure 4.11: Momentum distribution (dimensionless) as a function of the wavevector k (in units of inverse of lattice spacing) in the diagonal basis for strong inter-ring coupling $K/J = 1$ with **a,b** $\phi = 1/4$ **c,d** $\phi = 1/6$. **a,c**) shows the lowest branch, **b,d**) shows the upper branch. We take $N = 6$ particles in total in the two rings and $L = 12$ sites per ring.

4.4. Numerical results

ing interactions and small-inter-ring coupling it tends to the fermionic value, thereby further confirming the fermionized nature of the state.

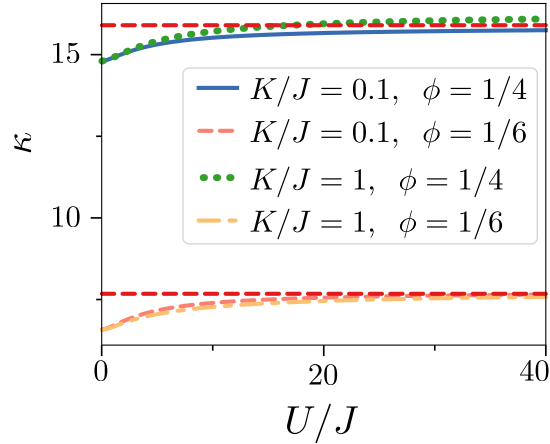


Figure 4.12: Width of the momentum distribution $\kappa = \sum_k k^2 n_k$ (in units of the inverse of the square of the lattice spacing) as a function of interaction strength U/J for various values of ϕ and K . The red dashed line is the corresponding value for non-interaction fermions. The calculations are performed for $N = 6$ particles, $L = 12$ sites.

We finally analyze the single particle density matrix (SPDM), which is independent of the chosen basis and whose Fourier transform yields the momentum distribution. By analyzing its eigenvalues, in the case of weak inter-ring coupling we find that for all values of interactions, it displays a double degeneracy of the two largest eigenvalues, as shown in Fig.4.13 and Fig.4.14. The degeneracy of the two largest eigenvalues of the one-body density matrix provides a strong indication of fragmentation.

As already noticed in the study of other observables, for strong inter-ring coupling the quasi-one dimensional description does not apply. We see in particular that the eigenvalues decay faster with increasing interactions, in a flux-dependent way, indicating the important role of the transverse direction in this case.

Degeneracy of eigenvalues : We provide further information about the eigenvalues of the reduced one-body density matrix of the double ring. In particular, Fig.4.14 shows the eigenvalues in decreasing order, at various values of the system parameters. One sees that the two largest eigenvalues are degenerate both at small and larger values of both K/J and ϕ , thus indicating fragmentation of the state for all choices of parameters investigated in this work.

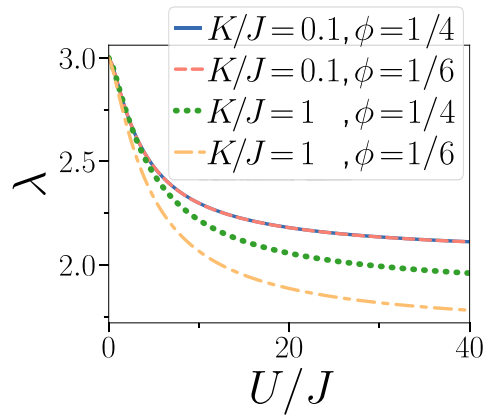


Figure 4.13: Two largest degenerate eigenvalues λ (superimposed, indicated by a single line) of the single particle density matrix as a function of interaction strength U/J for different values of flux ϕ and inter-ring coupling K/J as indicated in the legend. The parameters use in the calculation are $L = 12$, $N = 6$.

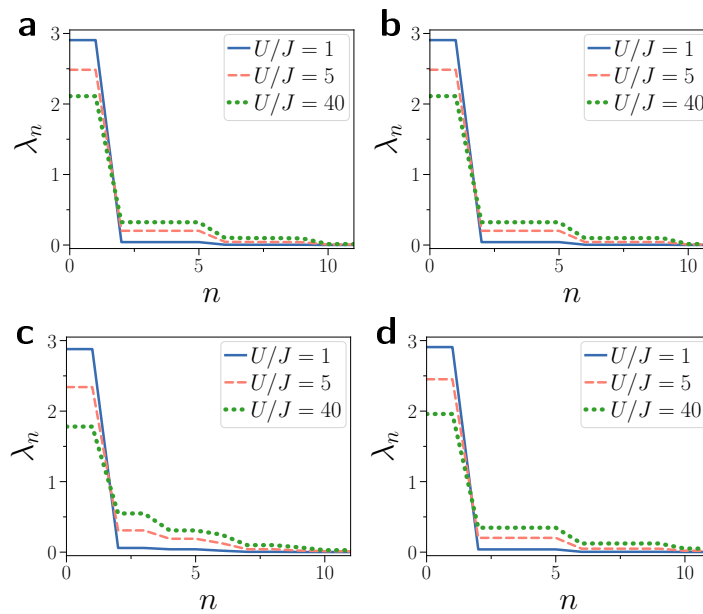


Figure 4.14: Single particle density matrix eigenvalues λ_n (dimensionless) ordered in descending order n for **a)** $K/J = 0.1$, $\phi = 1/4$ **b)** $K/J = 0.1$, $\phi = 1/6$ **c)** $K/J = 1$, $\phi = 1/4$ **d)** $K/J = 1$, $\phi = 1/6$. First two eigenvalues are degenerate. Results for $N = 6$ particles, $L = 12$ sites.

Conclusions of the chapter

In this chapter we have studied the ground-state properties of two tunnel-coupled lattice rings in the quantum regime. In particular, we have shown that the ground-state of the system is always fragmented at any interaction strength, and the nature of the fragmented

4.4. Numerical results

state depends on the interaction strength: for weak interactions it consists of fragmentation among two single-particle states, while for strong interactions it corresponds to two fragmented Fermi seas. This Fermi seas description holds provided that the tunnel coupling between the two rings is sufficiently weak and the flux threading the system relatively strong. This allowing for an analytical ansatz which well describes the limits of very weak or very strong interactions.

The information of the nature of the state can be inferred by combining the knowledge of various observables: the study of chiral currents and current-current correlation functions allow to identify the vortex phase. By increasing interactions, the flux dependence of the currents across the transitions between states with different winding numbers is smoothed out - see Fig.4.6. The density-density correlation function shows the onset to fermionization via the appearance of Friedel-like oscillations at large interactions, and a double-peak structure in the momentum distribution together with the demonstration of degenerate eigenvalues of the one-body density matrix establishes the fragmented nature of the state. In outlook, it would be interesting to explore the crossover from quantum regime at very weak filling considered in this work and the mean-field Gross-Pitaevskii description used in the case of very large number of bosons per lattice site.



Chapter 5

Quantum fluctuation effects, Luttinger liquid description

N this chapter we will use the framework of the Luttinger liquid approach to describe the double ring under artificial gauge fluxes. The approach consists of considering the continuous limit of the lattice system considered in the previous chapters. As mentioned earlier, many theoretical works have treated the subject of infinite bosonic ladder under gauge fluxes with contact interactions [12, 115], inter-rung interaction and long range interactions. The case of periodic boundary conditions have not been addressed so far, while studies have been carried out in the case of open boundary conditions in order to cope with density-matrix-renormalization-group numerical calculations (DMRG, a very powerful numerical tool to solve 1D problems).

The chapter is organized as follows: in Sec. 5.1 we introduce the fundamental notions of the Luttinger liquid theory as well as sine-Gordon model renormalization group equations. In Sec. 5.2 we bosonize the Hamiltonian of the double ring and, using the mode expansion of the field operators, we show the properties of mesoscopic rings in both Meissner and Vortex phase through the studies of various physical observables.

5.1 Bosonization and Luttinger liquid

A very elegant way of solving many-body strongly correlated fermionic system in 1D was provided by Luttinger [116]. As the interaction term between fermions is the product of four fermionic field operators and can naively be seen as a product of two bosonic fields corresponding to density fluctuations, he provided a solution in terms of free bosonic operators. Tomonaga[117] was the first to relate fermionic excitations to boson-like behaviour [117], paving the way for a description of many-body interacting fermionic system in terms of bosonic operators. Haldane was then the one who realized that a one-dimensional system who exhibit gapless linear spectrum can be treated within the same framework, defining a *universality class* of systems sharing similar behavior and critical

exponents. This universality class of systems called "Luttinger liquid" by Haldane includes 1D Hubbard model at half-filling, 1D electron-phonon systems or metals with impurities as well as the edge states in the quantum Hall effect. The Bose gas with repulsive contact interactions falls also in this universality class of fermionic systems due to the absence of well defined statistics in 1D.

Following Cazalilla [118] we introduce the harmonic-fluid approach developed by Haldane [119]. In order to describe 1D bosonic gases of size L , the relevant low-energy Hamiltonian is expressed as

$$H^L = \frac{\hbar v}{2\pi} \int_0^L dx \left[K_L (\partial_x \phi(x))^2 + \frac{1}{K_L} (\partial_x \theta(x))^2 \right] \quad (5.1)$$

where v is the sound velocity and K_L is the Luttinger parameter, corresponding to the compressibility of the gas. These coefficients are introduced phenomenologically in the equation. They depend on the microscopic properties of the system, usually accessible by means of numerical or, when available exact calculations: Bethe Ansatz for the Lieb-Liniger model of bosons or in the hard-core interaction limit via Tonks-Girardeau Bose-Fermi mapping. The two fields $\phi(x)$ and $\partial_x \theta(x)$ correspond respectively to phase and density fluctuations around a certain mean value, and satisfy the following commutation relation

$$[\partial_x \theta(x), \phi(x')] = i\pi \delta(x - x'). \quad (5.2)$$

One can then identify two regimes. For large values of the Luttinger parameter K_L , the system is in a weakly interacting regime where density fluctuations are important and phase fluctuations are reduced and behave classically. This regime is analogous to a BEC phase without symmetry breaking due to the Mermin-Wagner theorem [64]. If K_L is small then the phase has large fluctuations and the density behave classically corresponding almost to a crystal.

5.1.1 Correlation functions

Correlation function in the gapless phase

For a single-component Luttinger liquid Hamiltonian (see Eq. 5.1), the excitation spectrum is gapless and it is easy to calculate its correlation functions as the Hamiltonian is quadratic. Let us consider the following correlation function, that is the one-body density matrix $\langle \Psi^\dagger(x) \Psi(x') \rangle$. To lowest order, within bosonization, it reads

$$\langle \Psi^\dagger(x) \Psi(x') \rangle = \rho_0 \langle e^{-i\phi(x)} e^{i\phi(x')} \rangle \quad (5.3)$$

For an infinite system this can be calculated [120] using bosonization techniques and reads,

$$\langle \Psi^\dagger(x) \Psi(x') \rangle = \rho_0 \left(\frac{d}{x - x'} \right)^{\frac{1}{2K_L}} \quad (5.4)$$

5.1. Bosonization and Luttinger liquid

where d is a short distance cut-off. The situation becomes more complex when one needs to consider a finite system with given boundary conditions. A good way to treat boundary conditions is to use conformal field theory approach, that is well suited for Luttinger Hamiltonian as the theory is self critical [120]. When computing the correlation function with periodic boundary condition within the framework of conformal field theory (see Appendix of [118] and Appendix E of this thesis) one has

$$\langle \Psi^\dagger(x)\Psi(x') \rangle_{pbc} = c_{0,1}\rho_0 \left[\frac{1}{\rho_0 d(x-x'|L)} \right]^{\frac{1}{2K_L}} e^{i\pi\langle J \rangle(x-x')/L} \quad (5.5)$$

where $\langle J \rangle$ is the expectation value of the zero mode of the mode expansion of the field $\phi(x)$ and correspond to the kinetic momentum of the system, $c_{0,1}$ is a non-universal coefficient that depends on the system and $d(x|L) = L|\sin(\pi|x|/L)|/\pi$ is known as cord function, appearing due to the finite size of the system. It measures the length of a cord between two points separated by an arc x in a ring of circumference L .

Density-density correlation

We consider next the density-density correlation function, which does not depend on statistics, within harmonic fluid approach. Keeping only the leading term of the correlation function with periodic boundary conditions we have

$$\langle \rho(x)\rho(0) \rangle_{pbc} = \left[\frac{1}{\pi^2} \langle \partial_x \theta(x)\partial_x \theta(0) \rangle + \rho_0^2 \sum_{m=-\infty}^{\infty} e^{2\pi i m \rho_0 x} \langle A_{2m,0}(x)A_{-2m}(0) \rangle_{pbc} \right] \quad (5.6)$$

$$= \rho_0^2 \left[1 - \frac{K_L}{2\pi^2} \left[\frac{1}{\rho_0 d(x|L)} \right]^2 + \sum_{m>0} a_m \left[\frac{1}{\rho_0 d(x|L)} \right]^{2m^2 K_L} \cos(2\pi m \rho_0 x) \right] \quad (5.7)$$

where the vertex operators $A_{m,n}(x, \tau)$ are defined within conformal theory in the Appendix of [118]. For an infinite system this correlation function reads

$$\langle \rho(x)\rho(0) \rangle = \rho_0^2 \left[1 - \frac{K_L}{2} \frac{1}{(\pi \rho_0 x)^2} + \sum_{m>0} a_m \frac{\cos(2\pi m \rho_0 x)}{(\pi \rho_0 x)^{2K_L m^2}} \right], \quad (5.8)$$

as first derived by Haldane [119] and later improved [121].

5.1.2 Sine-Gordon model

We introduce here basics about renormalization group equation of the sine-Gordon model as they will be useful to treat the bosonized version of the double ring. The Hamiltonian for the sine-Gordon model reads

$$H = H^L + y \int dx \cos(\sqrt{8}\theta) \quad (5.9)$$

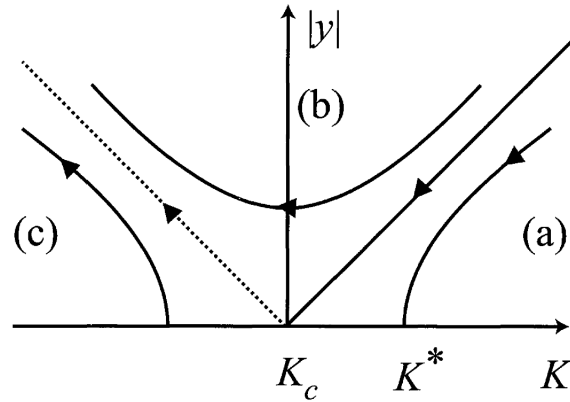


Figure 5.1: Renormalization flow corresponding to Eq 5.10. Left diagonal thick line separates regions (a) where y is irrelevant and region (b) where y flows to strong coupling and the cosine is relevant. From [120].

The flow equation for the sine-Gordon model are the following [120]

$$\begin{aligned} \frac{dK_L(l)}{dl} &= -\frac{y^2(l)K_L^2(l)}{2} \\ \frac{dy(l)}{dl} &= (2 - 2K_L(l))y(l) \end{aligned} \quad (5.10)$$

Indeed for $K_L < 1$ y is relevant (grows upon change of scale). For $K_L > 1$, y is irrelevant (decrease upon change of scale). The point $K_L = 1$ is marginal, and corresponds to the transition point between a phase where the cosine term is relevant and one where it is irrelevant. The spectrum of a sine-Gordon Hamiltonian is known, and displays solitons and anti-solitons excitations [122, 123]. This model describes the competition between the cosine term who wants to fix the phase and the kinetic part which impose a gradient. When the cosine term is dominating we face a transition towards a gapped phase.

We expect that the renormalization group equation should not differ from a infinite system and a system of finite size as the cord function can be Taylor expanded during the perturbative renormalization approach and bring back the power law decaying of the infinite correlation functions. The only difference between finite and infinite system is that the renormalization flow should stop at critical scale $l^* \propto \log(L)$. If the Hamiltonian has the form $H = H^L + y \cos(\sqrt{8}\phi)$ the flow equations are dual and corresponds to the transformation $K_L \rightarrow 1/K_L$.

5.2. Luttinger liquid description of the double ring

5.2 Luttinger liquid description of the double ring

5.2.1 Derivation of the Luttinger Liquid Hamiltonian of the double ring

Following [115], we apply Haldane's bosonization of interacting bosons [119, 118] to our Bose-Hubbard Hamiltonian. The tunneling coupling K between the two rings is assumed to be small compared to the longitudinal tunneling J , $K/J \ll 1$ in order to decouple the two rings. We introduce the canonically conjugate fields, $\partial_x \theta_p(x)/\pi = \Pi_p(x)$ and $\phi_p(x)$ accounting respectively for the fluctuation of the density and phase of the ring p . We perform a continuous limit of the Bose-Hubbard Hamiltonian and consider the bosonic field operator as

$$\frac{a^\dagger}{\sqrt{a}} = \psi_p^\dagger(x) = [\rho_{0,p} + \Pi_p(x)]^{1/2} \sum_{m \in \mathbf{Z}} e^{2im(\theta_p(x) - \pi \rho_{0,p} x)} e^{-i\phi_p(x)} \quad (5.11)$$

where a stand for the distance between two sites. Without the term of coupling between the rings, the Hamiltonian reads

$$H = \sum_p \int dx \left[J \rho_{0,p} (\partial_x \phi_p(x))^2 + \frac{U}{2\pi^2} (\partial_x \theta_p(x))^2 \right] \quad (5.12)$$

Defining $v_N = \frac{U}{\hbar\pi}$, $v_{J,p} = \frac{2\pi J}{\hbar} \rho_{0,p}$, $v_p = \sqrt{v_N v_{J,p}}$ and $\tilde{K}_p = \sqrt{v_{J,p}/v_N}$ we end up with

$$H = \sum_p \frac{\hbar}{2\pi} \int dx \left[v_p \tilde{K}_p (\partial_x \phi_p(x))^2 + \frac{v_p}{\tilde{K}_p} (\partial_x \theta_p(x))^2 \right] \quad (5.13)$$

The coupling term between the two rings in the lowest mode approximation can be written as a tunnel term in the following way:

$$H_T = -2K \sqrt{\rho_{0,1}} \sqrt{\rho_{0,2}} \int dx \cos(\phi_1(x) - \phi_2(x)) \quad (5.14)$$

We now turn to the representation in terms of spin (s) and charge (c) fields i.e

$$\phi_s = \phi_1 - \phi_2 \quad (5.15)$$

$$\phi_c = \frac{\phi_1 + \phi_2}{2}. \quad (5.16)$$

The density fluctuation field transforms in the following way in order to ensure the good commutation relation in both charge and spin sector

$$[\partial_{x'} \theta_s(x'), \phi_s(x)] = 2ia\delta(x-x') \quad (5.17)$$

$$[\partial_{x'} \theta_c(x'), \phi_c(x)] = ib\delta(x-x') \quad (5.18)$$

so that $\theta_s = a(\theta_1 - \theta_2) = \frac{\theta_1 - \theta_2}{2}$ and $\theta_c = b(\theta_1 + \theta_2) = \theta_1 + \theta_2$. We next add the flux in the same gauge as Chap. 2 and express the flux threading each ring Φ_1 and Φ_2 in terms of ϕ and Φ .

5.2. Luttinger liquid description of the double ring

Assuming that $\rho_{0,1} = \rho_{0,2}$, $v_1 = v_2 = v$, $\tilde{K}_1 = \tilde{K}_2 = \tilde{K}$ We see that the Hamiltonian transform in

$$H = \frac{\hbar}{2\pi} \int dxv \left[K_s \left(\partial_x \phi_s + \frac{2\pi}{L} \frac{\phi}{\Phi_0} \right)^2 + \frac{1}{K_s} (\partial_x \theta_s)^2 \right] + \frac{\hbar}{2\pi} \int dxv \left[K_c \left(\partial_x \phi_c + \frac{2\pi}{L} \frac{\Phi}{\Phi_0} \right)^2 + \frac{1}{K_c} (\partial_x \theta_c)^2 \right] - 2K\rho_0 \int dx \cos(\phi_s) \quad (5.19)$$

where we set $K_s = \frac{\tilde{K}}{2}$, $K_c = 2\tilde{K}$ and with Φ_0 being the quantum of flux already introduced in Chap. 2. We see that the mean flux couple to the charge sector of the phase field and the relative flux to the spin sector of the phase field. Moreover the hopping term of the Hamiltonian brings a cosine of the spin phase field so that it will induce a pinning of the phase under renormalization group as will be explained in the next section.

5.2.2 Meissner-Vortex transition

The quantum sine-Gordon Hamiltonian is an integrable model and exact solution are known [122, 123] in analogy with the massive Thirring model. In the classical picture the solutions are solitons, kinks and breathers and those topological object are still considered as solution of the quantum problem. A difficulty arise when one is faced with a flux that shifts the phase field, no solution are known, the problem is no longer integrable and the renormalization group equations are divergent [120]. This problem has been deeply studied in the context of the Mott transition in 1D [124] as the backscattering term of fermion evolving in a shallow lattice gives rise to a cosine term shifted by a term related to the deviation to the commensurate filling of the lattice (i.e when the number of particle per sites is an integer). Let's consider in the following the spin part of the Hamiltonian of the double ring under fluxes

$$H_s = \int \frac{dx}{2\pi} \left[u_s K_s \left(\partial_x \phi_s(x) + \frac{2\pi}{L} \frac{\phi}{\Phi_0} \right)^2 + \frac{u_s}{K_s} (\partial_x \theta_s(x))^2 \right] - 2K\rho_0 \int dx \cos(\phi_s) \quad (5.20)$$

For $\phi = 0$ the renormalization flow equation of Sec. 5.1.2 tell us that the spectrum is gapped for $K_s > 1/8$ and the phase field is pinned in the ground state to the maxima of the cosine term so that $\langle \phi_s(x) \rangle = 0$ modulo 2π . This phase is known as the commensurate phase in analogy with the Mott-insulator phase and corresponds to the Meissner phase.

As shown in [125], expanding $\left(\partial_x \phi_s(x) + \frac{2\pi}{L} \frac{\phi}{\Phi_0} \right)^2$ we see that up to a constant the term depending on the flux adds

$$\frac{u_s K_s \phi}{\Phi_0} \int \frac{dx}{L} \partial_x \phi_s \quad (5.21)$$

In a semi-classical picture, we can interpret this term as a chemical potential for the soliton antisoliton forming the vortex pattern. Indeed calling \tilde{N}_s the number of solitons and $\tilde{N}_{\bar{s}}$ the number of antisolitons of the sine-Gordon model, we have:

$$\tilde{N}_s - \tilde{N}_{\bar{s}} = \int \frac{dx}{L} \partial_x \phi_s, \quad (5.22)$$

5.2. Luttinger liquid description of the double ring

so that the flux-dependent term becomes

$$\frac{u_s K_s \phi}{\Phi_0} (\tilde{N}_s - \tilde{N}_{\bar{s}}). \quad (5.23)$$

This term acts as a chemical potential for the solitons and anti-solitons in the system. As the flux grows, it will become energetically advantageous to populate the ground state with solitons giving rise to incommensurate phase known as the vortex phase. In order to understand the Meissner to vortex transition we will fermionize the spin part of our Hamiltonian by making use of the Luther-Emery solution as already performed in [12, 115]. This way of solving the problem is very elegant, understandable and will be useful as a root to go beyond.

One special point of the sine-Gordon model is the Luther-Emery point [126], for $K_s = 1/4$. At this point, the sine-Gordon model can be fermionized and corresponds to a free gapful fermionic system. On the point of view of the renormalization group equation this point corresponds to a critical point where the operators K_s is said to be marginally irrelevant. Indeed the sine-Gordon Hamiltonian with rescaled fields $\tilde{\phi}_s = \phi_s/2$ and $\tilde{\theta}_s = 2\theta_s$ can be cast as follows

$$H_s = \int \frac{dx}{2\pi} v [(\partial_x \tilde{\theta})^2 + (\partial_x \tilde{\phi}_s)^2] - 2K \cos(2\tilde{\phi}_s). \quad (5.24)$$

Relating the bosons to the fermions with free fermionic field $\tilde{\psi}_\sigma = e^{i(\tilde{\theta} - \sigma\tilde{\phi})}$, where $\sigma = \pm$ depending if the fermions are right or left movers, we obtain the free fermionic Hamiltonian

$$H = \int dx \left[-iv \sum_\sigma \sigma \tilde{\psi}_\sigma^\dagger \partial_x \tilde{\psi}_\sigma - m \sum_\sigma \tilde{\psi}_\sigma \tilde{\psi}_{-\sigma} + h \sum_\sigma \tilde{\psi}_\sigma^\dagger \tilde{\psi}_\sigma \right] \quad (5.25)$$

with $h = \frac{4\pi}{L} v \frac{\phi}{\Phi_0}$ and $m = 2\pi K \rho_0$. We made use of the following equations that relate bosonic fields to fermionic field

$$\sum_\sigma \tilde{\psi}_\sigma^\dagger \tilde{\psi}_\sigma = \frac{\partial \tilde{\phi}_s}{2\pi} \quad (5.26)$$

$$-i \sum_\sigma \sigma \tilde{\psi}_\sigma^\dagger \partial_x \tilde{\psi}_\sigma = \frac{1}{2\pi} [(\partial_x \tilde{\phi}_s)^2 + (\partial_x \tilde{\theta}_s)^2] \quad (5.27)$$

$$\sum_\sigma \tilde{\psi}_\sigma^\dagger \tilde{\psi}_{-\sigma} = \frac{\cos(2\tilde{\phi}_s)}{\pi} \quad (5.28)$$

As the last equation is easy to derive, the first two are tricky and we advise the reader the following review [127]. We see that the flux dependent term h acts as a chemical potential and m as a gap term for the theory and correspond to a backscattering term in the fermionic language. This fermionic Hamiltonian can be diagonalized in k -space using the following two dimensional rotation of the fermionic field operators

$$\begin{pmatrix} \tilde{\psi}_+ \\ \tilde{\psi}_- \end{pmatrix} = \frac{1}{\sqrt{L}} \sum_k e^{ikx} \begin{pmatrix} \cos(\eta_k) & -\sin(\eta_k) \\ \sin(\eta_k) & \cos(\eta_k) \end{pmatrix} \begin{pmatrix} c_{k,U} \\ c_{k,D} \end{pmatrix} \quad (5.29)$$

5.2. Luttinger liquid description of the double ring

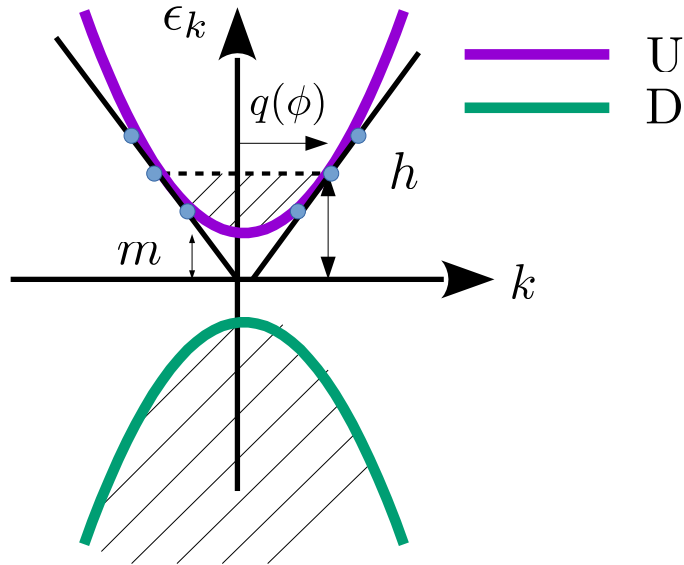


Figure 5.2: Representation of the gapful spectrum of the spin-less fermion with h chemical potential and m the gap of the excitation spectrum. Black lines represent the linearization for k values around $\bar{q}(\phi)$ with renormalized slope $v^*(\phi)$.

with $e^{2i\eta_k} = \frac{vk+im}{\sqrt{(vk)^2+m^2}}$. This leads to the following diagonal Hamiltonian

$$H_s = \sum_{k,\sigma=U/D} \epsilon_{k,\sigma} c_{k,\sigma}^\dagger c_{k,\sigma} \quad (5.30)$$

with a gapful spectrum $\epsilon_{k,U/D} = \pm \sqrt{(vk)^2 + m^2} - h$. The Meissner to vortex transition is then interpreted as follow, when $|h| < |m|$ we are in the Meissner and when $|h| > |m|$ we enter the vortex phase or in the language of Mott insulator transition the incommensurate phase. It is then possible from the above representation (see Fig. 5.2) to go back to the bosonic representation by linearizing the following theory around the Fermi points $\bar{q}(\phi) = \frac{1}{v} \sqrt{(\frac{\phi}{\Phi_0})^2 - (\frac{\phi_c}{\Phi_0})^2}$ where ϕ_c is related to the gap but take a more general sense as away from the Luther-Emery line the gap is renormalized but the spectrum keep its form [120]. The Fermi velocity is $v_s^* = \frac{v}{\hbar^2} \sqrt{(\frac{\phi}{\Phi_0})^2 - (\frac{\phi_c}{\Phi_0})^2}$ and the renormalized Luttinger Hamiltonian

$$H_s^* = \int \frac{dx}{2\pi} \left[v_s^*(\phi) K^*(\phi) (\partial_x \tilde{\phi}_s)^2 + \frac{v_s^*(\phi)}{K_s^*(\phi)} (\partial_x \theta_x)^2 \right] \quad (5.31)$$

where $\tilde{\phi}_s = \phi_s - \bar{q}(\phi)x$

5.2. Luttinger liquid description of the double ring

5.2.3 Mode expansion

It is possible to diagonalize the Luttinger Hamiltonian (5.19) by applying the mode expansion of the quantum fields [118, 119] in the spin and charge basis where $b_{q,s} = (b_{q,1} - b_{q,2})/\sqrt{2}$ and $b_{q,c} = (b_{q,1} + b_{q,2})/\sqrt{2}$ such that $[b_{q,v}^\dagger, b_{q',v'}] = \delta_{q,q'}\delta_{v,v'}$

$$\begin{aligned}\theta_{s,c}(x) &= \theta_{s,c}^{(0)} + \frac{\pi x}{L}\delta N_{s,c} + \frac{1}{2}\sum_{q\neq 0}\left|\frac{2\pi K_{s,c}}{qL}\right|^{1/2}\left[e^{iqx}b_{q,(s,c)} + e^{-iqx}b_{q,(s,c)}^\dagger\right] \\ \phi_s(x) &= \phi_s^{(0)} + \frac{\pi x}{L}J_s + \frac{1}{2}\sum_{q\neq 0}\left|\frac{2\pi}{K_s qL}\right|^{1/2}\text{sign}(q)\left[e^{iqx}b_{q,s} + e^{-iqx}b_{q,s}^\dagger\right] \\ \phi_c(x) &= \phi_c^{(0)} + \frac{\pi x}{L}J_c + \frac{1}{2}\sum_{q\neq 0}\left|\frac{2\pi}{K_c qL}\right|^{1/2}\text{sign}(q)\left[e^{iqx}b_{q,c} + e^{-iqx}b_{q,c}^\dagger\right]\end{aligned}\quad (5.32)$$

with $\delta N_c = (\hat{N}_1 + \hat{N}_2 - (N_1 + N_2))/2$, $\delta N_s = (\hat{N}_1 - \hat{N}_2 - (N_1 - N_2))$, $J_c = (J_1 + J_2)/2$ and $J_s = J_1 - J_2$ and are Haldane's topological excitations [119], $q = 2\pi j/L$ and $j \in \mathbb{Z}$, with N_1 and N_2 the particle number in ground state, taken equal in our case. The pairs $(\theta_p^{(0)}, J_p)$ and $(\phi_p^{(0)}, N_p)$ are conjugate action-angle variables with $[N_p, \phi_p^{(0)}] = [J_p, \theta_p^{(0)}] = i$ where the eigenvalues of J_s are even numbers $2m_s \in \mathbb{Z}$ i.e respecting the selection rule for bosons $(-1)^{J_s} = 1$, and N the particle number operator. Inserting the mode expansion (5.32) into (5.19) we get the following Hamiltonian

$$H = H_0 + H_Q + H_T \quad (5.33)$$

where H_Q is the free Hamiltonian in the bosonic excitation operators $b_{q,s/c}$, the zero mode Hamiltonian is given by

$$H_0 = \frac{\hbar v \pi}{\tilde{K}L}\left(\delta N_s^2 + \frac{\delta N_c^2}{4}\right) + \hbar v\left[\frac{2K_s\pi}{L}\left(J_s + \frac{\Phi}{\Phi_0}\right)^2 + \frac{2K_c\pi}{L}\left(J_c + \frac{\Phi}{\Phi_0}\right)^2\right] \quad (5.34)$$

and the tunneling part reads

$$H_T = -2K\rho_0\int dx \cos(\phi_s^{(0)} + \frac{\pi x}{L}J_s + \delta\phi_s(x)) \quad (5.35)$$

The tunneling Hamiltonian H_T is not easy to handle since it couples zero and non zero modes $\delta\phi_s(x) = \frac{1}{2}\sum_{q\neq 0}\left|\frac{2\pi}{K_s qL}\right|^{1/2}\text{sign}(q)\left[e^{iqx}b_{q,s} + e^{-iqx}b_{q,s}^\dagger\right]$. We'll treat with this by averaging over the non-zero modes with the average taken with respect to the quadratic Hamiltonian H_Q

$$H_q = \sum_{v,q\neq 0}\hbar v^v|q|b_{q,v}^\dagger b_{q,v} \quad (5.36)$$

Using Wick's theorem for quadratic Hamiltonian $\langle e^{\alpha x} \rangle = e^{\langle x^2 \rangle / 2\alpha^2}$ and the zero-temperature relations $\langle \beta_q^\dagger \beta_{q'} \rangle = 0$, $\langle \beta_q \beta_{q'}^\dagger \rangle = \delta_{q,q'}$ we evaluate the effective tunneling Hamiltonian as

$$\langle \langle H_T \rangle_{H_q} \rangle_{J_s} = -K^* \rho \int_0^L dx \left(\sum_{N_s} e^{ix\pi 2m_s/L} |N_s - 1\rangle \langle N_s| + e^{-ix\pi 2m_s/L} |N_s\rangle \langle N_s + 1| \right) \quad (5.37)$$

5.2. Luttinger liquid description of the double ring

with the renormalized tunneling due to non zero modes $K^* = K \left(\frac{d}{L}\right)^{\frac{1}{2K_s}}$, where d is a small-distance cut-off. We see that as we increase the strength of the interactions between particle (lowering K_s), the coupling between the rings decreases because of the effect of the quantum fluctuations of the phase. As N_s and the zero mode of the phase are action-angle variables i.e they verify the commutation relation $[N_s, e^{-i\phi_s^{(0)}}] = e^{-i\phi_s^{(0)}}$, it implies that the zero mode $\phi_s^{(0)}$ acts as a raising operator for the difference in particle number difference between the two rings, implying a Josephson effect, we then can write $e^{-i\phi_s^{(0)}} |N_s\rangle = |N_s + 1\rangle$. This allows us to introduce the completeness of the basis set $e^{-i\phi_s^{(0)}} = \sum_{N_s} |N_s + 1\rangle \langle N_s|$ leading to Eq. (5.37). We'll now evaluate the matrix structure in the basis of the particle number imbalance. We see that it is a tridiagonal matrix.

$$\sum_{N_s} e^{ix\pi 2m/L} |N_s - 1\rangle \langle N_s| + e^{-ix\pi 2m/L} |N_s\rangle \langle N_s + 1| = 2 \cos(x\pi 2m/L) Q_f \quad (5.38)$$

$$Q_f = \begin{pmatrix} | -N \rangle & \dots & | N \rangle \end{pmatrix} \begin{pmatrix} 0 & 1 & & 0 \\ 1 & \ddots & \ddots & \\ & \ddots & \ddots & 1 \\ 0 & & 1 & 0 \end{pmatrix} \begin{pmatrix} \langle -N | \\ \vdots \\ \langle N | \end{pmatrix} \quad (5.39)$$

Integration over x yields

$$\langle \langle H_T \rangle_{H_q} \rangle_{J_s} = 0 \quad (5.40)$$

The tunneling term, as it is oscillating, gives zero contribution to the Hamiltonian. Averaging the phase excitations within bosonization doesn't allow us to take into account the contribution of the tunneling part. We are only able to capture the physics of the Meissner phase since the phase is then locked in $\langle \phi_s \rangle = 0$. The flux dependence appears in the zero mode contribution of the Hamiltonian H_0 which shows a quadratic behaviour in the spin part of the angular momentum J_s (we recall that $J_s |m_s\rangle = 2m_s |m_s\rangle$) whose eigenvalues are even integers. As the relative flux increases, the spin part of the angular momentum increases in order to minimize the energy of the system (see Fig.5.3) In the case of ring geometry we have a periodic dependence of the energy as a function of the fluxes ϕ and Φ with period Φ_0 . The value of the fluxes fix the angular momentum of the ground state energy giving rise to a sequence of parabolas. This change of angular momentum gives rise to saw-tooth chiral current $I_c = -\partial_\phi \langle H \rangle$, analogue to persistent current of one-dimensional ring [26]. Notice that this change of angular momentum corresponds to a phase slip of the wave function i.e a change of its winding number corresponding to a vortex creation along the circumference of a ring. We remark that this is different from the vortex phase featured in this model as it corresponds rather to the creation of vortices in the bulk of the system i.e in the radial direction.

The decrease of the chiral current while entering the vortex phase as observed in Chap. 2 will be explicitly shown in Sec. 5.2.5.

5.2. Luttinger liquid description of the double ring

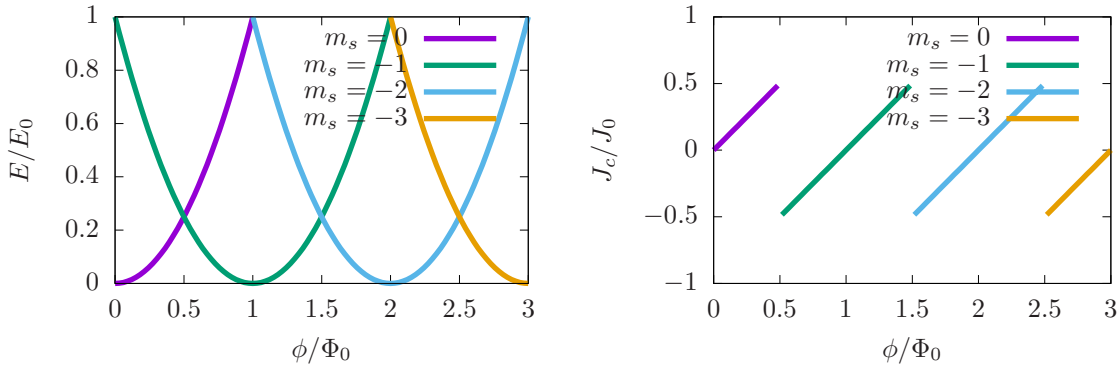


Figure 5.3: Left panel, ground state energy in units of $E_0 = \hbar v \tilde{K} \pi / L$ for different values of the relative angular momentum m_s between the two rings as a function of the applied gauge flux. Right panel, represents the associated chiral currents $I_c = -\partial_\phi E$ in units of $I_0 = 2\hbar v \tilde{K} \pi / L$

5.2.4 Weak link

As explained in Sec. 1.2.1, it is possible to implement a gauge field by rotating a defect. Placing this defect on one of the two ring we can access the spin sector of the Hamiltonian. We'll then consider the following static Hamiltonian.

$$H_b = U_0 \int_0^L dx \delta(x) \rho_1(x) \quad (5.41)$$

and add it to the previous Hamiltonian (5.19). We treat this term perturbatively in the weak barrier case and we keep only the lowest harmonics of the density field,

$$\rho_1(x) = (\rho^{(0)} + \partial_x \theta_s(x) / \pi + \partial_x \theta_c(x) / 2\pi) \sum_{l \in \mathbb{Z}} e^{2il(\theta_s(x) + \theta_c/2) - 2il\pi\rho^{(0)}x} \quad (5.42)$$

which reads,

$$\rho_1(x) \approx \rho^{(0)} (1 + 2 \cos(2\theta_s(x) + \theta_c(x))) + \partial_x (\theta_s(x) + \theta_c(x)/2) / \pi \quad (5.43)$$

We will focus on the spin part of the Hamiltonian as the charge part can be treated analogously. Using the mode expansion of the field and the action-angle properties of the $\theta_{0,s}$ and J_s operators, the impurity part of the Hamiltonian can be expressed as

$$H_b = U_0 \rho^{(0)} \left(1 + \sum_{m_s} |m_s - 1\rangle \langle m_s| e^{i2\delta\theta_s(0)} + |m_s\rangle \langle m_s + 1| e^{-i2\delta\theta_s(0)} \right) + \frac{U_0 \hat{N}_s}{2L}. \quad (5.44)$$

The second term $\frac{U_0 \hat{N}_s}{2L} = \sum_{N_s} \frac{U_0 N_s}{2L} |N_s\rangle \langle N_s|$ shifts the diagonal part of the Hamiltonian H_0 and can be considered as a flux for the relative number of particle. Thus, the diagonal part

5.2. Luttinger liquid description of the double ring

of Hamiltonian becomes

$$H_0 = \sum_{N_s} \left[E_c \left(N_s + \frac{U_0}{4E_c L} \right)^2 - \frac{U_0^2}{16L^2} \right] |N_s\rangle \langle N_s|, \quad (5.45)$$

with $E_c = \frac{\pi \hbar v_s}{\tilde{K}L}$, and $\langle \hat{N}_s \rangle$ is shifted from 0 to the value of $-\frac{U_0}{4E_c L}$ creating imbalance of the density fluctuation in the system. The first term in (5.44) opens a gap between different energy levels labelled by the angular momentum quantum number m_s . We see from this that the weak link can drive transition from different angular momentum states. We next average over the fluctuations with the same procedure as for the case of the coupling between the rings, thus obtaining $\langle e^{\pm 2i\delta\theta_s(0)} \rangle = (d/L)^{\tilde{K}/2}$. Finally, the Hamiltonian H_J for the angular momentum part reads:

$$H_J = \hbar v \tilde{K} \left[\frac{\pi}{L} \left(J_s + \frac{\phi}{\Phi_0} \right)^2 + \frac{4\pi}{L} \left(J_c + \frac{\Phi}{\Phi_0} \right)^2 \right] + \rho^{(0)} U_{\text{eff},c} \sum_{J_c} [|J_c - 1\rangle \langle J_c| + \text{h.c.}] \\ + \rho^{(0)} U_{\text{eff},s} \sum_{J_s} [|J_s - 1\rangle \langle J_s| + \text{h.c.}] \quad (5.46)$$

where $U_{\text{eff},c} = U_0 (d/L)^{K_c}$ and $U_{\text{eff},s} = U_0 (d/L)^{K_s}$. The presence of the barrier breaks rotational invariance along the ring and gives rise to coupling among angular momentum states. This leads to a smoothing of the perfect saw-tooth behaviour of the chiral current of Fig. 5.3.

5.2.5 Current and correlations functions in the vortex phase

In this section we calculate some observables at the Luther-Emery point, using the renormalized Luttinger-Liquid Hamiltonian of the spin sector (5.31) The chiral current is given within bosonization

$$j_c(x, \phi) = \frac{u_s K_s}{2\pi} \left(\partial_x \phi_s + \frac{2\pi}{L} \frac{\phi}{\Phi_0} \right). \quad (5.47)$$

The spatially averaged chiral current is then given in this point by

$$I_c = \frac{1}{L} \int dx \langle j_c(x, \phi) \rangle = \frac{u_s^* K_s^* \pi}{2\pi} \left(\frac{\phi}{\Phi_0} - \frac{2\pi}{L} E \left[\frac{L}{2\pi\Phi_0} \sqrt{\phi^2 - \phi_c^2} \right] \right) \quad (5.48)$$

where $E[x]$ is the integer part of x . This function is a step function, discontinuous for each multiple of $2\pi/L$ and explains the discrete jumps in the chiral current in the finite ring shown in Fig. 5.4. Within the fermionized language, each jump is associated to the creation of solitons in the field ϕ_s .

At the Luther-Emery point it is also possible to calculate the momentum distribution. The large-distance behaviour of the one-body density matrix in the vortex phase on a finite ring with periodic boundary conditions reads within conformal-field approach (see Appendix of [118])

$$\langle \Psi_p^\dagger(x) \Psi_p(x') \rangle = \rho_0 \frac{e^{i(-1)^{2p+1} \bar{q}(\phi)(x-x')}}{\left[\frac{L}{\pi} \sin \left(\frac{\pi |x-x'|}{L} \right) \right]^{1/(2K_c)+1/(4K_s^*)}} e^{-(-1)^{2p+1} i \frac{\pi}{L} m_s(x-x')} e^{i \frac{2\pi}{L} m_c(x-x')} \quad (5.49)$$

5.2. Luttinger liquid description of the double ring

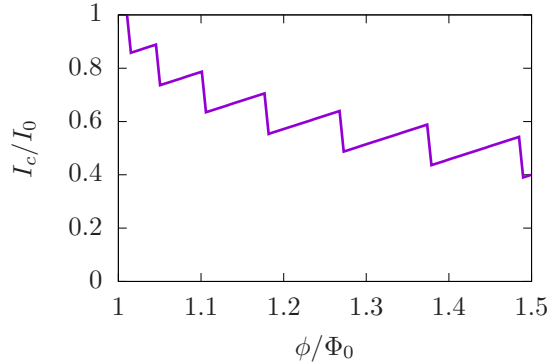


Figure 5.4: Sketch of the step-wise decrease of the chiral current in the vortex phase as a function of the applied flux ϕ/Φ_0 . With for simplicity $\phi_c/\Phi_0 = 1$

where the quantum numbers m_s and m_c represent the angular momentum along the ring (corresponding to the Meissner currents) and are found within conformal field theory approach, $p = 1, 2$ labels the rings and $\bar{q}(\phi)$ is given by fermionized approach and reads $\bar{q}(\phi) \propto \sqrt{\left(\frac{\phi}{\Phi_0}\right)^2 - \left(\frac{\phi_c}{\Phi_0}\right)^2}$. Let us consider the case where we have no charge flux, i.e $\Phi = 0$. In this situation the momentum distribution is given by:

$$n_p(n) = \frac{1}{L} \int_0^L dx \langle \Psi_p^\dagger(x) \Psi_p(x') \rangle e^{i\frac{2\pi}{L} n(x-x')} \quad (5.50)$$

where we used the following convention for the Fourier transform $u(x) = \sum_{n=-\infty}^{\infty} u(n) e^{i\frac{2\pi n}{L} x}$. The small k momentum distribution can be calculated analytically and give the following for $1/K_t \equiv 1/(4K_c) + 1/(4K_s^*) < 1$

$$n_p(k) = \frac{1}{\pi} \left(\frac{2\pi}{L} \right)^{1/K_t} \frac{\Gamma(1 - 1/K_t) \Gamma(1/2K_t + k) \sin(\pi/2K_t)}{\Gamma(1 - 1/2K_t + k)} \quad (5.51)$$

where one should replace $k \rightarrow k \pm (m_s - \frac{2\pi}{L} E[\frac{L}{2\pi} \bar{q}(\phi)])$ for $n_{1/2}$ respectively. This function is peaked whenever $k \pm (m_s - E[\frac{L}{2\pi} \bar{q}(\phi)]) = 0$. We notice that the gradient term of the Hamiltonian imposes the eigenvalue of the kinetic momentum J_s , m_s to change of an integer each time the flux increase by 2π . Then the $m_s(\phi)$ is a step function increasing by unity every integer value of ϕ/Φ_0 .

Current profile in the Meissner phase

As we saw in Sec. 5.2.2 for $K_s > 1/8$ the cosine term is relevant and fixe the phase $\langle \phi_s \rangle = 0 [2\pi]$, we are in the so called Meissner phase. Below the transition at critical flux ϕ_c the relevant form of the Hamiltonian is the following:

$$H_s = \int \frac{dx}{2\pi} \left[vK_s \left(\partial_x \phi_s + \frac{2\pi}{L} \frac{\phi}{\Phi_0} \right)^2 + \frac{v}{K_s} (\partial_x \theta_s)^2 \right] - 2K\rho_0 \int dx \cos(\phi_s) \quad (5.52)$$

5.2. Luttinger liquid description of the double ring

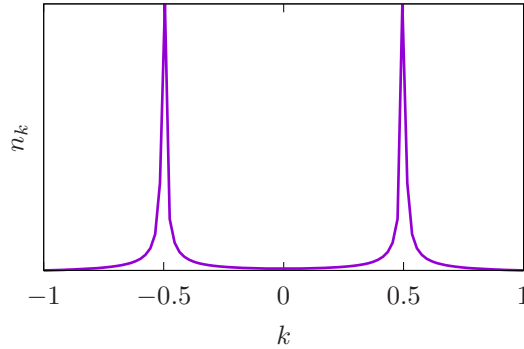


Figure 5.5: Total momentum distribution of the double ring $n_k = n_{1,k} + n_{2,k}$, as a function of the wavevector k in units of $2\pi/L$ for $1/(2K_c) + 1/(4K_c^*) = 1/2$, $m_s = m_c = 0$ and $\bar{q}(\phi) = 0.5$.

The bosonization form of the transverse current is the following

$$J_{\perp}(x) = 2K\rho_0 \sin(\phi_s) \quad (5.53)$$

whose expectation value vanishes, i.e. $\langle J_{\perp} \rangle = 0$ due to fixing of the phase field in the Meissner phase. Using the mode expansion we recover the saw-tooth behavior of the spatial averaged of chiral current predicted in Sec.5.2.3. It displays a non-zero expectation value growing linearly with applied flux

$$\langle I_c(\phi) \rangle = \frac{\pi v_s K_s}{L} \left(m_s + \frac{\phi}{\Phi_0} \right) \quad (5.54)$$

where we have used that $\langle J_s \rangle = 2m_s$ is the expectation value of the angular momentum zero mode, with $m_s \in \mathbb{Z}$.

Dynamical structure factor

We provide here a derivation of the dynamical structure factor for the ladder. The dynamical structure factor is the Fourier transform both in space and time of the density-density correlation function.

Single-component 1D Bose gas

We recall first the derivation of the dynamical structure factor for an infinite one-component Bose gas in one dimension. We evaluate the Fourier transform of the first leading term of the expansion (5.8), i.e. we take $\rho(x) \approx \frac{\partial_x \theta}{\pi}$. This term is related to the phononic modes and reads

$$S_0(q, \omega) = F.T. [\langle \rho(x, t) \rho(0, 0) \rangle]_0 = -\frac{K_L}{2\pi^2} \int_{\mathbb{R}} dx \int_{\mathbb{R}} dt e^{i(\omega t - qx)} \frac{1}{(x - vt + i\epsilon)^2}. \quad (5.55)$$

5.2. Luttinger liquid description of the double ring

By making the following change of coordinates, $u = x - vt$, the integral reads

$$S_0(q, \omega) = -\frac{K_L}{\pi} \int_{\mathbb{R}} du \frac{e^{-iqu}}{(u + i\epsilon)^2} = iq \frac{K_L}{\pi} \int_{\mathbb{R}} du \frac{e^{-iqu}}{u + i\epsilon} \quad (5.56)$$

Using the residue theorem, where the sign of the contour depend on the sign of q , we obtain

$$S_0(q, \omega) = K_L |q| \delta(\omega - |q|v_s) \quad (5.57)$$

The second term of the expansion corresponding to $m = 1$ is given by (for a full derivation see Guillaume Lang, PhD Thesis [128])

$$S_1(q, \omega) = \frac{a_1}{(2\pi\rho_0 v)^{2(K_L-1)} \Gamma(K_L)^2} \frac{1}{v} [\omega^2 - (q - 2\pi\rho_0)^2 v^2]^{K_L-1} \text{sign}(\omega - |q - 2\pi\rho_0|v) \quad (5.58)$$

This contribution corresponds to a broad continuum within two linear branches symmetric around the umklapp point ($k = 2\pi\rho_0 = 2k_F, \omega = 0$) with slope v .

Finite-size periodic system - one component

First contribution The first contribution of the dynamical structure factor $S_1(q, \omega)$ on a finite ring is related to the following integral

$$I_{\pm} = \int_{\mathbb{R}} dt e^{i\omega t} \int_0^L dx e^{-i\frac{2\pi}{L}qx} \frac{1}{|\sin(\frac{\pi}{L}(x \pm vt))|^2} \quad (5.59)$$

$$= \frac{L}{2\pi} \int_{\mathbb{R}} dt e^{-i(\frac{2\pi}{L}vq - \omega)t} \int_{-vt}^{2\pi-vt} du e^{-iuq} \frac{1}{|\sin(u/2)|^2} \quad (5.60)$$

by making the change of variable $u = \frac{2\pi}{L}(x - v_s t)$. The integral over u can be cast on a integral over closed contour \mathcal{C} corresponding to a circle unity centered around 0, by making the change $z = e^{iu}$ so that for $q > 0$

$$I_{\mathcal{C}} = 4i \oint_{\mathcal{C}} dz \frac{1}{z^q} \frac{1}{(z^2 - 2z + 1)} \quad (5.61)$$

with $dz = izdu$. Knowing the integral representation of Gegenbauer polynomials where \mathcal{C}' is a simple contour encircling $z = 0$ and avoiding $z = 1$

$$C_n^\lambda(x) = \frac{1}{2\pi i} \oint_{\mathcal{C}'} \frac{1}{z^n} \frac{1}{(z^2 - 2xz + 1)^\lambda} \quad (5.62)$$

we see that $I_{\mathcal{C}} = 8\pi C_{q-1}^1(1)$, so that $I_- = 16\pi^2 \delta(\omega - \frac{2\pi}{L}q v_s) C_{q-1}^1(1)$ for $q > 0$. This polynomial is behaving linearly with respect to q so we recover the behaviour of the infinite system for $L \rightarrow \infty$.

5.2. Luttinger liquid description of the double ring

Two components Near the incommensurate-commensurate transition, at the Luther-Emery point (See Sec. 5.2.2), we can use the renormalized Luttinger Hamiltonian (5.31) to evaluate the correlation function of the spin part. We next calculate the dynamical structure factor for a two-leg ladder. If one wants to compute $FT[\langle \rho_p(x) \rho_p(0) \rangle]$, with p the indice of the rung, one will deal with product of charge and spin. Let's take a close look at density-density correlation function on wire 1. It reads as follows

$$\langle \rho_1(x, t) \rho_1(x', t') \rangle = \left\langle (\rho_0 + \partial_x \theta_1(x, t)) (\rho_0 + \partial_{x'} \theta_1(x', t')) \sum_{m, m' = -\infty}^{+\infty} e^{2im[\theta_1(x, t) + \pi \rho_0 x]} e^{2i'm[\theta_1(x', t') + \pi \rho_0 x']} \right\rangle \quad (5.63)$$

Decomposing it in charge (c) and spin (s) sectors with respect to the renormalized Hamil-

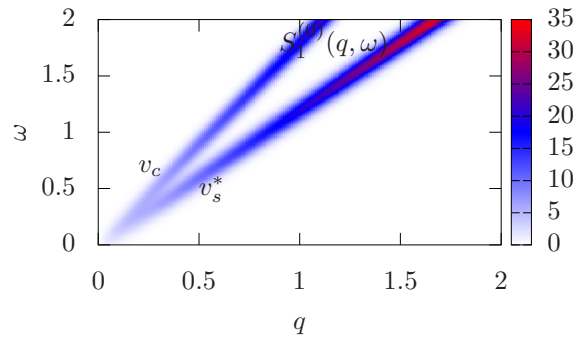


Figure 5.6: First contribution of the dynamical structure factor for $v_s^* = v_c =$.

tonian (5.31) one gets

$$\langle \rho_1(x, t) \rho_1(x', t') \rangle = \rho_0^2 \left[1 - \frac{K_s^*}{4\pi^2 \rho_0^2} \left[\frac{1}{(x-v_s^* t)^2} + \frac{1}{(x+v_s^* t)^2} \right] \right] + \frac{\rho_0^2}{4} \left[1 - \frac{K_c}{4\pi^2 \rho_0^2} \left[\frac{1}{(x-v_c t)^2} + \frac{1}{(x+v_c t)^2} \right] \right] + \frac{\rho_0^4}{4} \sum_{m=1}^{\infty} a_m^c a_m^s \frac{\cos(2\pi m \rho_0 x)}{[(x-v_s^* t)(x+v_s^* t)]^{K_s^* m^2}} \frac{1}{(\pi \rho_0)^{2K_s^* m^2}} \times \frac{\cos(2\pi m \rho_0 x)}{[(x-v_c t)(x+v_c t)]^{K_c m^2}} \frac{1}{(\pi \rho_0)^{2K_c m^2}} \quad (5.64)$$

The Fourier transform of the first term is easily computable and gives the sound waves contribution to the dynamical structure factor for $q > 0$,

$$S_1^{(0)}(q, \omega) = K_s^* |q| \delta(\omega - |q| v_s^*) + \frac{K_c}{4} |q| \delta(\omega - |q| v_c) \quad (5.65)$$

where $v_c = v$ is the sound speed in the "charge" branch (in-phase motion) and v_s^* is the sound speed of the spin branch (out-of-phase motion of the two-components). It is interesting to notice that we find the same features observed in the weakly interacting regime for the vortex phase, where two Goldstone modes were obtained (See Chap. 3) The calculation of the next order term $m = 1$ is non trivial and will be the object of future work.

Conclusions of the chapter

In this chapter we have used the Luttinger liquid method applied to the double ring Hamiltonian, assuming weak tunnel coupling between the rings. We have used the mode expansion to study the Meissner phase and the influence of a defect on the low-energy properties of the gas. The average over the phase fluctuations cancels the cosine term of the Hamiltonian, which was also shown to be fixing the phase fluctuation field in the Meissner phase. We have then seen that the bosonized version of the double ring features the Meissner to vortex transition and this transition is driven by the tunnel term in the Hamiltonian. In order to describe features of the vortex phase, we have worked at the Luther-Emery point, where a fermionization approach allows to compute a renormalized form of the Luttinger Hamiltonian. This has allowed us to calculate some relevant observables such as the chiral current, in which we saw the same behavior as in the non-interacting case, the momentum distribution, which exhibits two peaks related to the finite momentum of the dispersion relation in the vortex phase and lowest order term of the dynamical structure factor that displays a separation in spin and charge modes in direct correspondence with the results of Chapter 3. In outlook, our calculations for the dynamical structure factor could be extended to the study of the umklapp term for the two-leg ladder, as well as of the dispersion of the excitations at small frequency around wavevector $k = \bar{q}(\phi)$, corresponding to the typical density modulation in the vortex phase.

5.2. Luttinger liquid description of the double ring



Part II

Polaritons in honeycomb lattice

Chapter 6

Exciton-Polaritons and the honeycomb lattice

 BOSE-Einstein condensation is understood in thermal equilibrium as a macroscopic occupation of the ground state. Several theoretical works have been dedicated to the study of condensation away from the ground-state using resonant excitation of a ground state of cold atoms [129]. This approach should allow the study of processes of dynamical energy relaxation into the ground state. Thermal equilibrium is not perfectly achieved in condensing bosons since three-body losses give them a finite lifetime. The theoretical description of energy relaxation in non-equilibrium systems, with multiple states, is then an important issue. In solid-state systems such as exciton-polaritons in semiconductor microcavities the life time of particle is very short allowing the study of highly non-equilibrium bosonic gases[130].

Exciton-polaritons in semiconductor microcavities constitute an amazing playground to study quantum fluids of light where remarkable effects, analogous to those observed in cold atoms experiments, arise. Among those effects, superfluidity [131], topological excitations as solitons [132, 133] and quantized vortices [134, 135, 136] have been observed. The subject of superfluidity is still controversial: even though the experimental observation in exciton-polariton semiconductor microcavity has been reported [131], recent theoretical studies [137] claim the opposite, i.e that superfluid response - the difference between longitudinal and transverse current-current response - is zero. It appears that the observation of superfluidity highly depends on the criterion chosen to reveal it and there are as many superfluidities as criteria to define it. Even though this quantum fluid of light is assumed to be composed, almost [138], upon pure condensate, the non-equilibrium nature of the gas make the comparison with typical condensates in cold atom experiment rather non trivial.

This chapter is organized as follows: in Sec. 6.1 some aspects of exciton-polariton physics, then we will derive and review some general features of bosons in honeycomb lat-

tice in Sec.6.2 including retarded Green's functions, Brillouin-zone selection mechanism and a new contribution relating the geometry of the lattice and the decay of polariton into free photons. This decay mode will be shown to be suppressed as a consequence of the symmetry of the lattice.

6.1 Exciton-polaritons

Exciton result from Coulomb interactions between excited electrons and holes in a semiconductor. They require an almost filled valence band, with a small number of unoccupied states to give valence band holes, and a partly occupied conduction band. Classically, an exciton corresponds to polarization field in the material [139]. The lifetime of an excitonic state depends on the rate of transfer back to the valence band of conduction electron with emission of a photon and the on spatial overlap of the hole and electron wave function. Experimentally, it is then convenient to consider excitonic systems in quantum wells (QW), where the electrons and holes are spatially separated and choose materials with intrinsically lower dipole matrix elements to reduce optical recombination.

Microcavity exciton polaritons are the result of strong coupling between photons confined in semiconductor microcavities, and excitons in QWs. A polariton can then be seen as a photon dressed by a matter-field exciton.

The creation of a stable luminous fluid it is crucial to give a mass to the photon. This can be done by confining the photonic field inside a cavity so that the effective mass arise from momentum quantization due to spatial confinement. In a planar geometry with a dielectric medium of refractive index n_0 and thickness l_z enclosed within a pair of metallic mirrors, the photon motion along the perpendicular z direction is quantized as $q_z = \pi n/l_z$, with $n \in \mathbb{N}$. For each longitudinal mode, the frequency dispersion as a function of the in-plane wave vector \mathbf{k} has the form

$$\omega_{\text{cav},\mathbf{k}} = \frac{c}{n_0} \sqrt{q_z^2 + |\mathbf{k}|^2} \approx \omega_{\text{cav}}^0 + \frac{\hbar |\mathbf{k}|^2}{2m_{\text{eff}}} \quad (6.1)$$

where the effective mass m_{eff} and the cut-off frequency are related by

$$m_{\text{eff}} = \frac{\hbar n_0 q_z}{c} = \frac{\hbar \omega_{\text{cav}}^0}{c^2/n_0^2} \quad (6.2)$$

At the simplest level, the strong coupling between excitons and polaritons can be understood in terms of a model of non-interacting bosonic field of cavity photon and exciton, where $a_{\text{p},\mathbf{k}}^\dagger$ creates a cavity photon in in-plane momentum state \mathbf{k} and $a_{\text{e},\mathbf{k}}^\dagger$ creates an exciton in in-plane momentum state \mathbf{k}

$$\hat{\mathcal{H}} = \sum_{\mathbf{k}} \begin{pmatrix} a_{\text{p},\mathbf{k}}^\dagger & a_{\text{e},\mathbf{k}}^\dagger \end{pmatrix} \begin{pmatrix} \omega_{\text{cav},\mathbf{k}} & \Omega_R/2 \\ \Omega_R/2 & \epsilon_{\text{exc},\mathbf{k}} \end{pmatrix} \begin{pmatrix} a_{\text{p},\mathbf{k}} \\ a_{\text{e},\mathbf{k}} \end{pmatrix}, \quad (6.3)$$

where Ω_R is the light matter coupling strength. In the absence of disorder, the exciton energy in the QW is $\epsilon_{\text{exc},\mathbf{k}} = \epsilon_0 + |\mathbf{k}|^2/2M$, where M is the total exciton mass, and $\epsilon_0 =$

6.1. Exciton-polaritons

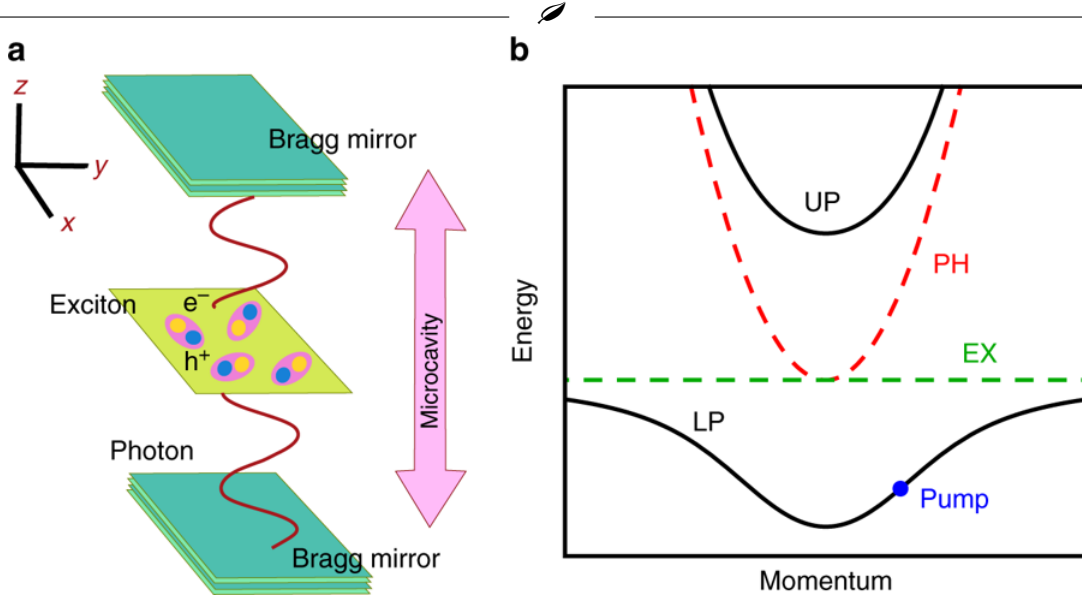


Figure 6.1: Polaritons in semiconductor microcavities. **a** Polaritons are quasi-particles formed when cavity photons, which are massive due to confinement in the z direction between two Bragg mirrors, interact strongly with excitons confined in a quantum well. Polaritons are free to move in the two-dimensional plane perpendicular to their confinement. **b** The excitonic dispersion (dashed green) is approximately constant compared to the photonic (dashed red) due to the much larger exciton mass. Strong coupling leads to anti-crossing and the formation of upper and lower polariton branches (solid black). Polaritons interact because of their excitonic component, while their photonic part causes decay and the need for an external drive. A coherent laser pump resonantly tuned to the polariton dispersion is marked by a blue dot. Figure taken from [137].

$E_{\text{gap}} - Ry_{\text{exc}}$ comes from the conduction-valence band gap E_{gap} including QW confinement and the exciton binding energy (Rydberg) Ry_{exc} . The above Hamiltonian (6.3) can be diagonalized and the corresponding quasi-particles made of a superposition of excitons and cavity photons are called polaritons, leading to

$$\hat{\mathcal{H}} = \sum_{\mathbf{k}} \omega_{\mathbf{k}}^{(\text{LP})} a_{\text{LP},\mathbf{k}}^\dagger a_{\text{LP},\mathbf{k}} + \omega_{\mathbf{k}}^{(\text{UP})} a_{\text{UP},\mathbf{k}}^\dagger a_{\text{UP},\mathbf{k}}, \quad (6.4)$$

which is diagonalized by the following transformation

$$\begin{pmatrix} a_{p,\mathbf{k}} \\ a_{e,\mathbf{k}} \end{pmatrix} = \begin{pmatrix} \cos(\theta_{\mathbf{k}}) & -\sin(\theta_{\mathbf{k}}) \\ \sin(\theta_{\mathbf{k}}) & \cos(\theta_{\mathbf{k}}) \end{pmatrix} \begin{pmatrix} a_{\text{UP},\mathbf{k}} \\ a_{\text{LP},\mathbf{k}} \end{pmatrix}. \quad (6.5)$$

The dispersion relation as shown in Fig 6.1 is composed of two branches $\omega_{\mathbf{k}}^{(\text{LP/UP})}$, called lower and upper polariton corresponding to the hybridization of the excitonic and cavity photon energies, given by

$$\omega_{\mathbf{k}}^{(\text{UP/LP})} = \frac{\omega_{\text{cav},\mathbf{k}} + \epsilon_{\text{exc},\mathbf{k}}}{2} \pm \sqrt{\Omega_R^2 + \left(\frac{\omega_{\text{cav},\mathbf{k}} - \epsilon_{\text{exc},\mathbf{k}}}{2}\right)^2}, \quad (6.6)$$

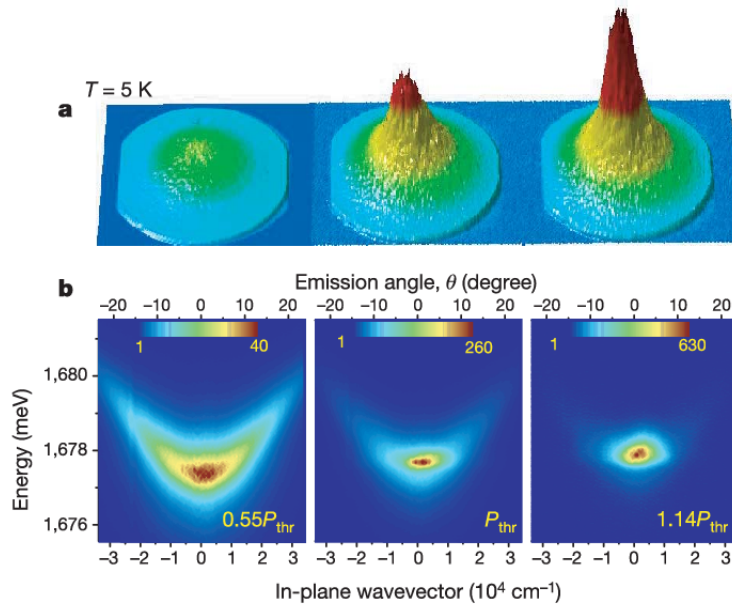


Figure 6.2: Experimental observation of polariton Bose-Einstein condensation obtained by increasing the intensity of the incoherent off-resonant optical pump. From [140]

where \pm refers to respectively upper (UP) and lower (LP) polariton branches. The strong light-matter coupling regime is defined when the light-matter coupling exceeds losses, $\Omega_R > \gamma$.

Microcavity polaritons are an interesting system in which to investigate condensation because they combine a very light effective mass (10^4 times smaller than the electron mass), with a matter component, and hence the possibility of collisions and thermalisation. These together open the possibility of polariton condensation at elevated temperatures. Polaritons however introduce another feature not normally present in, e.g., cold atomic gases, that is the finite lifetime of the quasi-particles: photons are imperfectly confined by the mirrors, and so can leak out. This means that the polariton condensate is best thought of as a non-equilibrium steady state, balancing pumping and decay. This motivates the approach in the following subsection to understand how to describe the light emission accounting for finite lifetimes as well as the polariton-polariton interaction.

6.1.1 Polariton-polariton interaction

As general description of a quantum object, light is dual, and so can be described either as a corpuscle, a photon, or an electromagnetic wave. Light is the most relativistic object as it is fixing an upper bound for the velocity of any propagating object, its dispersion relation is known to be linear as the photon is a relativistic particle without a mass, and its

6.1. Exciton-polaritons

| | Lifetime | Thermalization | Linewidth | Temperature |
|------------------|-----------|----------------|---------------------------|-------------|
| Atoms | 10s | 10ms | 2.5×10^{-13} meV | 10^{-8} K |
| Excitons | 50 ns | 0.2 ns | 5×10^{-5} meV | 1 K |
| Polaritons [141] | 2 ps | 5 ps | 0.5 meV | 200 K |
| Magnons | 1 μ s | 100 ns | 2.5×10^{-6} meV | 300 K |

Table 6.1: Summary the characteristic timescales and energies for: particle lifetimes, times to establish a thermal distribution, linewidth due to finite lifetime, and characteristic temperatures for various type of composite particles. The first two columns give information on the thermal properties, the latter two on coherence properties. Taken from [142]

velocity invariant in any frame. A crucial element is still missing for the photonic many-body system to acquire a collective fluid-like behavior namely, the possibility for the photons to collide. While photon-photon interactions have been predicted to occur even in vacuum via virtual excitation of electron-positron pairs [143], the probability for such a process in vacuum is so small that it can hardly be expected to play any role in realistic optical experiments. The interactions between polaritons is due to exciton-exciton interactions, which, thanks to the strong coupling with photons lead to an effective quantum fluid of light displaying effective photon-photon interaction. Exciton-exciton interactions is a rather complicated problem to solve as it is a 4-body problem interacting via long-range Coulomb potential. Indeed, it can be recast as a two-body contact interaction [144]

$$\hat{\mathcal{H}}_{\text{exc-exc}} = \int d^2\mathbf{r} \frac{V_{\text{exc-exc}}}{2} \hat{\Psi}_{\text{exc}}^\dagger(\mathbf{r}) \hat{\Psi}_{\text{exc}}^\dagger(\mathbf{r}) \hat{\Psi}_{\text{exc}}(\mathbf{r}) \hat{\Psi}_{\text{exc}}(\mathbf{r}) \quad (6.7)$$

where $\hat{\Psi}_{\text{exc}}(\mathbf{r})$ is the field operator for the exciton so that

$$\hat{\Psi}_{\text{exc}}(\mathbf{r}) = \frac{1}{\sqrt{S}} \sum_{\mathbf{k}} a_{e,\mathbf{k}} e^{i\mathbf{k}\cdot\mathbf{r}}. \quad (6.8)$$

Where S is the surface of the sample and \mathbf{k} is a 2D wavevector. The approximate value for effective interaction strength $V_{\text{exc-exc}}$ between two excitons has been calculated [145, 146]

$$V_{\text{exc-exc}} \approx 6e^2 a_B^* / \epsilon \quad (6.9)$$

a_B^* is the 2D Bohr radius and ϵ the dielectric constant of the QW. Using the transformation to the polariton basis, Eq. (6.5), the effective interaction among lower polaritons by neglecting upper polariton contributions can be expressed as

$$\hat{\mathcal{H}}_{LP} = \sum_{\mathbf{k}} \omega_{\mathbf{k}}^{(LP)} a_{LP,\mathbf{k}}^\dagger a_{LP,\mathbf{k}} + \sum_{\mathbf{k},\mathbf{k}'\mathbf{q}} \frac{V_{\mathbf{k},\mathbf{k}'\mathbf{q}}^{\text{eff}}}{2} a_{LP,\mathbf{k}+\mathbf{q}}^\dagger a_{LP,\mathbf{k}'-\mathbf{q}}^\dagger a_{LP,\mathbf{k}} a_{LP,\mathbf{k}'}, \quad (6.10)$$

where $V_{\mathbf{k}\mathbf{k}'\mathbf{q}}^{\text{eff}} = \frac{V_{\text{exc-exc}}}{2} \cos(\theta_{\mathbf{k}+\mathbf{q}}) \cos(\theta_{\mathbf{k}'-\mathbf{q}}) \cos(\theta_{\mathbf{k}}) \cos(\theta_{\mathbf{k}'})$. One can then show [144] that the interacting kernel $V_{\mathbf{k}\mathbf{k}'\mathbf{q}}^{\text{eff}}$ is mainly constant because of the parabolic dispersion of the lower polaritonic branch.

6.1.2 The driven-dissipative mean-field Gross-Pitaevskii equation

Interaction effects in exciton-polaritons are in general weak in current experimental setups so that a mean-field description of this quantum fluid is a very good approximation. We saw that the interactions between polariton is mainly due to Coulomb interactions between excitons and can be considered as contact interactions. Here, we present the description of polaritons in the mean-field approximation. We focus on the lower polariton branch, neglecting the upper polariton branch. For simplicity, we omit indices LP in the notations. As discussed before (Chapter 2 Sec. 2.1) the Gross-Pitaevskii equation can be derived from the Hamiltonian (6.10) and is given by

$$i\partial_t\Psi(\mathbf{r}, t) = -\frac{\hbar}{2m}\nabla_{\mathbf{r}}^2\Psi(\mathbf{r}, t) + V_{LP}|\Psi(\mathbf{r}, t)|^2\Psi(\mathbf{r}, t) \quad (6.11)$$

where $\Psi(\mathbf{r}) = \langle\hat{\Psi}_{LP}(\mathbf{r})\rangle$, $\hat{\Psi}_{LP}(\mathbf{r}) = \frac{1}{\sqrt{S}}\sum_{\mathbf{k}}a_{LP,\mathbf{k}}e^{i\mathbf{k}\cdot\mathbf{r}}$. As said before, polariton have a driven-dissipative nature. The main sources of decay of polariton come from radiative damping of the cavity field due to emission of light by the cavity and non radiative decay due to absorption in the cavity. We will refer to γ as a phenomenological parameter describing the losses of polariton in the system. To overcome this decay one introduce a pumping that correspond to the laser field imposed to the system. The phenomenological Gross-Pitaevskii equation considering loss and pumping can be expressed as

$$i\partial_t\Psi(\mathbf{r}, t) = \left(\omega_{LP}^0 - \frac{\hbar}{2m}\nabla_{\mathbf{r}}^2\right)\Psi(\mathbf{r}, t) + V_{LP}|\Psi(\mathbf{r}, t)|^2\Psi(\mathbf{r}, t) - i\frac{\gamma}{2}\Psi(\mathbf{r}, t) + E_{inc}(\mathbf{r}, t) \quad (6.12)$$

where ω_{LP}^0 is the frequency of the bottom of the lower polariton branch. This simplified description is generally well justified provided the Rabi frequency Ω_R is much larger than all other energy scales of the problem, namely, the kinetic and interaction energies, the pump detuning from the bottom of the lower polariton, and the loss rates.

6.1.3 Steady state and bistability

From the above Gross-Pitaevskii equation, it is possible to characterize the steady state solution of the lower polariton wave function under a coherent continuous wave pump $E_{inc}(\mathbf{r}, t) = E_{inc}e^{i\mathbf{k}_{inc}\cdot\mathbf{r}}e^{-i\omega_{inc}t}$, where E_{inc} is the incoming laser field. The wavefunction is cast into the form

$$\Psi(\mathbf{r}, t) = \Psi^{(0)}e^{i\mathbf{k}_{inc}\cdot\mathbf{r}}e^{-i\omega_{inc}t} \quad (6.13)$$

The steady-state solution of the system is given by the following equation.

$$\left[\omega_{inc} - \omega_{LP}^0 - \frac{\hbar|\mathbf{k}_{inc}|^2}{2m} + V_{LP}|\Psi^{(0)}|^2 - i\frac{\gamma}{2}\right]\Psi^{(0)} = E_{inc} \quad (6.14)$$

Several situations can arise [144]:

6.1. Exciton-polaritons

- If $\omega_{inc} < \omega_{LP}(\mathbf{k}_{inc}) = \omega_{LP}^0 + \frac{\hbar|\mathbf{k}_{inc}|^2}{2m}$, the density $n_{LP} = |\Psi^0|^2$ is growing monotonically with the laser intensity $I = |E_{inc}|^2$ (see Fig 6.3 upper-left panel). This behaviour is referred to as optical limiter. The Bogoliubov excitation spectrum is then gapped (see Fig 6.3 upper-right panel, case E)
- If $\omega_{inc} > \omega_{LP}(\mathbf{k}_{inc}) = \omega_{LP}^0 + \frac{\hbar|\mathbf{k}_{inc}|^2}{2m}$, the density n_{LP} is growing with the applied intensity I , but shows hysteretic behavior termed optical bistability in the nonlinear optics literature. The central branch of the hysteresis loop with a negative slope is always dynamically unstable. Depending on the specific values of pump parameters, other regions may also be dynamically unstable towards the parametric generation of polaritons into other modes at different $\mathbf{k} \neq \mathbf{k}_{inc}$ as can be seen from the Bogoliubov excitation spectrum (see Fig 6.3 upper-right panels from A to D).

A linear stability analysis of the Gross-Pitaevskii steady-state solution can be achieved by studying at the quadratic fluctuations around the steady state solution. It leads to the following Bogoliubov excitation spectrum [144]

$$\omega_{\text{Bog}}(\mathbf{k}) = \pm \sqrt{\left(\omega_{LP}^0 + \frac{\hbar|\mathbf{k}|^2}{2m} + 2V_{LP}n_{LP} - \omega_{inc}\right)^2 - (V_{LP}n_{LP})^2} - i\frac{\gamma}{2} \quad (6.15)$$

From point A to B' in Fig. 6.3 (right panel) a dynamical instability arises i.e the Bogoliubov excitation spectrum shows non zero dispersive imaginary part. The imaginary part is dispersionless at the special point C in Fig. 6.3 where the excitation spectrum becomes linear at low \mathbf{k} , that is where superfluid properties can arise. Then, at increasing pump intensity beyond point C, the spectrum is gapped.

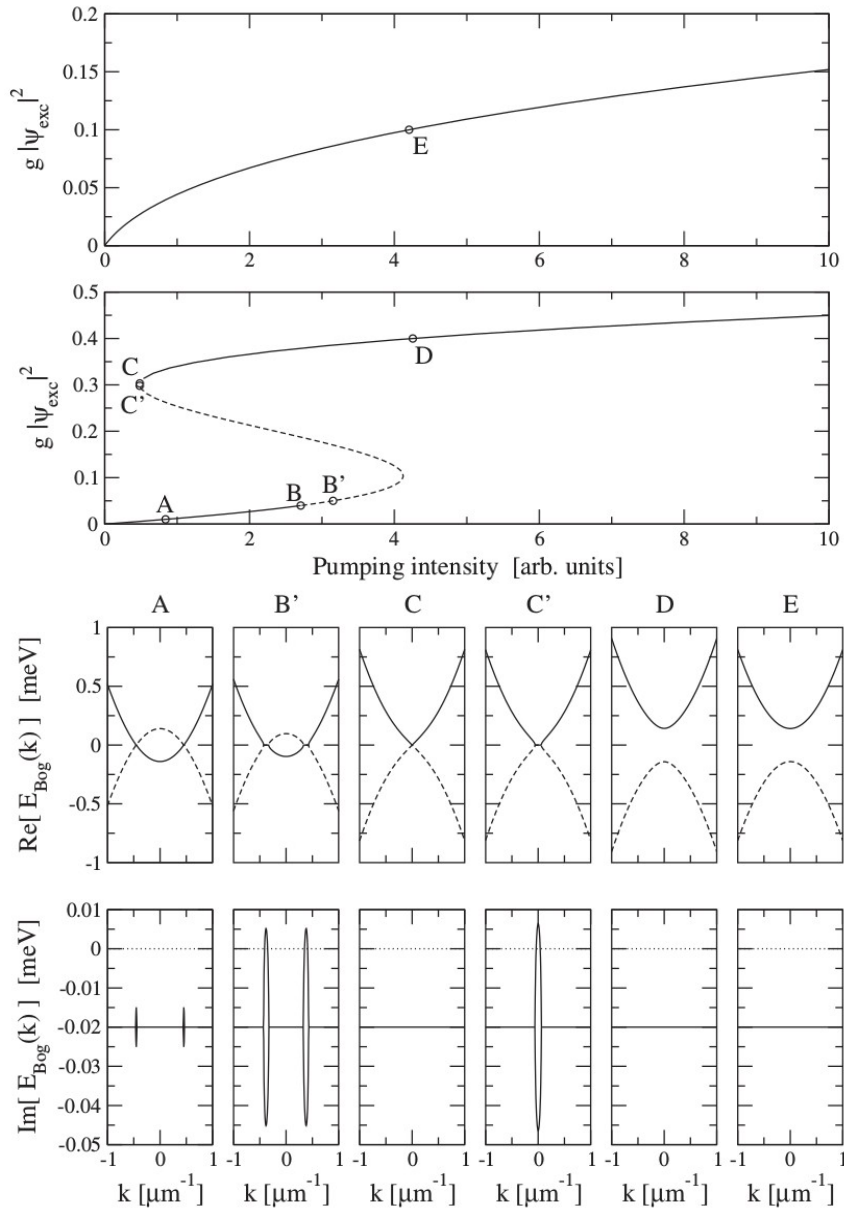


Figure 6.3: Upper panels: Polariton density vs pump intensity in the optical limiter regime (top) and bistable regime (bottom). The dashed line indicates the unstable regions. Top panels: Real part (top) and imaginary part (bottom) of the excitation frequencies for the non-equilibrium Bogoliubov modes corresponding to the points indicated as A, B', C, C', D, E in the left panel. Taken from [144]

6.2 Honeycomb lattice

Before presenting our studies of the polariton properties in a honeycomb lattice in the next chapter, we will review here the properties of a single quantum particle in a honeycomb lattice. The honeycomb lattice can be described by two triangular sub-lattices A and B (see Fig 6.2) forming a 2D plane paved by hexagons, and its reciprocal lattice is also hexagonal. Important point for the physics of the honeycomb lattice are the two points \mathcal{K} and \mathcal{K}' located at the corner of the Brillouin zone, called the Dirac points:

$$\mathcal{K} = \left(\frac{2\pi}{3a}, \frac{2\pi}{3\sqrt{3}a} \right) \quad \mathcal{K}' = \left(\frac{2\pi}{3a}, -\frac{2\pi}{3\sqrt{3}a} \right) \quad (6.16)$$

Their importance will be made clear later. When considering just the nearest neighbouring hopping in the tight-binding regime the Hamiltonian can be expressed by the following Bose-Hubbard Hamiltonian $H = H_0 + H_{\text{int}}$

$$H = - \sum_{\langle i,j \rangle} t_{ij} a_i^\dagger b_j + h.c - \frac{U}{2} \left[\sum_{i \in A} n_i^A (n_i^A - 1) + \sum_{i \in B} n_i^B (n_i^B - 1) \right] \quad (6.17)$$

where $\langle . \rangle$ restricts the sum over the nearest neighbours and A,B represent the two sub-lattice of the hexagonal lattice as shown in Fig.6.2. The non-interacting part of the Hamiltonian H_0 can be diagonalized in \mathbf{k} -space. We define the following operators for each sub-lattice

$$a_i^\dagger = \frac{1}{\sqrt{N_s^A}} \sum_k \exp(i\mathbf{k} \cdot \mathbf{A}_i) a_k^\dagger \quad (6.18)$$

$$b_i^\dagger = \frac{1}{\sqrt{N_s^B}} \sum_k \exp(i\mathbf{k} \cdot \mathbf{B}_i) b_k^\dagger \quad (6.19)$$

where N_s^A and N_s^B are the number of sites in sub-lattice A and B respectively, \mathbf{A}_i and \mathbf{B}_i are Bravais vectors of triangular sub-lattice A and B respectively. The Hamiltonian reads in \mathbf{k} -space,

$$H_0 = - \sum_k \begin{pmatrix} a_k^\dagger & b_k^\dagger \end{pmatrix} \begin{pmatrix} 0 & \phi(\mathbf{k}) \\ \phi^*(\mathbf{k}) & 0 \end{pmatrix} \begin{pmatrix} a_k \\ b_k \end{pmatrix} \quad (6.20)$$

where $\phi(\mathbf{k}) = (e^{i\mathbf{k} \cdot \mathbf{u}_1} + e^{i\mathbf{k} \cdot \mathbf{u}_2} + e^{i\mathbf{k} \cdot \mathbf{u}_3}) t_{AB}$. At this point we should mention that the value of the function $\phi(\mathbf{k})$ is not arbitrary and depends on the choice of the gauge [147]. The choice of the gauge is important as we will see in the next section, indeed the analysis of this chapter would be strongly modified by an other choice of gauge even though the observables stay gauge independent. The non-interacting Hamiltonian can be diagonalized, yielding eigenenergies $\epsilon_{\pm}(\mathbf{k}) = \pm |\phi(\mathbf{k})|$ with respective eigenvectors

$$\Psi_{\pm}(\mathbf{k}) = \frac{1}{\sqrt{2}} \begin{pmatrix} 1 \\ \pm e^{i\chi(\mathbf{k})} \end{pmatrix} \quad (6.21)$$

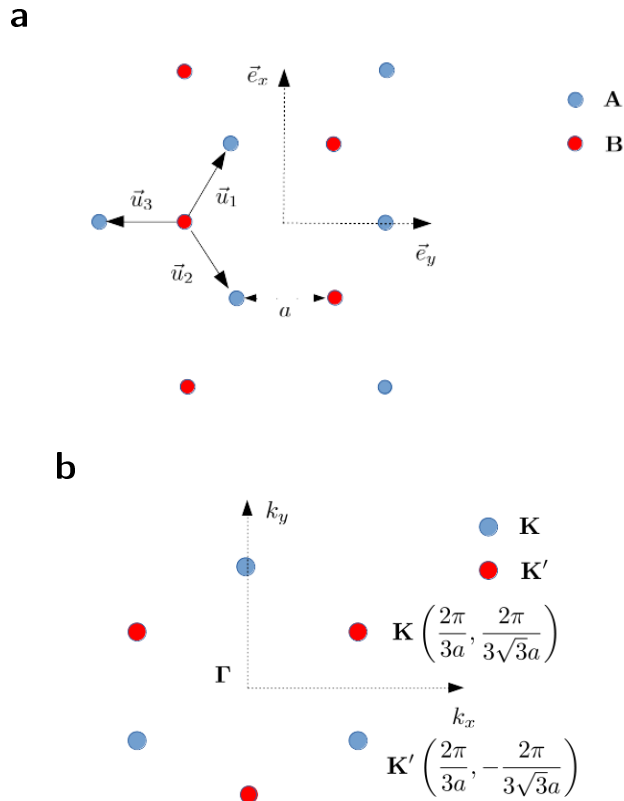


Figure 6.4: (a)-Representation of the hexagonal lattice with $\vec{u}_1 = a\left(\frac{1}{2}, \frac{\sqrt{3}}{2}\right)$, $\vec{u}_2 = a\left(\frac{1}{2}, -\frac{\sqrt{3}}{2}\right)$, $\vec{u}_3 = a(-1, 0)$. (b) Representation of the first Brillouin zone of the honeycomb lattice where \mathcal{K} and \mathcal{K}' represents the Dirac points and Γ the center of the Brillouin zone. It is important to stress that \mathcal{K} and \mathcal{K}' are not connected by a reciprocal lattice vector, they are truly independent values of \mathbf{k} .

where we have set $\phi(\mathbf{k}) = |\phi(\mathbf{k})|e^{i\chi(\mathbf{k})}$. The dispersion relation shown in Fig. 6.5 displays two bands in \mathbf{k} -space analogues to the π and π^* bands of the graphene [148] that we will refer to as + or -. These two bands are crossing at the Dirac points (\mathcal{K} and \mathcal{K}') in the vicinity of which the dispersion relation is linear. This linear dispersion relation implies an effective relativistic behaviour around the Dirac points where the particles become massless. Such a band structure has been experimentally observed with polariton gases [149].

Nearest neighbor tunneling Tunneling into the same sub-lattice A/B adds the following term in the tight binding Hamiltonian

$$H_{NN} = -t_{AA} \sum_{\langle\langle ij \rangle\rangle} a_i^\dagger a_j - t_{BB} \sum_{\langle\langle ij \rangle\rangle} b_i^\dagger b_j + h.c \quad (6.22)$$

6.2. Honeycomb lattice

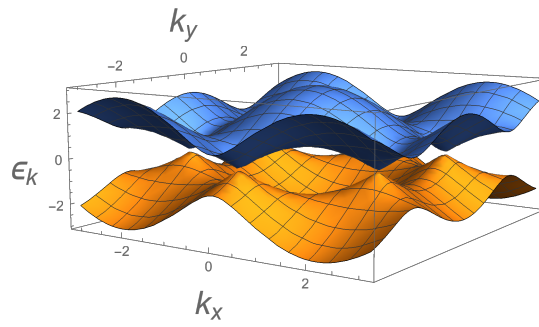


Figure 6.5: Dispersion relation of non-interacting particle in honeycomb lattice in units of the $t_{A,B}$. Positive and negative bands are observed and referred to as + or -.

We will call \mathbf{a}_1 , \mathbf{a}_2 , \mathbf{a}_3 the three vectors connecting a site to its nearest neighbor of the same sub-lattice. They connect to the known Bravais vector the following way $\mathbf{a}_1 = \mathbf{u}_1 - \mathbf{u}_3$, $\mathbf{a}_2 = \mathbf{u}_2 - \mathbf{u}_3$, $\mathbf{a}_3 = \mathbf{u}_1 - \mathbf{u}_2$. Assuming $t_{AA}/t_{AB} = t_{BB}/t_{AB} = t'$ and Fourier transforming H_{NN} we get that $H_0 + H_{NN}$ reads

$$H_0 + H_{NN} = - \sum_{\mathbf{k}} \begin{pmatrix} a_{\mathbf{k}}^\dagger & b_{\mathbf{k}}^\dagger \end{pmatrix} \begin{pmatrix} t' f(\mathbf{k}) & \phi(\mathbf{k}) \\ \phi^*(\mathbf{k}) & t' f(\mathbf{k}) \end{pmatrix} \begin{pmatrix} a_{\mathbf{k}} \\ b_{\mathbf{k}} \end{pmatrix} \quad (6.23)$$

where $f(\mathbf{k}) = 2 \cos(\sqrt{3}k_y) + 4 \cos(\frac{\sqrt{3}}{2}k_y) \cos(\frac{3}{2}k_x)$. This correction to the single-particle spectrum will affect only the high energy properties, so that close to the Dirac point no change are expected as $t_{AA} \ll t_{AB}$.

6.2.1 Berry phase

Let us consider a set of parameter $\lambda = (\lambda_1, \lambda_2, \dots)$ so that a generic Hamiltonian $H[\lambda]$ depend on this set. Let $|\Psi(t)\rangle$ be a quantum state whose evolution is

$$i\hbar \frac{d}{dt} |\Psi(t)\rangle = H[\lambda(t)] |\Psi(t)\rangle \quad (6.24)$$

We assume that the Hamiltonian is diagonalizable and $H[\lambda] |\Psi_n(\lambda)\rangle = E_n(\lambda) |\Psi_n(\lambda)\rangle$. We consider an adiabatic evolution of the parameters λ in time so that when the system is prepared in an eigenstate of $H[\lambda]$ it will stay in this state during the time evolution up to a phase

$$|\Psi(t)\rangle = c_n(t) |\Psi[\lambda(t)]\rangle \quad (6.25)$$

where $c_n(t)$ satisfy the equation of motion

$$i\hbar \dot{c}_n(t) = c_n(t) E_n[\lambda(t)] - i\hbar c_n(t) \langle \Psi_n[\lambda(t)] | \frac{d}{dt} | \Psi_n[\lambda(t)] \rangle \quad (6.26)$$

A formal solution of this equation is $c_n(t) = c_n(0)e^{i(\theta_{dyn} + \theta_{Berry})}$ where,

$$\theta_{dyn} = -\frac{1}{\hbar} \int_0^T E_n[\lambda(t)] dt \quad \theta_{Berry} = i \int_0^T \langle \Psi_n[\lambda(t)] | \frac{d}{dt} | \Psi_n[\lambda(t)] \rangle dt \quad (6.27)$$

θ_{dyn} represents the usual dephasing term due to the time evolution and θ_{Berry} is called the Berry phase. This Berry phase can be expressed as a closed path integral in parameter space of all the λ called Λ ,

$$\theta_{Berry} = i \oint_{\mathcal{C}} \langle \Psi_n[\lambda] | \nabla_{\lambda} | \Psi_n[\lambda] \rangle d\lambda \quad (6.28)$$

so that this phase indeed has a geometric character as it will only depend on the chosen path. In analogy with the Aharonov-Bohm effect we can define an analogue of the vector potential of the magnetic field called the Berry connexion that represent the parallel transport of the eigenfunction in the parameter space Λ .

$$\mathcal{A}(\lambda) = -i \langle \Psi_n[\lambda] | \nabla_{\lambda} | \Psi_n[\lambda] \rangle. \quad (6.29)$$

There is a strong analogy between the Berry phase and the Aharonov-Bohm phase as they are both geometrical phases, the difference being that the Aharonov-Bohm phase is dependent on the real space path whereas the Berry phase on the path in a more abstract parameter space Λ .

For crystal wave functions, the set of eigenfunction is of the Bloch form $\Psi_{n,\mathbf{k}}(\mathbf{r}) = u_{n,\mathbf{k}}(\mathbf{r})e^{i\mathbf{k}\cdot\mathbf{r}}$ where the $u_{n,\mathbf{k}}(\mathbf{r})$ are the eigenfunctions of the tight-binding Hamiltonian. The parameter space is the one of the crystal quasi-momenta \mathbf{k} and the Berry phase is the integral over a closed path of the connexion $\mathcal{A}^{(n)}(\mathbf{k}) = -i \langle u_{n,\mathbf{k}} | \nabla_{\mathbf{k}} | u_{n,\mathbf{k}} \rangle$ associated to the parallel transport of Bloch wave function over the Brillouin zone.

In the context of the honeycomb lattice we can define two connexion associated to the two bands (\pm),

$$\mathcal{A}^{(+)}(\mathbf{k}) = -\frac{i}{2} \left(1 - e^{-i\chi_{\mathbf{k}}} \right) i \nabla_{\mathbf{k}} \chi_{\mathbf{k}} \left(\frac{1}{e^{i\chi_{\mathbf{k}}}} \right) = \frac{1}{2} \nabla_{\mathbf{k}} \chi_{\mathbf{k}} \quad (6.30)$$

$$\mathcal{A}^{(-)}(\mathbf{k}) = -\frac{1}{2} \nabla_{\mathbf{k}} \chi_{\mathbf{k}} \quad (6.31)$$

Each connection integrated along a closed path cancels except around the Dirac points. The Dirac cones are then acting as Berry flux tubes in analogy with the Aharonov-Bohm effect where the flux comes from the connexity of the magnetic field, the Berry phase is non zero whenever discontinuity in of the derivative of the energy arise. Hence, the Berry phase around the Dirac point are given by (see Fig. 6.6),

$$\theta_{Berry, \partial\mathcal{K}}^{(+)} = \oint_{\partial\mathcal{K}} \mathcal{A}^{(+)}(\mathbf{k}) d\mathbf{k} = \pi \quad \theta_{Berry, \partial\mathcal{K}'}^{(+)} = \oint_{\partial\mathcal{K}'} \mathcal{A}^{(+)}(\mathbf{k}) d\mathbf{k} = -\pi \quad (6.32)$$

6.2. Honeycomb lattice

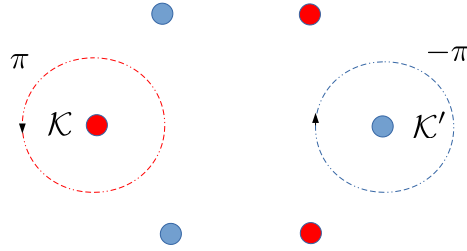


Figure 6.6: Representation of Berry flux acquired around two Dirac points

6.2.2 Brillouin zone selection

As already mentioned in Sec. 6, the band structure for polariton in honeycomb lattices has been experimentally observed. However due to the destructive interference between sub-lattice emitted photons, some branches are not visible as reported in [149, 150]. We sketch here a simple argument for this effect, in analogy with [151]. One can relate the photo-luminescence intensity of the emitted photon resulting from the decay of exciton-photon coupling seen in the experiment as the modulus squared of the time and space Fourier transform of the wave function $|\Psi_n(\mathbf{q}, \omega)|^2$. In order to do so, we express the Bloch function of a particle in the n^{th} -band and crystal momentum \mathbf{k} as follows

$$\Psi_{n\mathbf{k}}(\mathbf{r}) = \frac{1}{\sqrt{N/2}} \sum_j \left(e^{i\mathbf{k}\cdot\mathbf{R}_j^A} C_A^{n\mathbf{k}} \psi(\mathbf{r} - \mathbf{R}_j^A) + e^{i\mathbf{k}\cdot\mathbf{R}_j^B} C_B^{n\mathbf{k}} \psi(\mathbf{r} - \mathbf{R}_j^B) \right) \quad (6.33)$$

$$= \frac{1}{\sqrt{N/2}} \sum_j \left(e^{i\mathbf{k}\cdot\mathbf{R}_j^A} C_A^{n\mathbf{k}} \psi(\mathbf{r} - \mathbf{R}_j^A) + e^{i\mathbf{k}\cdot(\mathbf{R}_j^A + \boldsymbol{\delta}_1)} C_B^{n\mathbf{k}} \psi(\mathbf{r} - \mathbf{R}_j^A - \boldsymbol{\delta}_1) \right) \quad (6.34)$$

where $C_{A/B}^{n\mathbf{k}}$ are the coefficients of the eigenfunction of the tight binding problem of the n -band, $\mathbf{R}_j^{A/B}$ are the vector positions of the sub-lattice atoms A/B in the crystal. The Fourier transform reads

$$\int_{\mathbb{R}} d\mathbf{r} e^{-i\mathbf{q}\cdot\mathbf{r}} \Psi_{n\mathbf{k}}(\mathbf{r}) = \sum_j e^{-i(\mathbf{q}-\mathbf{k})\cdot\mathbf{R}_j^A} \tilde{\psi}(\mathbf{q}) C_A^{n\mathbf{k}} + \sum_j e^{-i(\mathbf{q}-\mathbf{k})\cdot\mathbf{R}_j^A} e^{-i(\mathbf{q}-\mathbf{k})\cdot\boldsymbol{\delta}_1} \tilde{\psi}(\mathbf{q}) C_B^{n\mathbf{k}} \quad (6.35)$$

where $\tilde{\psi}(\mathbf{q})$ is the Fourier transform of the Wannier function, \mathbf{q} is the physical momentum and $\boldsymbol{\delta}_1 = \mathbf{R}_j^B - \mathbf{R}_j^A$ is the distance between atom of type A and B in the unit cell. Noticing that

$$e^{-i(\mathbf{q}-\mathbf{k})\cdot\mathbf{R}_j^A} = \sum_{n_1, n_2} \delta(\mathbf{k} - \mathbf{q} - (n_1 \mathbf{b}_1 + n_2 \mathbf{b}_2)), \quad (6.36)$$

and within the first Brillouin zone this sum corresponds to $e^{-i(\mathbf{q}-\mathbf{k})\cdot\mathbf{R}_j^A} = \delta_{\mathbf{q},\mathbf{k}}$, one is left with the following expression for the Fourier transform of the Bloch function

$$\Psi_{\pm\mathbf{k}}(\mathbf{q}) = \delta_{\mathbf{k},\mathbf{q}}\tilde{\psi}(\mathbf{q})\left(1 \pm e^{i\chi(\mathbf{q})}\right). \quad (6.37)$$

The time dependence of the Bloch function is a phase, so that $\Psi_{n\mathbf{k}}(\mathbf{r}, t) = \Psi_{n\mathbf{k}}(\mathbf{r})e^{-i\epsilon_{n\mathbf{k}}t}$. Within the first Brillouin zone, we finally obtain

$$\Psi_{n\mathbf{k}}(\mathbf{q}, \omega) = \int_{\mathbb{R}} dt d\mathbf{r} e^{i\omega t} e^{i\mathbf{r}\cdot\mathbf{q}} \psi_{n\mathbf{k}}(\mathbf{r}, t) = \delta(\omega - \epsilon_{n\mathbf{k}}) \delta_{\mathbf{k},\mathbf{q}} \tilde{\psi}(\mathbf{q}) \left(1 \pm e^{i\chi(\mathbf{q})}\right) \quad (6.38)$$

Similarly, one has to be careful to include the extra phase (6.36) that needs to be added in higher order Brillouin zone. This leads to additional extinction of the intensity pattern [151]. Typical extinction in the (k_x, k_y) plane is illustrated in Fig. 6.7.

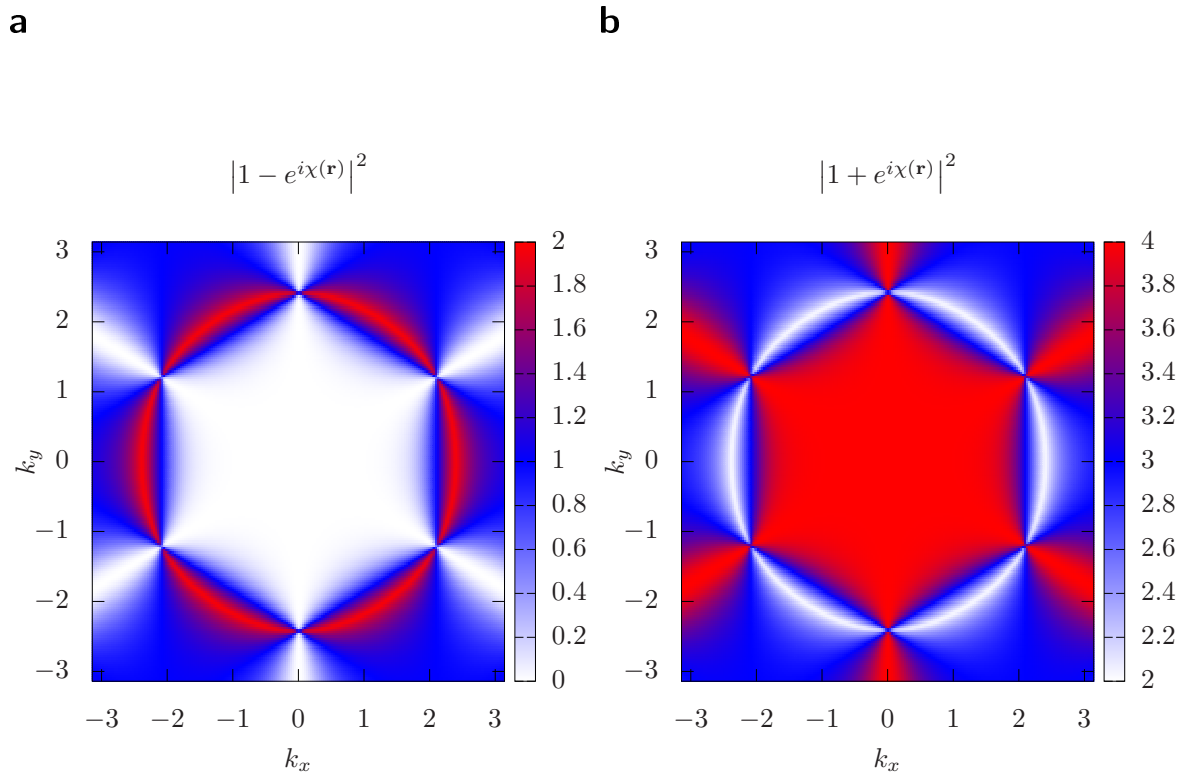


Figure 6.7: Behaviour of the phase $f(\mathbf{k})_{\pm} = |1 \pm e^{i\chi(\mathbf{k})}|^2$ term in the (k_x, k_y) plan for **a)** $f(\mathbf{k})_{-}$ and **b)** $f(\mathbf{k})_{+}$.

6.2.3 Coupling to photonic bath vacuum

We now proceed to add into the theoretical description of the system the effect of cavity losses. These are due to a coupling of photon modes inside the cavity and the electro-

6.2. Honeycomb lattice

magnetic modes outside the cavity (see e.g [152]). As there is a one to one correspondence between in plane cavity modes and electromagnetic modes (i.e that the coupling Hamiltonian is diagonal in Fourier space) we consider a constant tunneling matrix element $\alpha(x) = \alpha$ through the cavity mirror, whose value depends on the specific mirror structure. The coupling Hamiltonian accounting for the conversion of cavity modes in vacuum photons reads,

$$H_{\text{decay}} = i\alpha \left(\int dz d\mathbf{r} \Psi(\mathbf{r})^\dagger \phi(z, \mathbf{r}) - \text{H.c} \right) \quad (6.39)$$

where $\phi(\mathbf{x})$ is the vacuum photon field operator in the 3D space and $\Psi(\mathbf{r})$ the polaritonic field operator in the 2D space (in plane). We expand the polariton field operators in Wannier basis of the lattice A and B, i.e $\Psi(\mathbf{r}) = \sum_i a_i w(\mathbf{r} - \mathbf{R}_i^A) + b_i w(\mathbf{r} - \mathbf{R}_i^B)$, where $\mathbf{r} = (x, y)$ are in-plane coordinates and z the orthogonal direction. In this case the decay Hamiltonian becomes

$$H_{\text{decay}} = i\alpha \int dp e^{-ipz} \left(\sum_{\mathbf{q}} w(\mathbf{q})^* a_{\mathbf{q}}^\dagger c_{p,\mathbf{q}} + w(\mathbf{q})^* b_{\mathbf{q}}^\dagger c_{p,\mathbf{q}} - \text{H.c} \right) \quad (6.40)$$

where $c_{p,\mathbf{q}}^\dagger$ creates a vacuum photon with in-plane wave vector \mathbf{q} and orthogonal out-of-plane wave vector p . Transforming the lattice polariton field operators in the diagonal basis \pm , so that $a_{\mathbf{q}} = \frac{1}{\sqrt{2}} (\Psi_{+,\mathbf{q}} + \Psi_{-,\mathbf{q}})$ and $b_{\mathbf{q}} = \frac{e^{-i\chi\mathbf{q}}}{\sqrt{2}} (\Psi_{+,\mathbf{q}} - \Psi_{-,\mathbf{q}})$, we have

$$\tilde{H}_{\text{decay}} = i \left(\int dp \sum_{\mathbf{q} \in 1^{\text{st}}\text{BZ}, n} \zeta_{q,\mathbf{q},n} \Psi_{n,\mathbf{q}}^\dagger c_{p,\mathbf{q}} - \text{H.c} \right) \quad (6.41)$$

where $\zeta_{q,\mathbf{q}}^n = \alpha \frac{w(\mathbf{q})^* e^{-iqz}}{\sqrt{2}} (C_A^{n\mathbf{q}} + C_B^{n\mathbf{q}})$ is the coupling constant between the polariton evolving in the honeycomb lattice and electromagnetic vacuum modes. In order to treat the loss term due to decay of polariton in the vacuum, we treat the coupling of the system with a decay bath of photon. It is then modeled by the following Hamiltonian

$$\hat{\mathcal{H}} = \sum_{\mathbf{k}, n} \epsilon_{\mathbf{k}, n} \hat{\Psi}_{\mathbf{k}, n}^\dagger \hat{\Psi}_{\mathbf{k}, n} + \int dq \sum_{\mathbf{k}} \omega_{q,\mathbf{k}} c_{q,\mathbf{k}}^\dagger c_{q,\mathbf{k}} + i \int dp \sum_{\mathbf{q}, n} \left(\zeta_{p,\mathbf{q}}^n \Psi_{\mathbf{q}, n}^\dagger c_{p,\mathbf{q}} - \text{H.c} \right) \quad (6.42)$$

where $\omega_{p,\mathbf{q}}$ is the frequency of the free photonic field $c_{p,\mathbf{q}}$ with momentum in plane momentum \mathbf{q} and out-of-plane momentum p , $\zeta_{p,\mathbf{q}}^n$ is the coupling constant between photonic and honeycomb polaritonic field $\Psi_{\mathbf{k}, n}$ of branches $n = \pm$. We are interested in the equation of motion of the polaritonic and photon fields $\Psi_{\mathbf{k}, n}$ and $c_{p,\mathbf{q}}$

$$i \frac{d\Psi_{\mathbf{q}, n}(t)}{dt} = [\Psi_{\mathbf{q}, n}(t), \hat{\mathcal{H}}] = \epsilon_{\mathbf{q}, n} \Psi_{\mathbf{q}, n}(t) + i \int dp \zeta_{p,\mathbf{q}}^n c_{p,\mathbf{q}}(t) \quad (6.43)$$

$$i \frac{dc_{p,\mathbf{q}}(t)}{dt} = [c_{p,\mathbf{q}}(t), \hat{\mathcal{H}}] = \omega_{p,\mathbf{q}} c_{p,\mathbf{q}}(t) - i (\zeta_{p,\mathbf{q}}^n)^* \Psi_{\mathbf{q}, n}(t) \quad (6.44)$$

Formal solution for the photonic field is

$$c_{p,\mathbf{q}}(t) = e^{-i\omega_{p,\mathbf{q}}t} c_{p,\mathbf{q}}(0) - (\zeta_{p,\mathbf{q}})^* \int_0^t dt' e^{-i\omega_{p,\mathbf{q}}t'} \Psi_{\mathbf{q},n}(t') \quad (6.45)$$

Inserting it in the equation of motion for the polariton, we end up with the following equation,

$$\begin{aligned} i \frac{d\Psi_{\mathbf{q},n}(t)}{dt} &= \epsilon_{\mathbf{q},n} \Psi_{\mathbf{q},n}(t) + i \int dp \zeta_{p,\mathbf{q}} c_{p,\mathbf{q}} e^{-i\omega_{p,\mathbf{q}}t} \\ &- i \int dp |\zeta_{p,\mathbf{q}}|^2 \int dt' \theta(t') e^{-i\omega_{p,\mathbf{q}}(t-t')} \Psi_{\mathbf{q},n}(t') \end{aligned} \quad (6.46)$$

where we can identify $D_{c_{p,\mathbf{q}}^\dagger c_{p,\mathbf{q}}}^R(t, t') = -i\theta(t-t') e^{-i\omega_{p,\mathbf{q}}(t-t')}$ as the free photonic field retarded Green's function. The second term in r.h.s of Eq(6.46) refers to a noise term [153] and will be neglected in the following. Using the fact that transmission through the mirrors is almost instantaneous meaning that the coefficient γ is independent of the frequency ω (Markovian approximation), we have $\int d\omega \frac{\partial p}{\partial \omega} |\zeta_{p,\mathbf{q}}^n|^2 e^{-i\omega_{p,\mathbf{q}}(t-t')} \approx \delta(t-t') \gamma_{\mathbf{q}}$ where $\gamma_{\mathbf{k}} = 2\pi \frac{\partial p}{\partial \omega} |\zeta_{p(\omega),\mathbf{k}}|^2$ is independent of ω . It implies that equation of motion for $\Psi_{\mathbf{k},n}(t)$ reads

$$i\partial_t \Psi_{\mathbf{k},n}(t) = \epsilon_{\mathbf{k},n} \Psi_{\mathbf{k},n}(t) - i\gamma_{\mathbf{k}} \Psi_{\mathbf{k},n}(t) \quad (6.47)$$

One can then readily define the diagonal retarded Green's function as (see Appendix F)

$$G_{\pm}(\mathbf{k}, \omega) = \frac{1}{\omega - \epsilon_{\mathbf{k},\pm} + i\gamma_{\mathbf{k}}} \quad (6.48)$$

Finally we see that the spectral function $A(\mathbf{k}, n, \omega)$ of a given band $n = \pm$ is

$$A(\mathbf{k}, n, \omega) = -\frac{1}{\pi} \text{Im}[G_{n=\pm}(\mathbf{k}, \omega)] = \frac{1}{\pi} \frac{\gamma_{\mathbf{k}}}{(\omega - \epsilon_{\mathbf{k},\pm})^2 + \gamma_{\mathbf{k}}^2} \quad (6.49)$$

so that $A(\mathbf{k}, n, \omega)$ is Lorentzian peaked at $\omega = \epsilon_{\mathbf{k},\pm}$. One recovers the same effect as for the interference of the two sub-lattice. It should be emphasized that the geometry of the system, inserted in the coupling factor, induces the vanishing of the loss term so that decay of polaritons into photons is prohibited. The life-time of such particles is then infinite and one could be able to engineer dark-state of polariton so that regimes of high interactions among polaritons can be created. This extinction has the same physical origin as the one of Sec. 6.2.2.

Chapter 7

Bogoliubov excitation spectrum of polaritons in honeycomb lattice



THE formalism of the Bogoliubov approximation allows to study the properties of the a system around a steady-state solution and characterize its stability, as we saw in 6.

The chapter is organized as follows: In Sec. 7.1 we will derive the steady state equations of the system then the equation of motion of the Bogoliubov excitation in order to access and study the excitation spectrum of the system. Then we will explore the Bogoliubov excitation spectrum of exciton-polariton in honeycomb lattices in Sec. 7.2 that will be compared to experimental data.

7.1 Bogoliubov excitation spectrum

Steady state solution In order to obtain the Bogoliubov spectrum of a polariton condensate pumped at the \mathcal{K} point we first determine its steady state. As the coupling between the two sub-lattices vanishes when driving the condensate in the Dirac point, i.e $\phi(\mathbf{k} = \mathcal{K}) = 0$, we are left with two uncoupled Gross-Pitaevskii equations. The steady state solution in sub-lattice A or B $\psi_{A/B}^{(0)}$ is then solution of the following polynomial equation

$$\left(\left(\Delta_c + U |\psi_{A/B}^{(0)}|^2 \right)^2 + \frac{\gamma^2}{4} \right) |\psi_{A/B}^{(0)}|^2 = |F_0|^2 \quad (7.1)$$

where $\Delta_c = \omega_{LP} - \omega_{inc}$ and $\langle a_i \rangle = \psi_A^{(0)} e^{i\mathcal{K}\mathbf{r}_i} e^{-i\omega_{inc}t}$, $\langle b_i \rangle = \psi_B^{(0)} e^{i\mathcal{K}\mathbf{r}_i} e^{-i\omega_{inc}t}$. This means that the stability criterion for a polaritonic gas driven at wave vector equal to Dirac wavevector is the one of an one component system (Eq (6.3)) for a laser driving exactly at the Dirac point. Experimentally this is generally not the case but this decoupling approach provides a first approximation.

Condensation at the Dirac point $\mathbf{k} = \mathcal{K}$ Assuming equal condensation on the two sub-lattice i.e $a_{\mathbf{k}=\mathcal{K}} = \sqrt{N_a} = b_{\mathbf{k}=\mathcal{K}} = \sqrt{N_b} = \sqrt{N}$, the Bogoliubov Hamiltonian of the interacting gas on honeycomb lattice can be written in terms of the fluctuation fields on the two sub-lattices $\{\delta a_{\mathbf{k}}, \delta b_{\mathbf{k}}\}$.

$$H_{int,A} = \frac{U}{2N_s} \sum_{\mathbf{k}} \left[4N \delta a_{\mathbf{k}-\mathcal{K}}^\dagger \delta a_{\mathbf{k}-\mathcal{K}} + N \left(\delta a_{\mathbf{k}-\mathcal{K}}^\dagger \delta a_{-\mathbf{k}+\mathcal{K}}^\dagger + \delta a_{-\mathbf{k}+\mathcal{K}} \delta a_{\mathbf{k}-\mathcal{K}} \right) \right] \quad (7.2)$$

$$H_{int,B} = \frac{U}{2N_s} \sum_{\mathbf{k}} \left[4N \delta b_{\mathbf{k}-\mathcal{K}}^\dagger \delta b_{\mathbf{k}-\mathcal{K}} + N \left(\delta b_{\mathbf{k}-\mathcal{K}}^\dagger \delta b_{-\mathbf{k}+\mathcal{K}}^\dagger + \delta b_{-\mathbf{k}+\mathcal{K}} \delta b_{\mathbf{k}-\mathcal{K}} \right) \right] \quad (7.3)$$

$$H = H_0 + H_{int,A} + H_{int,B} \quad (7.4)$$

The equation of motion $i\partial_t \delta a_s = [\delta a_s, H_{\text{Bog}}]$ are forming a closed system of linearly coupled equations. When performing the Bogoliubov approximation for the field, $a_i = \psi_A^{(0)} + \delta a_i$, we have to solve the following non-Hermitian eigenvalue problem

$$\epsilon_{\mathbf{k}} \begin{pmatrix} \delta a_{\mathcal{K}+\mathbf{k}} \\ \delta a_{\mathcal{K}-\mathbf{k}}^\dagger \\ \delta b_{\mathcal{K}+\mathbf{k}} \\ \delta b_{\mathcal{K}-\mathbf{k}}^\dagger \end{pmatrix} = \eta \mathcal{L} \begin{pmatrix} \delta a_{\mathcal{K}+\mathbf{k}} \\ \delta a_{\mathcal{K}-\mathbf{k}}^\dagger \\ \delta b_{\mathcal{K}+\mathbf{k}} \\ \delta b_{\mathcal{K}-\mathbf{k}}^\dagger \end{pmatrix} - i \frac{\gamma}{2} \mathbf{Id} \quad (7.5)$$

the Bogoliubov excitation then corresponds to the eigenvalues of the following dynamical \mathcal{L} matrix,

$$\mathcal{L} = \begin{pmatrix} \Delta_c + 2Un & Une^{2i\theta_A} & -\phi(\mathbf{k} + \mathcal{K}) & 0 \\ -Une^{-2i\theta_A} & -\Delta_c - 2Un & 0 & \phi^*(\mathcal{K} - \mathbf{k}) \\ -\phi^*(\mathbf{k} + \mathcal{K}) & 0 & \Delta_c + 2Un & Une^{2i\theta_B} \\ 0 & \phi(\mathcal{K} - \mathbf{k}) & -Une^{-2i\theta_B} & -\Delta_c - 2Un \end{pmatrix} \quad (7.6)$$

The dynamical matrix with next nearest neighbour hopping reads

$$\mathcal{L}' = \mathcal{L} + \begin{pmatrix} -t' f(\mathcal{K} + \mathbf{k}) & 0 & 0 & 0 \\ 0 & t' f(\mathcal{K} - \mathbf{k}) & 0 & 0 \\ 0 & 0 & -t' f(\mathcal{K} + \mathbf{k}) & 0 \\ 0 & 0 & 0 & t' f(\mathcal{K} - \mathbf{k}) \end{pmatrix} \quad (7.7)$$

where $t' = t_{AA}/t_{AB} = t_{BB}/t_{AB}$ and $f(\mathbf{k}) = 2 \cos(\sqrt{3}k_y) + 4 \cos(\frac{\sqrt{3}}{2}k_y) \cos(\frac{3}{2}k_x)$. For the special case where we look at the cut for $k_x = 0$ the eigenvalues of the \mathcal{L} matrix can be found analytically and are given by

$$\epsilon_{\mathcal{K}}(k) = \frac{1}{2} \left[\pm (\phi(\mathcal{K} - \mathbf{k}) - \phi^*(\mathbf{k} + \mathcal{K})) \pm \sqrt{(2\Delta_c + 6Un \mp (\phi(\mathcal{K} - \mathbf{k}) + \phi^*(\mathbf{k} + \mathcal{K}))) (2(\Delta_c + Un) \mp (\phi(\mathcal{K} - \mathbf{k}) + \phi^*(\mathbf{k} + \mathcal{K})))} \right] \quad (7.8)$$

with $\psi_{A/B}^{(0)} = n_{A/B} e^{i\theta_{A/B}}$ assuming $n_A = n_B$ and $\mathcal{K} = a(0, 4\frac{\pi}{3\sqrt{3}})$ the momenta of the considered Dirac point. In the general case, when one considers $n_A \neq n_B$, one introduces anisotropy in the system leading to an opening of the gap. In polariton experiments, one

7.1. Bogoliubov excitation spectrum

can observe the Bogoliubov ghost branch that corresponds to negative energy excitation. This is due to parametric excitations [154, 155] and observed for both incoherent [156] and coherent [157] pumping. Ghost branches have then a highly relevant role as they correspond to the excitations holes. We remark that the matrix \mathcal{L} does not satisfy the inversion symmetry relation, i.e $\mathcal{L}^* = -\sigma\mathcal{L}\sigma$ where,

$$\sigma = \begin{pmatrix} 0 & 1 & 0 & 0 \\ 1 & 0 & 0 & 0 \\ 0 & 0 & 0 & 1 \\ 0 & 0 & 1 & 0 \end{pmatrix}, \quad (7.9)$$

which implies that there is no set of eigenvalues which are opposite $(\epsilon_{k_y}, -\epsilon_{k_y}^*)$. In other words, the ghosts branches are not expressed as the opposite of the physical excitation branches. They form a lattice structure in k -space shifted with respect to the normal branches lattice, as shown in Fig. 7.1. This is due to the scattering allowed by the Bogoliubov approximation, that transforms modes of the condensates into excitations with wavevector \mathbf{k} and $\mathbf{k} - 2\mathcal{K}$.

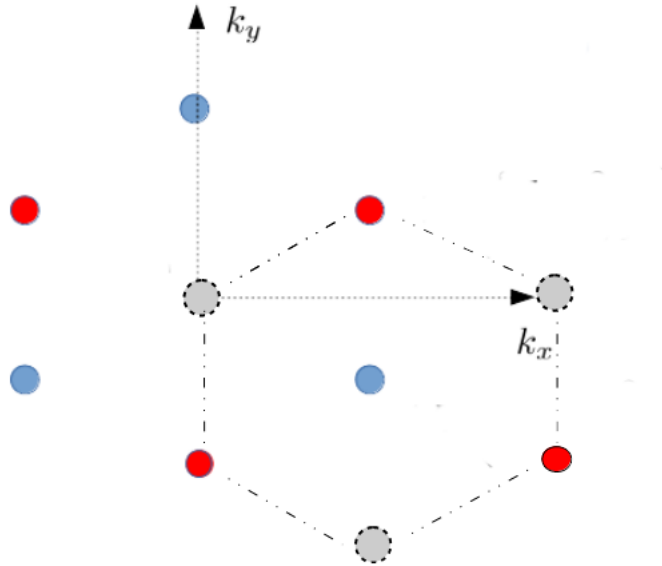


Figure 7.1: Sketch of the ghost lattice in k -space as compared to the real lattice.

The ghost branches corresponds to particles with opposite momenta and energy as can be clearly seen in Fig. 7.2 so that the Doppler effect for ghost excitations is opposite. Along the x direction, this symmetry is present and the spectrum is composed of a set of opposite complex conjugated eigenvalues $(\epsilon_{k_x}, -\epsilon_{k_x}^*)$. This is due to the fact that the condensate is not moving in the x direction. The spectrum is composed of multiple branches,

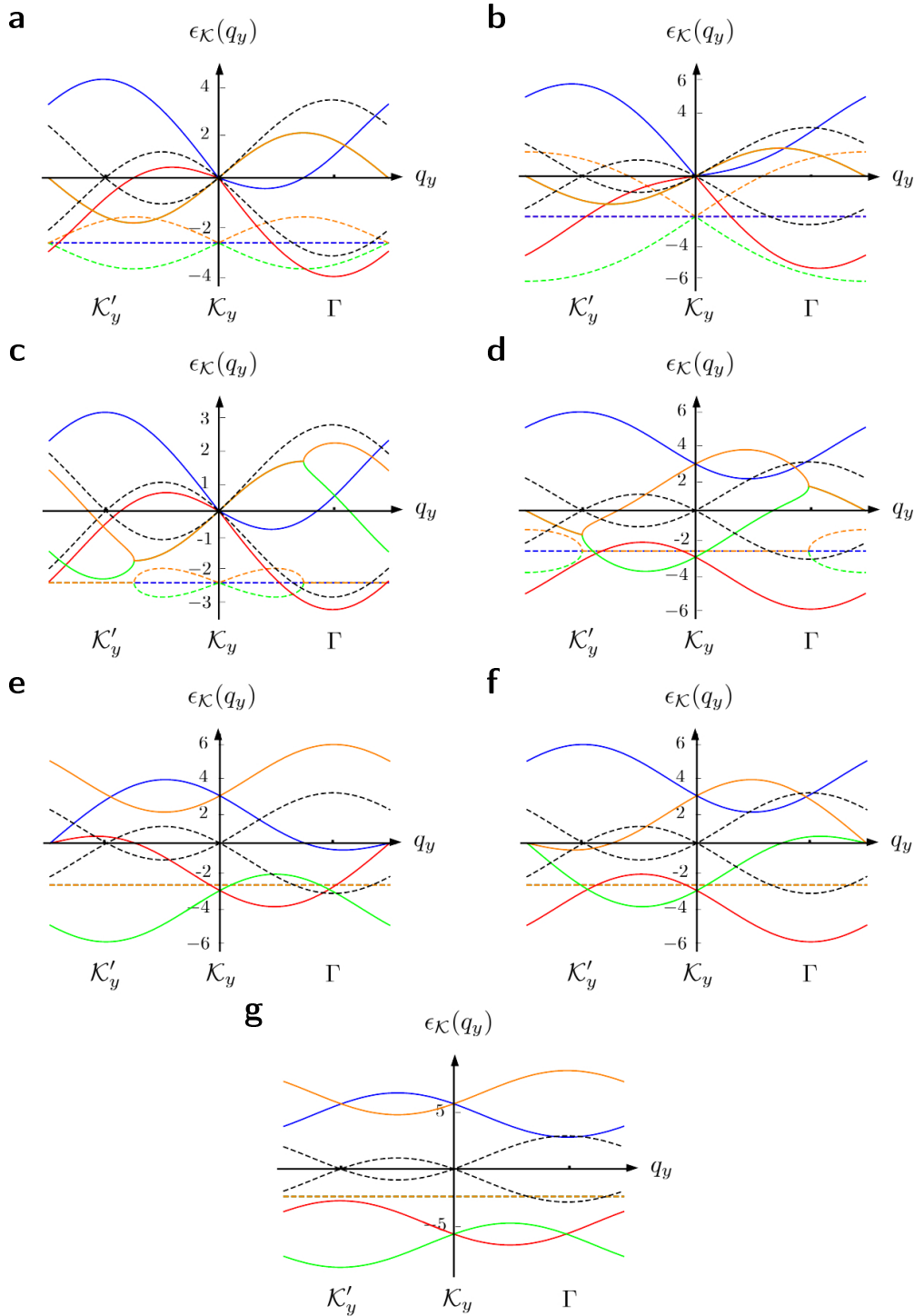


Figure 7.2: The excitation spectrum at different polariton densities and energy shift Δ_c . The real (solid) and the imaginary (dashed) parts of the spectrum in the frame of the pump momentum at the Dirac point, which is $\mathbf{k}_{\text{inc}} = \mathcal{K}$ in the y -direction, for $k_x = 0$. For **a**) $\Delta_c = -1$ and $Un = 1$, **b**) $\Delta_c = -5$ and $Un = 5$, **c**) $\Delta_c = -0.5$ and $Un = 0.5$, **d**) $\Delta_c = -0.5$ and $Un = 2$, **e**) $\Delta_c = -5$ and $Un = 1$, **f**) $\Delta_c = 1$ and $Un = 1$, **g**) $\Delta_c = -8$ and $Un = 1$. Black dashed line correspond to the single-particle dispersion.

7.1. Bogoliubov excitation spectrum

the real and imaginary part is plotted in Fig 7.2 for the case of the stable C point 6.3 in hysteresis loop (sub-panels **a**) to **c**) in Fig. 7.2). It appears that in this C point only one of the branch is stable (+ or – depending on the sign of Δ_c) so that only one sub k -space lattice Dirac points will be turned on, corresponding to the wavevector k_{inc} of the pump. This latter point is a manifestation of the symmetry of the system. This stability of the branch is in correspondence with observability of the branch, i.e unstable branches are not observable due to the interference of the two sub-lattices (See discussion in Sec. 6.2.2). Reducing the interactions, the + branch becomes stable. The spectrum in Fig. 7.2 **d**) corresponds to the stable region above the C point where the + branch becomes gapped in agreement with the prediction for one component case.

The spectrum at low energy close to the Dirac point is Doppler shifted, i.e as we are in the laboratory frame of, excitations at $q = \mathcal{K} + k$ or $q = \mathcal{K} - k$ will feel different sound velocities as they will flow against or with the flow of the condensate at velocity \mathcal{K} . In Fig. 7.2 panels **a**)**c**)**e**)**f**), the low- k dispersion relation around the Dirac point has sonic shape with sound speed lower than the speed of flow corresponding to a supersonic motion: here the system is not superfluid [158] as Bogoliubov modes can be resonantly excited by a defect inducing Rayleigh scattering ring. Fig. 7.2**b**) illustrate the case of a subsonic motion, where the polariton gas behaves as a superfluid: no Bogoliubov mode can be any longer resonantly excited and the resonant Rayleigh scattering ring disappears. It has been recently shown that the polaritonic systems are not Galilean invariant in the presence of a reservoir [159]. Then there is no one to one correspondence between Landau critical velocity and the Bogoliubov speed of sound, however this criterion still holds when the sound velocity is properly renormalized. Moreover, we observe that, strangely enough, the gas of polariton acquire superfluid property at momenta $\mathbf{k} \neq \mathcal{K}$ different from the driving of the pump as can be seen in panel **e**) and **f**). This two point are found to be stable without any dynamical instability and ghost and normal branches are exchanging position with respect the the horizontal axis.

7.1.1 Stability analysis

From the study of the above dynamical matrix \mathcal{L} one is able to link the stability of the polaritonic gas with the eigenvalues of the dynamical matrix. We define

$$\gamma_{\text{eff}}(\mathbf{k}) = \text{Im}[c(\mathbf{k})] \quad (7.10)$$

Following [144] the stability criterion is defined as follows, whenever $\gamma_{\text{eff}}(\mathbf{k}) + \gamma > 0$, $\forall \mathbf{k}$, the gas of polaritons is drawn to an instability as the excitations are damped. Thus, using this criterion we see that in the optical bistability regime, beyond the point C where $|Un| = |\Delta_c|$ the system is found to be unstable (see Fig. 7.3) and does not follow the usual behavior of a 2D polaritonic gas (see Fig. 6.3). Therefore, one can see that the mean-field analysis might be not suited to characterize the polaritonic gas and quantum-fluctuation should be high in those unusual regions of instability. At the C point, the symmetry of the Dirac cones is allowing momentum transfer processes that can empty the polaritonic con-

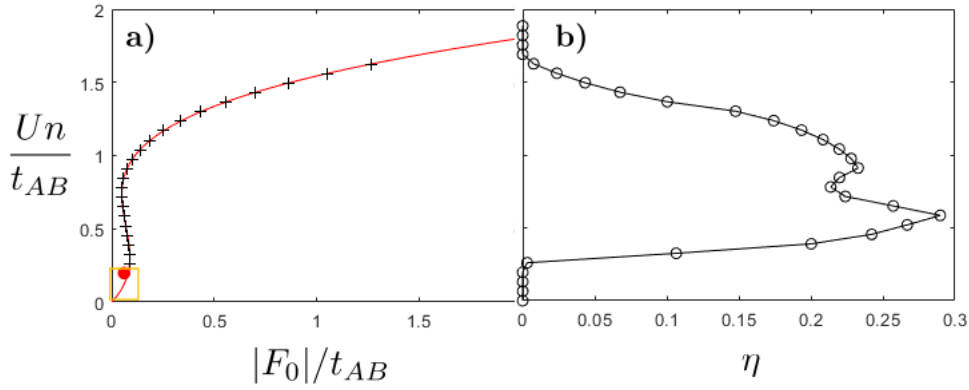


Figure 7.3: Panel **a)** represents the hysteresis loop in the optical bistability regime. The dots are marking the unstable region corresponding to panel **b)** where the fraction of unstable mode is plotted. We see that beyond the C point where $|Un| = |\Delta_c|$ the system is found to be unstable.

densate. In this case the Bogoliubov approximation of a macroscopically occupied ground state breaks down and a more refined theory would be needed.

7.2 Experimental excitation spectrum

As a matter of consistency with the earlier approach presented in Sec 6.2.2 we link the intensity of the excitation in terms of their Bloch wave expression. The contribution of Bogoliubov excitation to Bloch wave $\delta\Psi_{n,\mathbf{k}}(\mathbf{r})$ is expressed in term of the Bogoliubov amplitudes [160]

$$\begin{aligned} \delta\Psi_{n\mathbf{k}}(\mathbf{r}, t) = & \frac{1}{\sqrt{N/2}} \sum_j \left(e^{i\mathbf{k}\cdot\mathbf{R}_j^A} \left(u_{\mathbf{k},n}^A e^{-i\tilde{\epsilon}_{\mathbf{k},n}} + v_{-\mathbf{k},n}^A e^{i\tilde{\epsilon}_{\mathbf{k},n}} \right) \phi(\mathbf{r} - \mathbf{R}_j^A) \right. \\ & \left. + e^{i\mathbf{k}\cdot\mathbf{R}_j^B} \left(u_{\mathbf{k},n}^B e^{-i\tilde{\epsilon}_{\mathbf{k},n}} + v_{-\mathbf{k},n}^B e^{i\tilde{\epsilon}_{\mathbf{k},n}} \right) \phi(\mathbf{r} - \mathbf{R}_j^B) \right), \end{aligned} \quad (7.11)$$

so that the observed intensity within the first Brillouin zone and for a band $n = \pm$ reads

$$\begin{aligned} I &= |\delta\Psi_n(\mathbf{q}, \omega)|^2 \\ &= |\tilde{\psi}(\mathbf{q})|^2 \left[\delta(\omega - \tilde{\epsilon}_{\mathbf{k},n}) \left| u_{\mathbf{k},n}^A + u_{\mathbf{k},n}^B \right|^2 \delta_{\mathbf{k},\mathbf{q}} + \delta(\omega + \tilde{\epsilon}_{\mathbf{k},n}) \left| v_{-\mathbf{k},n}^A + v_{-\mathbf{k},n}^B \right|^2 \delta_{-\mathbf{k},\mathbf{q}} \right] \end{aligned} \quad (7.12)$$

In the limit where there is no interaction we recover $u_{nk}^{A/B} = C_{A/B}^{nk}$ consistent with the result of Sec. 6.2.2. The additional contribution coming from the ghost branch is weighted by the v amplitude that is weak compared to u coefficient of Bogoliubov transformation, as we see from the numerical diagonalization of \mathcal{L} (or \mathcal{L}'). The calculated intensity is given in Fig. 7.4 as a fit of experimental data of observed intensity pattern of polariton in honeycomb lattice structure.

7.2. Experimental excitation spectrum

7.2.1 Experimental realization

Experimental realization have been done in the group of Maxime Richard at Néel Institute in Grenoble with whom we were in close collaboration. Their experiment implements the honeycomb lattice with coupled micropillars etched in a planar semiconductor microcavity driven with coherent laser field at the Dirac point wavevector yielding a macroscopic occupation of the state at $k = \mathcal{K}$. As can be seen from Fig. 7.4 the system being unstable

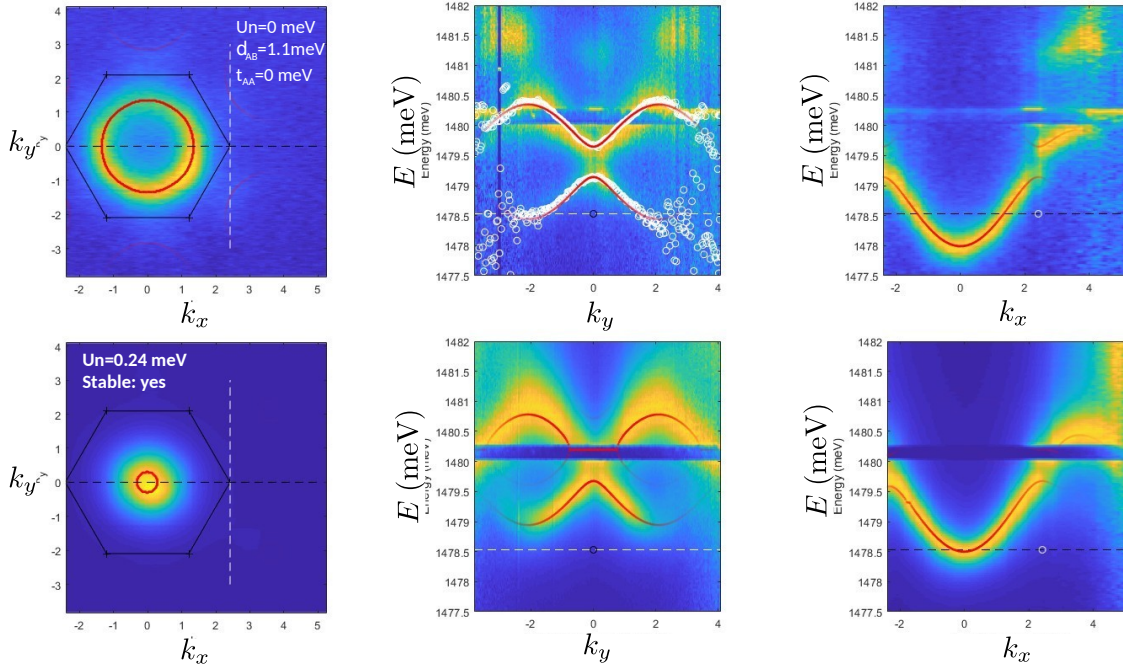


Figure 7.4: Experimental data of observed intensity pattern of polariton in honeycomb lattice for both zero (top panels) and finite (lower panels) interaction strength. Red curves correspond to theoretical fit from (Eq. 7.12). White dots are average data with Lorentzian weight. In the experiment the k -space is turned by 90° so that k_x and k_y are exchanged compared to the theoretical description.

at the C point, the Dirac cone structure is suppressed and the system is in a state below the C point (see red dot in Fig. 7.3, left panel, that represents the state of the system in the bistability one-component curve). The experimental data fit remarkably with Bogoliubov theory in both direction of momentum. We want to emphasize that the momentum space in the experiment is turned by 90° so that k_x and k_y are exchanged compared to the theoretical description. Annihilation of a part of the spectrum in the experiment as theoretically described in Sec. 6.2.2 is also seen. A gap is observed in the spectrum in the experimental k_y direction (Fig. 7.4 top middle panel). The theoretical fit is made possible thanks to energy shift between the sub-lattice. This shift might arise from the polarization

depend tunneling of polaritons in the honeycomb structure.

7.2.2 Retarded Green's function

Before concluding the Chapter, we would like to calculate the polariton spectral functions using the Green's function formalism. Since the Hamiltonian is time independent, the retarded Green's function dependent only on the time difference. We define the normal retarded Green's function as follow,

$$G_{\alpha,\beta}^R(\mathbf{k}, t) = -i\theta(t)\langle [\psi_{\mathbf{k},\alpha}(t), \psi_{\mathbf{k},\beta}^\dagger(0)] \rangle \quad (7.13)$$

and the anomalous retarded Green's function

$$\tilde{G}_{\alpha,\beta}^R(\mathbf{k}, t) = -i\theta(t)\langle [\psi_{-\mathbf{k},\alpha}(t), \psi_{\mathbf{k},\beta}(0)] \rangle \quad (7.14)$$

It is convenient to represent the Green's function in the so called Nambu structure

$$\hat{G}_{\alpha,\beta}^R(\mathbf{k}, t) = -i\theta(t) \left\langle \begin{bmatrix} \psi_{\mathbf{k},\alpha}(t)\psi_{\mathbf{k},\beta}^\dagger(0) & \psi_{-\mathbf{k},\alpha}(t)\psi_{\mathbf{k},\beta}(0) \\ \psi_{\mathbf{k},\alpha}^\dagger(t)\psi_{-\mathbf{k},\beta}^\dagger(0) & \psi_{\mathbf{k},\alpha}^\dagger(t)\psi_{\mathbf{k},\beta}(0) \end{bmatrix} \right\rangle \quad (7.15)$$

The equation of motion leads to

$$i\partial_t \hat{G}_{\alpha,\beta}^R(\mathbf{k}, t) = \delta(t)\delta_{\alpha,\beta} + \theta(t) \left\langle \begin{bmatrix} \partial_t \psi_{\mathbf{k},\alpha}(t)\psi_{\mathbf{k},\beta}^\dagger(0) & \partial_t \psi_{-\mathbf{k},\alpha}(t)\psi_{\mathbf{k},\beta}(0) \\ \partial_t \psi_{\mathbf{k},\alpha}^\dagger(t)\psi_{-\mathbf{k},\beta}^\dagger(0) & \partial_t \psi_{\mathbf{k},\alpha}^\dagger(t)\psi_{\mathbf{k},\beta}(0) \end{bmatrix} \right\rangle \quad (7.16)$$

where we used equal time commutation relation $[\psi_{\mathbf{k}',\alpha}(t), \psi_{\mathbf{k},\beta}^\dagger(t)] = \delta_{\alpha,\beta}\delta_{\mathbf{k}',\mathbf{k}}$. We next use the Bogoliubov equation of motion for the fields,

$$[i\partial_t \mathcal{S} - \mathcal{L}] \begin{pmatrix} \hat{G}_{A,A}^R(\mathbf{k}, t) & \hat{G}_{A,B}^R(\mathbf{k}, t) \\ \hat{G}_{B,A}^R(\mathbf{k}, t) & \hat{G}_{B,B}^R(\mathbf{k}, t) \end{pmatrix} = \delta(t)\mathcal{S} \quad (7.17)$$

where \mathcal{S} is the identity matrix. The equation leads to the following representation in momentum and frequency domain

$$[\omega\mathcal{S} - \mathcal{L}] \begin{pmatrix} \hat{G}_{A,A}^R(\mathbf{k}, \omega) & \hat{G}_{A,B}^R(\mathbf{k}, \omega) \\ \hat{G}_{B,A}^R(\mathbf{k}, \omega) & \hat{G}_{B,B}^R(\mathbf{k}, \omega) \end{pmatrix} = \mathcal{S} \quad (7.18)$$

leading us to the interpretation of this retarded Green's matrix as the inverse of $[\omega\mathcal{S} - \mathcal{L}]$. Considering the following Bogoliubov transformation

$$\delta a_{\mathbf{k}} = \sum_{n=\pm} u_{\mathbf{k},n}^A \gamma_{\mathbf{k},n} + (v_{-\mathbf{k},n}^A)^* \gamma_{-\mathbf{k},n}^\dagger \quad (7.19)$$

$$\delta b_{\mathbf{k}} = \sum_{n=\pm} u_{\mathbf{k},n}^B \gamma_{\mathbf{k},n} + (v_{-\mathbf{k},n}^B)^* \gamma_{-\mathbf{k},n}^\dagger \quad (7.20)$$

7.2. Experimental excitation spectrum

where the operators $\gamma_{\mathbf{k},n}^\dagger$ creates a Bogoliubov excitation in band $n = \pm$ of wave vector \mathbf{k} diagonalizing the Bogoliubov Hamiltonian

$$H_{\text{Bog}} = \sum_{n=\pm} \tilde{\epsilon}_{\mathbf{k},n} \gamma_{\mathbf{k},n}^\dagger \gamma_{\mathbf{k},n} \quad (7.21)$$

The retarded Green's function in the diagonal Bogoliubov basis is expressed by

$$G_{\gamma_n}^R(\mathbf{k}, t) = -i\theta(t) \langle [\gamma_{\mathbf{k},n}(t), \gamma_{\mathbf{k},n}^\dagger(0)] \rangle \quad (7.22)$$

$$G_{\bar{\gamma}_n}^R(\mathbf{k}, t) = -i\theta(t) \langle [\gamma_{\mathbf{k},n}^\dagger(t), \gamma_{\mathbf{k},n}(0)] \rangle \quad (7.23)$$

$$G_{\gamma_n}^R(\mathbf{k}, \omega) = \lim_{\eta \rightarrow 0} \frac{1}{\omega - \tilde{\epsilon}_{\mathbf{k},n} + i\eta} \quad (7.24)$$

$$G_{\bar{\gamma}_n}^R(\mathbf{k}, \omega) = \lim_{\eta \rightarrow 0} \frac{1}{\omega + \tilde{\epsilon}_{\mathbf{k},n} + i\eta} \quad (7.25)$$

where the mean value is taken over the Bogoliubov vacuum of excitation, i.e. $\gamma_{\mathbf{k},n}|0\rangle = 0$, $G_{\bar{\gamma}_n}^R(\mathbf{k}, \omega)$ refers to the ghost branch Green's function. Addition of the single particle loss rate $\gamma_{\mathbf{k}}$ as in Sec. 6.2.3 induces the mechanism of Brillouin zone selection for the Bogoliubov modes for the observed intensity of ghost $\bar{A}(\mathbf{k}, \omega, n) = -\frac{1}{\pi} \text{Im} \left[G_{\bar{\gamma}_n}^R \right]$ and normal branches $A(\mathbf{k}, \omega, n) = -\frac{1}{\pi} \text{Im} \left[G_{\gamma_n}^R \right]$.



Chapter 8

Conclusion and perspectives

IN this thesis we have studied the properties of a two-leg bosonic ring ladder subjected to a gauge field for wide range of interaction strengths between particles with specific application to ultra-cold atomic gases. Another type of quantum system, namely a gas of polaritons in honeycomb lattice has also been studied.

In chapter 2, we have studied the ground-state properties of weakly interacting bosons on a double ring lattice, subjected to two gauge fields. The phase diagram has been computed for high magnetic flux recovering known phases, namely the Meissner, the vortex and biased-ladder phase. An additional phase has been revealed due to the commensurability of the total flux with respect to the allowed momentum in the rings, showing imbalanced density in the Meissner phase. Also, for special values of total flux Φ , due to finite size effects, we have found that the ground state may host a single vortex even in the Meissner phase at zero interaction strength. An analysis of the persistent currents shows that it is possible to identify the Meissner, biased ladder and vortex phase. In the latter, due to finite-size of the double ring lattice, it is possible to monitor the appearance of pairs of vortices at increasing ϕ . The interference patterns among the two rings yield spiral images adapted to probe those various phases in a cold-atom experiment. In outlook of this chapter it would be interesting to study the influence of centrifugal forces to understand the threshold above which particles are ejected from the inner ring.

Beyond mean-field analysis, we computed the Bogoliubov equations in order to take into account quantum fluctuation in the double ring ladder. This has been the subject of chapter 3. We have performed a detailed study of the excitation spectrum of a weakly interacting Bose gas in a two-leg bosonic ring ladder subjected to an artificial gauge flux for all the three phases expected at weak interactions, i.e the Meissner, vortex and biased ladder phase. To capture the excitation spectrum in cold-atom experiment we have computed the dynamical structure factor accessible via angular momentum Bragg spectroscopy. Features of supersolidity have been highlighted, i.e high coherence of the gas over the ring and diagonal long-range order. The emergence of supersolidity in this system is quite remarkable, as, at difference from the spin-orbit coupled Bose gas, the visibility of the fringes can be arbitrarily tuned thanks to the absence of interspecies contact interac-



tions in the current model. Phonon like dispersion are visible in the dynamical structure factor in the Meissner phase as well as roton minima and double Goldstone mode in the vortex phase. Finally, we have shown the emergence of Josephson excitations in a finite ring, corresponding to population imbalance oscillations among the two rings. We have found that the Josephson modes appear both in the Meissner and vortex phase, in the latter case we have found both homogeneous oscillations as well as spin-like excitations carrying a longitudinal momentum. In outlook, it would be interesting to study the excitation spectrum at larger interaction strengths, where the nature of the ground state changes onto a fragmented condensate [71] or a fragmented Fermi sphere [103] at intermediate and large interactions respectively. Also a detailed study of the Josephson modes should be carried out as well as Goldstone and Higgs modes at the supersolid to BEC transition.

In chapter 4 we have studied the ground-state properties of a two-leg bosonic ring ladder subjected to gauge field in the quantum regime using both analytic and exact diagonalization techniques. The ground-state is always fragmented but its nature depends on the interaction strength, ranging from a fragmentation among two single-particle states at weak interactions to fragmented Fermi seas at very large interaction. This Fermi seas description holds provided that the tunnel coupling between the two rings is sufficiently weak and the flux threading the system relatively strong. This allows for an analytical ansatz which well describes the limits of very weak or very strong interactions. The chiral current and current-current correlation functions have been used to characterize the vortex phase. The density-density correlation function shows the onset to fermionization via the appearance of Friedel-like oscillations at large interactions, and a double-peak structure in the momentum distribution together with the demonstration of degenerate eigenvalues of the one-body density matrix establishes the fragmented nature of the state. In outlook, it would be interesting to explore the crossover from quantum regime at very weak filling considered in this work and the mean-field Gross-Pitaevskii description used in the case of very large number of bosons per lattice site.

In chapter 5, we bosonized the double ring Hamiltonian at low coupling between the rings and, thanks to the mode expansion, we have explored the influence of a defect in the Meissner phase. The bosonized Hamiltonian obtained is of the form of a sine-Gordon model with a flux. This Hamiltonian in the context of Mott insulator to superfluid transition is well known and features a commensurate-incommensurate transition that is the analogue of the Meissner to vortex transition. The vortex phase emerges when the cosine term is relevant in the sense of the renormalization group equations and is pinning the angular momentum of the system. Known fermionization approach allows to compute a renormalized form of the Luttinger Hamiltonian that permits the calculation of observables such as the chiral current in which we saw the same behavior as in the non-interacting case, and the momentum distribution, which exhibits two peaks related to the finite momenta of the solitons which are the excitations of the sine-Gordon there. We have also calculated the lowest order term of the dynamical structure factor in the vortex phase, that displays a separation in spin and charge modes. This is the same features as

what observed in Chapter 3 at weak interactions. Further studies need to be done in the calculation of the umklapp term in the dynamical structure factor. It would be an interesting point to carry numerical simulation in order to take into account finite size corrections on the dynamical structure factor and to calculate higher order terms.

In the last chapter 6 and 7 we studied the physics of a polaritonic gas in a honeycomb lattice. First we saw that the single particle description that interference between sub-lattice polariton decay into vacuum photon was inducing a disparition of a part of the spectrum, as experimentally observed. This interference has been shown to have a deeper origin, i.e that the coupling between the vacuum electromagnetic field and the polariton inside the honeycomb is suppressed. This implies the possibility of engineering dark states with very long life time. Then, considering the non-equilibrium nature of the polaritons we derived the steady state for a pumping at momentum equal to the Dirac point and contact interaction between the polaritons. As the steady-state Gross Pitaevskii equations decouple at the Dirac point we were able to derive an analogue of the one component bistability equation for polaritonic field. Quantum fluctuation on top of the steady state solution via Bogoliubov formalism enabled us to study the excitation spectrum of the interacting gas. A stability analysis of the Bogoliubov mode revealed the possibility of a physics beyond mean-field as the bistability curve shows unexpected instabilities. Finally, we drew a formal link between the excitation spectrum and the Green's function in order to account for the extinction due to the geometry of the lattice also in the case of an interacting gas. As an outlook it would be interesting to study in greater detail the origin of the dynamical instability and look for beyond mean-field states with advanced techniques, taking into account the quantum fluctuations. Moreover, the question of the topology of the Dirac point at varying interaction by the study of the Berry phase in the Bogoliubov formalism would be an interesting direction of investigation.



Appendix A

Diagonalization of the non interacting Hamiltonian

In order to diagonalize the Hamiltonian H_0 in Eq.(2.6) we introduce the Fourier transform of the field operator according to $a_{l,p} = \frac{1}{\sqrt{N_s}} \sum_k a_{k,p} e^{-ikp l}$. Periodic boundary conditions on each ring $a_{l,p} = a_{l+N_s,p}$ lead to quantized values for the wavevectors $k = \frac{2\pi}{N_s} j$, where $j \in [0, N_s - 1]$ is an integer number. The Hamiltonian in Fourier space then reads

$$\hat{H}_0 = \sum_k \begin{pmatrix} a_{k,1}^\dagger & a_{k,2}^\dagger \end{pmatrix} H(k) \begin{pmatrix} a_{k,1} \\ a_{k,2} \end{pmatrix}, \quad (\text{A.1})$$

where $H(k)$ is given by

$$H(k) = \begin{pmatrix} -2J \cos(k - \Phi - \phi/2) & -K \\ -K & -2J \cos(k - \Phi + \phi/2) \end{pmatrix}. \quad (\text{A.2})$$

We diagonalize it using the unitary transformation

$$\begin{pmatrix} a_{k,1} \\ a_{k,2} \end{pmatrix} = \begin{pmatrix} v_k & u_k \\ -u_k & v_k \end{pmatrix} \begin{pmatrix} \alpha_k \\ \beta_k \end{pmatrix}, \quad (\text{A.3})$$

where u_k and v_k are given by

$$v_k = \sqrt{\frac{1}{2} \left(1 + \frac{\sin(\phi/2) \sin(k - \Phi)}{\sqrt{(K/2J)^2 + \sin^2(\phi/2) \sin^2(k - \Phi)}} \right)} \quad (\text{A.4})$$

$$u_k = \sqrt{\frac{1}{2} \left(1 - \frac{\sin(\phi/2) \sin(k - \Phi)}{\sqrt{(K/2J)^2 + \sin^2(\phi/2) \sin^2(k - \Phi)}} \right)}. \quad (\text{A.5})$$

The final form for the Hamiltonian reads

$$\hat{H}_0 = \sum_k \alpha_k^\dagger \alpha_k E_+(k) + \beta_k^\dagger \beta_k E_-(k), \quad (\text{A.6})$$

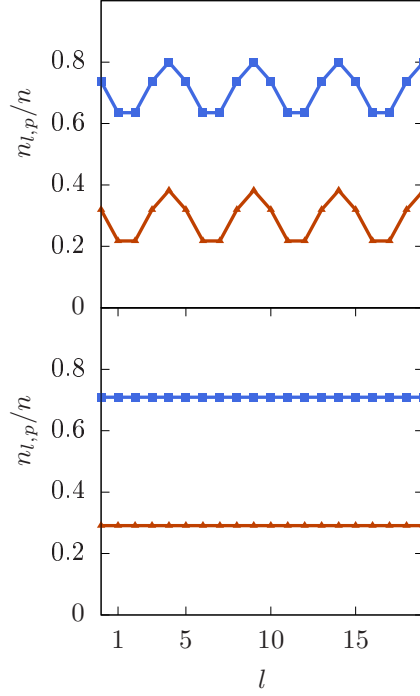


Figure A.1: Density on the double ring for $K/J = 0.95, N_s = 20, \phi = \pi/2$ and upper panel $\theta = 0.01$, down panel $\theta = 0$.

with

$$E_{\pm} = -2J \cos(\phi/2) \cos(k - \Phi) \quad (\text{A.7})$$

$$\pm \sqrt{K^2 + (2J)^2 \sin^2(\phi/2) \sin^2(k - \Phi)}. \quad (\text{A.8})$$

In the non-interacting regime, in the parameter region where the energy spectrum has a double minimum, the ground state has the form $|\psi\rangle = \frac{1}{\sqrt{N!}} \left(\cos(\theta/2) \beta_{k_1}^{\dagger} + \sin(\theta/2) \beta_{k_2}^{\dagger} \right)^N |0\rangle$. This state is fully degenerate in the occupancy of the minima, ie it provides the same ground-state energy for any choice of θ . As discussed in section IV, this degeneracy is broken at the level of mean-field by the interactions. In section III we chose to consider, in the non-interacting regime, only the case $\theta = \pi/2$ which leads to the same occupancy of the minima and hence the same density profiles on the two rings. Different choices for θ will induce different density profiles, eg an imbalanced vortex for $\theta \in]0, \pi[$ and $\theta \neq \pi/2$, and a biased-ladder for $\theta = 0$ and $\theta = \pi$ (see Fig. A.1).

Appendix B

Numerical method for the solution of the DNLSE

We provide here the details for the numerical solution of the DNLSE (3.20), obtained by iterative steps of the type

$$\begin{pmatrix} \Psi_1(t + \Delta t) \\ \Psi_2(t + \Delta t) \end{pmatrix} = U(\Delta t) \begin{pmatrix} \Psi_1(t) \\ \Psi_2(t) \end{pmatrix} \quad (\text{B.1})$$

where $U(\Delta t) = \exp(-iH\Delta t)$ is the time-evolution operator and we have introduced the vector notation $\Psi_p = \{\Psi_{1,p}, \dots, \Psi_{N_s,p}\}$. Using the Campbell Hausdorff formula we approximate it to order $(\Delta t)^2$ by

$$U(t, t + \Delta t) = e^{-iH_0\Delta t} e^{-iH_{int}\Delta t} + O(\Delta t)^2 \quad (\text{B.2})$$

The interacting Hamiltonian being diagonal in position space and the kinetic one in k -space, we use the split-step Fourier algorithm [70]. Furthermore, to obtain the ground-state wave function we perform an evolution in imaginary times. Hence the evolution of our wave function can be recast as follows:

$$\begin{pmatrix} \Psi_1(t + \Delta t) \\ \Psi_2(t + \Delta t) \end{pmatrix} = \mathcal{F}^{-1} \left[M \begin{pmatrix} e^{-E_+\Delta t} \mathbb{1}_{N_s} & \mathbf{0}_{N_s \times N_s} \\ \mathbf{0}_{N_s \times N_s} & e^{-E_-\Delta t} \mathbb{1}_{N_s} \end{pmatrix} M^{-1} \mathcal{F} \left[\begin{pmatrix} e^{-U|\Psi_1(t)|^2\Delta t} \Psi_1(t) \\ e^{-U|\Psi_2(t)|^2\Delta t} \Psi_2(t) \end{pmatrix} \right] \right] \quad (\text{B.3})$$

where $|\Psi_p(t)|^2 = \{|\Psi_{l,p}|^2, \dots, |\Psi_{N_s,p}|^2\}$, $E_{\pm} = \{E_{\pm}(2\pi/N_s), \dots, E_{\pm}(2\pi j/N_s), \dots, E_{\pm}(2\pi)\}$, and M is the unitary matrix which diagonalizes the non-interacting Hamiltonian $H(k)$ (A.2) according to

$$M = \begin{pmatrix} v_k & u_k \\ -u_k & v_k \end{pmatrix} \quad (\text{B.4})$$

and \mathcal{F} indicates the Fourier transform.



Appendix C

Interference patterns of expanding rings

We derive here the expression for the intensity of the interference pattern of expanding rings given in Eq.(2.21).

We consider first the expansion dynamics of a single condensate initially subjected to a tightly confining potential. We follow the time evolution of the condensate wavefunction following a sudden turn-off of the confinement at time $t = 0$. We will also assume that, due to a sudden decrease of the condensate density, interactions can be neglected during the dynamics, they indeed affect the dynamics of the condensate only in the initial stages of the expansion [161]. If $|\Psi(0)\rangle$ is the initial state of the system, its time evolution following the trap opening is given by

$$\begin{aligned}
 |\Psi(t)\rangle &= e^{-iHt/\hbar}|\Psi(0)\rangle \\
 &\simeq e^{-iH_{kin}t/\hbar} \sum_{\mathbf{k}} |\mathbf{k}\rangle \langle \mathbf{k} | \Psi(0)\rangle \\
 &= \sum_{\mathbf{k}} \tilde{\Psi}_0(\mathbf{k}) e^{-i\frac{\hbar\mathbf{k}^2}{2m}t} |\mathbf{k}\rangle
 \end{aligned} \tag{C.1}$$

where $H_{kin} = \hat{p}^2/2m$ is the kinetic part of the Hamiltonian. This readily yields

$$\Psi(\mathbf{x}, t) = \int d^2\mathbf{k} \tilde{\Psi}_0(\mathbf{k}) e^{-i\frac{\hbar\mathbf{k}^2}{2m}t} e^{i\mathbf{k}\cdot\mathbf{x}} \tag{C.2}$$

Using the saddle-point method to approximate the above integral, in the long-time limit we obtain

$$\Psi(\mathbf{x}, t) \approx \sqrt{\frac{2\pi m}{t\hbar}} \tilde{\Psi}_0(\bar{k}_x, \bar{k}_y) e^{i\frac{m}{2\hbar}(x^2+y^2)}, \tag{C.3}$$

where $\bar{k}_x = xm/(\hbar t)$, $\bar{k}_y = ym/(\hbar t)$, thus corresponding to the ballistic regime of the expansion – the condensate expands at constant velocity, reaching a point in space fixed by its initial momentum in the trap.

In the specific case where the initial confining potential is a double ring lattice, where $V(\mathbf{x}) = \sum_l \frac{1}{2} m\omega^2 |\mathbf{x} - \mathbf{x}_l|^2$ and \mathbf{x}_l indicate the minima of the double ring lattice in a two-dimensional plane, we study the expansion and interference of the condensates released

from each ring lattice. Assuming a deep lattice for each ring, and weak inter-ring tunneling, one may consider each lattice site l as occupied by a condensate with phase $\phi_{l,p}$ and density $n_{l,p}$ weakly coupled to the condensates on the adjacent sites.

After releasing both ring lattices, as well turning off the artificial gauge fields, using Eq.(C.3) above, the condensate wavefunctions will overlap and give rise to an interference pattern at position r . If the confinement is very tight in the radial direction or the inter-ring distance is larger than the distance among adjacent sites, the first interference fringes are obtained by the superposition of the condensates wavefunctions radially expanding, ie belonging to the same site index l . This is estimated assuming that each condensate has travelled a distance $(R_p - r)$ at constant velocity $k_{s,p} = (-1)^p (R_p - r) m / \hbar t_{TOF}$, where $p = 1, 2$ labels each ring, thus acquiring a dynamical phase $\hbar t_{TOF} k_{s,p}^2 / 2m$, which adds to the initial phase $\phi_{l,p}$. Taking into account the normalization of each condensate, one readily obtains Eq.(2.18). As discussed in [69, 162] these interference fringes, and in particular the spirals founds in the vortex phase, occur for typical times t_{TOF} of the order of $\tau_K = m(R_2 - R_1)\sigma_r / \hbar$ with σ_r the size of the initial condensate in each well. This time is large enough to ensure ballistic expansion (ie on times larger than $\tau_b = m\sigma_r^2 / \hbar$), but shorter than the time where neighbouring condensates would contribute to the interference pattern (ie $\tau_J = 2\pi m R_p \sigma_r / \hbar N_s$) and would wash out the spirals. At extremely long times, the time-of-flight images will correspond to the momentum distribution of the initial double ring lattice.

Appendix D

Rigol's method for hard-core bosons

In this appendix I present the exact approach used in Chapter 4 used to calculate the one-body density matrix in a one dimensional lattice. This approach has been introduced by Rigol [112]. The one-body Green's function for hard-core bosons can be written in the form

$$G_{ij} = \langle \Psi_{HCB}^G | b_i b_j^\dagger | \Psi_{HCB}^G \rangle = \langle \Psi_F^A | \Psi_F^B \rangle \quad (\text{D.1})$$

where we used the Jordan-Wigner transformation introduced in Chapter 4 Sec.3.51 Eq.4.19

$$|\Psi_F^A\rangle = f_j^\dagger \prod_{\gamma=1}^{j-1} e^{-i\pi f_\gamma^\dagger f_\gamma} |\Psi_F^G\rangle \quad (\text{D.2})$$

$$\langle \Psi_F^B | = \left(f_i^\dagger \prod_{\mu=1}^{i-1} e^{-i\pi f_\mu^\dagger f_\mu} |\Psi_F^G\rangle \right)^\dagger \quad (\text{D.3})$$

moreover $|\Psi_F^G\rangle$ refers to the non-interacting fermionic ground state and $|\Psi_{HCB}^G\rangle$ to the corresponding hard-core boson ground state. In general the non-interacting fermionic ground state can be put into a general form in term of the single-particle eigenfunction $P_{\sigma\delta}$ of the non-interacting problem

$$|\Psi_F^G\rangle = \prod_{\delta=1}^{N_f} \sum_{\sigma=1}^N P_{\sigma\delta} f_\sigma^\dagger |0\rangle \quad (\text{D.4})$$

where N_f is the number of fermions, N the number of sites and $|0\rangle$ the vacuum state. In order to calculate $|\Psi_F^{A/B}\rangle$ we observe that

$$\prod_{\gamma=1}^{j-1} e^{-i\pi f_\gamma^\dagger f_\gamma} = \prod_{\gamma=1}^{l-1} \left[1 - 2f_\gamma^\dagger f_\gamma \right] \quad (\text{D.5})$$

then, the action of $\prod_{\gamma=1}^{l-1} e^{-i\pi f_\gamma^\dagger f_\gamma}$ on the fermionic ground-state given by Eq. D.4 implies only a change of sign of the elements $P_{\sigma,\delta}$ for $\sigma \leq l-1$, and the creation of a particle at site

l implies the addition of one column to the matrix P , with the element $P_{l,N+1} = 1$ and all the others equal to zero. Thus, $|\Psi_F^A\rangle$, and $|\Psi_F^B\rangle$ can be rewritten as

$$|\Psi_F^{A/B}\rangle = \prod_{\delta=1}^{N+1} \sum_{\sigma=1}^M P_{\sigma\delta}^{A/B} f_{\sigma}^{\dagger} |0\rangle \quad (\text{D.6})$$

where the matrices $P^{A,B}$ are obtained from P changing the proper signs and adding the new column $N + 1$. The Green's function is then calculated numerically and the one-body density matrix ρ_{ij} is given in term of the one-body Green's function

$$\rho_{ij} = \langle b_i^{\dagger} b_j \rangle = G_{ij} + \delta_{ij}(1 - G_{ii}), \quad (\text{D.7})$$

Appendix E

Conformal field approach

It is known that the correlation of a Luttinger liquid in the massless phase corresponds to the correlation functions of a classical two-dimensional system that is at criticality since they decay as power laws. Correlation functions for critical systems are known to be invariant under a large class of transformation, including space and time rotation, scale transformations that can be included in a larger class of transformation, the conformal transformations (see Cardy(1996) Di Francesco et al (1997)). As the correlations function decay as power laws, correlations functions are invariant under rescaling so that, with ψ_i a field of the theory,

$$\langle \psi_1(r_1)\psi_1(r_2)\dots\psi_1(r_n) \rangle = b^{-\nu_1} b^{-\nu_2} \dots b^{-\nu_n} \langle \psi_1(\tilde{r}_1)\psi_1(\tilde{r}_2)\dots\psi_1(\tilde{r}_n) \rangle \quad (\text{E.1})$$

where $\tilde{r}_i = b^{-1} r_i$ and the ν_i are the scaling dimensions of the operators of the theory. The goal is then to find the proper set of $\{\nu_i\}$ that will leave the correlation function unchanged upon the rescaling. The idea of the conformal theory is to generalize these transformations to are locally simple rescalings, rotations or translations. The transformations that are locally identical to dilatation, rotations, translations are known as conformal transformation E.1. The class of conformal transformation has to preserve locally the metric so that if $r = (x_1, x_2, \dots, x_n)$,

$$\sum_i dx'_i dx'_i = b(r)^{-2} \sum_i dx_i dx_i \quad (\text{E.2})$$

The use of complex number is very useful as one is in $2D$ (space and time in our case), thus parametrizing the position as $z = x + iy$. The rescaling factor is then express in terms of analytic function f

$$dz' d\bar{z}' = |f'(z)|^2 dz d\bar{z} \quad (\text{E.3})$$

Let us take a correlation function that can be written in terms of the complex variable z as

$$G(z_1, z_2) = \left(\frac{1}{z_1 - z_2} \right)^h \left(\frac{1}{\bar{z}_1 - \bar{z}_2} \right)^{\bar{h}} \quad (\text{E.4})$$

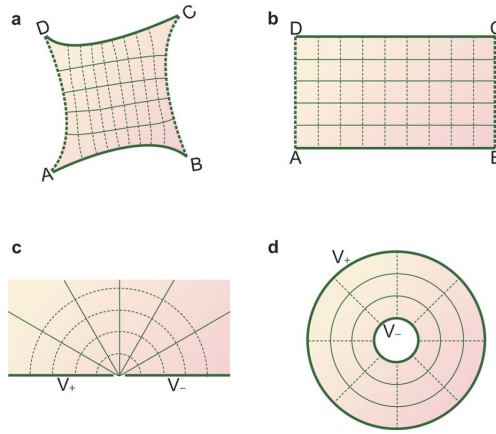


Figure E.1: Example of conformal transformation that preserves locally the angles of the original network. From [163]

Upon a change of coordinates $z \rightarrow z'$ the correlation function changes into

$$G(z'_1, z'_2) = \left[\frac{dz_1}{dz'_1} \right]^{h/2} \left[\frac{dz_2}{dz'_2} \right]^{h/2} \left[\frac{d\bar{z}_1}{d\bar{z}'_1} \right]^{\tilde{h}/2} \left[\frac{d\bar{z}_2}{d\bar{z}'_2} \right]^{\tilde{h}/2} G(z_1, z_2) \quad (\text{E.5})$$

This transformation is then allowing use to obtain correlation function in any geometry that can be obtained by a conformal transformation of the plane. It is then a incredible tool to consider special boundary condition of the system especially periodic boundary condition.

We then advice the reader to follow [118] for the technicalities of the conformal field approach for Luttinger Liquid theory with periodic boundary conditions.

Appendix F

Retarded Green's function

Green's Function One can link the retarded Green's function $G^R(\mathbf{k}, \sigma, t - t') = -i\theta(t - t') \langle [\psi_{\mathbf{k}, \sigma}(t), \psi_{\mathbf{k}, \sigma}^\dagger(t')] \rangle$ to the measured photo-emission spectra $A(\mathbf{k}, \sigma, \omega)$, where σ is a spin parameter.

$$A(\mathbf{k}, \sigma, \omega) = -\frac{1}{\pi} \text{Im} [G^R(\mathbf{k}, \omega)] \quad (\text{F1})$$

One can derive the Lehmann representation (in (\mathbf{k}, ω)) which reads

$$G^R(\mathbf{k}, \sigma, \omega) = \sum_{n,m} \frac{|\langle m | \psi_{\mathbf{k}, \sigma}^\dagger | n \rangle|^2}{\omega + E_n - E_m + i\eta} \quad (\text{F2})$$

where $\{|n\rangle\}$ is a set of eigenvector of the Hamiltonian of the system and η a regularizator parameter. For the case of single particle Hamiltonian $A(\mathbf{k}, \sigma, \omega) = \delta(\omega - \epsilon_{\mathbf{k}, \sigma})$.

Honeycomb lattice Green's function performing the equation of motion for the Green's function in an honeycomb lattice one get in the basis of site A and B .

$$G_{A/B}(\mathbf{k}, \omega) = \lim_{\eta \rightarrow 0} \frac{1}{\omega^2 - |\phi(\mathbf{k})|^2 + i\eta} \begin{pmatrix} \omega & \phi(\mathbf{k}) \\ \phi(\mathbf{k})^* & \omega \end{pmatrix} \quad (\text{F3})$$

One can then evaluate the limit in the sense of the distribution with $f(\omega)$ being a test function

$$\lim_{\eta \rightarrow 0} \int_{\mathcal{R}} d\omega \frac{\omega}{\omega^2 - |\phi_k|^2 + i\eta} f(\omega). \quad (\text{F4})$$

Let's make the following change of variable $g(\omega) = f(\omega)\omega$ so that g is still a test function and we can use known relation

$$\lim_{\eta \rightarrow 0} \int_{\mathcal{R}} d\omega \frac{1}{\omega^2 - |\phi_k|^2 + i\eta} g(\omega) = \int_{\mathcal{R}} d\omega \left(P \frac{1}{\omega^2 - |\phi_k|^2} - i\pi \delta(\omega^2 - |\phi_k|^2) \right) g(\omega) \quad (\text{F5})$$

Where P is the principal part, this term should vanish as it behaves as an odd function near 0. Then in the sense of the distribution we have that

$$\lim_{\eta \rightarrow 0} \int_{\mathcal{R}} d\omega \frac{\omega}{\omega^2 - |\phi_k|^2 + i\eta} f(\omega) = -i \frac{\pi}{2} [\delta(\omega - \epsilon_{k,+}) - \delta(\omega - \epsilon_{k,-})] \quad (\text{F.6})$$

In the same way,

$$\lim_{\eta \rightarrow 0} \int_{\mathcal{R}} d\omega \frac{\phi_k}{\omega^2 - |\phi_k|^2 + i\eta} f(\omega) = -i \frac{\pi}{2} e^{i\phi_k} [\delta(\omega - \epsilon_{k,+}) + \delta(\omega - \epsilon_{k,-})] f(\omega) \quad (\text{F.7})$$

$$\lim_{\eta \rightarrow 0} \int_{\mathcal{R}} d\omega \frac{\phi_k^*}{\omega^2 - |\phi_k|^2 + i\eta} f(\omega) = -i \frac{\pi}{2} e^{-i\phi_k} [\delta(\omega - \epsilon_{k,+}) + \delta(\omega - \epsilon_{k,-})] f(\omega) \quad (\text{F.8})$$

In the diagonal basis the Green's function reads

$$G_{\pm}(\mathbf{k}, \omega) = \begin{pmatrix} \delta(\omega - \epsilon_{k,+}) & 0 \\ 0 & \delta(\omega - \epsilon_{k,-}) \end{pmatrix} \quad (\text{F.9})$$

For a delta like source the wave function is equal to the Green's function of the problem.

Bibliography

- [1] M. H. Anderson, J. R. Ensher, M. R. Matthews, C. E. Wieman, and E. A. Cornell. Observation of Bose-Einstein condensation in a dilute atomic vapor. *Science*, 269(5221):198–201, 1995.
- [2] Bose. Plancks gesetz und lichtquantenhypothese. *Zeitschrift für Physik*, 26(1):178–181, Dec 1924.
- [3] A. Einstein. Quantentheorie des einatomigen idealen Gases. *Sitzungsberichte der Preußischen Akademie der Wissenschaften, Physikalisch-mathematische Klasse*:261–267, 1924.
- [4] Thierry Lahaye, Tobias Koch, Bernd Fröhlich, Marco Fattori, Jonas Metz, Axel Griesmaier, Stefano Giovanazzi, and Tilman Pfau. Strong dipolar effects in a quantum ferrofluid. *Nature*, 448:672 EP –, Aug 2007.
- [5] Jean Dalibard, Fabrice Gerbier, Gediminas Juzeliūnas, and Patrik Öhberg. Colloquium: Artificial gauge potentials for neutral atoms. *Rev. Mod. Phys.*, 83(4):1523, 2011.
- [6] M. Aidelsburger, M. Atala, S. Nascimbène, S. Trotzky, Y.-A. Chen, and I. Bloch. Experimental realization of strong effective magnetic fields in an optical lattice. *Phys. Rev. Lett.*, 107:255301, Dec 2011.
- [7] M. Aidelsburger, M. Atala, M. Lohse, J. T. Barreiro, B. Paredes, and I. Bloch. Realization of the Hofstadter Hamiltonian with ultracold atoms in optical lattices. *Phys. Rev. Lett.*, 111:185301, Oct 2013.
- [8] Ady Stern. Anyons and the quantum hall effect—a pedagogical review. *Annals of Physics*, 323(1):204 – 249, 2008.
- [9] Marcello Calvanese Strinati, Eyal Cornfeld, Davide Rossini, Simone Barbarino, Marcello Dalmonte, Rosario Fazio, Eran Sela, and Leonardo Mazza. Laughlin-like states in bosonic and fermionic atomic synthetic ladders. *Phys. Rev. X*, 7:021033, Jun 2017.
- [10] Eyal Cornfeld and Eran Sela. Chiral currents in one-dimensional fractional quantum hall states. *Phys. Rev. B*, 92:115446, Sep 2015.

-
- [11] Akiyuki Tokuno and Antoine Georges. Ground states of a Bose–Hubbard ladder in an artificial magnetic field: field-theoretical approach. *New Journal of Physics*, 16(7):073005, 2014.
- [12] E Orignac and T Giamarchi. Meissner effect in a bosonic ladder. *Phys. Rev. B*, 64(14):144515, 2001.
- [13] M. Piraud, F. Heidrich-Meisner, I. P. McCulloch, S. Greschner, T. Vekua, and U. Schollwöck. Vortex and Meissner phases of strongly interacting bosons on a two-leg ladder. *Phys. Rev. B*, 91:140406, Apr 2015.
- [14] Arya Dhar, Tapan Mishra, Maheswar Maji, R. V. Pai, Subroto Mukerjee, and Arun Paramekanti. Chiral mott insulator with staggered loop currents in the fully frustrated Bose-Hubbard model. *Phys. Rev. B*, 87:174501, May 2013.
- [15] Alexandru Petrescu and Karyn Le Hur. Bosonic Mott insulator with Meissner currents. *Phys. Rev. Lett.*, 111(15):150601, 2013.
- [16] Ran Wei and Erich J. Mueller. Theory of bosons in two-leg ladders with large magnetic fields. *Phys. Rev. A*, 89:063617, Jun 2014.
- [17] Shun Uchino and Akiyuki Tokuno. Population-imbalance instability in a bose-hubbard ladder in the presence of a magnetic flux. *Phys. Rev. A*, 92:013625, Jul 2015.
- [18] Ahmet Keleş and M. Ö. Oktel. Mott transition in a two-leg Bose-Hubbard ladder under an artificial magnetic field. *Phys. Rev. A*, 91:013629, Jan 2015.
- [19] Marcos Atala, Monika Aidelsburger, Michael Lohse, Julio T. Barreiro, Belén Paredes, and Immanuel Bloch. Observation of chiral currents with ultracold atoms in bosonic ladders. *Nature Physics*, 10:588 EP –, Jul 2014. Article.
- [20] B. K. Stuhl, H.-I. Lu, L. M. Aycock, D. Genkina, and I. B. Spielman. Visualizing edge states with an atomic bose gas in the quantum hall regime. *Science*, 349(6255):1514–1518, 2015.
- [21] M. Mancini, G. Pagano, G. Cappellini, L. Livi, M. Rider, J. Catani, C. Sias, P. Zoller, M. Inguscio, M. Dalmonte, and L. Fallani. Observation of chiral edge states with neutral fermions in synthetic hall ribbons. *Science*, 349(6255):1510–1513, 2015.
- [22] Vincenzo Savona, Carlo Piermarocchi, Antonio Quattropani, Paolo Schwendimann, and Francesco Tassone. Optical properties of microcavity polaritons. *Phase Transitions*, 68(1):169–279, 1999.
- [23] Adrien Dousse, Jan Suffczynski, Alexios Beveratos, Olivier Krebs, Aristide Lemaître, Isabelle Sagnes, Jacqueline Bloch, Paul Voisin, and Pascale Senellart. Ultrabright source of entangled photon pairs. *Nature*, 466:217 EP –, Jul 2010.

Bibliography

- [24] Marta Galbiati, Lydie Ferrier, Dmitry D. Solnyshkov, Dimitrii Tanese, Esther Wertz, Alberto Amo, Marco Abbarchi, Pascale Senellart, Isabelle Sagnes, Aristide Lemaître, Elisabeth Galopin, Guillaume Malpuech, and Jacqueline Bloch. Polariton condensation in photonic molecules. *Phys. Rev. Lett.*, 108:126403, Mar 2012.
- [25] M. I. Katsnelson, K. S. Novoselov, and A. K. Geim. Chiral tunnelling and the Klein paradox in graphene. *Nature Physics*, 2:620 EP –, Aug 2006. Article.
- [26] Marco Cominotti, Davide Rossini, Matteo Rizzi, Frank Hekking, and Anna Minguzzi. Optimal persistent currents for interacting bosons on a ring with a gauge field. *Phys. Rev. Lett.*, 113:025301, Jul 2014.
- [27] Luigi Amico, Gerhard Birkl, Malcolm Boshier, and Leong-Chuan Kwek. Focus on atomtronics-enabled quantum technologies. *New Journal of Physics*, 19(2):020201, 2017.
- [28] Davit Aghamalyan, Luigi Amico, and L. C. Kwek. Effective dynamics of cold atoms flowing in two ring-shaped optical potentials with tunable tunneling. *Phys. Rev. A*, 88:063627, Dec 2013.
- [29] H el ene Perrin and Barry M Garraway. Trapping Atoms With Radio Frequency Adiabatic Potentials. *Advances In Atomic, Molecular, and Optical Physics*, 66:181 – 262, 2017.
- [30] Mateusz Łacki, Hannes Pichler, Antoine Sterdyniak, Andreas Lyras, Vassilis E. Lembessis, Omar Al-Dossary, Jan Carl Budich, and Peter Zoller. Quantum hall physics with cold atoms in cylindrical optical lattices. *Phys. Rev. A*, 93:013604, Jan 2016.
- [31] Rudolf Grimm, Matthias Weidem uller, and Yurii B. Ovchinnikov. Optical dipole traps for neutral atoms. volume 42 of *Advances In Atomic, Molecular, and Optical Physics*, pages 95 – 170. Academic Press, 2000.
- [32] Immanuel Bloch. Ultracold quantum gases in optical lattices. *Nature Physics*, 1(1):23–30, 2005.
- [33] Matthew P. A. Fisher, Peter B. Weichman, G. Grinstein, and Daniel S. Fisher. Boson localization and the superfluid-insulator transition. *Phys. Rev. B*, 40:546–570, Jul 1989.
- [34] J. Stenger, S. Inouye, M. R. Andrews, H.-J. Miesner, D. M. Stamper-Kurn, and W. Ketterle. Strongly enhanced inelastic collisions in a Bose-Einstein condensate near Feshbach resonances. *Phys. Rev. Lett.*, 82:2422–2425, Mar 1999.
- [35] S. Franke-Arnold, L. Allen, and M. Padgett. Advances in optical angular momentum. *Laser & Photonics Reviews*, 2(4):299–313.

-
- [36] Robert Fickler, Radek Lapkiewicz, William N. Plick, Mario Krenn, Christoph Schaeff, Sven Ramelow, and Anton Zeilinger. Quantum entanglement of high angular momenta. *Science*, 338(6107):640–643, 2012.
- [37] Tomoki Ozawa, Hannah M. Price, Nathan Goldman, Oded Zilberberg, and Iacopo Carusotto. Synthetic dimensions in integrated photonics: From optical isolation to four-dimensional quantum Hall physics. *Phys. Rev. A*, 93:043827, Apr 2016.
- [38] K. v. Klitzing, G. Dorda, and M. Pepper. New method for high-accuracy determination of the fine-structure constant based on quantized Hall resistance. *Phys. Rev. Lett.*, 45:494–497, Aug 1980.
- [39] N.R. Cooper. Rapidly rotating atomic gases. *Advances in Physics*, 57(6):539–616, 2008.
- [40] Alexander L Fetter. Rotating trapped Bose-Einstein condensates. *Rev. Mod. Phys.*, 81(2):647, 2009.
- [41] D Jaksch and P Zoller. Creation of effective magnetic fields in optical lattices: the Hofstadter butterfly for cold neutral atoms. *New Journal of Physics*, 5:56–56, may 2003.
- [42] Bo-Nan Jiang, Xiao-Gang Wei, Guo-Wan Zhang, Jia-Hua Li, Yong-Jie Cheng, and Cheng Xu. The Sagnac effect in optical lattices with laser-assisted tunneling. *EPL (Europhysics Letters)*, 114(4):40006, may 2016.
- [43] Yanliang Guo, Romain Dubessy, Mathieu de Goër de Herve, Avinash Kumar, Thomas Badr, Aurélien Perrin, Laurent Longchambon, and H el ene Perrin. Supersonic rotation of a superfluid: a long-lived dynamical ring. *arXiv e-prints*, page arXiv:1907.01795, Jul 2019.
- [44] J. R. Abo-Shaeer, C. Raman, J. M. Vogels, and W. Ketterle. Observation of vortex lattices in Bose-Einstein condensates. *Science*, 292(5516):476–479, 2001.
- [45] Y. Aharonov and D. Bohm. Significance of electromagnetic potentials in the quantum theory. *Phys. Rev.*, 115:485–491, Aug 1959.
- [46] David J. Griffiths. *Introduction to Quantum Mechanics (2nd Edition)*. Pearson Prentice Hall, 2nd edition, April 2004.
- [47] M. B uttiker, Y. Imry, and R. Landauer. Josephson behavior in small normal one-dimensional rings. *Physics Letters A*, 96(7):365 – 367, 1983.
- [48] L. P. L evy, G. Dolan, J. Dunsmuir, and H. Bouchiat. Magnetization of mesoscopic copper rings: Evidence for persistent currents. *Phys. Rev. Lett.*, 64:2074–2077, Apr 1990.

Bibliography

- [49] Felix Bloch. Flux quantization and dimensionality. *Phys. Rev.*, 166(2):415, 1968.
- [50] A. J. Leggett. *Dephasing and Non-Dephasing Collisions in Nanostructures*, pages 297–311. Springer US, Boston, MA, 1991.
- [51] V. Chandrasekhar, R. A. Webb, M. J. Brady, M. B. Ketchen, W. J. Gallagher, and A. Kleinsasser. Magnetic response of a single, isolated gold loop. *Phys. Rev. Lett.*, 67:3578–3581, Dec 1991.
- [52] Tomoya Isoshima, Mikio Nakahara, Tetsuo Ohmi, and Kazushige Machida. Creation of a persistent current and vortex in a Bose-Einstein condensate of alkali-metal atoms. *Phys. Rev. A*, 61:063610, May 2000.
- [53] Douglas R. Hofstadter. Energy levels and wave functions of Bloch electrons in rational and irrational magnetic fields. *Phys. Rev. B*, 14:2239–2249, Sep 1976.
- [54] R. Peierls. Zur Theorie des Diamagnetismus von Leitungselektronen. *Zeitschrift für Physik*, 80(11):763–791, Nov 1933.
- [55] M Aidelsburger. Artificial gauge fields and topology with ultracold atoms in optical lattices. *Journal of Physics B: Atomic, Molecular and Optical Physics*, 51(19):193001, sep 2018.
- [56] Elliott H. Lieb and Werner Liniger. Exact analysis of an interacting Bose gas. i. the general solution and the ground state. *Phys. Rev.*, 130:1605–1616, May 1963.
- [57] Elliott H. Lieb. Exact analysis of an interacting Bose gas. ii. the excitation spectrum. *Phys. Rev.*, 130:1616–1624, May 1963.
- [58] Guillaume Lang, Frank Hekking, and Anna Minguzzi. Ground-state energy and excitation spectrum of the Lieb-Liniger model : accurate analytical results and conjectures about the exact solution. *SciPost Phys.*, 3:003, 2017.
- [59] Toshiya Kinoshita, Trevor Wenger, and David S. Weiss. Observation of a one-dimensional Tonks-Girardeau gas. *Science*, 305(5687):1125–1128, 2004.
- [60] Isabelle Bouchoule, N. J. Van Druten, and Christoph I. Westbrook. Atom chips and one-dimensional Bose gases. *arXiv e-prints*, page arXiv:0901.3303, Jan 2009.
- [61] Oliver Penrose and Lars Onsager. Bose-Einstein condensation and liquid Helium. *Phys. Rev.*, 104:576–584, Nov 1956.
- [62] C. N. Yang. Concept of off-diagonal long-range order and the quantum phases of liquid he and of superconductors. *Rev. Mod. Phys.*, 34:694–704, Oct 1962.
- [63] L. Pitaevskii and S. Stringari. Uncertainty principle, quantum fluctuations, and broken symmetries. *Journal of Low Temperature Physics*, 85(5):377–388, Dec 1991.

-
- [64] N. D. Mermin and H. Wagner. Absence of ferromagnetism or antiferromagnetism in one- or two-dimensional isotropic Heisenberg models. *Phys. Rev. Lett.*, 17:1133–1136, Nov 1966.
- [65] D. S. Petrov, G. V. Shlyapnikov, and J. T. M. Walraven. Regimes of quantum degeneracy in trapped 1d gases. *Phys. Rev. Lett.*, 85:3745–3749, Oct 2000.
- [66] Nicolas Victorin, Frank Hekking, and Anna Minguzzi. Bosonic double ring lattice under artificial gauge fields. *Phys. Rev. A*, 98:053626, Nov 2018.
- [67] L. Corman, L. Chomaz, T. Bienaimé, R. Desbuquois, C. Weitenberg, S. Nascimbène, J. Dalibard, and J. Beugnon. Quench-induced supercurrents in an annular Bose gas. *Phys. Rev. Lett.*, 113:135302, Sep 2014.
- [68] S. Eckel, F. Jendrzejewski, A. Kumar, C. J. Lobb, and G. K. Campbell. Interferometric measurement of the current-phase relationship of a superfluid weak link. *Phys. Rev. X*, 4:031052, Sep 2014.
- [69] Tommaso Roscilde, Michael F Faulkner, Steven T Bramwell, and Peter C W Holdsworth. From quantum to thermal topological-sector fluctuations of strongly interacting bosons in a ring lattice. *New Journal of Physics*, 18(7):075003, 2016.
- [70] Hanquan Wang Weizhu Bao. An efficient and spectrally accurate numerical method for computing dynamics of rotating Bose–Einstein condensates. *Journal of Computational Physics*, 217(2):612–626, 2006.
- [71] Andrey R. Kolovsky. Bogoliubov depletion of the fragmented condensate in the bosonic flux ladder. *Phys. Rev. A*, 95:033622, Mar 2017.
- [72] Eiji Kawasaki and Markus Holzmann. Finite-temperature phases of two-dimensional spin-orbit-coupled bosons. *Physical Review A*, 95(5):051601, 2017.
- [73] A. J. Leggett. Can a solid be "superfluid"? *Phys. Rev. Lett.*, 25:1543–1546, Nov 1970.
- [74] G. V. Chester. Speculations on Bose-Einstein condensation and quantum crystals. *Phys. Rev. A*, 2:256–258, Jul 1970.
- [75] E. Kim and M. H. W. Chan. Probable observation of a supersolid Helium phase. *Nature*, 427(6971):225–227, 2004.
- [76] E. Kim and M. H. W. Chan. Observation of superflow in Solid Helium. *Science*, 305(5692):1941–1944, 2004.
- [77] Alan T. Dorsey and David A. Huse. Shear madness. *Nature*, 450:800 EP –, Dec 2007.
- [78] James Day, Oleksandr Syshchenko, and John Beamish. Nonlinear elastic response in solid Helium: Critical velocity or strain? *Phys. Rev. Lett.*, 104:075302, Feb 2010.
-

Bibliography

- [79] Baumann Kristian, Guerlin Christine, Brennecke Ferdinand, and Esslinger Tilman. Dicke quantum phase transition with a superfluid gas in an optical cavity. *Nature*, 464:1301–1306, 2010.
- [80] Landig Renate, Hruby Lorenz, Dogra Nishant, Landini Manuele, Mottl Rafael, Donner Tobias, and Esslinger Tilman. Quantum phases from competing short and long-range interactions in an optical lattice. *Nature*, 532:476–479, 2016.
- [81] Eugene P. Gross. Unified theory of interacting bosons. *Phys. Rev.*, 106:161–162, Apr 1957.
- [82] Yun Li, Giovanni I. Martone, Lev P. Pitaevskii, and Sandro Stringari. Superstripes and the excitation spectrum of a spin-orbit-coupled Bose-Einstein condensate. *Phys. Rev. Lett.*, 110:235302, Jun 2013.
- [83] Jun-Ru Li, Jeongwon Lee, Wujie Huang, Sean Burchesky, Boris Shteynas, Furkan Çağrı Top, Alan O. Jamison, and Wolfgang Ketterle. A stripe phase with supersolid properties in spin-orbit-coupled bose-einstein condensates. *Nature*, 543:91 EP –, Mar 2017.
- [84] Nicolas Victorin, Paolo Pedri, and Anna Minguzzi. Excitation spectrum and super-solidity of a two-leg bosonic ring ladder, 2019.
- [85] Mathias Albert. *Superfluidity and Anderson localization in one dimensional Bose-Einstein condensates*. Theses, Université Paris Sud - Paris XI, October 2009.
- [86] D. M. Stamper-Kurn, A. P. Chikkatur, A. Görlitz, S. Inouye, S. Gupta, D. E. Pritchard, and W. Ketterle. Excitation of phonons in a bose-einstein condensate by light scattering. *Phys. Rev. Lett.*, 83:2876–2879, Oct 1999.
- [87] S. Utsunomiya, L. Tian, G. Roumpos, C. W. Lai, N. Kumada, T. Fujisawa, M. Kuwata-Gonokami, A. Löffler, S. Höfling, A. Forchel, and Y. Yamamoto. Observation of Bogoliubov excitations in exciton-polariton condensates. *Nature Physics*, 4:700 EP –, Aug 2008.
- [88] M. Lewenstein and L. You. Quantum phase diffusion of a bose-einstein condensate. *Phys. Rev. Lett.*, 77:3489–3493, Oct 1996.
- [89] B.D. Josephson. Possible new effects in superconductive tunnelling. *Physics Letters*, 1(7):251 – 253, 1962.
- [90] Michael Albiez, Rudolf Gati, Jonas Fölling, Stefan Hunsmann, Matteo Cristiani, and Markus K. Oberthaler. Direct observation of tunneling and nonlinear self-trapping in a single bosonic Josephson junction. *Phys. Rev. Lett.*, 95:010402, Jun 2005.
- [91] Alexandre L. Fetter. Nonuniform states of an imperfect Bose gas. *Annals of Physics*, 70:67–101, March 1972.

-
- [92] F. Zambelli, L. Pitaevskii, D. M. Stamper-Kurn, and S. Stringari. Dynamic structure factor and momentum distribution of a trapped Bose gas. *Phys. Rev. A*, 61:063608, May 2000.
- [93] Giovanni I. Martone, Yun Li, Lev P. Pitaevskii, and Sandro Stringari. Anisotropic dynamics of a spin-orbit-coupled Bose-Einstein condensate. *Phys. Rev. A*, 86:063621, Dec 2012.
- [94] A. Minguzzi, N. H. March, and M. P. Tosi. First-order quantum phase transition driven by rotons in a gaseous Bose-Einstein condensate irradiated by a laser. *Phys. Rev. A*, 70:025601, Aug 2004.
- [95] A. Brunello, F. Dalfovo, L. Pitaevskii, S. Stringari, and F. Zambelli. Momentum transferred to a trapped Bose-Einstein condensate by stimulated light scattering. *Phys. Rev. A*, 64:063614, Nov 2001.
- [96] Nathan Goldman, Jérôme Beugnon, and Fabrice Gerbier. Detecting chiral edge states in the Hofstadter optical lattice. *Phys. Rev. Lett.*, 108:255303, Jun 2012.
- [97] Christophe Mora and Yvan Castin. Extension of Bogoliubov theory to quasicondensates. *Phys. Rev. A*, 67:053615, May 2003.
- [98] Luca Fontanesi, Michiel Wouters, and Vincenzo Savona. Superfluid to Bose-glass transition in a 1d weakly interacting Bose gas. *Phys. Rev. Lett.*, 103:030403, Jul 2009.
- [99] Alessia Burchianti, Chiara Fort, and Michele Modugno. Josephson plasma oscillations and the Gross-Pitaevskii equation: Bogoliubov approach versus two-mode model. *Phys. Rev. A*, 95:023627, Feb 2017.
- [100] G-S Paraoanu, S Kohler, F Sols, and A J Leggett. The Josephson plasmon as a Bogoliubov quasiparticle. *Journal of Physics B: Atomic, Molecular and Optical Physics*, 34(23):4689–4696, nov 2001.
- [101] Charles-Edouard Bardyn, Torsten Karzig, Gil Refael, and Timothy C. H. Liew. Chiral Bogoliubov excitations in nonlinear bosonic systems. *Phys. Rev. B*, 93:020502, Jan 2016.
- [102] J.P. Blaizot and G. Ripka. *Quantum Theory of Finite Systems*. Cambridge, MA, 1986.
- [103] Nicolas Victorin, Tobias Haug, Leong-Chuan Kwek, Luigi Amico, and Anna Minguzzi. Nonclassical states in strongly correlated bosonic ring ladders. *Phys. Rev. A*, 99:033616, Mar 2019.
- [104] Nozières, P. and Saint James, D. Particle vs. pair condensation in attractive Bose liquids. *J. Phys. France*, 43(7):1133–1148, 1982.
- [105] Erich J. Mueller, Tin-Lun Ho, Masahito Ueda, and Gordon Baym. Fragmentation of Bose-Einstein condensates. *Phys. Rev. A*, 74:033612, Sep 2006.
-

Bibliography

- [106] Tin-Lun Ho and Sung Kit Yip. Fragmented and single condensate ground states of spin-1 Bose gas. *Phys. Rev. Lett.*, 84:4031–4034, May 2000.
- [107] N. K. Wilkin, J. M. F. Gunn, and R. A. Smith. Do attractive bosons condense? *Phys. Rev. Lett.*, 80:2265–2268, Mar 1998.
- [108] M. Girardeau. Relationship between systems of impenetrable bosons and fermions in one dimension. *Journal of Mathematical Physics*, 1(6):516–523, 1960.
- [109] Belén Paredes, Artur Widera, Valentin Murg, Olaf Mandel, Simon Fölling, Ignacio Cirac, Gora V. Shlyapnikov, Theodor W. Hänsch, and Immanuel Bloch. Tonks-Girardeau gas of ultracold atoms in an optical lattice. *Nature*, 429:277 EP –, May 2004.
- [110] François Crépin, Nicolas Laflorencie, Guillaume Roux, and Pascal Simon. Phase diagram of hard-core bosons on clean and disordered two-leg ladders: Mott insulator–Luttinger liquid–Bose glass. *Phys. Rev. B*, 84(5):054517, 2011.
- [111] P. Jordan and E. Wigner. Über das Paulische Äquivalenzverbot. *Zeitschrift für Physik*, 47(9):631–651, Sep 1928.
- [112] Marcos Rigol and Alejandro Muramatsu. Ground-state properties of hard-core bosons confined on one-dimensional optical lattices. *Phys. Rev. A*, 72:013604, Jul 2005.
- [113] Yun Li, Lev P. Pitaevskii, and Sandro Stringari. Quantum tricriticality and phase transitions in spin-orbit coupled bose-einstein condensates. *Phys. Rev. Lett.*, 108:225301, May 2012.
- [114] Min-Chul Cha and Jong-Geun Shin. Two peaks in the momentum distribution of bosons in a weakly frustrated two-leg optical ladder. *Phys. Rev. A*, 83:055602, May 2011.
- [115] Edmond Orignac, Roberta Citro, Mario Di Dio, Stefania De Palo, and Maria-Luisa Chiofalo. Incommensurate phases of a bosonic two-leg ladder under a flux. *New J. Phys.*, 18(5):055017, 2016.
- [116] J. M. Luttinger. An exactly soluble model of a many-fermion system. *Journal of Mathematical Physics*, 4(9):1154–1162, 1963.
- [117] Sin-itiro Tomonaga. Remarks on Bloch’s Method of Sound Waves applied to Many-Fermion Problems. *Progress of Theoretical Physics*, 5(4):544–569, 07 1950.
- [118] M A Cazalilla. Bosonizing one-dimensional cold atomic gases. *Journal of Physics B: Atomic, Molecular and Optical Physics*, 37(7):S1, 2004.
- [119] F. D. M. Haldane. Effective harmonic-fluid approach to low-energy properties of one-dimensional quantum fluids. *Phys. Rev. Lett.*, 47:1840–1843, Dec 1981.

-
- [120] T. Giamarchi. *Quantum Physics in One Dimension*. International Series of Monographs on Physics. Clarendon Press, 2003.
- [121] N. Didier, A. Minguzzi, and F. W. J. Hekking. Complete series for the off-diagonal correlations of a one-dimensional interacting bose gas. *Phys. Rev. A*, 80:033608, Sep 2009.
- [122] Sidney Coleman. Quantum sine-gordon equation as the massive thirring model. *Phys. Rev. D*, 11:2088–2097, Apr 1975.
- [123] F D M Haldane. Quantum field ground state of the sine-gordon model with finite soliton density: exact results. *Journal of Physics A: Mathematical and General*, 15(2):507–525, feb 1982.
- [124] Wilhelm Zwerger. Mott hubbard transition of cold atoms in optical lattices. *Journal of Optics B: Quantum and Semiclassical Optics*, 5(2):S9–S16, apr 2003.
- [125] E. Orignac, R. Citro, M. Di Dio, and S. De Palo. Vortex lattice melting in a boson ladder in an artificial gauge field. *Phys. Rev. B*, 96:014518, Jul 2017.
- [126] A. Luther and V. J. Emery. Backward scattering in the one-dimensional electron gas. *Phys. Rev. Lett.*, 33:589–592, Sep 1974.
- [127] D. Sénéchal. *An Introduction to Bosonization*, pages 139–186. Springer New York, New York, NY, 2004.
- [128] Guillaume Lang. *Correlations in low-dimensional quantum gases*. PhD thesis, 2017. Thèse de doctorat dirigée par Minguzzi, Anna et Hekking, Frank W. J. Physique de la Matière Condensée et du Rayonnement Grenoble Alpes 2017.
- [129] V. I. Yukalov, E. P. Yukalova, and V. S. Bagnato. Non-ground-state Bose-Einstein condensates of trapped atoms. *Phys. Rev. A*, 56:4845–4854, Dec 1997.
- [130] Michiel Wouters and Iacopo Carusotto. Excitations in a nonequilibrium Bose-Einstein condensate of exciton polaritons. *Phys. Rev. Lett.*, 99:140402, Oct 2007.
- [131] Alberto Amo, Jérôme Lefrère, Simon Pigeon, Claire Adrados, Cristiano Ciuti, Iacopo Carusotto, Romuald Houdré, Elisabeth Giacobino, and Alberto Bramati. Superfluidity of polaritons in semiconductor microcavities. *Nature Physics*, 5:805 EP –, Sep 2009.
- [132] A. Amo, S. Pigeon, D. Sanvitto, V. G. Sala, R. Hivet, I. Carusotto, F. Pisanello, G. Leménager, R. Houdré, E Giacobino, C. Ciuti, and A. Bramati. Polariton superfluids reveal quantum hydrodynamic solitons. *Science*, 332(6034):1167–1170, 2011.

Bibliography

- [133] S. Barland, M. Giudici, G. Tissoni, J. R. Tredicce, M. Brambilla, L. Lugiato, F. Prati, S. Barbay, R. Kuszelewicz, T. Ackemann, W. J. Firth, and G.-L. Oppo. Solitons in semiconductor microcavities. *Nature Photonics*, 6:204 EP –, Mar 2012. Correspondence.
- [134] K. G. Lagoudakis, M. Wouters, M. Richard, A. Baas, I. Carusotto, R. André, Le Si Dang, and B. Deveaud-Plédran. Quantized vortices in an exciton-polariton condensate. *Nature Physics*, 4:706 EP –, Aug 2008.
- [135] D. Sanvitto, F. M. Marchetti, M. H. Szymanska, G. Tosi, M. Baudisch, F. P. Laussy, D. N. Krizhanovskii, M. S. Skolnick, L. Marrucci, A. Lemaître, J. Bloch, C. Tejedor, and L. Viña. Persistent currents and quantized vortices in a polariton superfluid. *Nature Physics*, 6:527 EP –, May 2010. Article.
- [136] Gaël Nardin, Gabriele Grosso, Yoan Léger, Barbara Pietka, François Morier-Genoud, and Benoît Deveaud-Plédran. Hydrodynamic nucleation of quantized vortex pairs in a polariton quantum fluid. *Nature Physics*, 7:635 EP –, Apr 2011. Article.
- [137] R. T. Juggins, J. Keeling, and M. H. Szymanska. Coherently driven microcavity-polaritons and the question of superfluidity. *Nature Communications*, 9(1):4062, 2018.
- [138] Petr Stepanov, Ivan Amelio, Jean-Guy Rousset, Jacqueline Bloch, Alberto Amo, Anna Minguzzi, Iacopo Carusotto, and Maxime Richard. Two-components nature of the excitations in a polariton superfluid. *arXiv e-prints*, page arXiv:1810.12570, Oct 2018.
- [139] J. J. Hopfield. Theory of the contribution of excitons to the complex dielectric constant of crystals. *Phys. Rev.*, 112:1555–1567, Dec 1958.
- [140] J. Kasprzak, M. Richard, S. Kundermann, A. Baas, P. Jeambrun, J. M. J. Keeling, F. M. Marchetti, M. H. Szymanska, R. André, J. L. Staehli, V. Savona, P. B. Littlewood, B. Deveaud, and Le Si Dang. Bose-Einstein condensation of exciton polaritons. *Nature*, 443(7110):409–414, 2006.
- [141] Sebastian Klemmt, Petr Stepanov, Thorsten Klein, Anna Minguzzi, and Maxime Richard. Thermal decoherence of a nonequilibrium polariton fluid. *Phys. Rev. Lett.*, 120:035301, Jan 2018.
- [142] Jonathan Keeling, Marzena H. Szymańska, and Peter B. Littlewood. *Keldysh Green's function approach to coherence in a non-equilibrium steady state: connecting Bose-Einstein condensation and lasing*, pages 293–329. Springer Berlin Heidelberg, Berlin, Heidelberg, 2010.
- [143] W. Heisenberg and H. Euler. Folgerungen aus der Diracschen Theorie des Positrons. *Zeitschrift für Physik*, 98(11):714–732, Nov 1936.

-
- [144] Iacopo Carusotto and Cristiano Ciuti. Quantum fluids of light. *Rev. Mod. Phys.*, 85:299–366, Feb 2013.
- [145] C. Ciuti, V. Savona, C. Piermarocchi, A. Quattropani, and P. Schwendimann. Role of the exchange of carriers in elastic exciton-exciton scattering in quantum wells. *Phys. Rev. B*, 58:7926–7933, Sep 1998.
- [146] F. Tassone and Y. Yamamoto. Exciton-exciton scattering dynamics in a semiconductor microcavity and stimulated scattering into polaritons. *Phys. Rev. B*, 59:10830–10842, Apr 1999.
- [147] Cristina Bena and Gilles Montambaux. Remarks on the tight-binding model of graphene. *New Journal of Physics*, 11(9):095003, sep 2009.
- [148] A. H. Castro Neto, F. Guinea, N. M. R. Peres, K. S. Novoselov, and A. K. Geim. The electronic properties of graphene. *Rev. Mod. Phys.*, 81:109–162, Jan 2009.
- [149] T. Jacqmin, I. Carusotto, I. Sagnes, M. Abbarchi, D. D. Solnyshkov, G. Malpuech, E. Galopin, A. Lemaître, J. Bloch, and A. Amo. Direct observation of Dirac cones and a flatband in a honeycomb lattice for polaritons. *Phys. Rev. Lett.*, 112:116402, Mar 2014.
- [150] Aaron Bostwick, Taisuke Ohta, Thomas Seyller, Karsten Horn, and Eli Rotenberg. Quasiparticle dynamics in graphene. *Nature Physics*, 3:36 EP –, Dec 2006. Article.
- [151] Eric L. Shirley, L. J. Terminello, A. Santoni, and F. J. Himpsel. Brillouin-zone-selection effects in graphite photoelectron angular distributions. *Phys. Rev. B*, 51:13614–13622, May 1995.
- [152] Cristiano Ciuti and Iacopo Carusotto. Input-output theory of cavities in the ultra-strong coupling regime: The case of time-independent cavity parameters. *Phys. Rev. A*, 74:033811, Sep 2006.
- [153] C. W. Gardiner and M. J. Collett. Input and output in damped quantum systems: Quantum stochastic differential equations and the master equation. *Phys. Rev. A*, 31:3761–3774, Jun 1985.
- [154] Cristiano Ciuti, Paolo Schwendimann, and Antonio Quattropani. Parametric luminescence of microcavity polaritons. *Phys. Rev. B*, 63:041303, Jan 2001.
- [155] P. G. Savvidis, C. Ciuti, J. J. Baumberg, D. M. Whittaker, M. S. Skolnick, and J. S. Roberts. Off-branch polaritons and multiple scattering in semiconductor microcavities. *Phys. Rev. B*, 64:075311, Jul 2001.
- [156] Maciej Pieczarka, Marcin Syperek, Łukasz Dusanowski, Jan Misiewicz, Fabian Langer, Alfred Forchel, Martin Kamp, Christian Schneider, Sven Höfling, Alexey Kavokin, and Grzegorz Sęk. Ghost branch photoluminescence from a polariton fluid under nonresonant excitation. *Phys. Rev. Lett.*, 115:186401, Oct 2015.

Bibliography

- [157] V. Kohnle, Y. Léger, M. Wouters, M. Richard, M. T. Portella-Oberli, and B. Deveaud-Plédran. From single particle to superfluid excitations in a dissipative polariton gas. *Phys. Rev. Lett.*, 106:255302, Jun 2011.
- [158] Iacopo Carusotto and Cristiano Ciuti. Probing microcavity polariton superfluidity through resonant Rayleigh scattering. *Phys. Rev. Lett.*, 93:166401, Oct 2004.
- [159] Petr Stepanov, Ivan Amelio, Jean-Guy Rousset, Jacqueline Bloch, Aristide Lemaître, Alberto Amo, Anna Minguzzi, Iacopo Carusotto, and Maxime Richard. Dispersion relation of the collective excitations in a resonantly driven polariton fluid. *arXiv e-prints*, page arXiv:1810.12570, Oct 2018.
- [160] C Menotti, A Smerzi, and A Trombettoni. Superfluid dynamics of a bose–einstein condensate in a periodic potential. *New Journal of Physics*, 5:112–112, sep 2003.
- [161] Y. Castin and R. Dum. Bose-einstein condensates in time dependent traps. *Phys. Rev. Lett.*, 77:5315–5319, Dec 1996.
- [162] Tobias Haug, Joel Tan, Mark Theng, Rainer Dumke, Leong-Chuan Kwek, and Luigi Amico. Readout of the atomtronic quantum interference device. *Phys. Rev. A*, 97:013633, Jan 2018.
- [163] Weimin Wang, Wenying Ma, Qiang Wang, and Hao Ren. Conformal mapping for multiple terminals. *Scientific Reports*, 6:36918 EP –, Nov 2016. Article.